THEORETICAL AND EXPERIMENTAL STUDIES OF A SUPERCONDUCTIVE DETECTOR OF ENERGETIC PARTICLES

by

GEORGE ANTHONY MAY

M.A., University of Western Ontario 1964
B.Sc. Hon., University of Toronto 1962

A THESIS SUBMITTED IN PARTIAL FULFILMENT OF

THE REQUIREMENTS FOR THE DEGREE OF

DOCTOR OF PHILOSOPHY

in the Department

of

Physics

We accept this thesis as conforming to the required standard

THE UNIVERSITY OF BRITISH COLUMBIA

May, 1975

In presenting this thesis in partial fulfilment of the requirements for an advanced degree at the University of British Columbia, I agree that the Library shall make it freely available for reference and study. I further agree that permission for extensive copying of this thesis for scholarly purposes may be granted by the Head of my Department or by his representatives. It is understood that copying or publication of this thesis for financial gain shall not be allowed without my written permission.

Department of PHYSICS

The University of British Columbia
2075 Wesbrook Place
Vancouver, Canada
V6T 1W5

Date 22 July 75'

Theoretical and Experimental Studies of a Superconductive Detector of Energetic Particles.

ABSTRACT:-

In nuclear-particle energy-loss spectrometers, it is desirable to have the signal charge per unit energy loss as large as possible, because the fractional resolution due to statistical fluctuations in the signal charge is inversely proportional to the square root of the number of charge carriers generated. Thus superconductors with an inherently narrow energy-gap 2Δ would be of interest if the quasiparticles generated from the energy of the incident particle could be distinguished from the Cooper-pairs. A superconductive tunnelling junction (STJ) satisfies this condition because the current flow consists essentially of quasiparticle tunnelling current provided that the Josephson-supercurrent is suppressed by a steady magnetic field. Thus if the particle energy is used to create quasiparticles in a STJ the increase in quasiparticle density causes a measurable increase in the tunnelling current, which constitutes the signal. The mechanism proposed for the transformation of the particle energy to quasiparticles involves the conversion of energy to heat when the particle penetrates the STJ and enters the substrate. The transient increase in the temperature of the junction films increases the thermally generated quasiparticle density. This thermal model gave numerical results in good agreement with experimental results obtained with 5.13 MeV α-particles incident on thin film lead and tin STJ's deposited on microscope glass slide substrate.

The SJT's used for the experiments consisted of crossed 2000 A thick

metal films, separated by an oxide barrier of approximately 12 A thick produced by glow-discharge anodization. Reproducible fabrication of arrays of STJ's was achieved by this method. Measurements were made on the junctions at different temperatures between 1.2 K and about half the critical temperature, and with different junction bias voltages. A steady magnetic field of 15 gauss was used to suppress the Josephson supercurrent.

5.13 MeV α-particles were directed at the junctions, and voltage signals caused by the particle impacts were observed across the junction. The signal amplitudes were temperature and bias-voltage dependent. The best signal to noise ratios (peak signal/rms noise) observed were 20 and 40 respectively for lead and tin junctions, using a transformer-input N-channel metal oxide semiconductor preamplifier operated at liquid helium temperatures. The pulse amplitude distributions were analysed and found to consist of an initially decreasing pulse-density with increasing pulse amplitude, then a nearly flat plateau region followed by a rapid drop off. This type of distribution curve was theoretically predicted using the thermal model mentioned above. The form of the distribution curve is a consequence of the distribution of the position of the particle impacts on the STJ, and of the angle of the particle impact. Thus superconductive particle detectors with this type of geometry and with uncollimated particle sources do not give rise to line spectra. Based on the physical understanding of the nature of signal-pulses from the α-bombarded STJ's on glass substrates, a heat-sink chip type detector is proposed. This is expected to be a superior and practical particle energy spectrometer.

Theoretical investigations were made into the relative merits of superconductor-insulator-superconductor (SS) and normal metal-insulator-

superconductor (NS) tunnelling junctions as fast response thermometers. For $\omega < 10^9$ Hz, SS junctions were shown to be theoretically superior in sensitivity and signal to noise ratio. It was also found theoretically that for the SS junctions, there is a temperature which for a specified bandwidth, junction capacitance, and superconductor type optimises the signal amplitude. Moreover, the inherent junction electrical noise, essentially shot noise, was shown to be inversely proportional to Δ.

CONTENTS

		Page
CHAPTER 1	INTRODUCTION	1
CHAPTER 2	THEORY OF OPERATION OF THE SUPERCONDUCTIVE QUASIPARTICLE TUNNELLING JUNCTION PARTICLE DETECTOR.	9
	- Introduction	9
	- Types of Superconductive Particle-Detectors.	25
	1. Glass-substrate type.	28
	2. Phonon-barrier type.	30
	- Scaling Theory	31
	- Response of a Superconductive Tunnelling Junction S.T.J. to Small Temperature Changes	32
	- Superconductor-Superconductor Superconductive Tunnelling Junctions	33
	- Choice of Superconductive Tunnelling Junctions for Use as Particle-Detectors	37
	- Metal-Superconductor (N.S.) Superconductive Tunnelling Junctions	37
	- Comparisons of N.S. and S.S. Superconductive Tunnelling Junctions	39
	- Performance Figures for S.S. S.T.J.'s	41
	- Inherent Noise in S.T.J.'s	45
	- Other Factors Affecting the Resolution of Superconductive Particle-Detectors	50
	- Statistical fluctuation of total number N of charge carriers generated by particle	50
	- Barrier oxide thickness fluctuations	50
	- 'Angle' effect	50
	- Finite junction-size effect	51

		Page
CHAPTER 3	NUMERICAL METHODS AND RESULTS.	52
	- Introduction	52
	- Modification of the Form of the Classical Heat-Diffusion Equation	52
	- Boundary Conditions for the Heat-Diffusion Problem, Glass-Substrate Type Superconductive Particle-Detector	54
	- Phonon-Barrier Type Superconductive Particle-Detector	58
	- Numerical Solutions with Radial Symmetry	60
	- Translation to Finite-Differences Equations	61
	- Initial and Boundary Conditions	63
	- Thermophysical Data Used for Numerical Calculations	63
	- Temperature and Signal-Current Calculations	65
	- Stability Considerations	66
	- Computer-Program Organisation for the One-Dimensional Radially Symmetric Approximations	68
	- Verification of Numerical Methods	73
	- Results: One-Dimensional Radially Symmetric Approximations for Glass Substrated S.P.D., Valid for Early Times	73
	- Results: One-Dimensional Radially Symmetric Approximations for the Phonon-Barrier S.P.D.	75
	- Spherically-Symmetric Approximations	80
	- Calculation of Glass-Substrated S.P.D. Response to α-Particle Impact Assuming Finite Length, Normal Incident α-Particle Track, with a Finite Sized Junction	82
	- Finite Junction Size Effects	85
	- Magnitude of the Angle-Effect	93
	- Conclusion	95

		Page
CHAPTER 4	SUPERCONDUCTIVE-TUNNELLING JUNCTION FABRICATION	96
	- Introduction	96
	- S.T.J. Sample Fabrication	98
	- Substrate cleaning	98
	- Evaporation mask and positioning	101
	- Deposition of junction films by evaporation	101
	- Plasma cleaning and anodization	103
	- Typical S.T.J. Fabrication Run	104
	- Visual Inspection	105
	- Sample Passivation	107
	- Group Separation	107
	- Lead Attachment	107
	- Sample Stability	107
	- Variations of Sample Fabrication Procedures	108
	- Vapour depositions of polyethylene	108
	- Photo resist covered substrate	108
	- Al_2O_3 barrier	109
CHAPTER 5	EXPERIMENTAL METHODS AND RESULTS	110
	- Cryogenics	110
	- Junction Selection	113
	- Junction D.C. Characteristics Measurements	115
	- Junction-Degradation	123
	- 'S' Type Negative-Resistance (fold back)	123
	- Pulse Measurements with Room Temperature Preamplifier	125
	- Pulse Amplitude Dependence on Bias-Voltage	128
	- Pulse Amplitude Dependence on Temperature; Sn Junctions	128
	- α-Particle Induced Pulse-Signals and Noise	129

Page

CHAPTER 5 Cont'd...

- Pulse Measurements with Directly-Coupled Liquid-Helium Temperature Amplifier 131
  - Liquid helium amplifier details 131
  - Low temperature preamplifier test and calibration at liquid helium temperature and measurement of junction capacitance 134
- Measurements with Liquid Helium Temperature Amplifier with Input Voltage Step-Up Pulse-Transformer 137
  - Voltage step up pulse-transformer fabrication and tests 137
  - Pulse-transformer-input low-temperature preamplifier room-temperature tests 141
  - Measurements of Pb junctions with the transformer-input low temperature amplifier 142
  - Discriminator-counter readings 144
  - Effect of temperature variation on signals 144
  - The signal to noise ratio for Pb junction R148S2J2 147
- Measurements on Sn Junctions Using the Transformer Input Low-Temperature Preamplifier 149
  - Amplifier system calibration 149
  - α-Particle induced pulses, direct oscilloscope measurements 149
  - Kicksorter measurements 151
- Summary 152

CHAPTER 6 REDUCTION OF EXPERIMENTAL RESULTS AND COMPARISON WITH THEORY 153

- Introduction 153
- Junction Quasiparticle Current Dependence on Temperature at Constant Bias Voltage 153
- Variation of R_{dyn} with Temperature at Constant Bias Voltage 158
- Dependence Upon Ambient (Mean Junction) Temperature of Junction Voltage 161
- Response to Low and High Frequency Temperature Changes
- Effect of Junction-Capacitance on Junction Voltage Waveform 162

Page

CHAPTER 6 Cont'd...

- Scaling of Theoretical Signal Current for a Reference Junction $I_{Sref}(t)$ to Specified Junction Parameters 163

- Numerical Calculations of the Effect of Junction Capacitance and Amplifier Rise-Time on Signal Voltage Output Waveform and Comparisons with Experimental Observations. Room-Temperature Preamplifier Case 168

- Numerical Calculation of α-Particle Induced Output Signal Voltage from the Transformer Input Amplifier System and Comparison with Experiments 170

- Comparison of Theoretically Derived and Observed Output Pulse Amplitude Distribution 173

- Summary 174

CHAPTER 7 A PROPOSED SUPERCONDUCTIVE PARTICLE DETECTOR, THE HEAT-SINK CHIP TYPE 175

- Description and Analysis

- Limits on Performance of the SPD 182

CHAPTER 8 CONCLUSIONS 185

- Principal Results from the Present Work 185

- Expected Performance of Superconductive Particle-Detectors 187

- Future Work 188

Page

APPENDIX 5.1 EXPLANATION OF OBSERVED FALSE-PEAK EFFECT DUE TO SIGNAL PULSE CLIPPING BY A CURRENT-STEP ON THE JUNCTION I.V. CHARACTERISTIC. 189

LIST OF TABLES

TABLE		Page
3.1	Specific Heat and Thermal Conductivity Data of Glass Used in Numerical Calculations Relating to the Glass-Substrated Superconductive Particle-Detector.	64
5.1	Discriminator Counter Readings on Alpha-Particle Induced Pulses from R67S1J3.	124a
5.2	Record from Discriminator Counter Measurements of R148 S2J2 at 1.2 K.	143
5.3	Temperature Dependence of Alpha-Particle Induced Pulses in Lead Junction R148S2J2.	145

LIST OF FIGURES

FIGURE		Page
2.1	Energy-Diagram for a Metal-Insulator-Metal Junction with Applied Potential Difference V, (at finite temperature).	10
2.2	Energy-Diagram of an NS Junction in the Semiconductor Representation, at Finite Temperature, with Applied Potential Difference V.	10
2.3	Energy-Diagram for a S.S. Junction in the Semiconductor Representation, at Finite Temperature with Applied Potential Difference V.	17
2.4	Alpha-Particle Impinging on Glass-Substrate Type Superconductive Quasiparticle Tunnelling Junction Particle-Detector.	26
2.5	Alpha-Particle Impinging on Phonon-Barrier Type Superconductive Quasiparticle Tunnelling Junction Particle-Detector.	26
2.6	Equivalent Circuit for a Superconductive Quasiparticle Tunnelling Junction.	34
2.7	Current-Response Sensitivity per Unit Junction Normal Tunnel-Conductance.	42
2.8	Voltage-Response Sensitivity, of SS Junction to Temperature Pulse, Frequency as Parameter.	43

List of Figures Cont'd...

FIGURE		Page
2.9	Variation of Signal Due to Angle of Incidence of Impinging Particle.	49
2.10	Variation of Signal Due to Impact of Incoming Particle at Different Points of a Finite Sized Junction.	49
3.1A	Alpha-Particle Penetrating a Glass-Substrated Superconductive Tunnelling Junction.	59
3.1B	1-Dimensional Radially Symmetric Approximation of the Thermal Situation of an Alpha-Particle Penetrating a Glass-Substrated Superconductive Tunnelling Junction.	59
3.2	Comparison of Temperature Profiles Obtained Analytically and by Finite-Difference Method.	70
3.3	Temperature Profiles, 1-Dimensional Radially Symmetric Heat-Diffusion in Glass-Substrate.	71
3.4	Signal-Current as a Function of Time, 1-Dimensional Radially Symmetric Approximation of an Alpha-Particle Impact on a Glass-Substrated Superconductive Tunnelling Junction.	72
3.5	Normal Radius as a Function of Time, Derived from a 1-Dimensional Radially Symmetric Approximation of an Alpha-Particle Impact on a Glass-Substrated Superconductive Tunnelling Junction.	74
3.6	Temperature Profiles as a Function of Time for a Tin Superconductive Tunnelling Junction on a Phonon-Barrier.	76

List of Figures Cont'd...

FIGURE		Page
3.7	Signal Current as a Function of Time for a Tin Phonon-Barrier Type Superconductive Particle-Detector at 1.2°K (theoretical).	77
3.8	Temperature Profiles as a Function of Time for a Lead Superconductive Tunnelling Junction on a Phonon-Barrier (theoretical).	78
3.9	Signal Current as a Function of Time for a Lead Phonon-Barrier Type Superconductive Particle-Detector at 2.4°K (theoretical).	79
3.10A	Cross-Section of a Normal-Incidence Alpha-Particle Impact on a Glass-Substrated Superconductive Particle-Detector.	81
3.10B	Geometry of 'Cell' Array Used for Numerical Calculations.	81
3.11	Temperature Profiles at Different Depths in the Glass Substrate as a Function of Time.	83
3.12	Junction Signal Current as a Function of Time for an Infinite-Area Junction.	84
3.13	Alpha-Particle Impact Point Coordinate Map.	86
3.14	Calculated Signal Currents as a Function of Time for Different Alpha-Particle Impact-Points.	87
3.15	Calculated Probability Density of Signal-Current Amplitudes.	89
3.16	Calculated Probability Density of Accumulated Signal Charge to Time = 0.56 μs.	90
3.17	Effects of Angle of Impact and Junction Size on Signal Current.	92

List of Figures Cont'd...

FIGURE		Page
4.1	Superconductive Tunnelling Junction Samples.	97
4.2	Superconductive Tunnelling Junction Sample Details.	97
4.3	Apparatus for Junction Fabrication Inside Vacuum Chamber.	97
4.4	Evaporation Masks and Mask-Changer Details.	97
4.5	Diagram of Apparatus for Sample Fabrication Inside Vacuum Chamber.	100
4.6	Superconductive Tunnelling Junction Structural Details.	100
4.7	Heated-Wire Sample Separator.	106
5.1	Sample-Holder for Experiments with Sample Mounted, Alpha-Particle Source and Low-Temperature Preamplifier.	114
5.2	Slide Switch Details on Sample Holder.	114
5.3	Sample Mounted on Sample Holder, with Alpha-Particle Source Facing Junctions.	114
5.4	Sample Mounted on Sample Holder, with Alpha-Particle Source Turned Away from Junctions.	114
5.5	Junction D.C. Characteristics Measurement Circuit Using a 4-Point Method.	116
5.6	Current Stream-Lines and Voltage Equipotentials for a Junction Without Oxide Barrier, Giving Rise to "Negative-Resistance" in 4 Point Measurements.	116
5.7	D.C. Junction Characteristics of Lead Junction R123S6J2 at $4.2^{o}K$.	118
5.8	I.V. Characteristics of Tin Junction R77S1J3 at $1.2^{o}K$.	120

List of Figures Cont'd...

FIGURE		Page
5.9	Temperature Dependence of I.V. Characteristics of Tin Junction R67S1J3.	121
5.10	'S' Type Negative Resistance in Junction I.V. Characteristics of Thermal Origin.	124
5.11	Amplifier Circuiting for Alpha-Particle Induced Pulse Observations.	124a
5.12	Alpha-Particle Induced Pulses in Tin Junction R67S1J3.	124
5.13	Pulse Amplitude as a Function of Bias Voltage.	127
5.14	Pulse-Amplitude as a Function of Junction Temperature.	127
5.15	Circuit Diagram of Direct-Coupled Low-Temperature Preamplifier, Connected to a Tunnelling Junction and 'Post' Amplifier.	130
5.16	Junction Capacitance Measurement and Amplifier Calibration Using the I.V. Characteristics.	130
5.17	Variation of Decay Time Constant of Voltage-Response to Calibration Charge with Junction Bias-Voltage.	135
5.18	Dust-Iron Pulse-Transformer Core Configurations (1.4 times actual size).	138
5.19	Pulse-Transformer Test-Circuit and Waveforms.	138
5.20	Circuit Diagram of Transformer Input Low-Temperature Preamplifier Connected to Junction and 'Post' Amplifier.	140
5.21	Alpha-Particle Induced-Pulses from Lead Junction R148S2J2, Using the Transformer Input Low Temperature Preamplifier.	140
5.22	Pulse-Amplitude Distribution Curve from Discriminator Counter Readings for Lead Junction R148S2J2.	143

List of Figures Cont'd...

FIGURE		Page
5.23	Amplifier System/Junction Combination Calibration Curve.	148
5.24	'Kicksorter' Record of Pulse-Amplitude Distribution from Tin Junction R164S1J5, (record made with transformer input low-temperature preamplifier).	150
5.25	Alpha-Particle Induced Pulses in Tin Junction R164S1J5, Using Transformer-Input Low-Temperature Preamplifier.	148
6.1	Ratio of Junction Quasiparticle Tunnelling Current at Constant Bias Voltage to Junction Normal Conductance as a Function of Temperature Parameter $\beta\Delta$ for Lead Junctions (theory and experiment).	154
6.2	Ratio of Junction Quasiparticle Tunnelling Current at Constant Bias Voltage to Junction Normal Conductance as a Function of Temperature Parameter $\beta\Delta$ for Tin Junctions (theory and experiment).	155
6.3	Variation of the Ratio of Junction Dynamic Tunnel Conductance to Junction Normal Conductance with Temperatur Parameter $\beta\Delta$.	157
6.4	Temperature Dependence of Junction Voltage-Response to Alpha-Particle Caused Temperature-Pulse.	160
6.5	Calculated Reference-Junction Signal-Current.	166
6.6	Output Signal Voltage from Room Temperature Amplifier System (theory and experiment).	167
6.7	Alpha-Particle Generated Output Response for Tin Junction R164S1J5.	171

List of Figures Cont'd...

FIGURE		Page
7.1	Alpha-Particle Impinging on Heat-sink Chip Type Superconductive Quasiparticle Tunnelling Junction Particle-Detector.	176
APP. 5.1		189
1	Current-Step Signal-Voltage Clipping Effect.	190
2	Observed False-Peak Effect Due to Clipping.	190

ACKNOWLEDGEMENTS

Special thanks are due to my supervisor Dr. B.L. White for his generous assistance, understanding, and encouragement, especially during the writing of this thesis.

Valuable discussions with Dr. R.E. Burgess are acknowledged with gratitude.

Helpful suggestions and other assistance from other members of my supervisory committee Drs. G. Jones, A.V. Gold, and P. Matthews are gratefully acknowledged.

Thanks are due to Dr. G.H. Wood my predecessor, in this study, who left me the cryogenic system he built for his experiments, and valuable information related to the experiments.

Thanks are due to the Van de Graaff Group for providing assistance and a friendly environment.

CHAPTER ONE

INTRODUCTION

In experimental studies of energetic charged particles and photons (energy $\gtrsim$ 1keV) the name detector is often applied to a class of devices which provide as output an impulsive voltage or current signal which is correlated in time with the passage of the particle or photon into or through the device, and whose amplitude contains information about the amount of energy lost by the particle or photon in the device; where the energy is of primary interest, the detector is called a spectrometer. In many detectors, the current signal is integrated on the detector capacitance, giving an output signal proportional to the collected charge. In this thesis we will use the term "detector" to mean a spectrometer, and will refer only to charged particles and not specifically to photons. A large variety of different physical effects are used in detectors, briefly described below, (see Dearnaley & Northrop (Ref. 1.1) for a good detailed account of detectors).

The ionization chamber and the proportional counter are based on gas ionization, combined with proportional avalanche multiplication in the case of the latter. They exhibit a reasonably linear relationship between the signal charge (number of gaseous ions collected on the electrodes multiplied by the electronic charge) and the energy lost in the gas by the primary

energetic particle. Statistical fluctuations in the number of ions collected for given energy loss (which is related to the average energy loss required to generate an ion pair in the gas, about 30 eV for most spectrometer gases) give an energy resolution which is typically of the order of 2.5 keV for 100 keV electrons. When an energetic charged particle passes through a scintillation crystal part of the energy deposited by the particle results in the emission of fluorescent photons by the crystal. The photons are collected (by an optical system) and measured by a photomultiplier. The photomultiplier output (charge) is proportional to the number of fluorescent photons, which in turn is proportional to the charged particle energy loss. Thus the photomultiplier output is proportional to the particle energy loss; this is the basis of the scintillator counter, with typical resolution of 150 keV FWHM for a 5 MeV α-particle, for example.

Semiconductor junction detectors will be discussed in more detail because of their practical importance in high-resolution particle-energy spectrometry, where they are currently the highest resolution energy-loss spectrometers available. Thus they constitute a suitable basis for the comparison and evaluation of the superconductive tunnelling junction detectors to be described in this thesis. In operation the semiconductor junction detector is reverse biased such that the high electric field intensity depletion layer extends as completely as possible throughout the volume of the detector. A charged particle passing through and stopped in the detector has part of its kinetic energy converted to electrons and holes (the rest of the energy ends up as phonons and radiation damage if any). The electrons and holes are acted on by the depletion-layer field such that the electrons move towards the 'n' region and holes towards the 'p' region.

The carriers are said to be "collected", and the collected charge constitutes the signal. For a given type of incident particle the average number of charge carriers generated, 'N', is proportional to the energy loss in the depletion region, thus the measured signal-charge is proportional to the energy of the particle W. For a given junction type and particle we can thus specify the energy w required to generate a single ion pair $w = W/N$. If the charge production processes were uncorrelated then the standard deviation of the number of particles produced, σ_N, would be equal to $\sqrt{N}$. But the processes are in fact correlated by the requirement that $N \cdot w = W$ (Ref. 1.2), and $\sigma_N = \sqrt{FN}$ where F is the "Fano-factor", with a value of $0 \leq F \leq 1$, ($F = 1$ for completely independent charge-carrier production and $F = 0$ for complete dependence). The 'energy-resolution' R can then be defined as:-

$$R = \frac{\sigma_q}{\overline{q}} = \frac{\sqrt{FN} \cdot e}{N \cdot e} = \sqrt{\frac{F}{N}} = \sqrt{\frac{Fw}{W}} \qquad (1.1)$$

where σ_q is the standard deviation of signal charge, equal to $\sigma_N \cdot e$ and $\overline{q}$ is average signal charge equal to $N \cdot e$.

This definition of resolution is related to the 'FWHM' definition (full width at half maximum , often used in spectrometry application) by:-

$$2.35 \cdot \frac{\sigma_q}{\overline{q}} = \frac{\text{FWHM(eV)}}{\text{Peak Energy(eV)}} \qquad (1.2)$$

if the peak is gaussian in shape. Ref. (1.2).

If the optimum mean square system noise voltage within the bandwidth required to measure the signal is $\overline{V_o^2}$ (this includes shot, junction leakage, Johnson[Ref.1.3], and preamplifier noise), the energy output resolution in the output is:-[Ref. 1.1]

$$\frac{\text{Standard deviation of preamp. output}}{\text{Signal amplitude from preamp.}} = \sqrt{\frac{Fw}{W}}\left(1 + \frac{w \cdot \overline{V_o^2} \cdot C^2}{F \cdot W \cdot e^2}\right)^{\frac{1}{2}} \qquad (1.3)$$

where C = detector capacitance.

To improve resolution the preamplifier noise performance must be improved, the detector leakage current decreased and w decreased. The most important factor is the decrease of w; with consequent increase of N, large improvements in resolution can result. The best semiconductor detectors are made from Ge, with an energy gap of 0.67 eV, and w = 2.94 eV, and a measured Fano factor of < 0.08 (Ref.1.3). Semiconductors of lower energy gap like indium antimonide of Eg = 0.17 eV have been tried, but were found to be unsuitable because of leakage currents due to impurity band conduction.[Ref. 1.1]

The energy gap associated with superconductivity is sufficiently small to create interest in using some suitable superconductivity effect in particle detection. The quasi particles excited in a superconductor can be detected by observing the tunnel-current between two superconductors (or superconductor and normal metal) separated by a thin insulating barrier. Quasiparticle superconductive tunnelling junctions were first studied in 1960 by Giaver[Ref.1.4]. In NS (normal-superconductive) tunnel junctions biased below Δ/e and SS (superconductive-superconductive) tunnel junctions biased below $2\Delta/e$, with a magnetic field to bias off the Josephson supercurrent[Ref.1.5], the junction current results from the tunnelling of

thermally generated quasiparticles. (The Cooper pairs do not contribute to the tunnelling current significantly[Ref.1.6], although small contributions due to subharmonic tunnelling and multi-particle tunnelling are possible). Thus some analogy exists between the charge collection process in a semiconductive tunnelling junction. If the particle energy could be used to produce quasiparticles (from the Cooper pairs) in the superconductive tunnelling junction, and the superconductive tunnelling junction were properly biased, then the increase in quasiparticle density would cause a momentary increase of tunnelling current, providing a signal charge, analogous to electron and holes is collected as a signal in a semiconductor junction detector. This is the basis of the superconductive quasiparticle tunnelling junction particle detector proposed by B.L. White[Ref.1.7], (hereafter called "superconductive particle detector".

Note that the analogy between the PN junction particle detector and the superconductive particle detector is not exact. As will be shown later in this thesis, in the superconductor, quasiparticles are mostly thermally generated and only a small fraction are generated by interaction of the primary particle and secondary particles with the Cooper pairs. Also, the quasiparticles are 'collected' by diffusing in a field free region, whereas in a semiconductor the electrons and holes drift in the depletion region field. Assuming the ratio $^{W}/Eg = 5$ (eg. for Si = 3.34, for Ge = 4.34), then the mean energy loss by a charged particle required to create a quasi particle pair in superconducting Sn will be $W_{Sn} = 5.6 \times 10^{-3}$ eV. Assuming the Fano factor = 1 (the worst possible case), then compared to a Ge detector the statistical signal fluctuation

is less by $\sqrt{\frac{W_{Ge} \cdot F_{Ge}}{W_{Sn} \cdot F_{Sn}}} \approx 64$, i.e. the statistical fluctuation is reduced by this factor. With low-temperature low noise amplifiers the total electronic noise can conceivably be reduced, giving potentially vastly improved energy resolution. G.H. Wood (Ref. 1.7, 1.8, 1.9) fabricated Sn superconductive tunnelling junctions on glass substrates and observed tunnel current pulses caused by α-bombardment from a 5.13 MeV α-particle source of Pu^{239}. It was definitely established that superconductive tunnelling junctions could detect particles, but the data obtained by Wood was insufficient to determine the mode of operation and the energy resolution performance.

The Author's contributions described in this thesis are:

1. The experimental work done to achieve a reproducible junction fabrication process;
2. The experimental work done on measurements of junction parameters and α-particle induced current pulses with improved instrumentation, obtaining sufficient data to enable comparison with theory;
3. The theoretical and numerical work done to provide a detailed understanding of the mode of operation of the superconductive particle detector, verified by the experimental data;
4. The design of a theoretically better superconductive particle detector configuration, the heat-sink chip type, based on the theoretical understanding of the mode of operation of the glass-substrated superconductive particle detector investigated experimentally in this work.

This thesis contains six subsequent chapters.

Chapter 2 is the "theory" chapter where the theory of superconductive tunnelling is developed with emphasis on the response of the junction to a temperature change so that the theory is substrate-independent and thus universally applicable to different substrates. The theoretical expressions employ $\beta\Delta$ as a parameter where $\beta = {}^{1}/K_B T$ and $\Delta = \frac{1}{2}$ (the energy gap of a superconductor), and are thus applicable to any type of superconductors. The physical model of the mode of operation of the glass-substrated superconductive particle detector is defined. Scaling theory necessary for comparison of results from junctions with different parameters is investigated. The temperature response sensitivity and the inherent noise properties of SS and NS junctions are investigated and compared, demonstrating the superiority of SS junctions as superconductive particle detectors. Finally physical models of two proposed types of superconductive particle detectors, the phonon-barrier type, and the heat-sink-chip type are discussed, and the theoretical performance limits of the heat-sink-chip type (theoretically the better) operated at conveniently achievable conditions are calculated.

Chapter 3 is the numerical methods and results chapter. Here the non-linear partial differential equation describing the diffusion of the "heat-spike" (generated by the α-particle track in the glass substrate) is modified to a form suitable for and translated to a finite-differences equation. Numerical stability conditions are investigated, and the computer programs for the solutions of the finite differences equation and the calculation of junction current response described. The calculated results include the numerical solution of a linear heat-diffusion problem

using one of the computer programs mentioned above, compared with the analytical solution of the same problem to verify the methods used and the computer program. Also calculated are α-particle induced current waveforms, the dependence of current waveform and amplitude on the location of the α-particle impact with respect to a finite-sized junction on a glass substrate, the expected pulse-amplitude distribution, and the effects of the angle of impact on the current-pulse waveform and amplitude.

Chapter 4 describes the junction fabrication process details and some variations. This Chapter describes a large experimental effort but may be omitted in the reading of this thesis if junction-fabrication is of no interest to the reader.

Chapter 5 describes the apparatus instrumentation used to measure the junction parameters and pulse response of Pb and Sn junctions, and the results of those measurements.

Chapter 6 compares the theoretical and numerical results of Chapter 2, and 3, with the experimental results of Chapter 5. The experimental data and the theory appear to agree.

Chapter 7 is the conclusion chapter. It is concluded that the mode of operation of the superconductive particle detector should theoretically give better energy resolution than existing semiconductor junction particle detectors.

CHAPTER TWO

THEORY OF OPERATION OF THE SUPERCONDUCTIVE QUASIPARTICLE TUNNELLING JUNCTION PARTICLE DETECTOR

INTRODUCTION:

A brief review of quasiparticle tunnelling in Superconductive Tunnelling Junctions is in order. We consider first tunnelling in normal metal-insulator-metal tunnelling junctions. Referring to Figure (2.1), the energy vs. density of states curves for the metals are shown on either side of the representation of the barrier, and occupied states are represented by shaded portions under the curves. The Fermi-energy level of side 2 is used as the reference '0' of energy measurement. The situation in Figure (2.1) represents the application of -V volts to side 1, referenced to side 2, so that the Fermi level of side 1 is eV above the Fermi level of side 2. The contribution to the tunnelling current density from electrons tunnelling from side 1 to side 2 at energy E, in a range dE is proportional to the product of the number of electrons in that energy range on side 1 and the number of unoccupied levels on side 2 in the same energy range, thus

$$-dJ_{12} = e.P_{12}\, N_{N1}(E-eV)\, f(E-eV) \cdot N_{N2}(E)(1-f(E)).dE \qquad (2.1)$$

where $N_N(E)$ = density of states, normal metal.

and P_{12} is a proportionality constant, having the physical meaning of the number of electrons tunnelling from side 1 to side 2, per

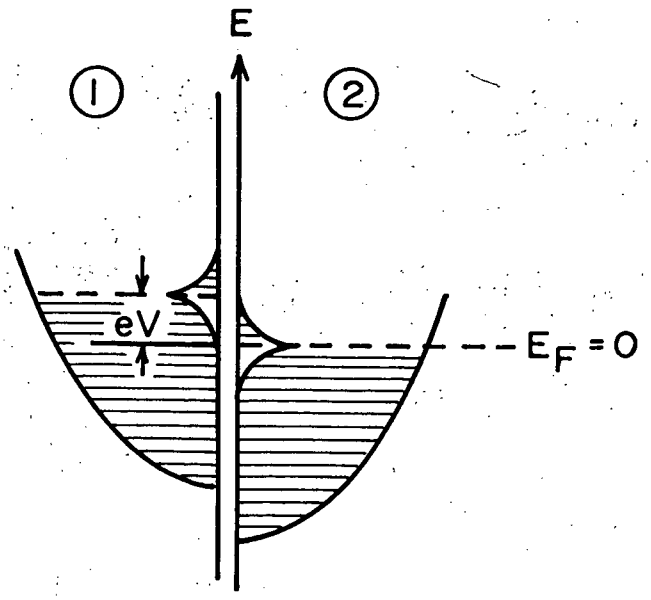

Fig. 2.1 Energy-Diagram for a Metal-Insulator-Metal Junction with Applied Potential Difference V.

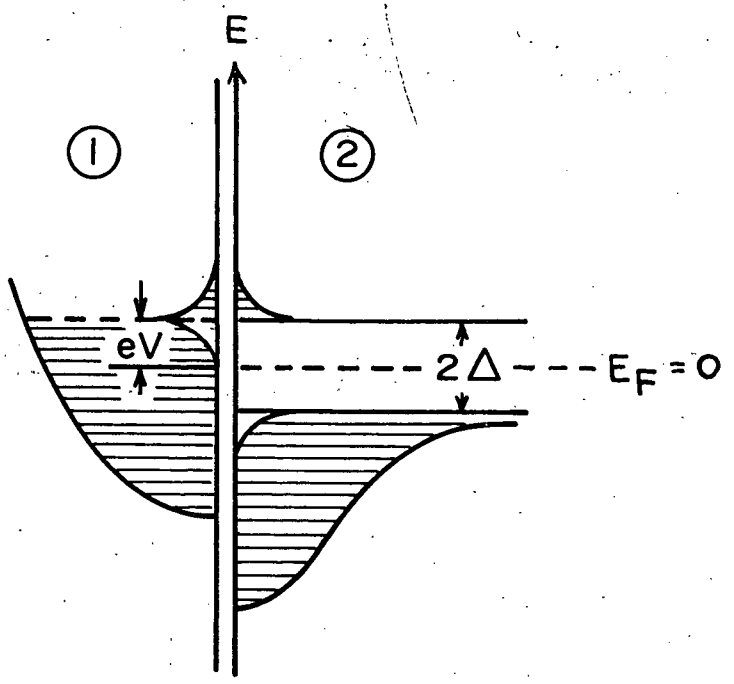

Fig. 2.2 Energy-Diagram of an NS Junction in the Semiconductor Representation, at Finite Temperature with Applied Potential Difference V.

unit junction area, per unit time, per unit occupied state density on side 1, per vacant state-density on side 2, per unit energy range.

$f(E)$ = Fermi function, giving the probability of occupancy of state at energy E. (note: - (1-f(E)) then gives the probability of vacancy of state at E).

e = the electronic charge

Similarly considering the electrons tunnelling from side 2 to side 1 we get

$$-dJ_{21} = e \cdot P_{21} N_{N2}(E)\, f(E) \cdot N_{N1}(E-eV)\,(1-f(E-ev))\, dE \qquad (2.2)$$

where P_{21} is a proportionality constant, corresponding to P_{12} for tunnelling from side 2 to side 1.

Thus the net tunnelling current density from side 1 to side 2 is given by:

$$J_{NN} = \int_{-\infty}^{\infty} dJ_{12} - dJ_{21} = -eP_{12} \int_{-\infty}^{\infty} N_{N1}(E-V) N_{N2}(E)\,(f(E-eV)-f(E))\,dE \qquad (2.3)$$

Where we assumed $P_{12} = P_{21}$.

At low temperatures, levels slightly above the Fermi level are unoccupied, and the levels slightly below becomes fully occupied, thus from equation (2.3) we see that the tunnelling current results from states immediately above and below the Fermi level, and we can approximate $N_{N1}(E-eV)$, $N_{N2}(E)$ by $N_{N1}(0)$, $N_{N2}(0)$ respectively, assuming eV is small. Also $f(E-eV) - f(E) \approx -\frac{\partial f(E)}{\partial E} \cdot eV$ for small eV. Thus equation (2.3) becomes:

$$J_{NN} = + e^2 P_{12} N_{N1}(0) N_{N2}(0) \cdot V \int_{-\infty}^{\infty} \frac{\partial f(E)}{\partial E}\, dE$$

$$= -V \cdot e^2 P_{12} N_{N1}(0) N_{N2}(0)$$

$$= -V \cdot \sigma$$

or $$I_{NN} = V \cdot G_{NN} \qquad (2.4)$$

where $G_{NN} = P_{12} e^2 N_{N1}(0) N_{N2}(0) .A.$ is the junction conductance.

$$= \sigma \cdot A$$

σ = junction conductance per unit area

A = junction area

Thus we get the well known ohmic (linear) behavior of normal-normal tunnel junctions for small bias voltages, the negative sign of earlier equations resulted from the choice of $-|V|$ for bias. We went through the above calculations to get the expression for G_{NN} for use later, and to establish the procedure for the calculation of tunnelling currents.

Following GIAVER (reference 2.1) and using the semiconductor band gap model for the superconductor we can derive the tunnelling-current characteristics of a metal (normal)-insulator-superconductor (NS) tunnelling junction. Referring to Figure (2.2) we have a schematic representation of a NS tunnelling-junction with side '1' the normal metal biased to raise the energy level eV relative to side 2 the superconductor. Proceeding as in the normal-normal tunnelling case considered above we get:

$$I_{NS} = eA \int_{-\infty}^{\infty} P_{12}\, N_{N1}(0)\, N_{S2}(E)\, (f(E-ev) - f(E))dE \qquad (2.5)$$

where $N_S(E)$ is the density of states of the superconductor at energy "E" and $N_{N1}(0)$ replaced $N_{N1}(E-eV)$, valid for low applied voltages V. From De Gennes (reference 2.2), we get the expression for $N_S(E)$

$$N_{S2}(E) = N_{N2}(E) \frac{|E|}{\sqrt{E^2-\Delta^2}} \quad \text{for } |E| > \Delta$$

$$= 0 \quad \text{for } |E| < \Delta \quad \text{energy measured from the Fermi level.}$$

and Δ = ½ the energy gap of the Superconductor.

Approximating $N_{N2}(E)$ by $N_{N2}(0)$ (valid for low temperature) we get:

$$I_{NS} = A \cdot e \cdot P_{12} N_{N1}(0) N_{N2}(0) \left[\int_{\Delta}^{\infty} \frac{E}{\sqrt{E^2-\Delta^2}} \cdot (f(E-ev)-f(E))dE + \int_{-\infty}^{-\Delta} \frac{|E|}{\sqrt{E^2-\Delta^2}} [f(E-ev)-f(E)] \cdot dE \right]$$

$$= \frac{G_{NN}}{e} [INT_1 + INT_2]$$

$$INT_2 = -\int_{\infty}^{\Delta} \frac{E}{\sqrt{E^2-\Delta^2}} \cdot [f(-(E+eV)) - f(E)]\, dE$$

$$= -\int_{\Delta}^{\infty} \frac{E}{\sqrt{E^2-\Delta^2}} (f(E+eV) - f(E))dE$$

$$I_{NS} = \frac{G_{NN}}{e} \int_{\Delta}^{\infty} \frac{E}{\sqrt{E^2-\Delta^2}} [f(E-eV)-f(E+eV)]dE = \frac{G_{NN}}{e} \int_{0}^{\infty} \frac{E+\Delta}{\sqrt{E^2+2E\Delta}}$$

$$\cdot\ (f(E+\Delta-eV)-f(E+\Delta+eV)).dE \qquad (2.6)$$

Expanding the Fermi-function:

$$f(E) = \frac{1}{(1+e^{\beta E})} = e^{-\beta E} \sum_{m=0}^{\infty} (-1)^m \exp(-m\beta E)$$

therefore

$$I_{NS} = \frac{2G_{NN}}{e} \sum_{m=p}^{\infty} (-1)^{m+1} \exp(-m\beta\Delta) \sinh(m\beta eV)$$

$$\cdot \int_0^{\infty} \frac{E+\Delta}{\sqrt{E^2+2E\Delta}} \cdot \exp(-m\beta E)\, dE$$

where $\beta = \frac{1}{k_B \cdot T}$, k_B = Boltzmann constant and T = temperature.

From Laplace transform tables (reference 2.3)

$$\int_0^{\infty} \frac{E+\Delta}{\sqrt{E^2+2E\Delta}} \cdot e^{-(m\beta E)}\, dE = \Delta \exp(m\beta\Delta) . K_1(m\beta\Delta)$$

where K_1 is the Bessel function of the second kind, 1st order.

We finally get (reference 2.1)

$$I_{NS} = \frac{2\Delta G_{NN}}{e} \sum_{m=1}^{\infty} (-1)^{m+1} \sinh(meV\beta) K_1(m\beta\Delta) \qquad (2.7)$$

This is an alternating series which converges rapidly for the applied bias voltage of $V = \frac{\Delta}{2e}$, and $\beta\Delta \geq 6$ thus we can approximate I_{NS} by taking the 1st term, and by the theory of alternating series, the error in omitting the following terms in smaller than the magnitude of the 2nd term. The ratio of term 2/term 1 for bias $V = \frac{\Delta}{2e}$ (so as to bias near the maximum dynamic resistance point) at $\beta\Delta = 6$ is 0.034, meaning the error of approximation is smaller than 3.4%.

The approximation is good over the range of $\beta\Delta$ values 3 to 8, the range of interest in the operation of the superconductive tunnelling juction as a particle detector. The approximation can be seen to improve with increasing $\beta\Delta$, thus:

$$I_{NS} \simeq \frac{2\Delta G_{NN}}{e} \sinh(\beta eV)\, K_1(\beta\Delta) \tag{2.8}$$

Differentiating (2.7) with respect to V we obtain an expression for the dynamic resistance R_{dyn}:

$$\left(\frac{\partial I_{NS}}{\partial V}\right)_T = \frac{1}{R_{dyn}}_{NS} = \frac{2G_{NN}\cdot\beta\Delta}{e} \sum_{m=1}^{\infty} (-1)^{m+1} m\cdot\mathrm{Cosh}(m\beta eV) K_1(m\beta\Delta) \tag{2.9}$$

Equation (2.9) can be approximated as before by taking the first term only. The ratios of term 2/term 1 (for bias voltage $V = \frac{\Delta}{2e}$). $\beta\Delta = 6$ is +3.4%, and improves with increasing $\beta\Delta$, thus:

$$\left(\frac{1}{R_{dyn}}\right)_{NS} = \left(\frac{\partial I_{NS}}{\partial V}\right)_T \simeq \frac{2\beta\Delta G_{NN}}{e} \mathrm{Cosh}(\beta eV) K_1(\beta\Delta) \tag{2.10}$$

To get the sensitivity of I_{NS} to temperature change we differentiate (2.7) with respect to 'T' (temperature) and get:

$$\left(\frac{\partial I_{NS}}{\partial T}\right)_V = \frac{2G_{NN}}{e}\left[\frac{\partial \Delta}{\partial T}\sum_{m=1}^{\infty}(-1)^m\, m\beta\Delta\, \sinh(m\beta eV)K_0(m\beta\Delta)\right.$$

$$+\sum_{m=1}^{\infty}(-1)^{m+1}\, m\beta^2\Delta^2 k_B\{\sinh(m\beta eV)[K_0(m\beta\Delta)+K_1(m\beta\Delta)/m\beta\Delta]$$

$$\left.-\frac{eV}{\Delta}\,\mathrm{Cosh}\,(m\beta eV)K_1(m\beta\Delta)\}\right] \qquad (2.11)$$

Equation (2.11) as it stands is too complicated to allow a simple physical interpretation but some simplifying approximations can be made since $\Delta(T)/\Delta(0) > 0.95$ for $T < \frac{T_c}{2}$, (from the $\Delta(T)$ vs. T expression of the B.C.S. theory (reference 2.4)). The $\frac{\partial \Delta}{\partial T}$ term may be omitted as an approximation (see numerical value given below). The remaining summation is an alternating series and as before can be approximated by taking only the m=1 term, the error then being smaller than the m=2 term. The factor $(K_0(m\beta\Delta) + K_1(m\beta\Delta)/m\beta\Delta)$ in (2.11) came from the differentiation of $K_1(m\beta\Delta)$ and can be approximated by $K_1(m\beta\Delta)$. The accuracy of the approximation:

$$\left(\frac{\partial I_{NS}}{\partial T}\right)_V = \frac{2G_{NN}}{e}\,\beta^2\Delta^2 k_B\left(\sinh(\beta eV)-\frac{eV}{\Delta}\,\mathrm{Cosh}(\beta eV)K_1(\beta\Delta)\right) \qquad (2.12)$$

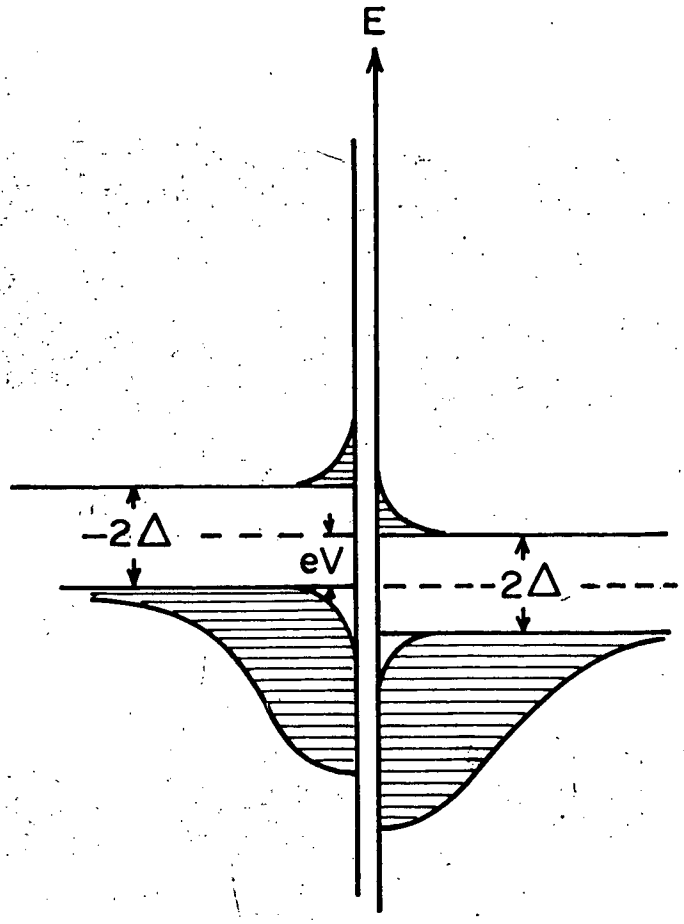

Fig. 2.3 Energy Diagram for a SS Junction in the Semiconductor Representation, at Finite Temperature with Applied Potential Diff. V.

is better than 14% over the $\beta\Delta$ range 5→7 ; and at bias voltages near $\Delta/2e$, and improves with increase of $\beta\Delta$ beyond 7.

Proceeding as in the above derivation of the tunnelling current for a NS junction and referring to Figure (2-3) the schematic representation of a superconductor-insulator-superconductor tunnel junction (SS) we get:

$$I_{SS} = \frac{G_{NN}}{e}\int_{-\infty}^{\infty} \frac{N_{S1}(E-eV)}{N_{N1}(E-eV)} \cdot \frac{N_{S2}(E)}{N_{N2}(E)} \cdot [f(E-eV)-f(E)]dE \qquad (2.13)$$

where N_{S1}, N_{S2}, are the density of states in the superconductors on side 1, 2, respectively.

$$N_S(E) = \frac{|E|}{\sqrt{E^2-\Delta^2}} \cdot N_N(E) \qquad \text{for } |E| > 0$$

$$= 0 \qquad \text{for } |E| < 0 \quad \text{energy measured from the Fermi level}$$

Substituting for N_S in (2.13) we get

$$I_{SS} = \frac{G_{NN}}{e}\left[\int_{\Delta_1+eV}^{\infty} \frac{|E-eV|}{((E-eV)^2-\Delta_1^2)^{\frac{1}{2}}} \cdot \frac{|E|}{(E^2-\Delta_2^2)^{\frac{1}{2}}} \cdot [f(E-eV)-f(B)]dE \right.$$

$$\left. + \int_{-\infty}^{-\Delta_2} \frac{|E-eV|}{[(E-eV)^2-\Delta_1^2)^{\frac{1}{2}}} \cdot \frac{|E|}{(E^2-\Delta_2^2)^{\frac{1}{2}}} [f(E-eV)-f(E)]dE \right]$$

$$= \frac{G_{NN}}{e}[INT_1 + INT_2]$$

For our purposes the superconductors on the two sides are the same kind,

$\Delta_1 = \Delta_2 = \Delta$

$$INT_1 = \int_0^\infty \frac{(E + \Delta)}{(E^2+2E\Delta)^{\frac{1}{2}}} = \frac{(E + \Delta + eV)}{[(E^2+eV)^2+2(E+eV)\cdot\Delta]^{\frac{1}{2}}}$$

$$\cdot [f(E + \Delta) - f(E + eV + \Delta)]dE$$

$$INT_2 = \int_\Delta^\infty \frac{(E + eV)}{((E+eV)^2-\Delta^2)^{\frac{1}{2}}} \cdot \frac{E}{(E^2-\Delta^2)^{\frac{1}{2}}} [f[-(E+eV)]-f(-E)]dE$$

$$= \int_\Delta^\infty \frac{(E + eV)}{((E+eV)^2=\Delta^2)^{\frac{1}{2}}} \cdot \frac{E}{(E^2-\Delta^2)^{\frac{1}{2}}} [f(E) -f(E+eV)]dE$$

$$= \int_0^\infty \frac{(E + eV + \Delta)}{[(E+eV)^2+2(E+eV)\Delta]^{\frac{1}{2}}} \cdot \frac{(E + \Delta)}{(E +2E\Delta)^{\frac{1}{2}}} [f(E+\Delta)-f(E+eV+\Delta)]dE$$

$$= I_{NT_1}$$

$$\text{Thus } I_{SS} = \frac{2G_{NN}}{e} \int_0^\infty \frac{(E + \Delta)}{[E +2E\Delta]^{\frac{1}{2}}} \cdot \frac{(E + \Delta + eV)}{[(E+eV)^2+2(E+eV)\Delta]^{\frac{1}{2}}} \cdot [f(E+\Delta)-f(E+eV+\Delta)]dE \qquad (2.14)$$

Equation (2.14) can be integrated only numerically (ref. 2.5,2.6) for $T \neq 0$, i.e. the integral cannot be expressed in tabulated mathematical functions. To obtain a tractable expression approximations must be made.

$$[f(E+\Delta)-f(E+eV+\Delta)] = \frac{1}{1+e^{\beta(E+\Delta)}} - \frac{1}{1+e^{\beta(E+\Delta+eV)}}$$

$$= (e^{\beta eV}-1)e^{\beta(E+\Delta)} \cdot (1+e^{\beta(E+\Delta)}+e^{\beta(E+\Delta+eV)}$$
$$+e^{\beta(2E+2\Delta+eV)})^{-1}$$

$$= (e^{\beta eV}-1)\ (e^{-\beta(E+\Delta)} + 1 + e^{\beta eV} + e^{\beta(E+\Delta+eV)})^{-1}$$

$$\simeq (e^{\beta eV}-1)e^{-\beta(E+\Delta+eV)} = \underline{e^{-\beta\Delta}(1-e^{-\beta eV})\cdot e^{-\beta E}.}$$

The approximation consists of the omission of the first three terms of the second factor. For an operating bias voltage $V > \frac{\Delta}{e}$, and $\beta\Delta > 3$, the error of this approximation is less than 5% at E = 0, improving with increase of V, $\beta\Delta$, and E.

The factor $\frac{E + \Delta + eV}{((E+\Delta+eV)^2-\Delta^2)^{\frac{1}{2}}}$ in the integrand of equation (2.14) can be written as:-

$$[1 - (\frac{\Delta}{E+\Delta+eV})^2]^{-\frac{1}{2}} = (1 + \frac{1}{2}(\frac{\Delta}{E+\Delta+eV})^2 + \frac{3}{8}(\frac{\Delta}{E+\Delta+eV})^4 + \frac{5}{16}(\frac{\Delta}{E+\Delta+eV})^6 + ..).$$

the series converges rapidly for $E > 0$, $V > \frac{\Delta}{e}$.

At E = 0, and $V = \frac{\Delta}{e}$, 'Its' value is 1.155. The fractional error in approximating the expression by 1.000 in the integrand is -0.134. The error decreases with the increase of E, thus the contribution to the error in the integral by this factor is less than this. Thus the total error in the Fermi factors approximation and the above approximation in the integrand is less than -0.177, for E = 0, $V = \frac{\Delta}{e}$, and $\beta\Delta = 3$. As the error is less for larger values of E encountered in the integration, the error of the approximate integral is less than -17.7%. For $\beta\Delta > 6$ the error is less than -13.5%.

Thus equation (2.14) approximates to:

$$I_{SS} = \frac{2G_{NN}}{e}(1 - e^{-\beta eV}) \int_0^\infty \frac{(E + \Delta)e^{-\beta(\Delta+E)}}{((E+\Delta)^2-\Delta^2)^{\frac{1}{2}}}\, dE$$

$$= \underline{\frac{2G_{NN}}{e}(1 - e^{-\beta eV})\Delta.K_1(\beta\Delta)} \qquad (2.15)$$

where $K_1(\beta\Delta).\Delta$ came from the integral as in the derivation of equation (2.7).

By partial differentiation of equation (2.15) we get:-

$$\left(\frac{\partial I_{SS}}{\partial V}\right)_T = \frac{1}{R_{dyn_{SS}}} \simeq 2G_{NN}\beta\Delta e^{-\beta eV}.K_1(\beta\Delta) \qquad (2.16)$$

where the errors resulting from the approximations in equation (2.15) and from assuming proportional scaling of the derivative the errors are of the same order. Also by partial differentiation of equation (2.15) we get:-

$$\left(\frac{\partial I_{SS}}{\partial T}\right)_V \simeq \frac{2G_{NN}}{e} K_B\left[\beta\Delta\ [(1+\beta eV)e^{-\beta eV}+1]K_1(\beta\Delta) + \beta\Delta(1-e^{-\beta eV})K_0(\beta\Delta)\right.$$

$$\left. - \frac{1}{K_B} . \frac{\partial\Delta}{\partial T} (1-e^{-\beta eV})K_0(\beta\Delta)\right] \qquad (2.17)$$

where the approximation signs result from the approximation of I_{SS} in equation (2.15). Equation (2.17) can be further approximated by dropping the $\frac{\partial\Delta}{\partial T}$ term, feasible because Δ is nearly a constant of temperature for $T/T_c < 1/2$, thus:-

$$\left(\frac{\partial I_{SS}}{\partial T}\right)_V \simeq \frac{2G_{NN}}{e} K_B\left[\beta\Delta\ [(1+\beta eV)e^{-\beta eV}+1]K_1(\beta\Delta) + \beta\Delta(1-e^{-\beta eV})K_0(\beta\Delta)\right] \qquad (2.18)$$

The fractional error in dropping the $\frac{\partial\Delta}{\partial T}$ term, and the total error resulting from the approximation of I_{SS} and dropping the $\frac{\partial\Delta}{\partial T}$ term, are tabulated in Table (2-3). The form of equation (2.18) is still too complicated for discussions, and can be approximated by replacing

$\frac{\partial K_1(\beta\Delta)}{\partial(\beta\Delta)} = -\left(\frac{K_1(\beta\Delta)}{\beta\Delta} + K_0(\beta\Delta)\right)$ by $-K_1(\beta\Delta)$. The resulting expression is:

$$\left(\frac{\partial I_{SS}}{\partial T}\right)_V \simeq \frac{2G_{NN}}{e} K_B.\beta^2\Delta \left[\Delta - (eV+\Delta)e^{-\beta eV}\right] . K_1(\beta\Delta) \qquad (2.19)$$

The error of approximation (2.19) is less than -30% at $\beta\Delta = 4$, decreasing to less than -14% at $\beta\Delta = 7$, for bias voltage $V = \Delta/e$ applied across the junction.

In the approximations above we ignored the $\partial\Delta/\partial T$ term; that is equivalent to regarding Δ as a constant (for $T/T_c < 0.5$). Thus for the range of valid approximation ($\rho\Delta > 3.5$) we can approximate $\beta\Delta$ by $\beta\Delta(0)$.

A large effort was made in this section to obtain approximations with simple functional forms and to calculate the errors involved in the approximations. This is done so that relatively simple algebraic derivations can be used in later sections to obtain results on noise, signal and other performance parameters of NS and SS tunnel junctions used as particle detectors with the results quantitatively significant, with errors or error bounds known. It is possible to calculate all the junction parameters using the exact expressions numerically but the consequent loss of comprehensibility is not justified by the gain in numerical accuracy.

When an α-particle impacts a superconductive tunnelling junction deposited on a substrate the particle depending on its energy either penetrates part of the junction films and stops or penetrates all of the junction-films and part of the substrate and stops. The kinetic energy of the particle is deposited along the particle track by interactions with the electrons of the atoms of the junction-films and substrate material and the conduction electrons in the metal, creating ions, and electrons with kinetic-energy mostly smaller than the energy of ionization, a maximum energy of ~ $4m E_p/M$. (reference 2.7) where m = electron mass, Ep = particle energy and M = particle mass. The electrons with kinetic energy greater than the ionization energy can cause more ionization. In the junction superconductive films some 'Cooper-pairs' are broken up to quasiparticles by interactions with the primary particle and electrons and phonons with energy greater than the superconductor energy gap. This

results in an abrupt increase of quasiparticles density and consequent increase of junction current. Thus far the analogy to the semiconductor-junction detector is good, the quasiparticles tunnelling corresponding to the charge collection in the semiconductor junctions. The Cooper pairs recombine with a time constant of the order of $<10^{-8}$ sec. (reference 2.8). The particle energy is thus 'thermalized'; i.e. may be considered to produce a local increase in temperature. The resultant increase in thermally generated quasiparticle causes a corresponding increase in the junction tunnelling current. The particle energy deposited in the substrate also thermalizes and warms up the substrate and the junction films near the particle track. This further contributes to the thermal generation of quasiparticles and tunnelling current.

Because of the small recombination and thermalization time-constant for the quasiparticles generated by the primary and secondary particles as compared to the thermal time constants (of the order of microseconds), the signal-charge (which is the time integral of the signal current) is mostly derived from the thermal contribution. This is where the analogy to semiconductor-detectors is no longer valid. At 1.2 K for Sn, E gap/K_BT = 12.08.Thus, for example, an increase of temperature of the junction (resulting from the particle kinetic energy) of 0.2 K to 1.4 K causes an increase in the junction current of 464%, whereas for a Si junction detector at room temperature of 293 K, Egap/k_BT = 42.78 the same increase in temperature would cause an increase in thermally generated current of only 3%. Further, the heat required to produce the change of temperature is greater for the

room temperature Si case because of the generally lower specific heats at cryogenic temperatures. Thus the thermally generated junction current resulting from the particle energy thermalizing is even less for the semiconductor-junction detector. In contrast for the superconductive particle detector the junction signal-current is practically all due to the thermal contribution, and in the following chapter, the numerical calculations of junction signal-current will be based on this thermal model.

The following sections of this chapter will consider:-

- Physical models of 2 types of superconductive particle detectors, the glass substrate type, and the phonon barrier type. The first model applies directly to the experiments discussed, while the second is a hypothetical model, examined to see where either experimental or theoretical methods may be improved in future.
- Scaling theory, which allows junctions with different parameters to be compared.
- The response of SS and NS junctions to steady and fluctuating temperature changes at different operating temperatures.
- Noise inherent in SS and NS superconductive quasiparticle tunnelling-junctions, i.e. Shot noise.
- Oxide-barrier thickness fluctuations and the effect on the signal (i.e. particles impacting a region with thinner oxide-barriers than average would give a larger signal-charge because of the larger junction conductance per unit area in the region).
- Angle of impact effect on the signal current waveform: (The

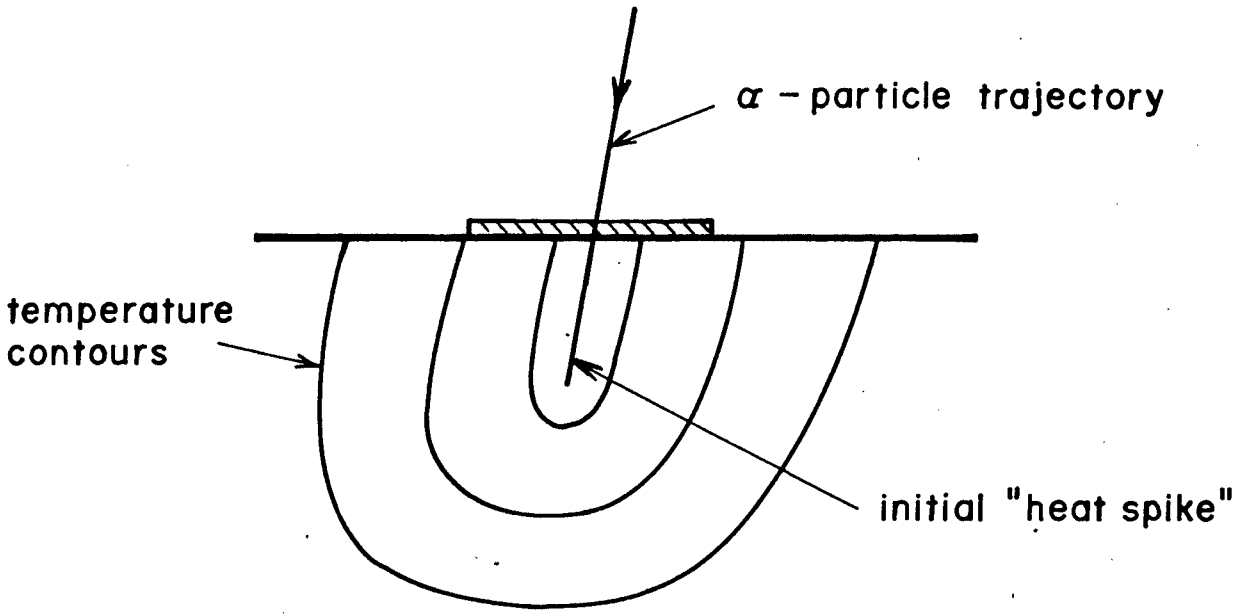

Fig. 2.4 Alpha-Particle Impinging on Glass Substrate Type Superconductive Quasiparticle Tunnelling Junction Particle Detector.

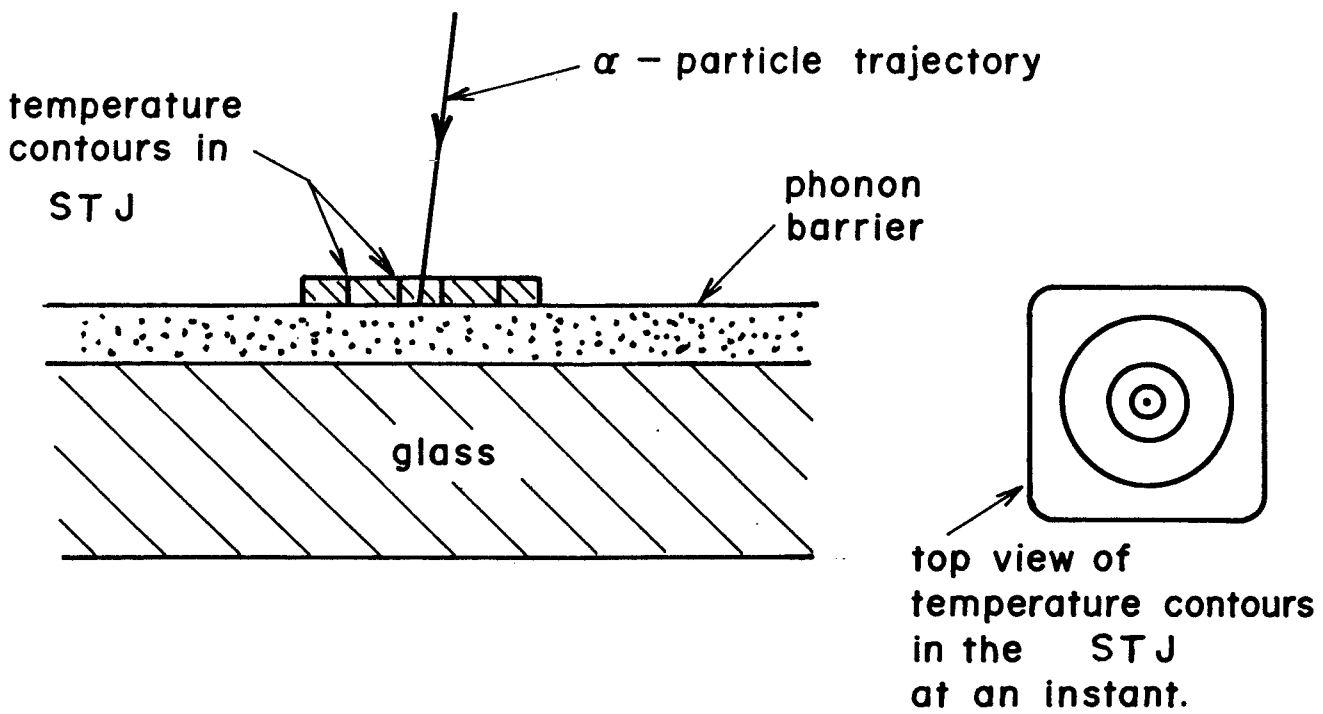

Fig. 2.5 Alpha-Particle Impinging on Phonon-Barrier Type Superconductive Quasiparticle Tunnelling Junction Particle Detector.

evolution of the thermal profiles at the junction film depends on the angle of impact of the particle; the junction current waveform is thus dependent on the angle of impact).

- Junction size effect on the signal current waveform: - (The junction deposited on a glass substrate or a phonon-barrier has a finite area. As the junction current is dependent on the temperature at each point of the junction, impacts at different points inside the junction area (and outside, for the case of the glass-substrate type) produce different thermal profiles at the junction films and thus different junction current waveforms).

TYPES OF SUPERCONDUCTIVE PARTICLE DETECTORS

1. Glass Substrate Type

This type of Superconductive Particle detector consists of a superconductive tunnelling junction deposited on and in good thermal contact with a substrate which was a soda-glass microscope slide. Referring to Figure (2.4), the particle deposits most of its energy in the substrate which results in a high temperature track, (the "heat-spike"). The heat then diffuses as described by classical heat diffusion equations. The tunnel-current density of the S.T.J. on the substrate at each point depends on the temperature at that point. The total increased tunnel-current is the output signal current response. To simplify the heat diffusion problem the S.T.J. is regarded as a thermometer sitting on the glass substrate, not significantly affecting heat-diffusion in the substrate. This assumption is valid if the heat deposited in the S.T.J. is a negligible fraction of the total, and if the heat capacity of the junction film is a small fraction of that of the thermally active portion of the glass substrate, i.e. that part of the substrate down to the full depth of the "heat-spike",) and if heat conduction along the plane of the junctions films is small. The heat deposited in 4000Å of Sn is 1.47×10^{-14} joules, negligible compared to the total of 0.82×10^{-12} joules for the 5.13 MeV α-particles used in the experiments. The heat capacity of a 0.2 mm x 0.2 mm x 4000Å STJ is 4.03×10^{-12} J/°K, the heat capacity of the active portion of the glass substrate: 0.2 mm x 0.2 mm x 32 μm is = 14.84×10^{-12}

joules/deg.K, much larger than that of the junction film. Finally because of the small heat conductivity of bulk Sn (Superconducting) and further reduction of heat-conductivity along the plane of the film due to diffused scattering of quasiparticles and phonons at the film boundary with mean free path determined by the 2000Å thickness of the STJ films, the heat conductivity along the plane of the film is a small fraction of that of the glass substrate. The numerical details are given in Chapter 3. Thus the simplifying assumption in the heat diffusion problem is justifiable. Depending on the geometry of the situation a 1, 2, or 3 dimensional non-linear partial-differential equation needs to be solved, the non-linearity coming from the temperature dependence of specific-heat and thermal conductivity. The solution of these heat-diffusion problems is possible only by numerical methods described in the next Chapter. This type of superconductive particle detector has inherently the worst resolution of the three types, the factors degrading resolution will be described later in this chapter. This type of Superconductive particle detector (S.P.D.) is the easiest to fabricate, and once the details of the operation of this type are understood, the operation of the other types can be predicted theoretically with reasonable confidence. This type of Superconductive Particle detector together with the phonon-barrier type are probably subject to radiation damage. The high-temperature particle track in the junction films probably causes break-down of the barrier oxide (at the track), resulting

in microshorts, and gradual degradation of the S.T.J. (The junctions appear to keep indefinitely if stored at 77°K, however some degradation is noticable if the junction is exposed to the α-particle source during storage for a few weeks).

2. Phonon-barrier type

This type of Superconductive Particle detector consists of a S.T.J. deposited on a "phonon-barrier", a polymer of poor acoustical-match to the junction film, for example polymerized photo-resist deposited on a glass substrate. The phonon-barrier inhibits heat flow between the junction film and the substrate, and thus when a particle is stopped in the junction films the heat deposited essentially diffuses 2 -dimensionally (Figure 2.5) Because of the temperature dependence of specific heat and thermal conductivity, the heat-diffusion problem can be solved only numerically, by methods described in the next chapter. This type of S.P.D can operate as a spectrometer only if the particle is stopped in the junction films. Because of practical difficulties in fabricating S.T.J.s' with thick junction films, this type of S.P.D. is suitable only for low energy particles or X-rays. This type of S.P.D. should give better resolution of particle energy than the glass-substrate type. The phonon-barrier type, has yet to be fabricated and tested.

Scaling Theory

From equations (2.8), (2.15) we see that I_{NS}, I_{SS} are both directly proportional to the normal tunnel conductance "G". Thus for a given type of superconductor, the family of I, V, characteristics with temperature as a parameter for any junction can be obtained from a reference set by adjusting the current-scale by multiplying it by a factor proportional to the ratio of the normal tunnel conductances $G/G_{ref.}$. Thus the calculated signal-current response for a junction with a given normal tunnelling conductance can be scaled to provide the signal-current response of a junction of the same material having a different normal tunnelling conductance exposed to the same temperature-profile as a function of time by simply changing the current-scale in the ratio of normal tunnel conductances.

From equations (2.10), and (2.16) we see that:

$$\frac{1}{R_{dyn}} = G \cdot F_1(T,V). \qquad (2.20)$$

This means for a given bias voltage V and temperature T, the junction dynamic conductance is proportional to the normal tunnelling conductance. This relation is useful for checking the quality of the junction: Because of the presence of leakage resistances across the junction

$$\frac{1}{R_{dyn,G}} \geq F_1(T_1V)$$

Thus the ratio of measured maximum R_{dyn} at a fixed temperature (for example 1.2 K) to the normal tunnel-resistance is a measure of quality (or lack of leakage) of the junction, independent of the actual junction parameters.

From equations (2.12), (2.19) we see that:

$$\left(\frac{\partial I}{\partial T}\right)_V = G_{NN} \cdot F_2 \ (T_1 V) \qquad (2.21)$$

That is, for a given operating temperature and bias-voltage the current response to a given temperature change is proportional to the normal junction-tunnel conductance.

From equations (2.16) and (2.17) we get:

$$\left(\frac{\partial I}{\partial T}\right)_V \cdot R_{dyn} = F_2/F_1 \qquad (2.22)$$

which states the voltage-response to a given temperature change is the same for all junctions with the same superconducting film materials, but of course the measured voltage response depends on the characteristics of the preamplifier as well as the junction.

Response of a S.T.J. to Small Temperature Changes

In this section we concentrate on the responses of a S.T.J. to a small temperature change δT, because that is a basic property of the S.T.J. and is not substrate dependent. In S.P.D. applications the substrate thermal properties, (of the junction film thermal properties in the case of the phonon-barrier type S.P.D.), determine the temperature

Vs. time at each point of the S.T.J. (due to a particle impact) and the response of the S.P.D. results from the temperature increase at each point of the S.T.J. The responses of the S.T.J. to temperature change are expressed as functions of $\beta\Delta$, i.e. using $\beta\Delta$ as a temperature parameter. This is accomplished by chosing the applied voltage V such that Ve is some multiple γ of Δ (half the energy gap), where γ is determined by the desired bias point, constrained by the restrictions on V introduced in deriving equations (2.8), (2.15). Using $\beta\Delta$ as a temperature parameter the response equations (and curves) are then applicable to S.T.J.'s with any Δ.

Superconductor - Superconductor (S.S) S.T.J.

We choose V such that $Ve = \Delta$, as that is near the maximum R_{dyn} point, and is within the range for validity of equation (2.15). From equation (2.19) substituting Δ for Ve and rearranging terms we get:-

$$\delta I = \frac{2G_{NN}\alpha K_B}{e} (\beta\Delta)^2 \quad e^{-\beta\Delta} \quad (1 - 2e^{-\beta\Delta}). \ \delta T \qquad (2.23)$$

where we have set $K_1 (\beta\Delta) = \alpha \quad (\beta\Delta) \ e^{-\beta\Delta}$

For $\beta\Delta \gtrsim 3.5$ (2.23) can be approximately represented by:

$$\delta I = \frac{2G_{NN}\alpha K_B}{e} (\beta\Delta \quad e^{-\beta\Delta}. \ \delta T$$

Thus we see that the current-response to δT is a monotonically decreasing function of $\beta\Delta$, for $\beta\Delta \gtrsim 3.5$.

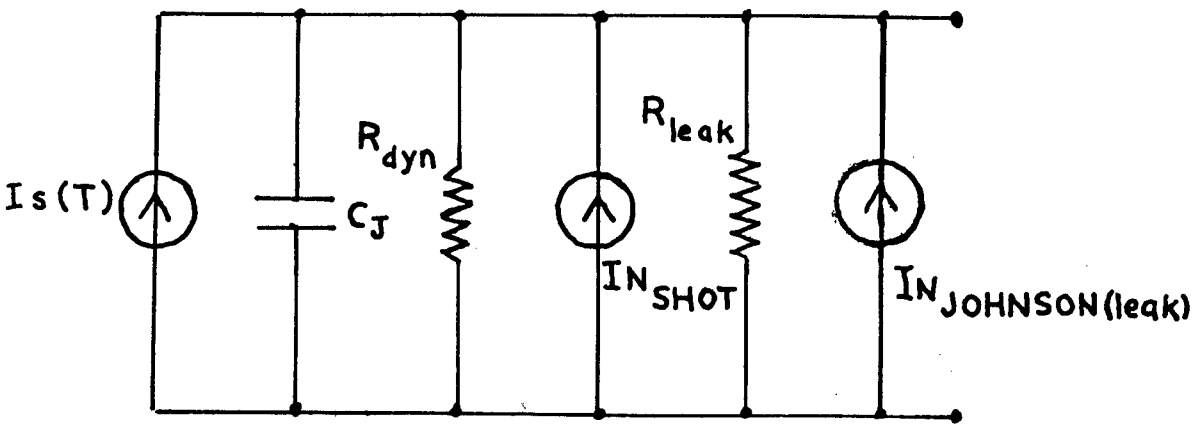

Fig.2.6 Equivalent Circuit for a Superconductive Quasiparticle Tunnelling Junction.

In the following we work with the maximum frequency Fourier component of a gaussian pulse, (angular frequency ω) to obtain a pessimistic approximate voltage response for the temperature pulse.

Referring to Figure (2.6) the S.T.J. equivalent circuit, we see that the voltage response δV to δT is:

$$\delta V = \delta I / \left(j\omega c_J + \frac{1}{Rdyn} + \frac{1}{R_{leak}} \right) \qquad (2.24)$$

For $\omega \to 0$ and $R_{leak} = \infty$ (no leakage and slow temperature changes) equation (2.24) becomes:

$$\delta V = \delta I \, R_{dyn}$$

Substituting the expressive for R_{dyn} equation (2.16) and replacing Ve by Δ, and δI from (2.23) we get:

$$\delta V = \frac{K_B}{e} \beta\Delta \quad (e^{\beta\Delta} - 2) \; . \; \delta T \qquad (2.25)$$

The voltage response is thus independent of G, and increases monotonically with $\beta\Delta$. This increase is due to the rapid increase of R_{dyn} with $\beta\Delta$, overcoming the decrease of δI. For practical cases R leak is finite. Thus the voltage response rises initially with increasing $\beta\Delta$ until R_{dyn} becomes comparable with R leak, thereafter $\delta V/\delta T$ falls with increasing $\beta\Delta$.

For $\omega \neq 0$ under conditions where $(j\omega c_J)$ is comparable to 1/Rdyn., the capacitance reactance acts as a shunting impedance across Rdyn. Thus the voltage response increases initially

with increasing $\beta\Delta$. it is conceivable that R_{leak} may be eliminated with improved technology but junction capacitance C_J cannot be avoided. For the general case considering the effect of C_J and R_{leak}, substituting the expression for δI from equation (2.23) and R_{dyn} from Equation (2.16) into equation (2.24) we get:

$$\delta V = \frac{2G_{NN}\alpha K_B}{e}(\beta\Delta^2)\ e^{-\beta\Delta}\ \delta T \Big/ \left(j\omega C_J + \frac{1}{R_{leak}} + (2G_{NN}\beta\Delta e^{-\beta ev}K_1(\beta\Delta)\ )\right) \tag{2.26}$$

The power-response δW to δT is:

$$\delta W = \delta I.\delta V = \delta I^2\ |Z_J|$$

(of this a maximum of ½ is available to a matched load). For $\omega \to o$ and $R_{leak} = \infty$ using equations (2.23), (2.25) we get:

$$\delta W = \frac{2G_{NN}\alpha K_B^2}{e^2}\ (\beta\Delta)^3\ \ (1 - 2e^{-\beta\Delta})^2\ \delta T^2 \tag{2.27}$$

For $\beta\Delta > 3.5$ equation (2.36) can be approximated by

$$\delta W = \frac{2G_{NN}\alpha K_B^2}{e^2}\ (\beta\Delta)^3\ .\ \delta T^2 \tag{2.28}$$

Thus the signal power increases as $(\beta\Delta)^3$ and is proportional to G. This monotonic increase in signal-power is due to the rapid increase in R_{dyn}, overcoming the decrease of $(\delta I)^2$. When R_{leak} is finite, or the frequency $\neq$ o such that $(j\omega c_J)$ is a significant portion of $1/R_{dyn}$.

the increase in $|Z_J|$ is limited, and with increase of $\beta\Delta$, δW increases initially, then decreases.

Choice of S.T.J. for use as Particle-detectors

By using $\beta\Delta$ as the temperature parameter for expressing δI, δV, δW, the resulting equations apply to any S.S. S.T.J.'s. Thus the optimum $\beta\Delta$ operating values for maximum response to δT are the same for all values of Δ. Total mean square noise voltage (for all frequencies) to be shown in the "inherent-noise" section to be proportional to Δ, thus for a given G, and C_J, (and bandwidth) we use the smallest Δ such that at the lowest operating temperature $\beta\Delta$ is the value for maximum (V response to thermal input /Vn Total). Another factor favouring small Δ and low operating temperatures for S.T.J. used as particle detectors is the decrease of specific heat of the substrate and the junction films with decrease of temperature. Summing up the choice of Δ: use the lowest available Δ the value consistent with being able to operate at the optimum $\beta\Delta$ value.

Metal-Superconductor (N.S.) S.T.J.

From equation (2.12) and choosing the bias voltage V such that $eV = \Delta/2$, close to the maximum dynamic impedance point, we get:

$$\delta I = \frac{G_{NN}\alpha K_B}{2e} (\beta\Delta)^2 \, e^{-\frac{\beta\Delta}{2}} [1 - 3e^{-\beta\Delta}]. \quad \delta T. \qquad (2.29)$$

We have $\beta\Delta$ as the only temperature dependent parameter, thus this equation describes all N.S. junctions biased at $V = {}^{\beta\Delta}/2e$. As in the S.S. case the approximations leading to this equation is valid for $\beta\Delta > 3.5$. From (2.29) we can see that for large $\beta\Delta$, δI is proportional to $(\beta\Delta)^2 e^{-\frac{\beta\Delta}{2}}$, and decreases monotonically with $\beta\Delta$. From Figure (2.6) we arrive at the same equation for δV as in the S.S. S.T.J. case (given by equation (2.24)).

$$\delta V = \delta I \; / \; (j\omega C_J + \frac{1}{R_{dyn}} + \frac{1}{R_{leak}})$$

For $\omega \to o$ and R leak $= \infty$ i.e. no leakage and low frequency temperature changes, we have:

$$\delta V = \delta I \cdot R_{dyn}$$

substituting for R_{dyn} from equation (2.2) and $\frac{\Delta}{2}$ for Ve, and δI from (2.29) we get:

$$\delta V = \frac{K_B}{2e}\beta\Delta \; [\frac{1 - 3e^{-\beta\Delta}}{1 + e^{-\beta\Delta}}] \quad \delta T. \qquad (2.30)$$

$$\simeq \frac{K_B}{2e} \beta\Delta \; . \; \delta T \qquad \text{for (large)} \quad \beta\Delta > 3.5$$

Thus the voltage response as in the S.S. S.T.J. case is independent of junction normal tunnel-conductance G_{NN}, and δV increases linearly with $\beta\Delta$ increase. With the presence of R_{leak}, δV increases initially with $\beta\Delta$ until the increase in R_{dyn} makes R_{leak} significant, then δV decreases as the decrease in δI. For $\omega \neq o$ as in the S.S. S.T.J. case the reactance of C_J acts as a shunting impedance, causing a decrease in δV with increasing $\beta\Delta$ when R_{dyn} is comparable to $|Xc|$.

The power response δW to δT is:

$$\delta W = \delta I . \quad \delta V = \delta I^2 |Z_J|$$

for $\omega \to o$ and $R_{leak} = \infty$, using equations (2.29), (2.30) we get:

$$\delta W = \frac{G_{NN} K_B^2}{4e^2} (\beta\Delta)^3 \; e^{-\frac{\beta\Delta}{2}} \; \frac{1 - 3e^{-\beta\Delta}}{1 + e^{-\beta\Delta}} \; \delta T^2 \qquad (2.31)$$

$$\approx \frac{G_{NN} \alpha K_B^2}{4e^2} (\beta\Delta)^3 \; e^{-\frac{\beta\Delta}{2}} \; \delta T^2$$

Thus the signal power initially increases as in the S.S. S.T.J. case as $(\beta\Delta)^3$ then decreases, damped by the $e^{-\frac{\beta\Delta}{2}}$ factor from the current response, even for an ideal junction. The maximum occurs at $\beta\Delta \sim 6$.

Comparisons of N.S. and S.S. S.T.J.'s

From equations (2.23) and (2.29) we get for N.S., and S.S. S.T.J. with the same G_{NN} and biased respectively at $V = \frac{\Delta}{2e}$, and $V = \frac{\Delta}{e}$:

$$\frac{\delta I_{SS}}{\delta I_{NS}} = 4e^{-\frac{\beta\Delta}{2}} \left[\frac{1 - 2\, e^{-\beta\Delta}}{1 - 3\, e^{-\beta\Delta}}\right] \qquad (2.32)$$

$$\approx 4\, e^{-\frac{\beta\Delta}{2}}$$

Thus for $\beta\Delta > 2.8$ the ratio is < 1, and decreases for increasing $\beta\Delta$. This result originates from the fact that for a quasi-particle to tunnel in the N.S. junction at zero bias the energy needed is Δ, whereas 2Δ is needed in the case of S.S. junctions.

From equations (2.24) and (2.30) for N.S. and S.S. S.T.J.'s with the same G_{NN} , C_J, and biased respectively at $V = \frac{\Delta}{2e}$ and $V = \frac{\Delta}{e}$, we get:

$$\left(\frac{\delta V_{SS}}{\delta V_{NS}}\right)_\omega = \frac{\delta I_{SS} \,/\, (1/R_{dynSS} + 1/R_{leak} + jwC_J)}{\delta I_{NS} \,/\, (1/R_{dynNS} + 1/R_{leak} + jwC_J)}$$

Substituting for δIss/δIns from equation (2.32) and using the expressions for $R_{dyn_{SS}}$, $R_{dyn_{NS}}$, we get:

$$\left(\frac{\delta V_{SS}}{\delta V_{NS}}\right)_\omega \simeq 2e^{\beta\Delta}\left[1 + \frac{(e^{-3/2\beta\Delta} - 1)\,(1/R_{leak} + jwC_J)}{(1/R_{dynSS} + jwC_J + 1/R_{leak})}\right] \quad (2.33)$$

For $\omega \to o$ and $R_{leak} = \infty$

$$\left(\frac{\delta V_{SS}}{\delta V_{NS}}\right)_\omega \simeq 2e^{\beta\Delta} \quad (2.34)$$

Thus for low frequencies the S.S. S.T.J. gives better voltage response, the difference increasing with βΔ.

For $\omega C_J R_{dyn} >> 1$.

$$\left(\frac{\delta V_{SS}}{\delta V_{NS}}\right)_{\omega \to \infty} \simeq 4e^{-\frac{\beta\Delta}{2}} \quad (2.35)$$

This results from the junction capacitance swamping the R_{dyn} of the junctions, making the junctions essentially equal in impedance leaving the voltage ratios equal to the current ratios. This does not occur until $\omega \sim 10^9 \rightarrow 10^{10}$ for the junctions of interest. For particle detector applications $\omega \sim 10^6$ and equation (2.34) still applies. From the equation for δW (2.27) and (2.31), for $\omega \rightarrow 0$, R leak $\rightarrow \infty$ and biasing at $V = \frac{\Delta}{2e}$, and $V = \frac{\Delta}{e}$ for N.S. and S.S. junctions respectively, we get:

$$\frac{\delta W_{SS}}{\delta W_{NS}} = \frac{(1 - 2e^{-\beta\Delta})^2}{(1 - 3e^{-\beta\Delta})^2} \cdot \frac{(1 + e^{-\beta\Delta})}{e^{-\frac{\beta\Delta}{2}}} \approx 2\, e^{\beta\Delta/2} \qquad (2.36)$$

We see that for low frequencies for which $|Xc_J| >> R_{dynss}$ the S.S. junctions give better signal-power. The ratio (2.36) is significant when amplifier-noise is the dominating factor.

Performance figures for S.S. S.T.J.'s

A useful performance parameter relating to current response of a S.T.J. is the current-response per degree change in temperature, per unit junction normal tunnel conductance.

From equation (2.23) we get:

$$\frac{(\frac{\partial I}{\partial T})}{G_{NN}} = \frac{2 K_B}{e} K_1 (\beta\Delta)^2 (\beta\Delta)^2 (1 - 2e^{-\beta\Delta}) \qquad (2.37)$$

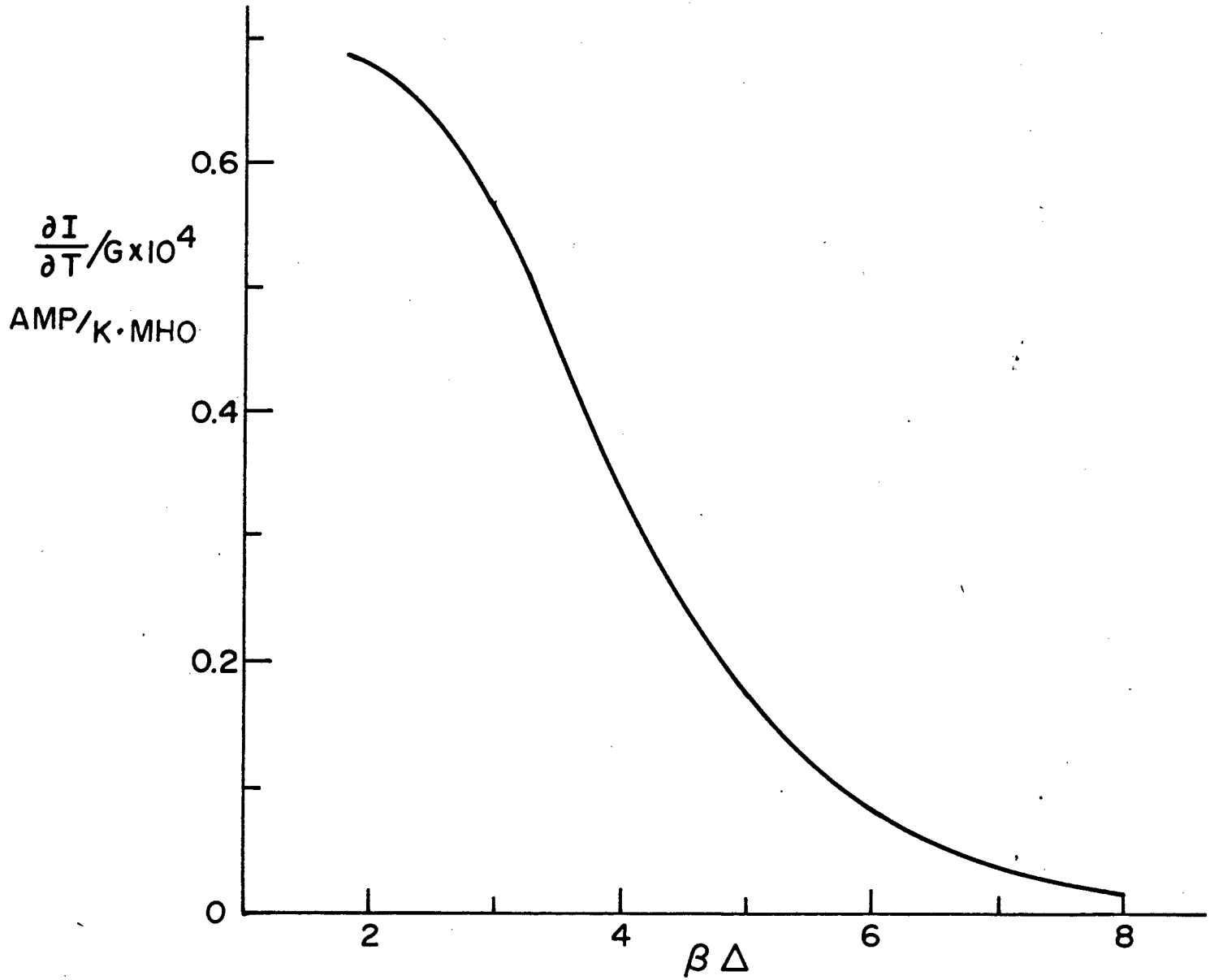

Fig. 2.7 Current Response Sensitivity Per Unit Junction Normal Tunnel Conductance.

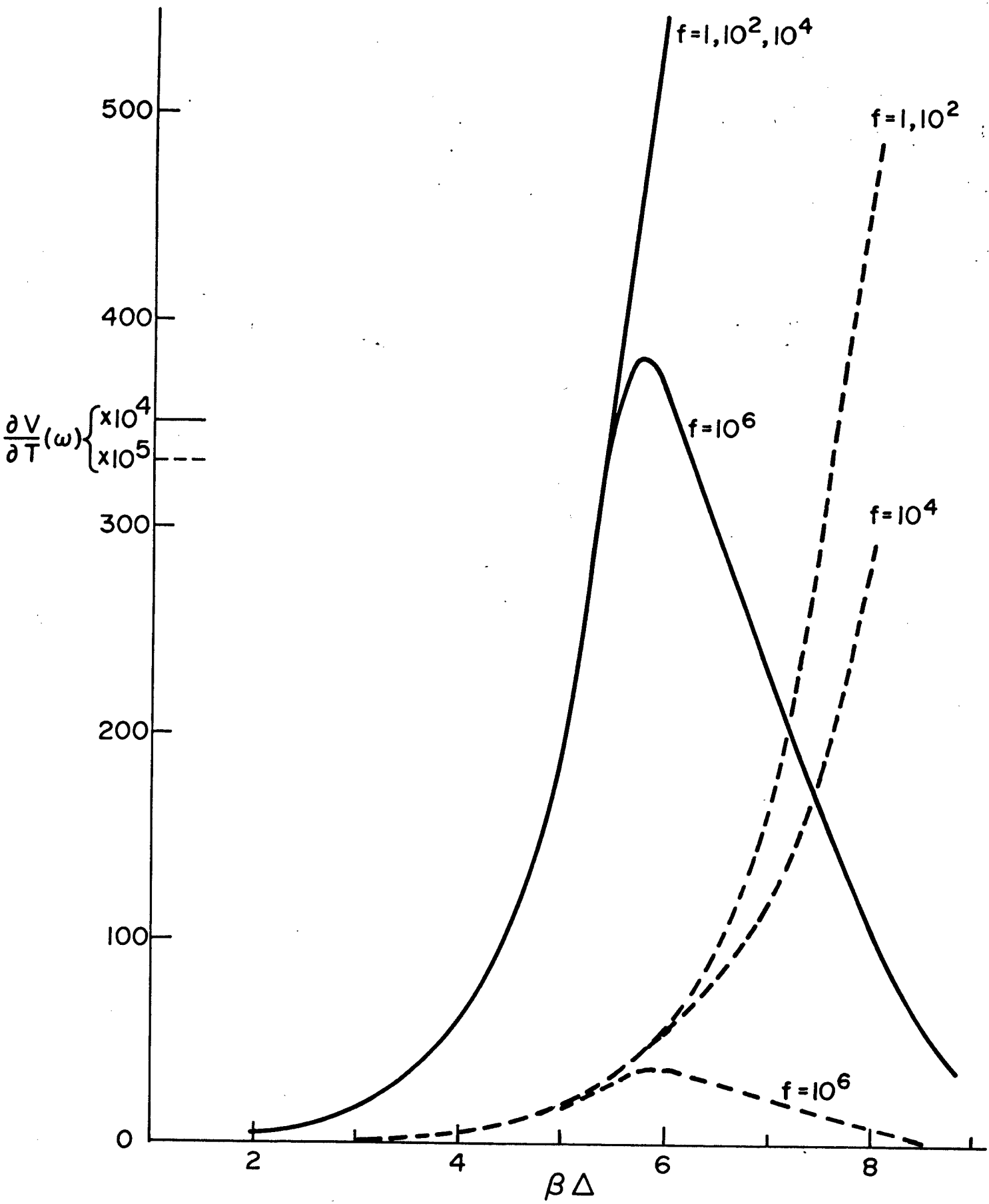

Fig. 2.8 Voltage Response Sensitivity, Frequency as Parameter.

where K_1 ($\beta\Delta$) is the modified 1st order Bessel function of the second kind.

The function of equation (2.37) is plotted in Figure (2.7) and it shows clearly the decrease of the normalized current response with increase of $\beta\Delta$. With the voltage-response it is not possible to get such universally applicable relation as (2.37) because of junction capacitance which is a different function of area and barrier thickness than G, and R_{leak} can be any value, except for the special case of $\omega \to o$ and $R_{leak} = \infty$. For this special case representing low-frequency temperature changes and no leak in the junction, from equation (2.25)

$$\left(\frac{\partial V}{\partial T}\right) \simeq \frac{K_B}{e} \cdot \beta\Delta \, (e^{\beta\Delta} - 2) \qquad (2.38)$$

For $\omega C_J R_{dyn} \gtrsim 1$ where the effect of C_J is significant it becomes necessary to use examples. We take for this example the parameters of a junction we used in an experiment, as shown below:-

$R^*_{dyn} = 72.5 \qquad = \left(\frac{1}{R_{dyn}} + \frac{1}{R_{leak}}\right)^{-1}$

$G_{NN} = 2.9$ mho

$C_J = 1500$ pF

$\Delta = 0.8905 \times 10^{-22}$ J

at 1.2°K corresponding to $\beta\Delta = 5.375$,

The voltage response curves are shown in Figure (2.8). They were calculated using

$$\frac{\partial V_{SS}}{\partial T}\Big|_{\omega} = \left| \frac{\partial I_{SS}}{\partial T} \cdot \left(jwc_J + \frac{1}{R^*_{dyn}}\right)^{-1} \right|$$

The curves clearly show the increase of $\frac{\partial V(\omega)}{\partial T}$ with increase of $\beta\Delta$ and for the $\omega = 10^6$ curve the decrease of $\frac{\partial V}{\partial T}(\omega)$ beyond $\beta\Delta = 5.8$. The other curves ($\omega = 10^2$, 10^4) would also show such a decline in $\frac{\partial V}{\partial T}$ for sufficiently high $\beta\Delta$.

Inherent Electrical Noise in S.T.J.'s

Because of the low temperature of operation of the S.T.J.'s the only electrical noise of significance, is shot-noise from the junction bias-current. The equivalent circuit of Figure (2.6) is used for the following calculations.

Shot-noise:-

$$I_n{}^2{}_{shot} = 2\, I\, e\, \Delta f \qquad (2.39)$$

where I_{Qp} = bias current

Δf = frequency interval of interest.

$$\therefore \quad V_N{}^2{}_{shot} = \int_0^{\omega o} I_N{}^2{}_{shot} \cdot \frac{Rd^2}{1 + \omega^2 C_J{}^2 R_d{}^2}\, df$$

$$= \frac{I_{qp}\ e\ Rd}{\pi\ C_J} \tan^{-1}(\omega o\, C_J R_d) \qquad (2.40)$$

where: ω_o = the high frequency limit of the frequency band of interest, here we go from $\omega = 0$ to $\omega = \omega_o$

$R_d = (1/R_{dyn} + 1/R_{leak})^{-1}$, the effective dynamic resistance.

(R_{dyn} is the inherent junction dynamic resistance).

from (2.40) the noise power contribution of shot noise is:

$$\overline{P_N} = V_{N_{shot}}^2 / R_d = \frac{I_{Qp.e.}}{\pi . C_J} \tan^{-1} (\omega_o C_J R_D) \qquad (2.41)$$

For the special case of $\omega_o = \infty$:

$$\overline{V_N^2}_{shot} = \frac{I_{Qp} . e . R_d}{2C_J} \qquad (2.46)$$

$$\overline{P_{N_{shot}}} = \frac{I_{Qp} . e}{2C_J} \qquad (2.43)$$

The noise powers are useful in determining the amplifier noise level to aim for to take advantage of the full capability of the superconductive particle detector. For typical operating frequency bandwidth of 10^6 Hz , C_J ~ 2000 pF and R_{dyn} ~ 100 $\tan^{-1}(w_o C_J R_{dyn}) \approx 51.5°$, that is, the noise is about 0.57 of the all frequency case.

Note that the above equations (2.40) to (2.43) applies to both N.S. and S.S. S.T.J.'s.

For S.S. junctions we get from equations (2.15), (2.16) I_{SS} and R_{dyn} and substituting in equation (2.42) we get:

$$\overline{V_N^2}_{shot_{SS}} = \Delta \frac{(e^{\beta\Delta} - 1)}{2 C_J \beta\Delta} \qquad (2.44)$$

For N.S. we get from equations (2.8) and (2.10) I_{ns} and R dyn (N.S.) and substituting in equation (2.42) we get :-

$$\overline{V_N^2}_{shot_{NS}} = \frac{\tanh(\beta\Delta/2)}{2C_J \beta\Delta} \qquad (2.45)$$

In the above equations for mean-square noise voltages the junction normal-tunnelling conductance G_{NN} does not appear as a result of our assumption of no leakage, thus for shot-noise the I_{SS} (and I_{NS}) and R_{dynSS} (and R_{dynNS}) dependences on G_{NN} cancels. The above equations are written with $\beta\Delta$ grouped as a parameter. In equations (2.44) and (2.45) we see Δ multiplied into functions of $\beta\Delta$, which because of $\beta\Delta$ dependence apply to all superconductive quasiparticle tunnelling junctions. The

presence of Δ thus indicate a linear dependence of mean square noise voltages on Δ. Since we previous found (equation (2.25))that the voltage response is independent of Δ for junctions operating at the same $\beta\Delta$, the signal to noise ratio is dependent on $^1/\Delta$.

For S.S. junctions we get the noise power from equations (2.44) (2.16):-

$$\overline{P_{N\ total}} \approx \overline{P_{N\ shot}} = \frac{\Delta G_{NN}}{C_J} . K_1(\beta\Delta)\ [1 - e^{-\beta\Delta}] \qquad (2.46)$$

and for N.S. junctions we get the noise power from equations (2.45) (2.10):-

$$\overline{P_{N\ total}} \approx \overline{P_{N\ shot}} = \Delta . \frac{G_{NN}}{C_J}\ K_1(\beta\Delta)\ \ Cosh\ (\beta\Delta/2) \qquad (2.47)$$

The noise power and mean-square noise voltages also depend linearly on Δ. The noise powers are also proportional to G, (as for signal-power). From equations (2.46) (2.47) we get the ratio of noise powers for S.S. and N.S. junctions (with the same G_{NN}, C_J and biased at $V = {}^{\Delta}/e$ and $V = {}^{\Delta}/2e$ respectively, $\omega_o = \infty$ and $R_{leak} = \infty$).

$$\frac{\overline{P_{NT\ SS}}}{\overline{P_{NT\ NS}}} = \frac{(1 - e^{-\beta\Delta})}{Cosh\ (\beta\Delta/2} = 2\ e^{-\beta\Delta/2}\ \tanh(\beta\Delta/2) \qquad (2.48)$$

$$\approx 2\ e^{-\beta\Delta/2};\ \text{approximations valid for } \beta\Delta > 3.5$$

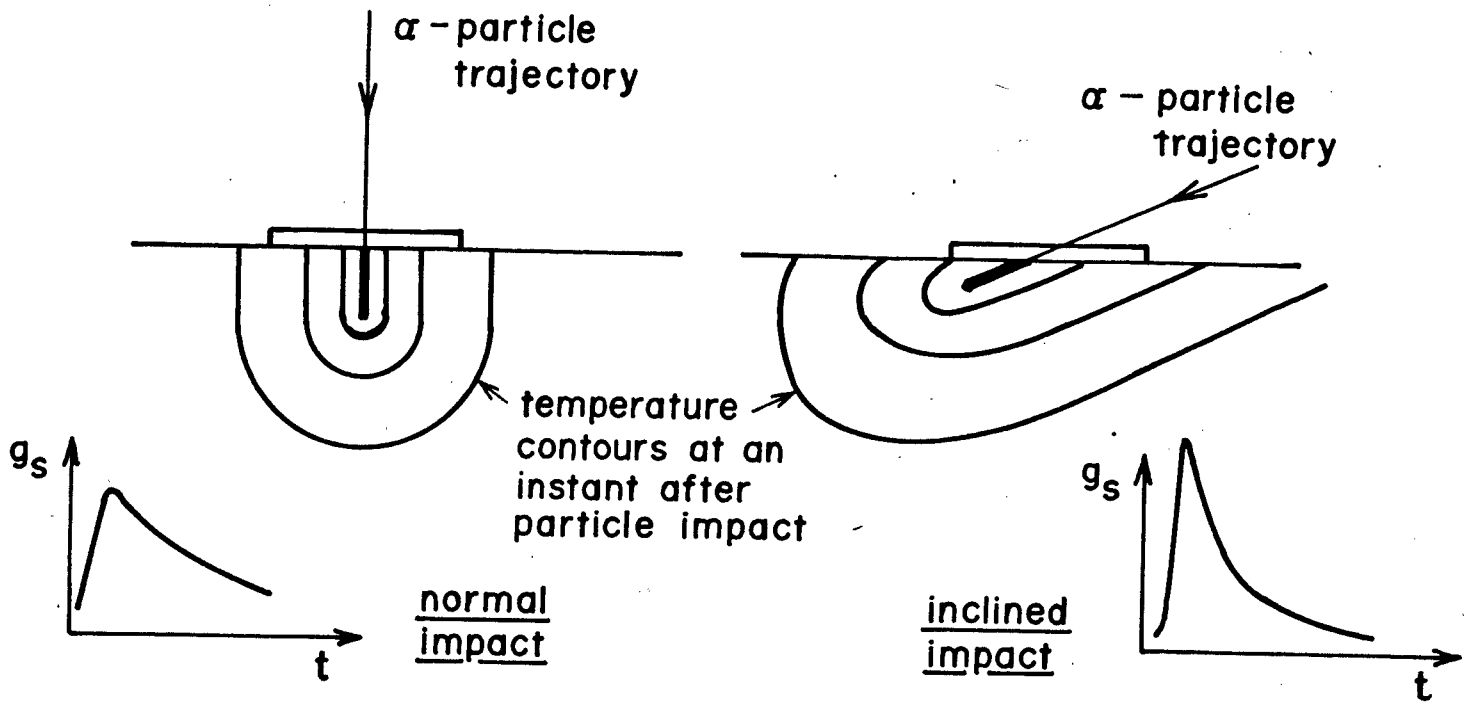

Fig. 2.9 Variation of Signal due to Angle of Incidence of Impinging Particle.

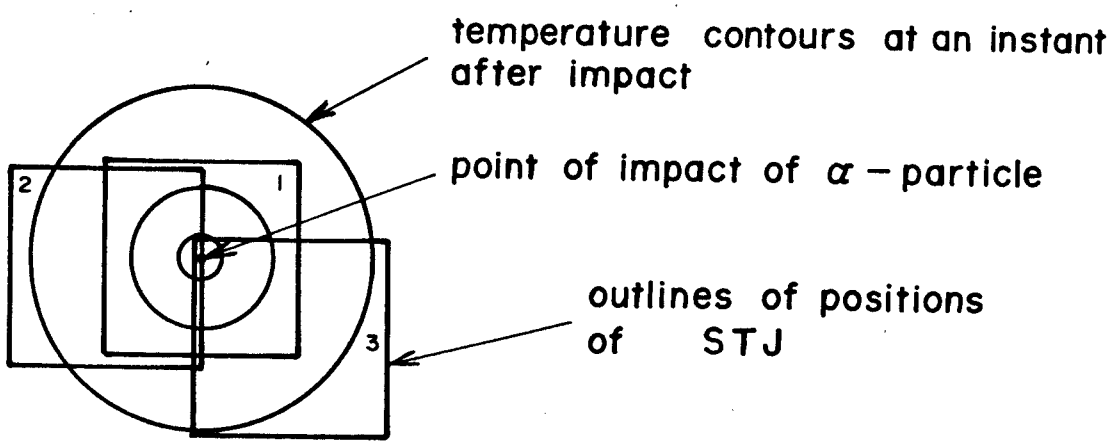

Fig. 2.10 Variation of Signal due to Impact of Incoming Particle at Different Points of a Finite Sized Junction.

We see that the noise power is smaller for S.S. junctions. We can get the power signal-to-noise ratios(S.N.R.) from equations (2.36), and (2.48):

$$S.N.R._{power} \approx e^{\beta\Delta} \qquad (2.49)$$

We see that S.S. junctions are clearly favoured for use as superconductive particle detectors, where the frequency response required is smaller than 10^6 Hz, (far below 10^9 Hz when N.S. junctions show comparable performance.)

Other factors affecting the resolution of SPD's.

Statistical fluctuation of total number N of charge carriers generated by particle. This effect has been considered in detail in Chapter 1. As the fluctuations in the number is of the order of $\sqrt{N}$ the loss of resolution due to this effect is $\sqrt{N}/N = 1/\sqrt{N}$. This favours a large signal current, thus small Δ.

Barrier oxide thickness fluctuation. Due to the fluctuation of oxide thickness the local tunnel cond per unit area can fluctuate and thus cause variation in output current with impact location. This factor was investigated theoretically and was found to be insignificant due to the relatively large area of increased temperature as compared to the size of an area in which the average deviation from the mean thickness is significant.

Angle Effect. The angle of the particle track relative to the substrate surface of the STJ for the glass-substrate type particle detectors, can cause changes in output signal waveform. The two extreme cases are normal-incidence and grazing-incidence. The latter shows a higher signal waveform amplitude, but decays faster as compared to the former, as expected from the physical situation shown in Fig. (2.9). Calculations to be

described in the "numerical calculations" chapter to follow give details on the calculations performed to estimate this effect. The 'angle-effect' does not exist for the heat-sink chip type of particle detector where the heat pulse is assumed to be spread uniformly in the chip in negligible time in relation to thermal relaxation and electrical time-constants of the STJ; or the phonon-barrier type where the heat-spread is essentially 2-dimensional.

Finite Junction-Size Effect. The effect is so named because the particle can impact at the edge or outside the junction, also the thermally affected zone of significance can be greater than the junction-size. The signal output depends on the point of impact of the particle, as can be seen from Fig. (2.1), where the temperature contours at an instant due to a particle impact are drawn and the STJ outline superimposed at 3 different relative locations. It is clear that location (1) gives the greatest signal, and at (3) the signal decays more rapidly than at (2). This effect was so dominant that no energy 'line' or 'peak' was visible in the analysis of the output signals by a pulse amplitude analyser. Instead a relatively sharp high-energy end cut off, corresponding to signal-output due to impacts in the central regions of the STJ, was observed. This effect is calculated in detail in the "numerical calculations" Chapter 3. This effect occurs to a lesser extent for the phonon-barrier type of particle detector. Here it is properly called "Edge effect", because the substrate is absent thermally, impact near the edge does not cause heat to be lost to the STJ (if the electrical contacts are such as to minimize heat loss), but the signal output is affected because of the different time-development of temperature contours.

CHAPTER THREE

NUMERICAL METHODS AND RESULTS

INTRODUCTION

In the previous Chapter theoretical expressions for the characteristics of STJ were derived, in particular the response of the STJ to a small temperature change was calculated. Except for the case of the "heat-sink chip" model the temperature of the junction as a function of time and position on the junction, could not be calculated analytically because of the rapid change of thermal-constant values with temperature at the low temperatures. Consequently numerical solutions of the non-linear heat diffusion problems had to be made. In this Chapter the method of finite differences with variously 1,2, and 3 dimensional arrays of cells is applied to the calculation of temperatures in the phonon-barrier and glass-substrated SPDs. (The phonon-barrier superconductive particle detector was not fabricated. Calculations were made only to estimate the performance of this possible type of particle detector).

Modification of the form of the classical heat-diffusion equation

The classical heat-diffusion equation for temperature dependent specific heat Cp(T), thermal conductivity K(T) and density $\rho(T)$ is:

$$\nabla \cdot (K(T) \cdot \bar{\nabla} T) = Cp(T) \rho \cdot \frac{\partial T}{\partial t} \qquad (3.1)$$

In this form the equation is too complicated for effective numerical solution. The equation can be simplified using the methods described in Jaeger and Carslaw (Ref. 3.4). We define a transformed temperature $\theta(T)$ by

$$\theta(T) = \frac{1}{Ko} \int_{To}^{T} K(T')dT' \tag{3.2}$$

where To is a reference temperature equal to or less than the lowest temperature of the system under consideration, and Ko is an arbitrary constant. Note that $\theta(T)$ is a monotonically increasing function of T by its definition. Using equation (3.2) we get:

$$\nabla\theta(T) = \left(\frac{\partial}{\partial x_i}\vec{e}_i\right) \cdot \theta(T) = \frac{\partial\theta(T)}{\partial x_i}\vec{e}_i$$

$$= \frac{d\theta}{dT} \cdot \frac{\partial T}{\partial x_i}\vec{e}_i$$

$$= \frac{K(T)}{Ko}\nabla(T)$$

Thus equation (3.1) can be written as:

$$\nabla \cdot (Ko\nabla\theta(T)) = Ko\nabla^2\theta(T) = Cp(T)\rho(T)\frac{\partial T}{\partial t} \tag{3.3}$$

Since $\frac{\partial T}{\partial t} = \frac{dT}{d\theta} \cdot \frac{\partial\theta}{\partial t} = \frac{Ko}{K(T)} \cdot \frac{\partial\theta}{\partial t}$,

(3.3) becomes:

$$\nabla^2\theta = \frac{Cp(T(\theta))\rho(T(\theta))}{K(T(\theta))} \cdot \frac{\partial\theta}{\partial t} \qquad (3.4)$$

Equation (3.4) is much more suitable than (3.1) for numerical solutions.

Boundary conditions for the heat diffusion problem glass-substrate type superconductive particle detector

The glass-substrate superconductive particle detector is shown in Figure 2.1 of Chapter 2. The top-surfaces of the junction film and that of the glass substrate not under the junction film are considered insulating boundaries. If the surfaces were coated with a protective layer of rosin (see Chapter 4 for details of protective layer), this layer would form a phonon-barrier. Alternatively the junction film surface or glass surface and the super-fluid film which is assumed to cover the junction film at the operating temperature of 1.2 K, constitutes an insulating boundary because of the acoustical mismatch Ref.(3.1) The glass-metal (junction film) interface is considered to be thermally well coupled to the glass substrate at the glass metal interface.

For the present experiment 98% of the α-particle energy (5.13 MeV) was deposited in the glass substrate. Thus to simplify the computational problem the particle energy was assumed to be all deposited in the substrate. The superconductive tunnelling junction is assumed to be a thermometer, the thermal-presence of which was ignored in the calculations. This approximation is valid only if the heat-capacity of the junction film is a small fraction of that of the heat affected volume of the glass substrate, and if the thermal conductance from the impact zone along the plane of the junction film is small compared to that of the heat affected volume of

glass.

The heat capacity of the 0.2 mm x 0.2 mm x 4000A Sn junction films was 1.03×10^{-12} J/ K, as compared to the heat capacity of the heat affected volume of glass ($\sim$0.2 mm x 0.2 mm x 32μ) of 1.484×10^{-11} giving a ratio of 0.07. Thus we can ignore the heat-capacity of the junction films without introducing too much error.

Because of the small film thickness of 2000A and the low temperatures and consequently long mean free path, boundary scattering of electrons and phonons becomes very prominant and drastically decrease the thermal conductivity. Deriving a value for the film thermal conductivity requires a chain of arguments, in which the most pessimistic supportable extrapolation procedures have been used in order to arrive at a valid upper limit.

From Andrew's (Ref. 3.7) data in Table 2 of his paper we can derive the resistivity ratio $\rho_{F/\rho_B}\big|_{3.8K}$ (where ρ_F = foil resistivity (for a 3.34μ Sn foil in this case) and ρ_B = bulk resistivity (using the value given for a 1950μ thick foil)) as follows:

$$\frac{\rho_{F\ 3.8K}}{\rho_{F\ 291K}} \Big/ \frac{\rho_{B\ 3.8K}}{\rho_{B\ 291K}} = \frac{\rho_{F\ 3.8K}}{\rho_{B\ 3.8K}}$$

Here, we have set $\rho_{F\ 291K} = \rho_{B\ 291}$, because of the small electron mean free path at 291K as compared to the foil thickness. Thus from Andrew's data for his specimen E18, foil thickness = 3.34μ , $\rho_{F\ 3.8K}/\rho_{F\ 291K} = 20.1 \times 10^{-4}$ and for specimen E7 foil thickness = 1950μ , $\rho_{B\ 3.8K}/\rho_{B\ 291K} = 1.80 \times 10^{-4}$, we get:

$$\frac{\rho_{F\ 3.8K}}{\rho_{B\ 3.8K}} = 11.167$$

Using the Fuchs-Sondheimer formula for size effect on resistivity ratio (Ref.3.9) for $x = t/\ell << 1$, where t = film thickness and ℓ = electron mean free path, for diffuse scattering at film boundaries:

$$\frac{\rho_B}{\rho_F} = 0.75x \cdot (0.423 - \ell n\ x)$$

it was possible to solve for x given ρ_F/ρ_B.

Using the above $\rho_F/\rho_B \mid 3.8K$, $x = 109.2$. The electron mean free path is expected to increase with decreasing temperature, thus this ratio should be larger at 1.2 K, our operating temperature for the junction. To get some idea of the value at 1.2 K, the resistivity ratio ρ_F/ρ_B for Andrew's specimen E18 were plotted vs. temperature and extrapolated graphically to 1.2 K. It was found that the ratio was most probably greater than 14, corresponding to a calculated electron mean free path of > 0.15 mm. Thus for normal Sn at 1.2 K the resistivity ratio ρ_F/ρ_B calculated using the Fuchs-Sondheimer formula was > 142, (for film thickness = 2000A).

For superconducting Sn, the mean free path of the quasiparticles would be of the order of normal Sn conduction electron mean free path value. Some of the conduction electrons condense to form Cooper-pairs, removing them from heat conduction contributions. When the quasiparticles form the major contribution to the thermal conductivity, then the Wiedemann-Franz Law $\left(K = \frac{\pi^2 K_B^2}{3e^2} T \cdot \sigma\right)$ applies and the thermal conductivity ratios of the

film to bulk value is the same for the corresponding ratios of electrical conductivity. The phonon contribution to thermal conductivity becomes significant at lower temperatures (for To <0.3Tc See Ref. 3.15) with decrease of quasiparticle density. Size effect reduction of thermal conductivity contribution of the phonon component due to film boundary scattering also occurs (Ref.3.8). In general it is expected that the phonon mean free path is not smaller than the electron mean free path. Thus it is reasonable to assume the same size effect reduction factor for the phonon component of thermal conductivity as for the electron component. Therefore:

$$\frac{K_F}{K_B}\Big|_{T,t} = \frac{K_{Fph}}{K_{Bph}} = \frac{K_{FQp}}{K_{BQp}} = \frac{K_{Fel}}{K_{Bel}} = \frac{\sigma_{Fel}}{\sigma_{Bel}}$$

where K = film thermal conductivity, σ = electrical conductivity.

Subscripts F = film, B = bulk, Ph = phonon, Qp = quasiparticle, el = electron.

In conclusion,

$$K_F/K_B \mid_{Sn,1.2} < 1/142.$$

and since $K_B \mid_{Sn,1.2K} = 71 w/mK$ (Ref.3.5) we get $K_F \mid_{Sn,1.2K} < 0.500$ w/mK, in the plane of the film.

Thus the ratio of (radial) thermo-conductance of junction films to that of the heat affected volume of glass $= \frac{2tK_F}{Z\,K_G} = \underline{0.178}$

where

K_F = thermal conductivity of Sn film in the plane of the film at 1.2K = 0.500 w/mk

K_G = thermal conductivity of glass = 0.035 w/mk at 1.2K

Z = penetration depth of the α particle in glass = 32μ

t = thickness of Sn junction film, factor 2 because of the two layers of junction films.

We see that the junction film does play a part in heat transport but can be ignored to a first approximation. The effect of the heat transport by the junction film is to increase the rate of heat dissipation from the hot central region of the α-particle impact and decrease the signal current decay time constant.

Phonon-barrier type superconductive particle detector

The structure of the proposed phonon-barrier type superconductive particle detector is shown in Figure 2.2 of Chapter 2. The performance of this type of superconductive particle detector is expected to be better than the glass-substrate type, in particular at low particle energies, and is easier to fabricate than the heat-sink chip type superconductive particle detector. Thus the performance figures are of sufficient interest to justify the numerical calculations to derive them.

The top surface of the junction films as in the glass substrate type particle detector is an insulating boundary, for the same reason. The bottom of the junction films in contact with the phonon-barrier layer is also an insulating boundary. Thus the heat flow is essentially 2-dimensional,

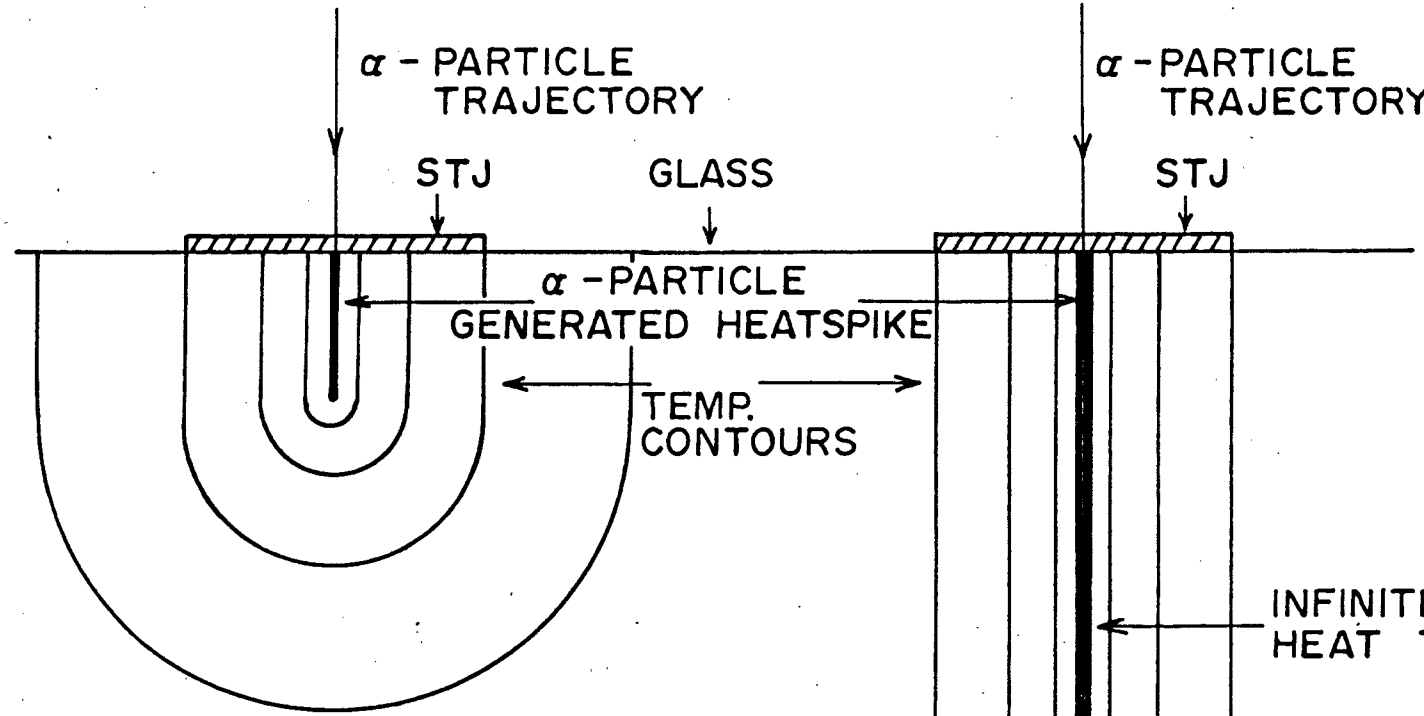

FIG. 3.1A α-PARTICLE PENETRATING A GLASS -SUBSTRATED STJ..

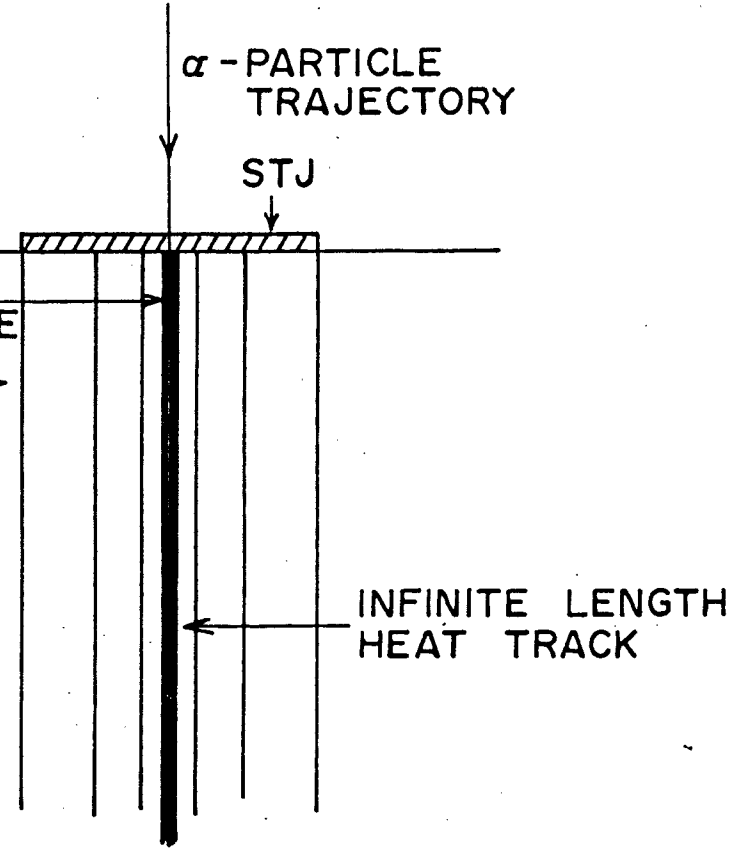

FIG. 3.1B 1-DIM. RADIALLY SYMMETRIC APPROX. OF AN α-PARTICLE PENETRATING A GLASS-SUBSTRATED STJ..

in the plane of the junction film between the two insulating boundaries. (Note that as above, because of size effect the thermal conductivity along the direction of the film is reduced and this reduced value must be used in the calculations.

Numerical solutions with radial symmetry

An α-particle penetrates a glass-substrated STJ at normal incidence, shown in Fig.3.1a. Restricting ourselves to early times of the α-particle induced temperature-transient (time shorter than that required for significant heat to diffuse a distance equal to the depth of penetration of the heat spike into the substrate), the temperature profiles at the surface (with insulating boundary condition) can be approximated by a 1-dimensional radially symmetric model shown in Fig.3.1b, with the initial deposition of heat per unit length along the symmetry axis given by the average heat deposited per unit length in the α-particle generated heat-track (Ref. 3.3) ("heat spike"). This approximation results in R the radius being the only spatial coordinate for temperature.

In Fig.2.2 and in associated discussions in Chapter 2, page 5, we saw that for the phonon-barrier type SPD the heat diffusion essentially occurs 2-dimensionally along the plane of the junction film. Ignoring the edge boundaries of the junction films, a valid approximation for impacts in the central area of the junctions, the heat diffusion problem resulting from an α-particle impact is radially symmetric. It therefore differs from the glass-substrate case only in that the diffusion equation uses the thermal properties of the metal film. Thus the heat diffusion problem can be approximated by the cylindrical symmetry as shown in Fig.3.1b, with the

initial deposition of heat per unit length in the axis given by the heat deposited in the film divided by the film thickness.

Translation to Finite-Differences equations

From Equation (3.4) substituting the Laplacian for radial symmetry, we get:

$$\nabla^2\theta = \frac{\partial^2\theta}{\partial r^2} + \frac{1}{r}\frac{\partial\theta}{\partial r} = \frac{Cp(T(\theta))\cdot\rho(T(\theta))}{K(T(\theta))}\cdot\frac{\partial\theta}{\partial t} \qquad (3.5)$$

Translating to finite differences (Ref.3.4) using $r = m\varepsilon$, and $t = n\tau$ we get:

$$\frac{\partial\theta(r,t)}{\partial r} = \frac{\theta m+1,\ n - \theta m-1,\ n}{2\varepsilon} \quad \text{or} \quad \frac{\theta m+1,\ n - \theta m,n}{\varepsilon}$$

where $\theta m,n = \theta(m\varepsilon,n\tau) \equiv \theta(r,t)$.

Both forms of the first derivative are given because the first is used as the expression for the first derivative, and the second is used to derive the second derivative expression shown below:

$$\frac{\partial^2\theta(r,t)}{\partial t^2} \longleftrightarrow \frac{1}{\varepsilon^2}\ [\theta m+1,n - 2\theta m,n + \theta m-1,n]$$

Thus

$$\nabla^2\theta \longleftrightarrow \frac{1}{2m\varepsilon^2}\ [(2m+1)\ \theta m+1,n - 4m\theta m,n + (2m-1)\ \theta m-1,n]$$

further $\frac{\partial\theta}{\partial t} \longleftrightarrow \frac{1}{\tau}(\theta m,n+1 - \theta m,n)$.

Thus Equation (3.5) written in finite differences form is as follows:

$$\frac{1}{2m\varepsilon^2}\left[(2m+1)\ \theta m+1,n - 4m\theta m,n + (2m-1)\ \theta m-1,n\right] = \frac{Cp\rho}{K}\cdot\frac{1}{\tau}(\theta m,n+1 - \theta m,n) \tag{3.6}$$

Solving (3.6) for $\theta m,n+1$ we get:

$$\theta m,n+1 = \frac{K}{Cp\rho}\ \frac{\tau}{2m\varepsilon^2}\left[(2m+1)\ \theta m+1,n - 4m\theta m,n + (2m-1)\ \theta m-1,n\right] + \theta m,n \tag{3.7}$$

The Equation (3.7) gives the transformed temperature at $r = m\varepsilon$(cell 'm') at time $t = (n+1)\tau$ in terms of the transformed temperatures of itself and its neighbours at time $t = n\tau$. Using the configuration shown in Fig.3.1b for 'cells', 'm' takes half integer values ($\frac{1}{2}, 1\frac{1}{2}, 2\frac{1}{2}\ldots$) m = 0 does not occur, thus avoiding the singularity for r = 0 (m = 0), ensuring the validity of (3.7) for all the m values used. For the calculations of $\theta\frac{1}{2},n+1$ we need the values of $\theta-\frac{1}{2},n$. This value is provided by the axial "boundary" condition, namely no heat flows into or out of the axis, thus $\frac{\partial T}{\partial r} = 0$ at r = 0, implying $\frac{\partial\theta}{\partial r} = 0$ at the axis because of the monotonic dependence of θ on T. This is equivalent to the finite difference expression for an insulating boundary namely $\theta-\frac{1}{2},n = \theta\frac{1}{2},n$, which is the required expression for $\theta-\frac{1}{2}n$.

Initial and boundary conditions

For the present problem the energy of the α-particle was assumed to be deposited as heat in the axial cell (m=½). The resulting temperature and transformed temperature θ of the axial cell was calculated and the transformed temperature used as the initial θ of the m=½ cell. The rest of the cells start at the operating bath temperature expressed in θ. It is not possible to have boundaries at infinity in a finite difference problem, but the boundary can be placed sufficiently far away such that the effect of heat-flow or lack of heat-flow through the boundary (corresponding to constant temperature and insulating boundary conditions respectively) is negligible for the duration of physical interest. For the solutions discussed in this Chapter, the boundary cells were fixed in temperature at the "bath-temperature", i.e. a constant temperature outer boundary condition was used.

Thermophysical data used for numerical calculations

Since the properties of the glass substrates used (Corning "Process Clean" #2947 microscope slides) were not available in the literature or from Corning, values of specific heat Cp(T) and thermal conductivity K(T) were taken from References (3.10), (3.11) respectively. The Cp(T) values From Reference (3.10) are for "pyrex" glass and the values were provided for 1K to 20K. The thermal conductivity values given in Reference (3.11) were 'averages' of quartz, pyrex and borosilicate glasses, and values were given down to 4K. Values of K(T), for 1K to 4K were obtained by extrapolating a θ(T) (thermal boundary potential) vs. T curve for pyrex glass, Ref.(3.12), then calculating K(T) by the relation $K(T) = \frac{\partial \theta(T)}{\theta \tau}$. The K(T)

TEMP.K	Cp(T)J/Kg·K	K(T)W/m·K	TEMP.K	Cp(T)J/Kg·K	K(T)W/m·K
1.0	0.109×10^{-1}	0.305×10^{-1}	5.5	0.590	0.110
1.2	0.126 "	0.350 "	6.0	0.770	0.113
1.4	0.142 "	0.400 "	6.5	0.100×10^{1}	0.115
1.6	0.163 "	0.460 "	7.0	0.130 "	0.117
1.8	0.197 "	0.520 "	8.0	0.200 "	0.119
2.0	0.238 "	0.570 "	9.0	0.300 "	0.120
2.2	0.289 "	0.600 "	10.0	0.410 "	0.120
2.4	0.360 "	0.650 "	11.0	0.570 "	0.121
2.6	0.448 "	0.700 "	12.0	0.720 "	0.123
2.8	0.552 "	0.750 "	14.0	0.110×10^{2}	0.129
3.0	0.686 "	0.790 "	16.0	0.160 "	0.133
3.2	0.850 "	0.820 "	18.0	0.210 "	0.140
3.4	0.104 "	0.840 "	20.0	0.270 "	0.146
3.6	0.127 "	0.900 "	22.0	0.320 "	0.152
3.8	0.154 "	0.920 "	24.0	0.380 "	0.162
4.2	0.223 "	0.100 "	26.0	0.430 "	0.170
4.6	0.330 "	0.102 "	30.0	0.550 "	0.190
5.0	0.420 "	0.107 "	35.0	0.710 "	0.210

Density $\rho = 0.223 \times 10^{4}$ Kg/m^{3} negligible variations over temperature range of interest.

TABLE: 3.1 Specific Heat and Thermal Conductivity Data of Glass Used in Numerical Calculations Relating to the Glass-Substrated Super-Conductive Particle Detector

curve between 1K and 4K so obtained was matched to the K(T) curve given by Ref.(3.11) at 4K to obtain a smooth transition. The values of Cp(T), K(T) used for the numerical calculations on the glass substrated S·P·D are tabulated in Table (3.1). Because of the uncertainty in the values of Cp(T), K(T) used, the calculated results are expected to be uncertain to the same degree, but should have similar characteristic shapes as observed results. However, being a glass substrate, the thermal constants are probably not too different from the values used, possibly within a factor of 2. Thus the numerical results are quantitatively significant to this degree. (If the actual thermal constants for the glass substrate could be determined and used, the numerical results would be quantitatively valid.) Thermal constants for Sn and Pb used for the phonon-barrier type S·P·D calculations were obtained from data given in Ref.(3.13), (3.14) respectively. For thin junction films the data on K(T) was modified to account for the size-effect reduction of thermal conductivity in the plane of the junction film. The reduction of the K(T) value is dependent on the junction film thickness and also dependent on the temperature, since the mean free path of the conduction electron is temperature dependent. However, the change in temperature over the major portion of the signal-current pulse duration is small, thus the reduction factor is essentially that at the operating temperature.

Temperature and signal-current calculations

With the initial and boundary conditions described in the previous section the Equation (3.7) was then used to calculate the transformed temperature for all the cells for a time 'τ' later. This process was repeated

for as long as desired, giving the temperature-profiles at intervals of τ. The calculated surface temperatures at each cell was used to calculate the excess junction current flowing through the area of that cell. The total excess-current from all areas of the junction covering 'cells' was summed to give the junction signal-current.

Stability Considerations

In finite difference calculations ε and τ cannot be chosen independently, since the round-off errors must not propagate and diverge (Ref.3.9). Writing M for $\left[\frac{T}{\varepsilon^2} \left(\frac{K}{C\rho}\right) \right]$ in (3.7) we get:

$$\theta_{m,n+1} = M\left(1 + \frac{1}{2m}\right) \theta_{m+1,n} + (1-2M)\, \theta_{m,n} + M\left(1 - \frac{1}{2m}\right) \theta_{m-1,n} \qquad (3.8)$$

Representing errors in θ by $\delta\theta$ we can derive from (3.8):

$$\delta\theta_{m,n+1} = M\left(1 + \frac{1}{2m}\right) \delta\theta_{m+1,n} + (1-2M)\, \delta_{m,n} + M\left(1 - \frac{1}{2m}\right) \delta\theta_{m-1,n} \qquad (3.9)$$

$$\therefore \quad |\delta\theta_{m,n+1}| \leq \left|M\left(1 + \frac{1}{2m}\right)\right| |\delta\theta_{m+1,n}| + |(1-2M)|\,|\delta\theta_{m,n}| + \left|M\left(1 - \frac{1}{2m}\right)\right| \cdot |\delta\theta_{m-1,m}| \qquad (3.10)$$

If η is the largest of $|\delta\theta|$ then

$$|\delta\theta_{m,n+1}| < \left|M\left(1 + \frac{1}{2m}\right)\right| + |(1 - 2M)| + \left|M\left(1 - \frac{1}{2m}\right)\right|)n \qquad (3.11)$$

Since M is greater than zero (by the definition of M) and $m > \frac{1}{2}$ the right hand

side of Equation (3.11) = $(2M + |(1 - 2m)|)\eta$.

For errors not to propagate $|\delta\theta_{m,n+1}|$ must be $\leq \eta$ for all m,n+1.

Now

$$(2M + |1 - 2M|) = 1 \quad \text{for } M < \tfrac{1}{2};$$
$$> 1 \quad \text{for } M > \tfrac{1}{2} \tag{3.12}$$

For errors not to propagate, $(2M + |1 - 2M|)$ must not be greater than 1, thus requiring $M < \frac{1}{2}$. This condition is sufficient for convergence but not necessary in all cases, since in Equation (3.10) we have used the worst case errors by taking the absolute values. In practice, $M = \frac{1}{2}$ is a borderline case, and may result in oscillatory but finite solutions, hence for the present solutions an additional factor of 2 for safety was used by chosing M to be smaller than $\frac{1}{4}$, i.e.

$$\frac{K}{C\rho} \cdot \frac{\tau}{\varepsilon^2} < \tfrac{1}{4}$$

$$\text{or} \quad \tau < \frac{\varepsilon^2 C\rho}{4K} \tag{3.13}$$

This meant that for numerical stability once ε^2 was chosen, then the maximum value for τ was fixed. In the present problem $(\frac{C\rho}{K})$ was a function of temperature, since (3.13) must be satisfied at all times and locations, thus the minimum value of $\frac{C\rho}{K}$ expected to be encountered in the solution had to be used in determining the maximum value of τ.

Computer program organization for the 1-dimensional radially symmetric approximations

The value of Cp, ρ, K obtained from Refs.(3.10), (3.11), (3.12), (3.13) and (3.14) for Sn and Pb were supplied in table form at discrete temperatures, from which values for inbetween temperatures were obtained by interpolation. From K and the Equation (3.2), chosing Ko = 1 we get the corresponding scale of transformed temperature. The transformed temperature of the bath ("UBTH") is first calculated and was used as the starting temperature for all but the axial cell (m = ½), and as the boundary constant temperature. The intial temperature of the axial cell for a quantity of heat Q deposited by the particle (Q = equivalent heat/unit length of α-particle track, for the present approximation. In calculating Q, the energy dependence of dE/dx of the particle traversing the substrate was ignored, and it was assumed that dE/dx = constant so that $Q = E\alpha/\ell$ where $E\alpha$ was the total α particle energy loss in the substrate and ℓ was the track length. This assumption was necessary to provide the uniform heat energy per unit length along the central cell required for the 1-dimensional approximation to be valid. Q was calculated by the integral relation

$$Q = \int_{T_{bath}}^{T_{initial}} Cp\rho dT(\pi\varepsilon^2) \qquad (3.14)$$

The initial temperature was then translated to transformed-temperature, completing the initial and boundary condition specifications.

U(N,1) was used to label the transformed temperature of the $(N-1)^{th}$ cell. The transformed temperature of the axial cell was thus U(2,1) and

U(1,1) = U(2,1) provided the axial boundary condition. The U corresponding to the outer boundary cell was set at "UBTH" to provide the constant temperature outer boundary condition. The second label '1' of U(N,1) was used to indicate the known temperature at the current value of time, while in U(N,2) the label '2' indicates the transformed temperatures for the subsequent time, calculated using Equation (3.7). Because of the stability condition, the time interval τ was too short for the data to be of interest at each step, thus the program repeated the calculations a specified number of times before translating the U values to temperature (°K) values for printout. Using these temperature values and a table of excess current-density as a function of temperature and bias values (for a reference function) the excess-junction current contribution of each element of junction area was summed up to give the total excess junction current, i.e. the signal-current I_s. (The junction bias-voltage value used for the calculations was the specified applied voltage less the linearly extrapolated I_s times the specified 'load-line' equivalent resistance). In this program when the ratio of the transformed-temperature of the cell adjacent to the axial cell, and that of the axial cell falls below a specified value, the cell sizes were doubled by averaging the heat between pairs of adjacent cells, and adding cells (of the new size and at bath temperature) to make up the numbers. The time step τ was quadrupled as permitted by the stability-condition Equation (3.13), and calculations were continued with the results of the previous calculations as new initial conditions. In this manner, when the thermal gradients were small, needless detail in calculations were eliminated, shortening the calculations required to reach a specified value of the pulse-evolution time.

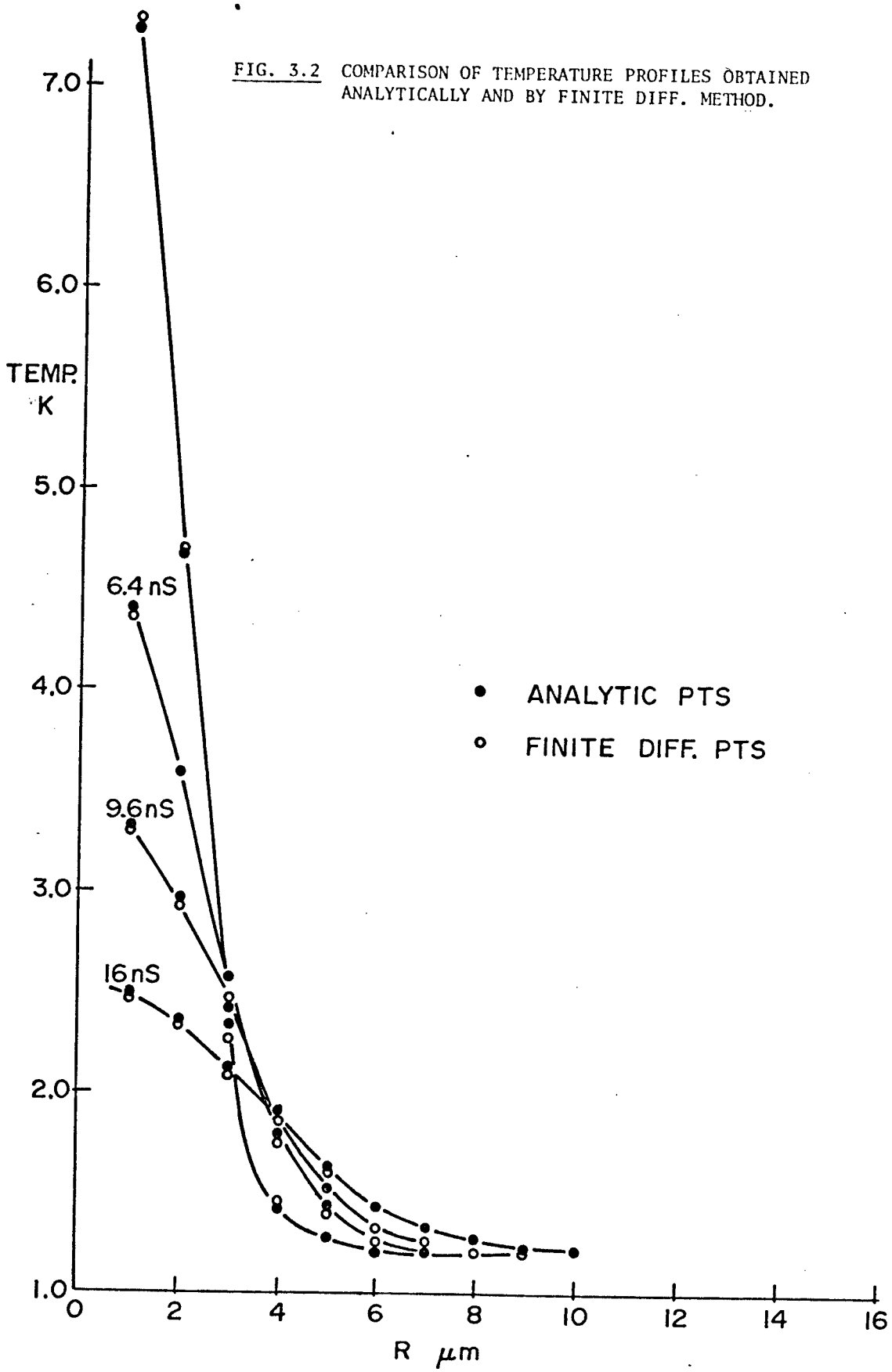

FIG. 3.2 COMPARISON OF TEMPERATURE PROFILES OBTAINED ANALYTICALLY AND BY FINITE DIFF. METHOD.

FIG. 3.3 TEMP. PROFILES 1-DIM. RADIALLY SYMMETRIC HEAT-DIFFUSION IN GLASS.

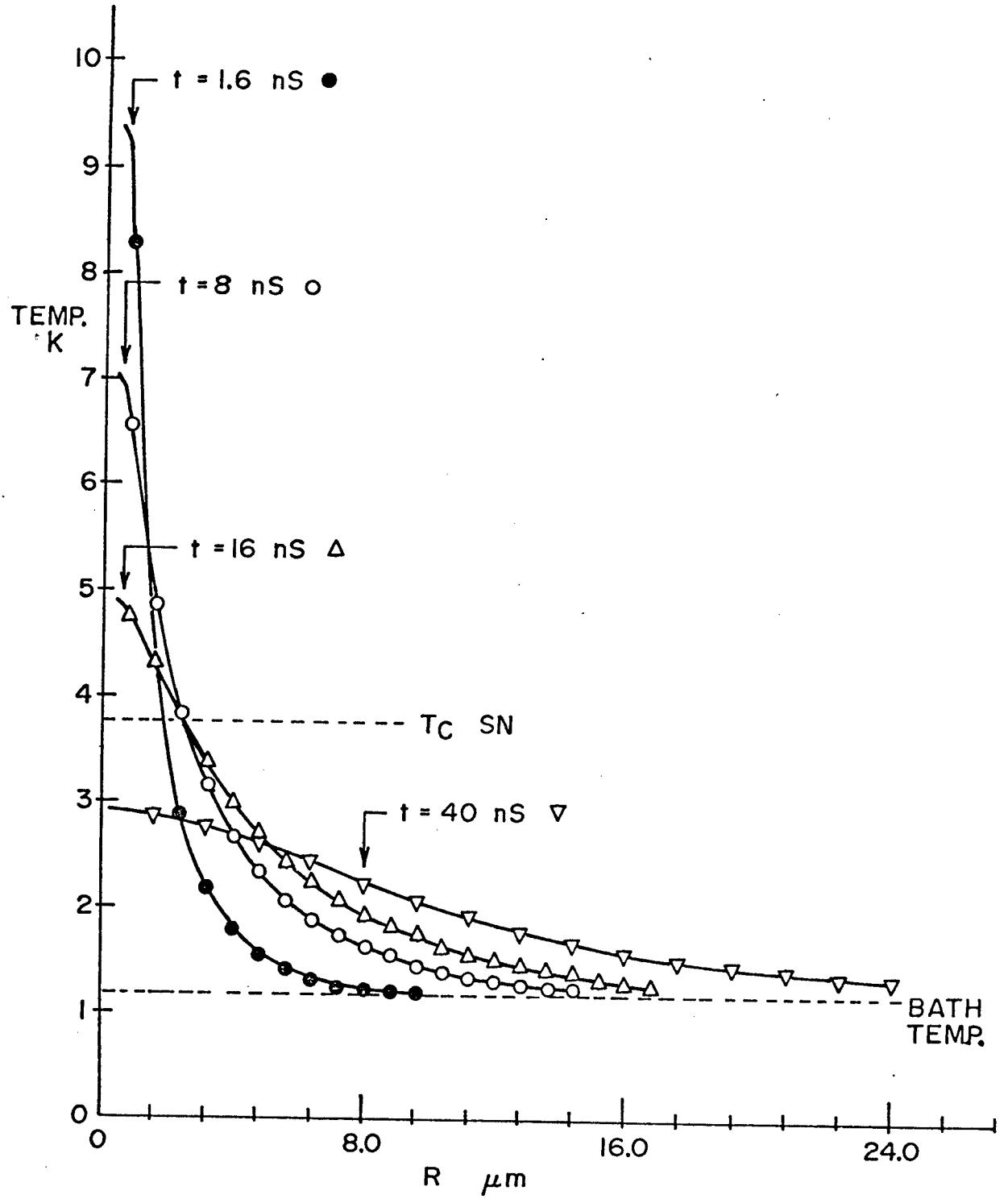

FIG. 3.4 Is Vs TIME, 1-DIM. RADIALLY SYMMETRIC APPROX. of α-PARTICLE IMPACT ON GLASS-SUBSTRATED STJ.

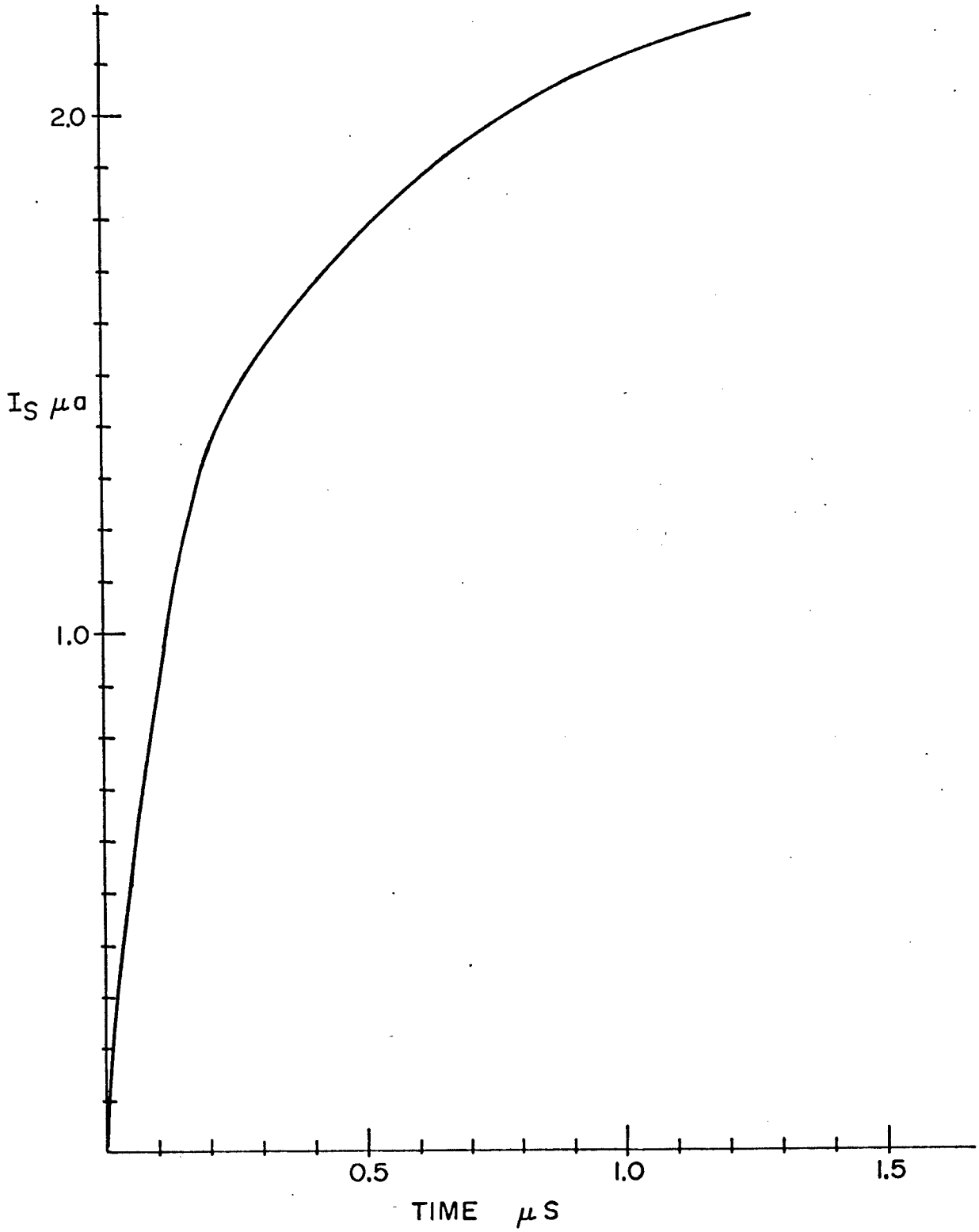

Verification of numerical methods

To test for errors in the program or the method of calculation, the program was used to calculate the temperatures with non-temperature dependent Cp, ρ, K and the results compared with an analytic solution of the same problem:-

$$\Delta T(r,t) = \frac{Q}{4\pi Kt} e^{-\frac{r^2}{4t(\frac{K}{C\rho\rho})}} \qquad (3.15)$$

where ΔT is the rise in temperature, and Q the heat per unit lengths of axis. Some of the resulting temperature profiles from both methods were plotted for comparison in Fig. (3.2). It is clear that the agreement is very good, indicating the validity of the numerical methods and the computer program.

Results: 1-Dimensional radially symmetric approximations for glass substrated SPD, valid for early times

The calculated temperature-profile Vs. time is plotted in Fig. (3.3). The results are good approximations of the resulting surface temperature profiles of normal-incidence α-particle impact with a finite track-length (∿ 32 μm) up to the time when the effects of the finite length of the heat track begin to show at the surface. Assuming this occurs approximately at times when temperature changes start to occur at radial distances equal to the expected track length, (32 μm), the time interval of valid approximation is at least 40 ns. The calculated junction-current is thus expected to be valid during this interval Fig. (3.4). For times greater

FIG. 3.5 NORMAL-RADIUS Vs TIME, DERIVED FROM 1-DIM. RADIALLY SYMMETRIC APPROX. OF α-PARTICLE IMPACT ON GLASS-SUBSTRATED STJ..

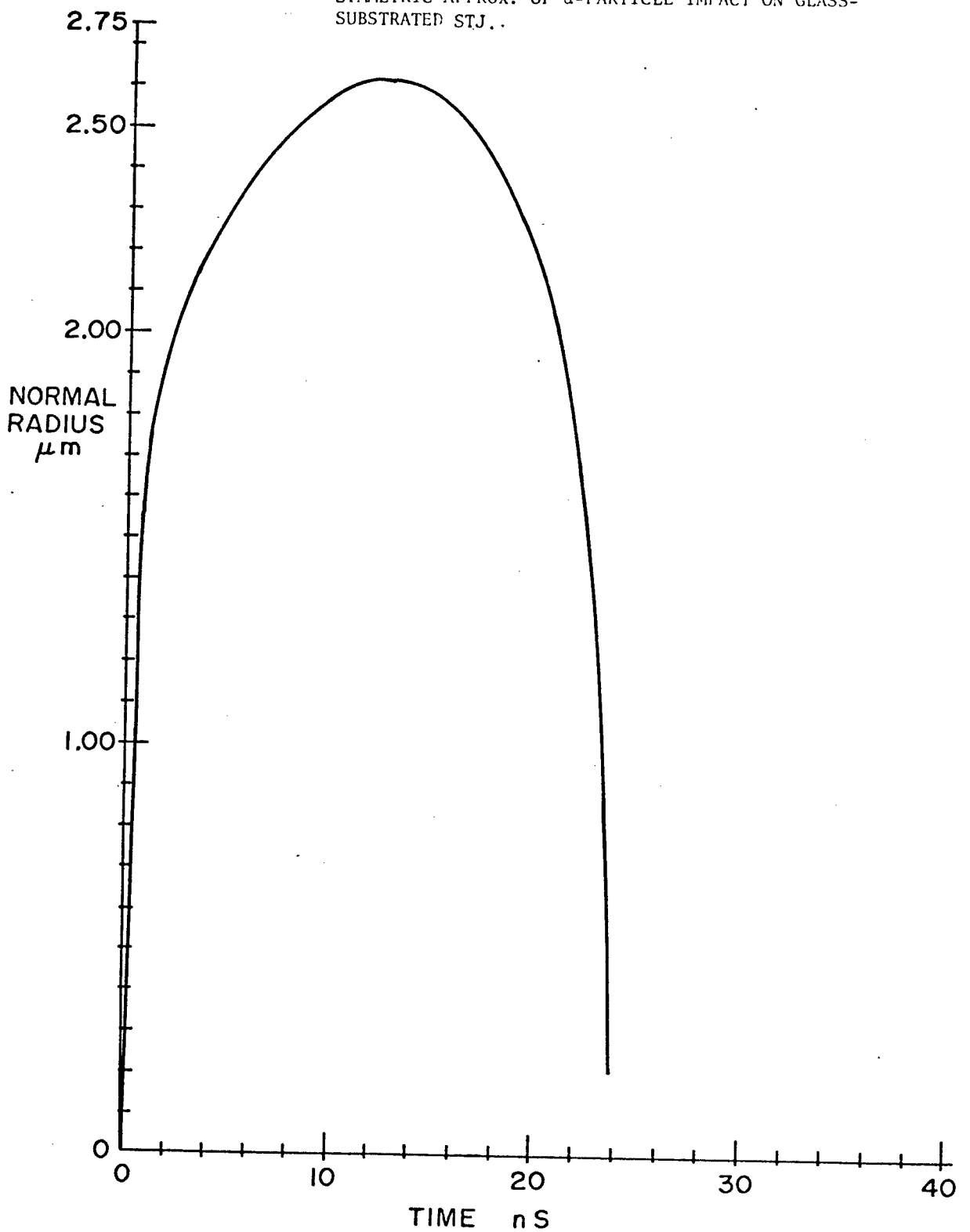

than this it is necessary to use a more complicated geometry to do the heat-diffusion calculation, which requires large cell sizes to accommodate computer limitations. For large times (t>> time for significant heat to diffuse over a distance equal to particle track length) a different approximation is valid, the spherically symmetric approximation which is discussed later in this Chapter. The results of calculations using the present approximation are useful in supplying a detailed fine mesh look (at the early stages) of temperature-profile development, to make sure that the use of the larger cell size later did not obscure any significant phenomenon. From the temperature profile plot we can see the initial increase, then decrease of the normal radius, i.e. the radius inside which the temperature is greater than the critical temperature of the superconductor which for this instance was Sn, T_C = 3.75 K. The time development of the normal radius is plotted in Fig.(3.5).

Results: 1-Dimensional radially symmetric approximation for the phonon-barrier SPD

The same computer program as above was used to calculate the response of the phonon-barrier SPD to α-particle impact. The thermal properties Cp, ρ, K for Sn were supplied in table form for discrete temperatures, and the excess current densities for a reference Sn junction for discrete temperatures and bias voltages were used. Q, the particle energy deposited per unit length, in this case was the value given by E/t where E = particle energy and t = total film thickness.

The temperature profiles as a function of time for the Sn phonon-barrier SPD with operating bath temperature of 1.2 K are shown in

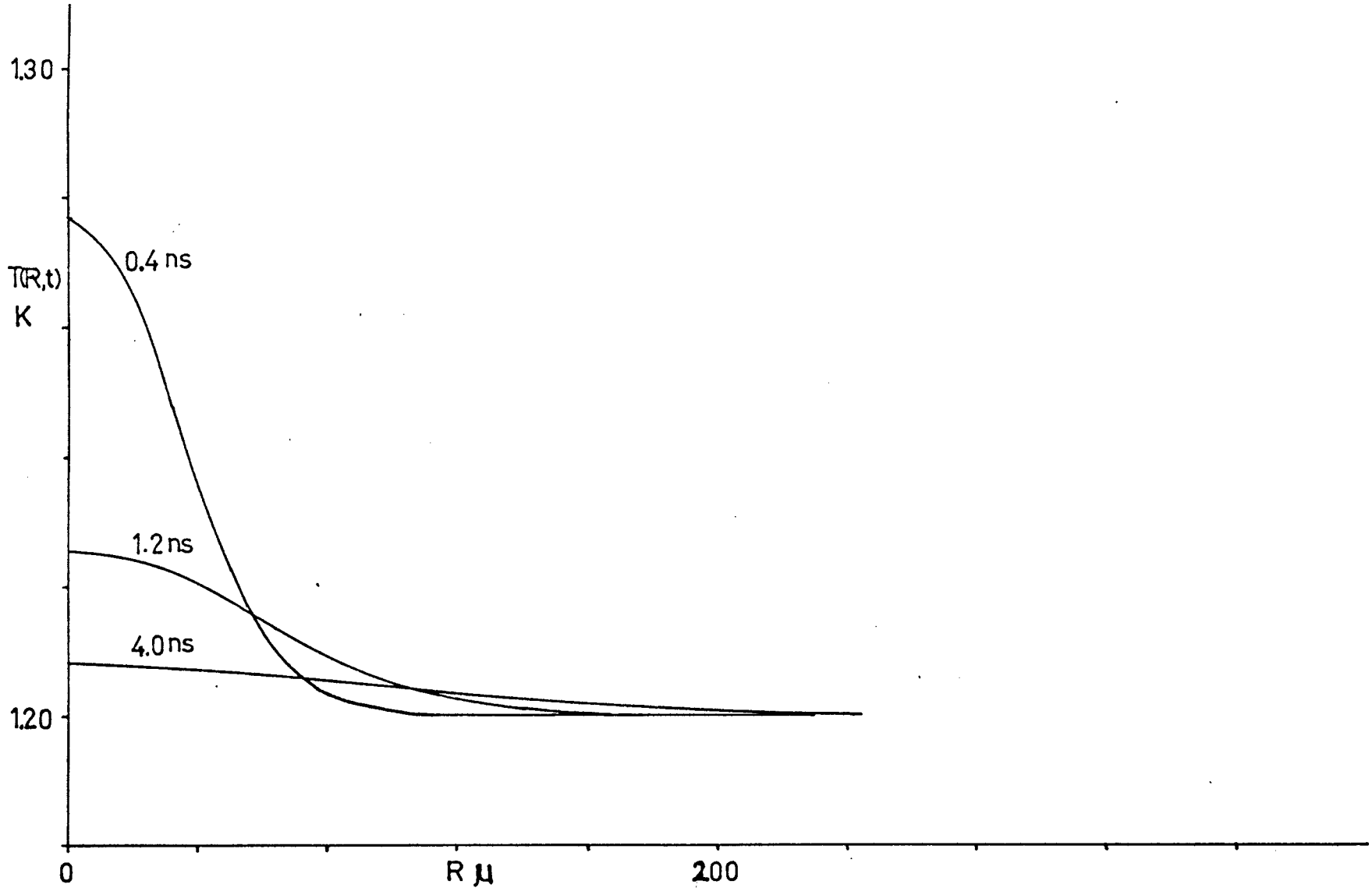

FIG. 3.6 TEMPERATURE PROFILES AS A FUNCTION OF TIME FOR Sn S.T.J. ON A PHONON-BARRIER.

FIG. 3.7 Sn PHONON-BARRIER TYPE STJ Is Vs TIME AT 1.2 K (THEORETICAL)

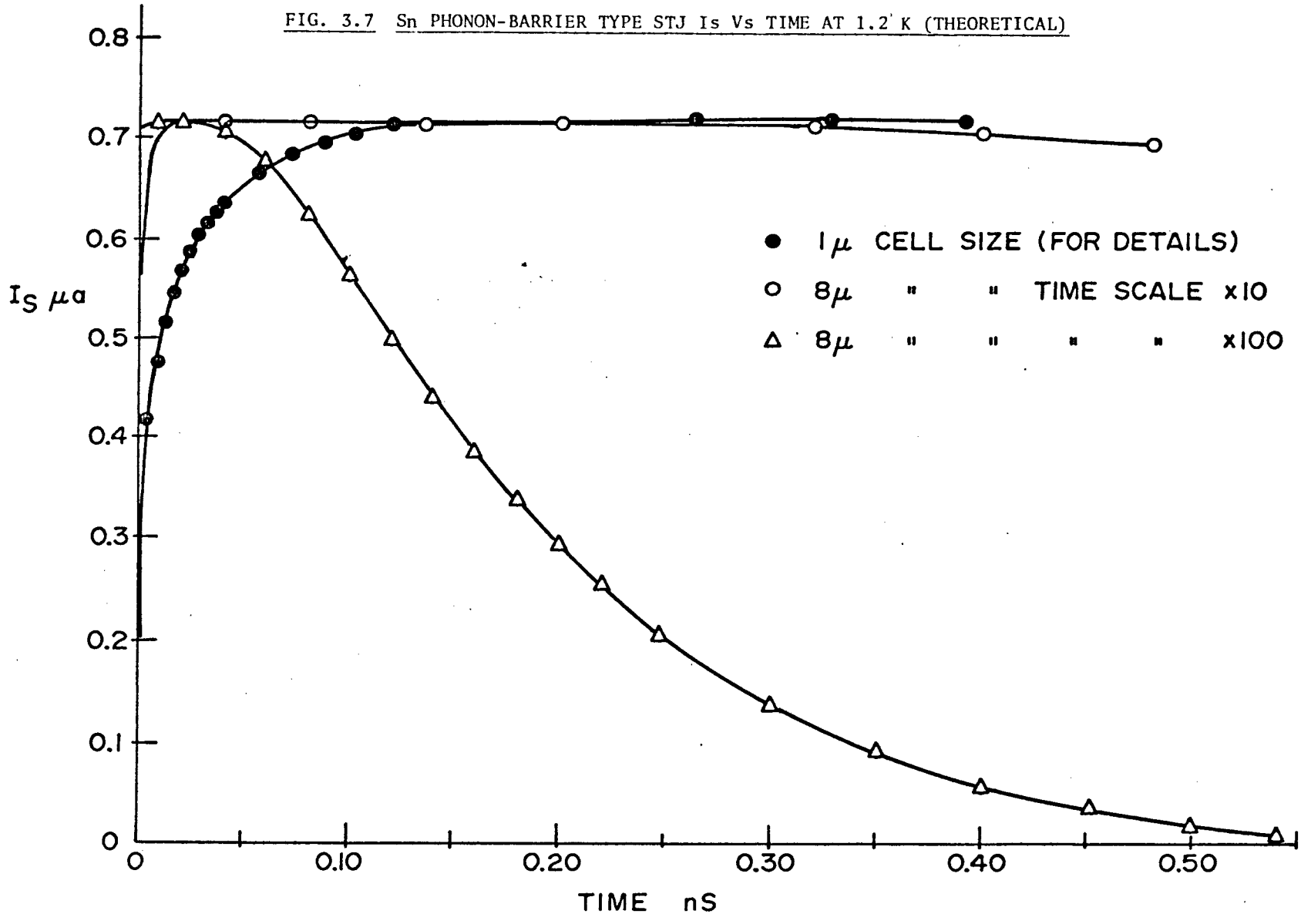

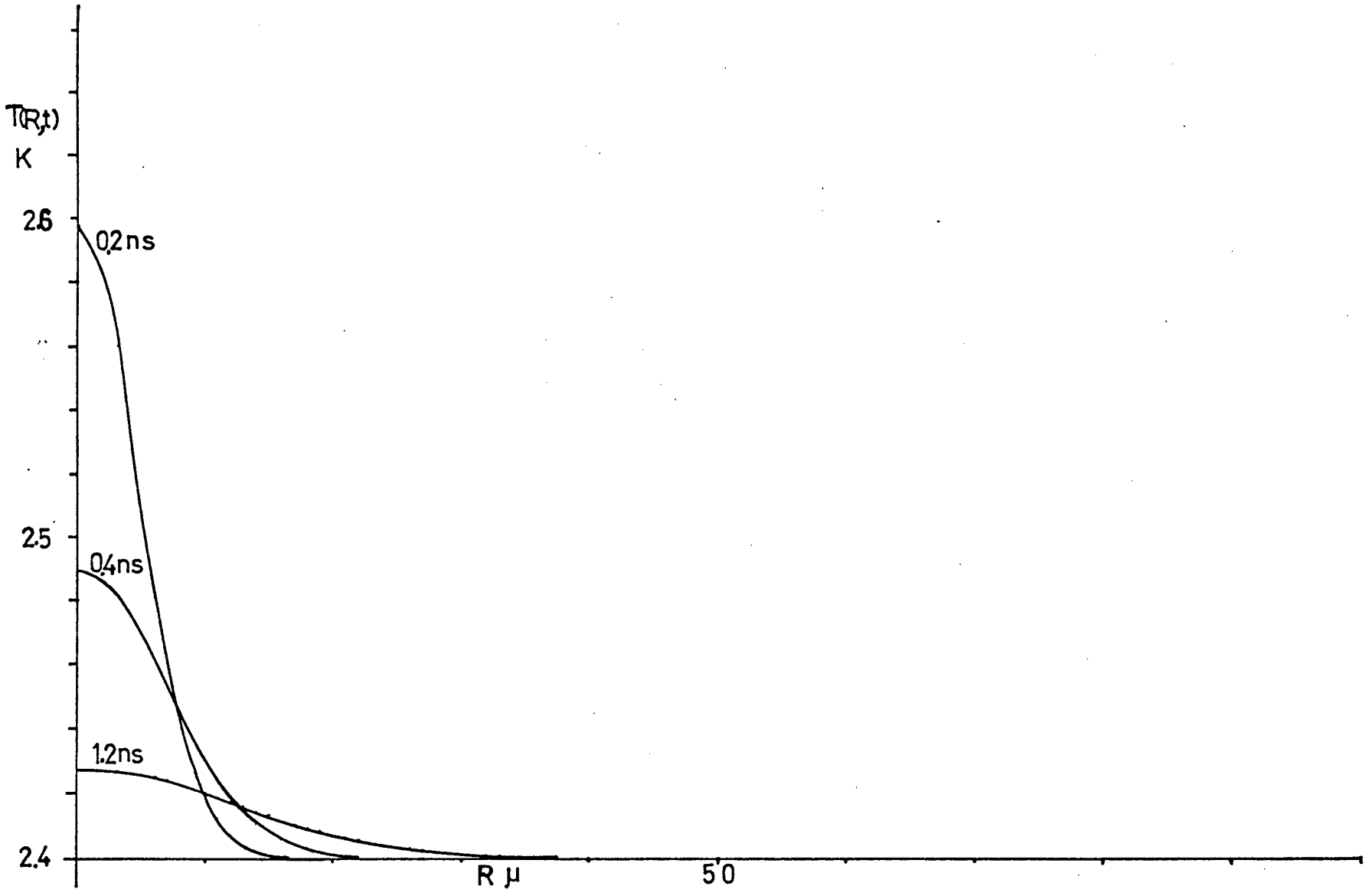

FIG. 3.8 TEMPERATURE PROFILES AS A FUNCTION OF TIME FOR Pb S.T.J. ON A PHONON-BARRIER.

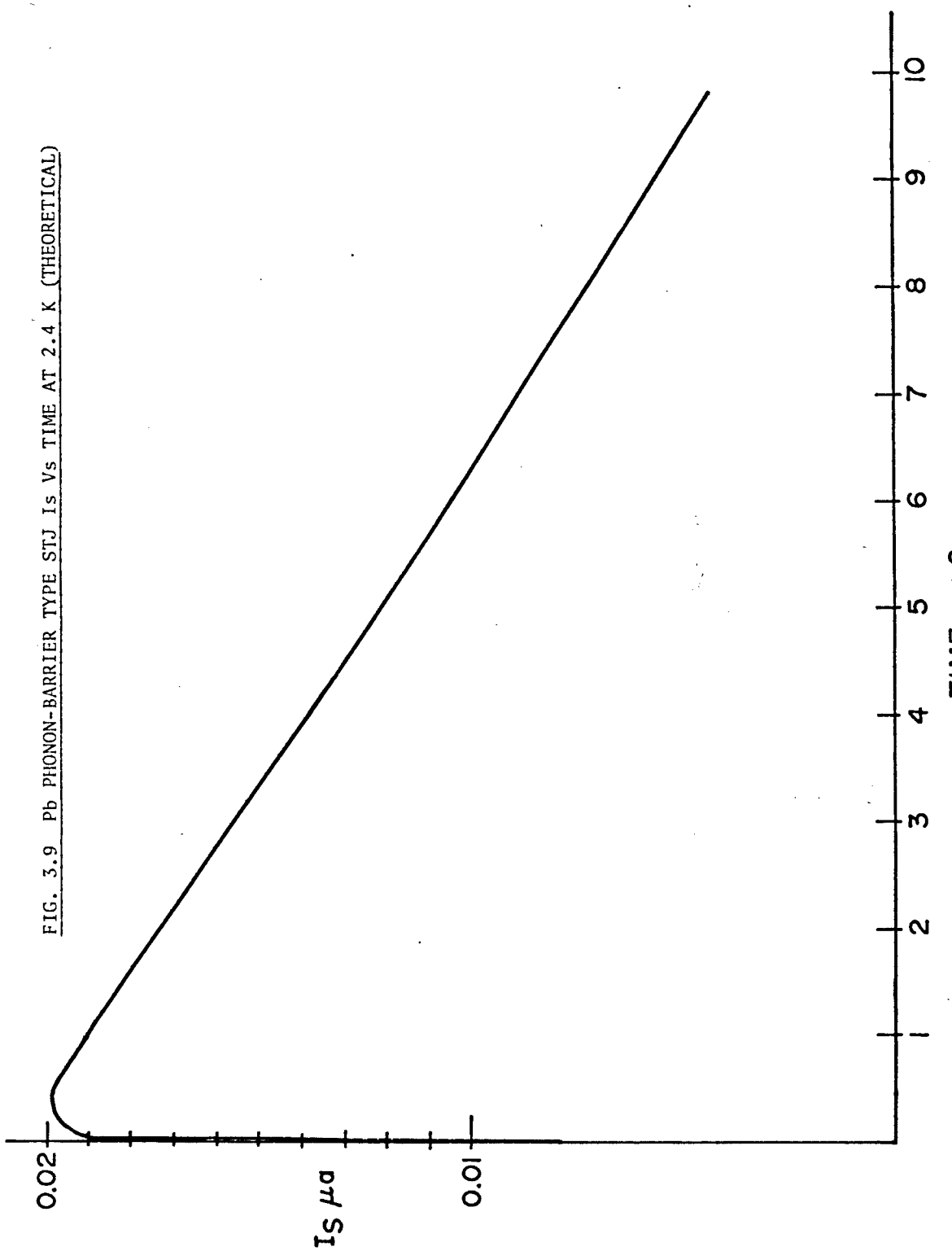

FIG. 3.9 Pb PHONON-BARRIER TYPE STJ Is Vs TIME AT 2.4 K (THEORETICAL)

Fig.(3.6) and I_S as a function of time in Fig.(3.7). Using the same methods and the thermal properties of Pb, and a set of Pb reference junction characteristics the temperature profiles vs. time, and I_S vs. time were calculated and plotted in Fig.(3.8), Fig.(3.9) respectively. A higher bath temperature of 2.4 K was used for the Pb case to get a larger $\frac{\partial I}{\partial T}$ value for the junction, but the resultant increase of Cp and K resulted in the I_S being much smaller than for the Sn case. Note that though we have ignored the finite area of the junction in the calculations, the approximations should provide a description valid for particle impacts near the centre of the junction.

Spherically-symmetric approximation

For a glass-substrated SPD if the α-particle energy were considered to be deposited at a point uniformly distributed in a hemispherical volume with its planar surface coincident with the tunnel junction, then by the insulating surface boundary condition we have spherical symmetry in the heat-diffusion problem. This model applies if the length of the particle-track can be ignored compared with the size of the heat affected zone as is the case for large times (or short track, due to a low energy or heavy particle). This approximation was used to give a preliminary indication of the response of the glass-substrated SPD to an α-particle impact at large times. The computer program used was different from that of the radially symmetric case only in the Laplacian, and the formula for the 'cell' volume which were spherical shells instead of cylindrical shells. The finite-difference expression for the new transformed temperature was:

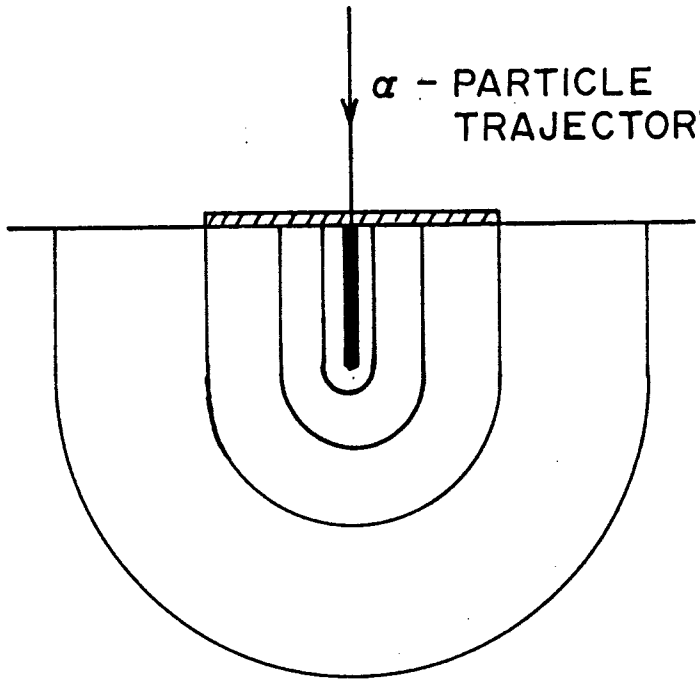

CROSS-SECTION OF A NORMAL-INCIDENCE α-PARTICLE IMPACT ON A GLASS-SUBSTRATE SPD

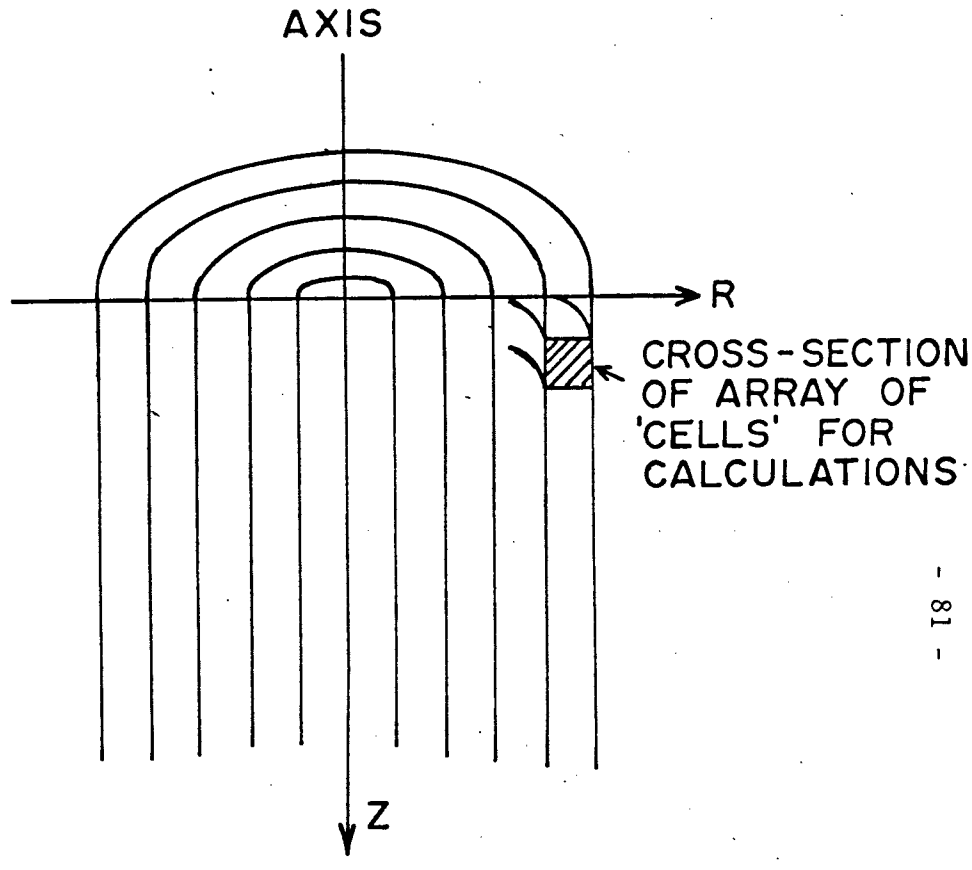

GEOMETRY OF 'CELL' ARRAY USED FOR CALCULATIONS.

FIG. 3.10

$$\theta m,n+1 = \frac{T}{M\varepsilon^2} \cdot \frac{K}{Cp\rho} \left[(m-1)\ \theta m-1,\ n+ \left(\frac{m\varepsilon^2 Cp}{\tau\ K} - 2m\right)\ \theta m,n \right.$$

$$\left. + (m+1) \cdot \theta m+1,n\right] \qquad (3.16)$$

Because of the similarity no further discussions are necessary.

Calculations of glass-substrated SPD response to α-particle impact assuming finite-length, normal-incidence α-particle track, with a finite sized junction.

Fig.(3.10) shows the cross section of the normal incidence α-particle impact, with a finite particle track in the glass substrate. The heat diffusion problem still had a rotational symmetry, but now a 2-dimensional array of cells (each ring-shaped) was needed for the finite difference numerical solution. This meant a different Laplacian compared to the 1-dimensional radially symmetric problem. With the new Laplacian the transformed temperatures for the next time step were given by:

$$\theta\ell,m,n+1 = \frac{K\tau}{Cp} \left[(\theta\ell,m+1,n - 2\theta\ell,m,n + \theta\ell,m-1,n)/\varepsilon_z^2 + ((1+\tfrac{1}{2}\ell) \cdot \right.$$

$$\left. \theta\ell+1,m,n - 2\theta\ell,m,n + (1-\tfrac{1}{2}\ell) \cdot \theta\ell-1,m,n)/\varepsilon^2)\right] + \theta\ell,m,n \qquad (3.17)$$

Where $\theta\ell,m,n$ is the transformed temperature of the cell at $r = \ell G$, $z = m\varepsilon_z$ and $t = n\tau$ and ε, ε_z are the radial dimension and the z axis dimension of the cells and the value of $\frac{K}{Cp\rho}$ is that at transformed temperature of $\theta\ell$,

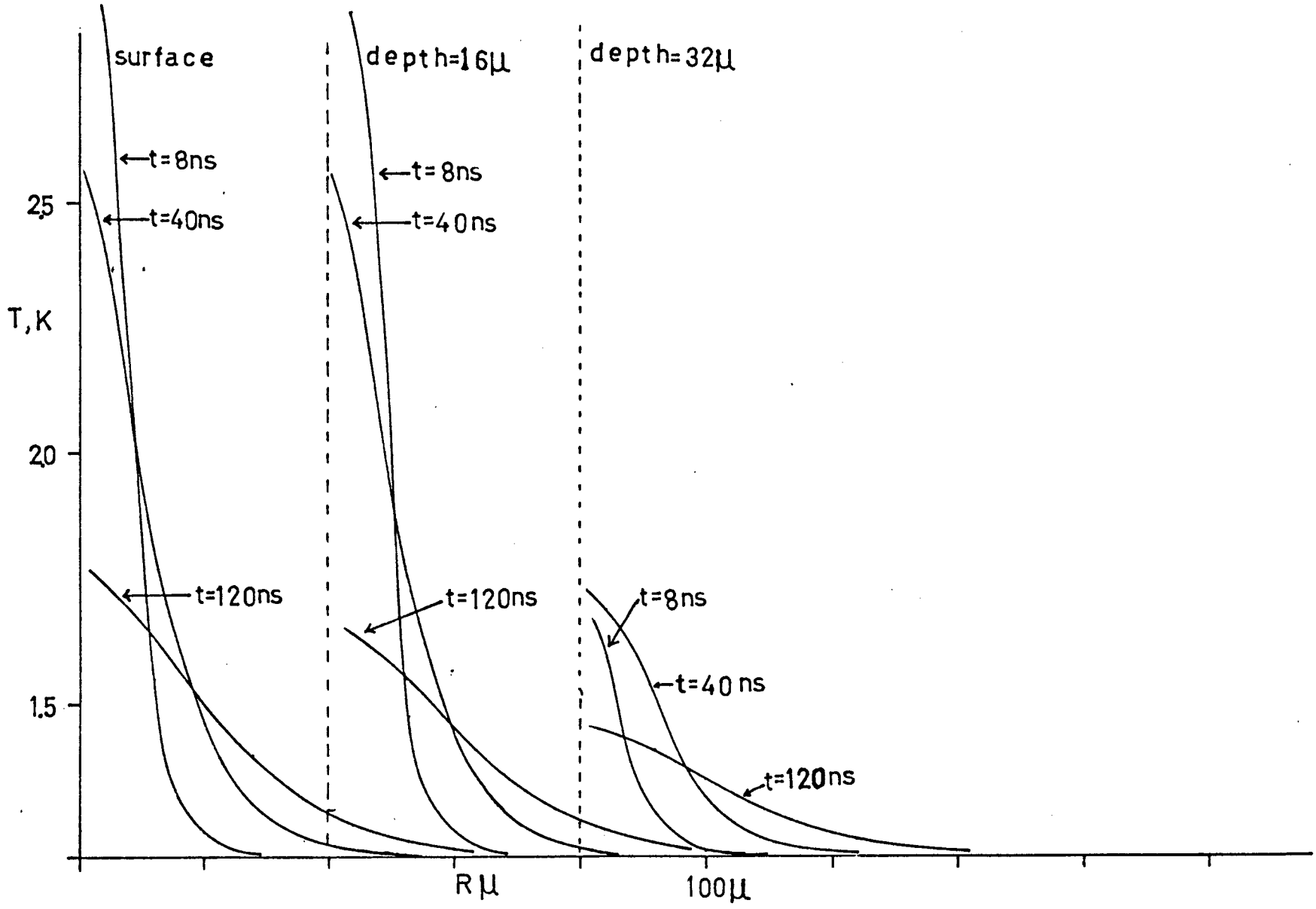

FIG. 3.11 TEMPERATURE PROFILES AT DIFFERENT DEPTHS IN THE GLASS SUBSTRATE AS A FUNCTION OF TIME.

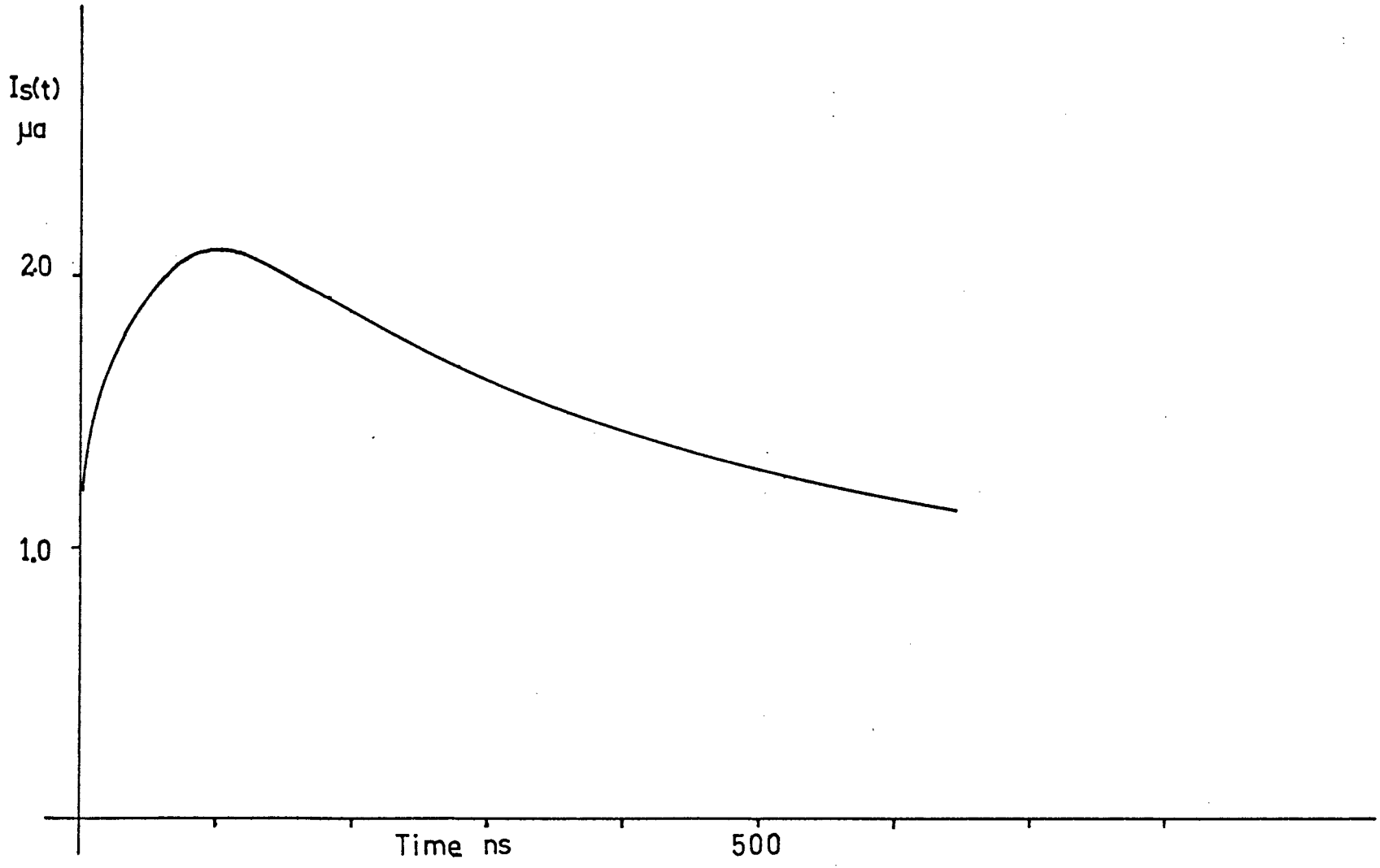

FIG. 3.12 JUNCTION SIGNAL-CURRENT AS A FUNCTION OF TIME FOR AN INFINITE AREA JUNCTION.

m,n. The cell shape and location is shown in Fig.(3.10). The initial condition is given by calculating the depth of penetration of the α-particle (PENZ) at normal incidence and considering the energy of the α-particle uniformly deposited in the axial cells from the surface to the depth of penetration, i.e. to z = PENZ. As before the boundary cells were kept at bath-temperature. The size of the array of cells used was 20 x 20 or 400 cells, thus the cell dimensions had to be larger than that in the 1-dimensional cases (8μ vs. 0.8μ) to prevent the boundary from affecting the heat diffusion significantly. In addition, since the array size had become 4 times larger, and the calculating more complicated, the increase in cell size allowed the use of a larger time step τ, reducing the number of steps to reach a specified physical time. The possible loss of significant detail in the information about junction response-current as a function of time through the use of a larger cell size was checked by comparison with the 1-dimensional radially symmetric approximation. No loss of significant detail in the junction current response was evident. However, as expected the temperature profiles for earlier times showed a lower peak temperature for the present case, resulting from the initial quantity of heat being distributed in a larger volume initially. The temperature-profiles as a function of time for different depths and the junction response current as a function of time for an infinite junction are plotted and shown in Fig.(3.11) and Fig.(3.12) respectively.

Finite junction size effects

The STJ's used in this experiment were square ($0.2 \times 0.2 mm^2$), and finite

IMPACT-POINT COORDINATE MAP FIG. 3.13

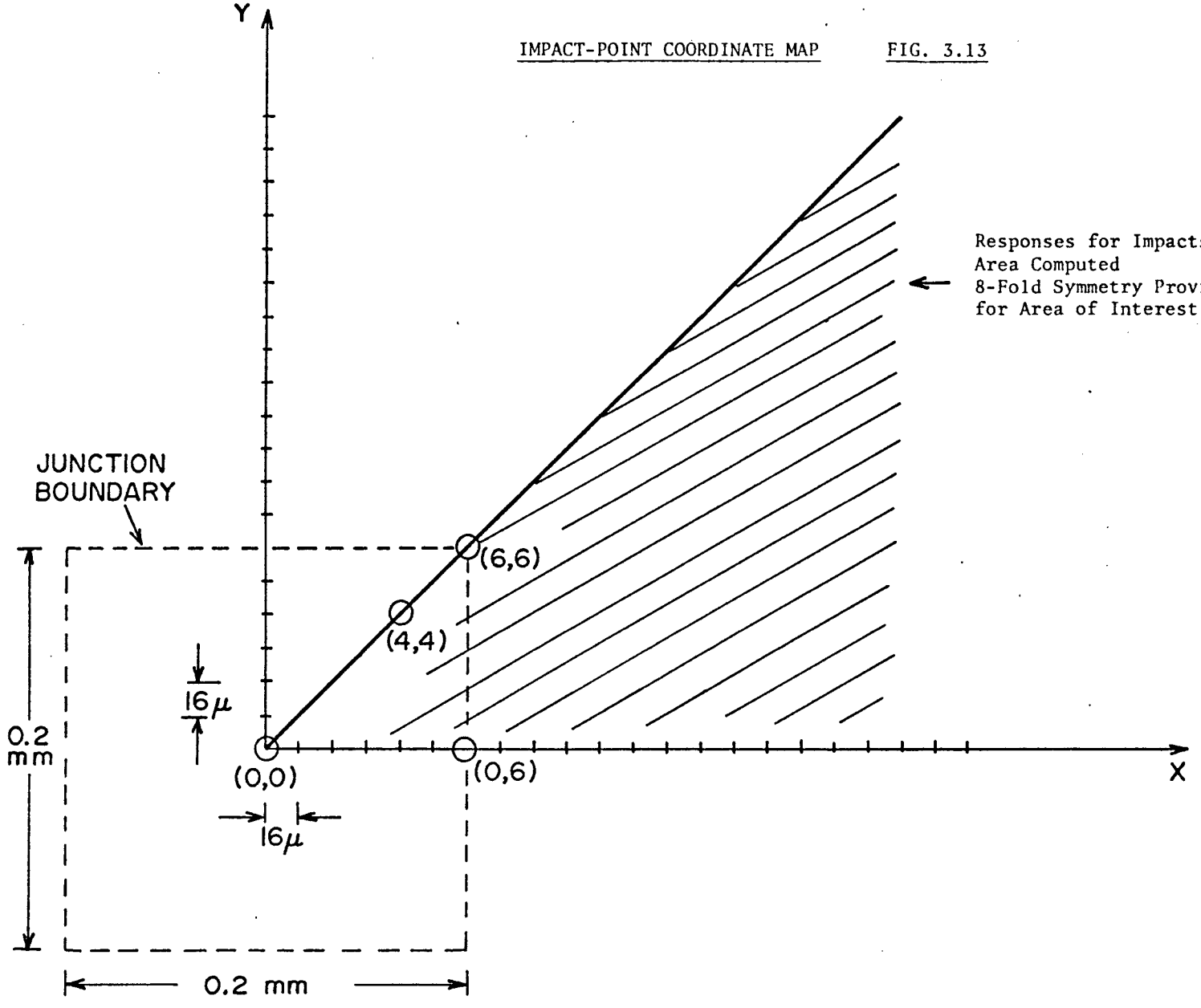

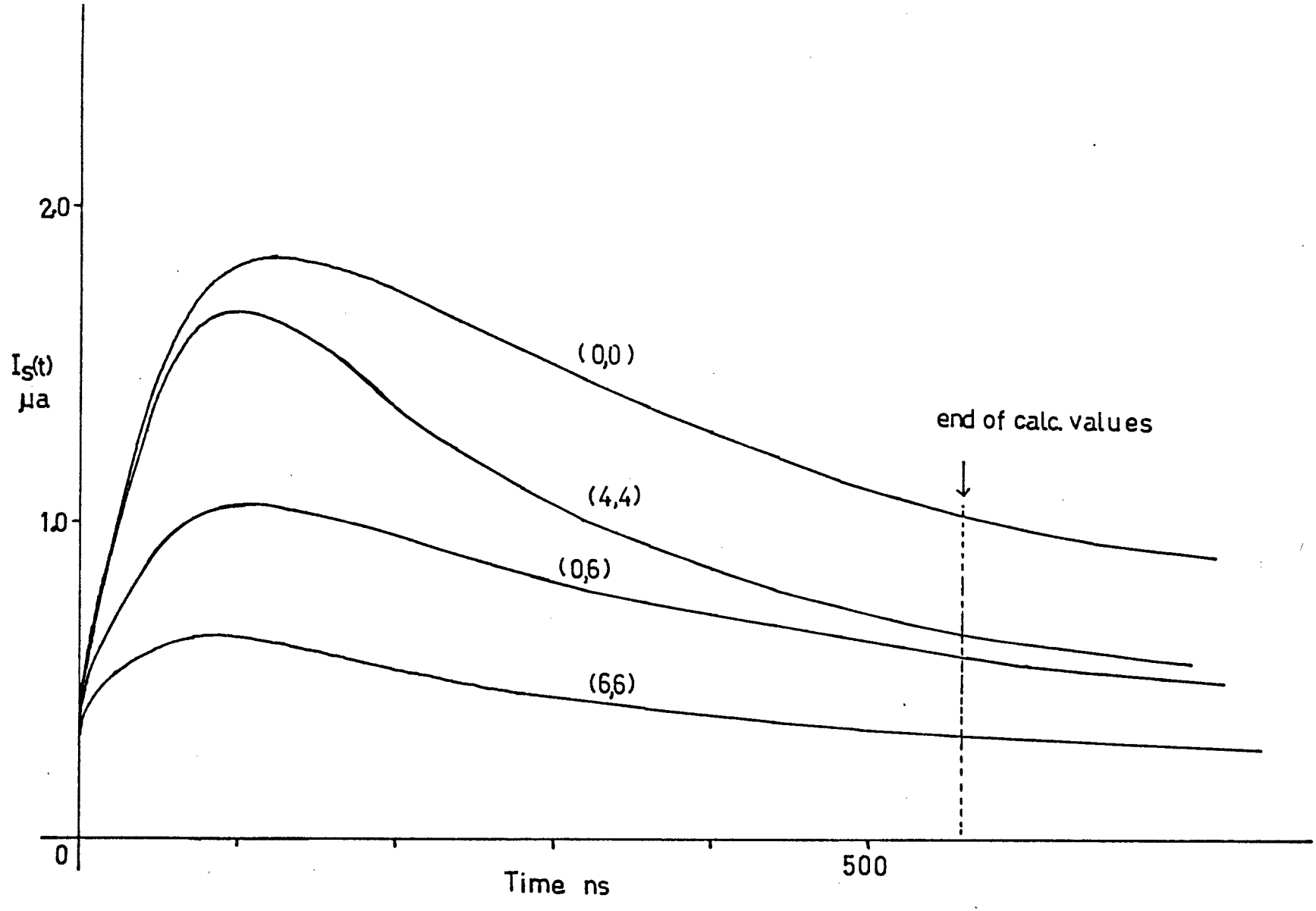

FIG. 3.14 CALCULATED SIGNAL-CURRENTS AS A FUNCTION OF TIME FOR DIFFERENT α-PARTICLE IMPACT POINTS.

and particle impact with the substrate could occur anywhere inside or outside the junction. The junction current-response to the α-particle impact is the excess-current density due to the increased temperature integrated over the junction area. Fig.(3.13) shows a coordinate system for locating the impact point. Because of the 8-fold symmetry only impacts in the shaded triangular area shown in the figure need to be considered, the effect of impacts in the other locations being obtained by symmetry. The surface temperatures centered about the impact point at a given time were calculated. Thus on specifying the impact-point location relative to the junction coordinates the temperature at all points of the junction were known. (Cf. Fig.(3.11)). Integrating over the finite area of the junction we got the finite junction current-response, for α-particle impact at a specified point relative to the junction. Fig.(3.14) shows the junction-current response to normal-incidence 5.13 MeV α-particle impact at four different locations. As expected the impact at junction centre (0,0) resulted in the maximum amplitude and duration of the response. Impact just inside the corner of the junction at (4,4) produces almost the same amplitude of response as the impact at (0,0) but decayed more rapidly. This is expected since at first the temperature rise was confined to a small area and was fully covered by the junction for either impact positions. The difference was more pronounced as the heat diffused over a larger volume, as the impact at (0,0) allowed the junction to cover the area of increased temperature better. Impacts outside the junction can also cause junction-current response because of heat diffusion, but of smaller amplitudes because of the smaller temperature increases at the junction. The accumulated signal-charge was also calculated for each time and impact

CALCULATED PROBABILITY DENSITY OF I_{SIG} (PEAK) FIG. 3.15

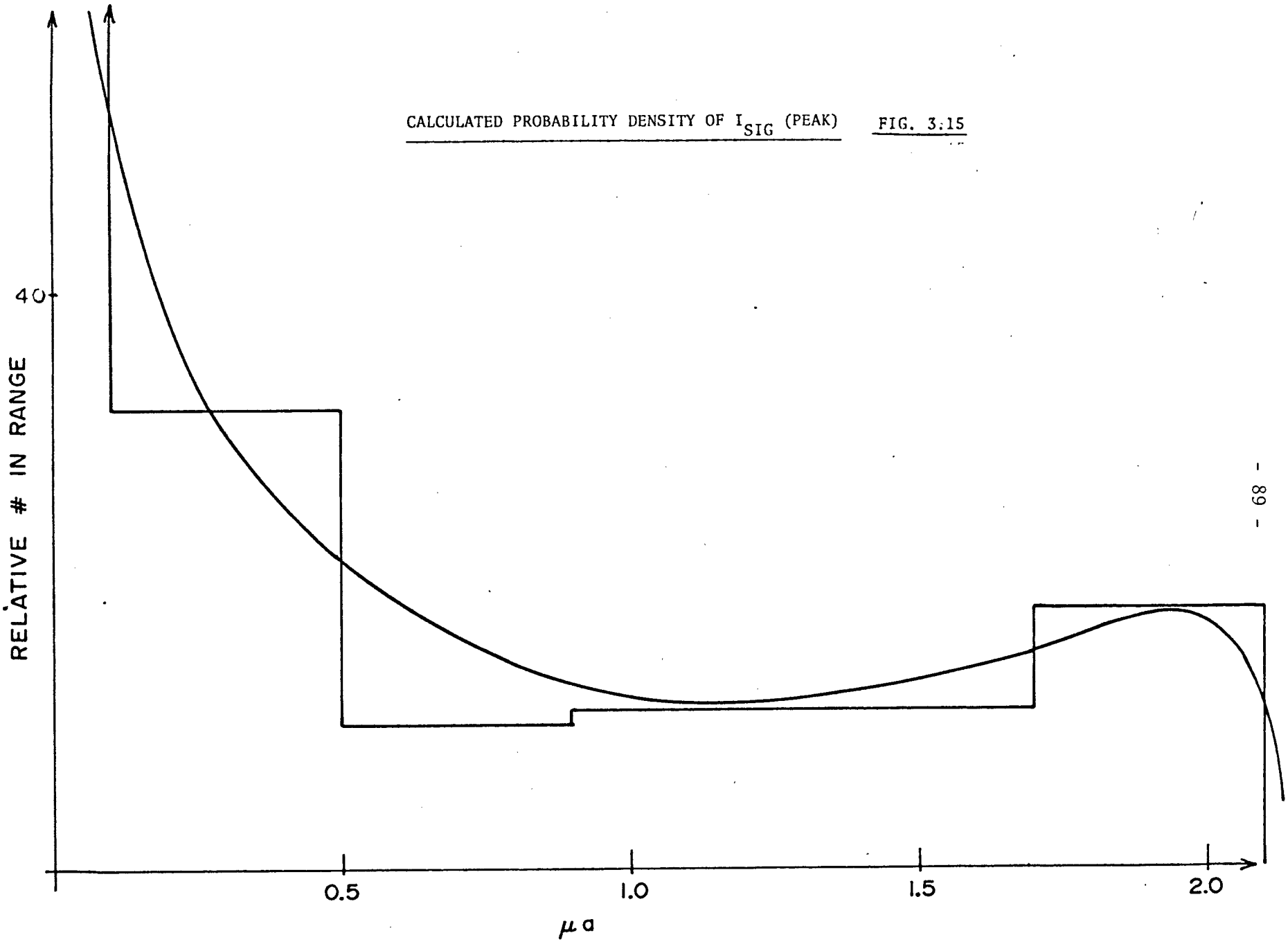

CALCULATED PROBABILITY DENSITY OF Q_{TOTAL} AT 0.56μs

FROM 1 α-PARTICLE IMPACT AT EACH GRID-POINT SHOWN IN "IMPACT POINT COORDINATE MAP"

FIG. 3.16

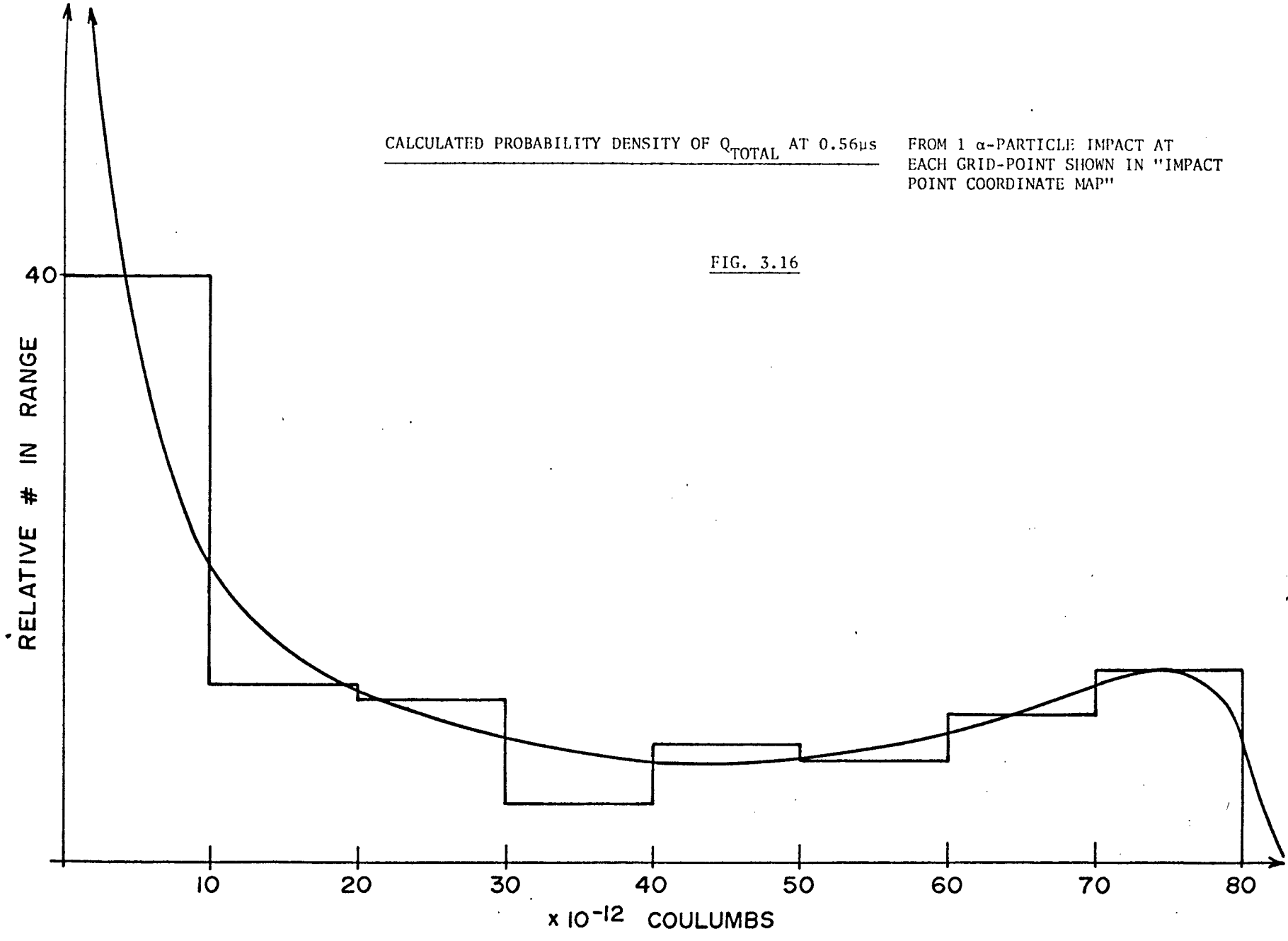

point. The computations were terminated at a pulse evolution time of 0.56 μs as the amount of computer-time required was considerable. (3000 sec. Cpu time) and further computations would not have given results to justify the cost.

From the computed values of $I_S(t)$ for each impact location, I_S peak, the signal-current amplitude was picked out. From the geometry of the impact-coordinate grid (Fig.(3.13) and the set of I_S peak values, assuming equal probability of impact at each coordinate point a current-amplitude distribution histogram was calculated and plotted in Fig.(3.15). Similarly from the accumulated signal-charge values (accumulated to 0.56 μs) at each impact point an accumulated signal charge amplitude distribution histogram was calculated by summing overall impact coordinates and plotted in Fig.(3.16). Both histograms show a sharp rise towards the low amplitude end because of the larger area (hence probability) in which impact would cause a lower amplitude response. A fairly sharp high energy cutoff is expected because impacts in the junction central area gives the maximum amplitude response. The angle-effect" discussed later would cause some increase in response amplitude for inclined impacts over the normal-incidence impacts, thus smearing out of the high energy cutoff. These predicted amplitude distributions are characteristic of the "thermometer-model" of the glass-substrated SPD, in which the STJ is regarded as a thermometer measuring the temperature increase of the substrate due to an α-particle impact. Whereas a semiconductor junction-detector equivalent model of the SPD with quasiparticles regarded as direct analogs of holes and electrons can only give a 'line' spectrum from the monoenergetic α-particle source. As will be shown in Chapter 6, the experimental "Kicksorter" records agree

FIG. 3.17 EFFECT OF ANGLE OF IMPACT AND JUNCTION SIZE ON Is.

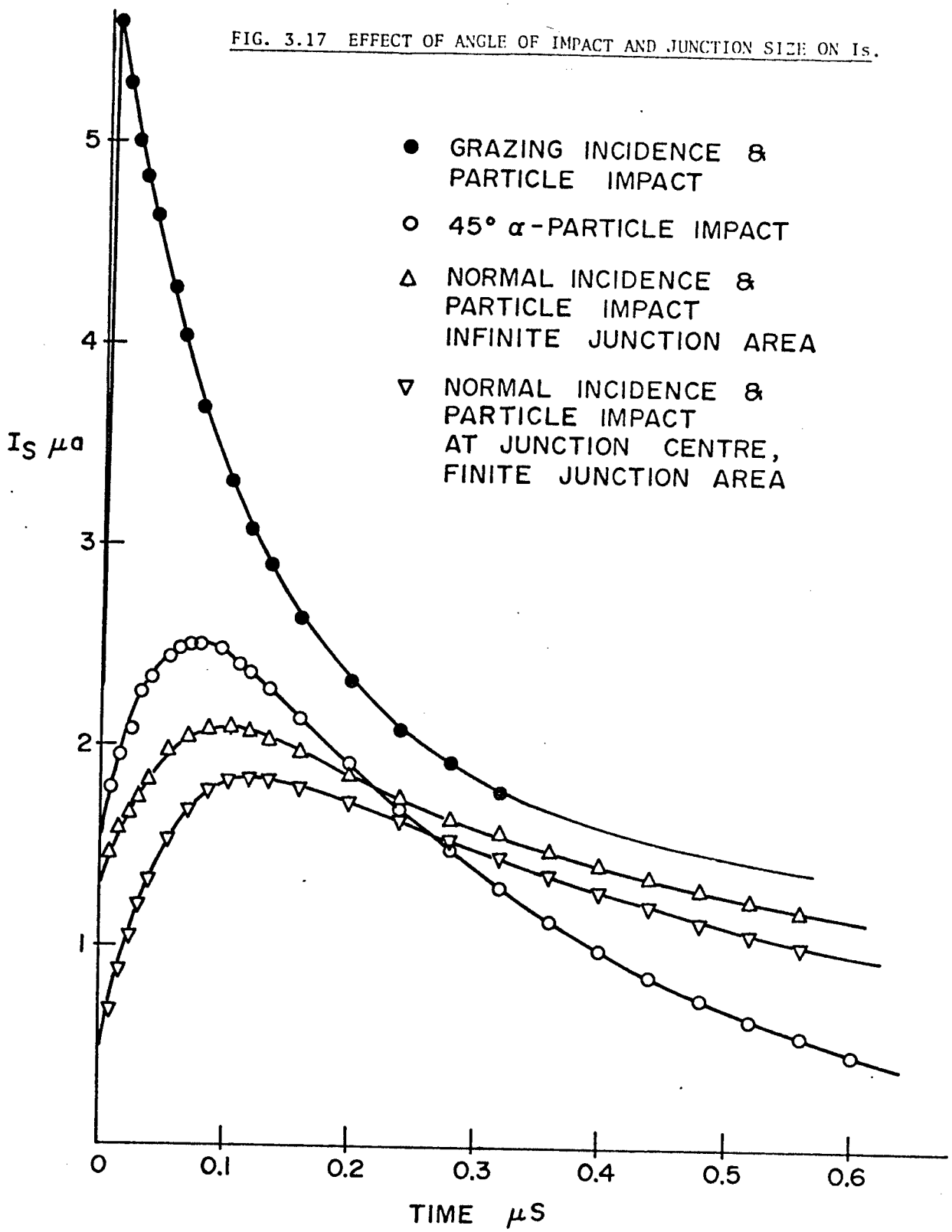

with the thermometer model.

Magnitude of the "Angle-Effect"

An α-particle with non-normal impacting angle causes a larger signal-current amplitude than an impact at normal incidence because a larger area of the surface is at a higher temperature for the inclined impact. The limiting case is the grazing impact, i.e. the α-particle penetrates the surface at a very shallow angle. By the method of images we see that the heat-diffusion problem is very similar to the normal-incidence finite length α-particle track problem described above, except that here we regard the temperatures of a plane section through the track as the surface temperatures. The equivalent heat dissipated per unit track length is doubled because of the 'image' track resulting from the insulating surface boundary condition. With these modifications to the computer program the signal-current due to a grazing impact was calculated for an 'infinite' sized junction and plotted in Fig.(3.17). Note the rapid rise and fall of the signal-current compared to that of normal-incidence, finite α-particle track length results, and the much higher current amplitudes.

For the experimental geometry used the maximum angle of incidence was smaller than 45°. Thus the calculated signal-current response to an α-particle impact at this angle represents the limit of current amplitude excursion due to angle effect for the present experimental geometry.

For impact at an angle rotational symmetry was lost, the only symmetry left was the reflection about the plane of incidence, for the

heat-diffusion problem. Thus a 3-dimensional rectangular array of 'cells' had to be used for the numerical calculations, resulting in a large number of cells even for a very coarse and limited array, consequently a large number of calculations per time step. The computer program for this case is practically the same as the others,
except for the expression for calculating the transformed temperature of a cell for the next time step, resulting from the different Laplacian for the 3-dimensional rectangular coordinates, and the three space-coordinate indices for labelling the transformed-temperature of each cell, instead of the one or two for previous programs. The calculated signal current vs. time is also plotted in Fig. (3.17). The signal-current peak-amplitude for 45° impact angle on an 'infinite' area STJ chosen to have the reference-junction current density characteristics was 2.5 μa, as compared to 2.09 μa for a normal-incidence α-particle impact. Thus for the present experimental geometry the 'angle-effect' can account for nearly 20% spread in signal-current amplitude. Comparing accumulated signal-charges Qs, the value for 45° impact was 0.864 pc. as compared to 0.913 pc. for the normal incidence case. The smaller Qs for 45° α-particle impact resulted from a computational deficiency; the array-size used was too small, thus with the boundaries at a constant temperature the excessive heat loss due to the closeness of the boundaries to the point of impact was not negligible at larger times. In general the Qs values are larger for impacts at a greater angle, (eg. at t = 0.32 μs Qs = 0.947 pc. for the grazing incidence case) but varies to a smaller extent because though the signal-current amplitudes were larger for greater angles of impact, the $I_S(t)$ rise and fall time-constants were correspondingly smaller.

In Fig.(3.17) the current-response for an α-particle impact at normal incidence, at the centre of a finite-junction (of the nominal experimental STJ size) was also plotted for comparison with the corresponding current-response for an infinite-area junction. The current amplitudes were 1.84 μa and 2.09 μa respectively, indicating that the infinite-area junction model was a fair approximation for impacts at the junction centre of a finite-sized junction.

Conclusion

The numerical results of this Chapter enabled the comparisons of theory and experiment and thus the verification of the theoretical models used as the basis of the calculations.

CHAPTER FOUR

SUPERCONDUCTIVE-TUNNELLING JUNCTION FABRICATION

INTRODUCTION:

My predecessor in this study, G.H. Wood, encountered great difficulties in the fabrication of good superconductive-tunnelling junctions (S.T.J.s). He fabricated six S.T.J.s per evaporation run and because of poor reproducibility, all six were tested in liquid helium to check the current-voltage characteristics, and then a good junction selected, separated from the other junctions and mounted on a special sample holder for the measurement of α-particle induced current pulses at 1.2 K. In practice the good junction if any was nearly always degraded when the subsequent low temperature run was made due to low tolerance of the S.T.J. to thermal cycling. With great patience G.H. Wood got one junction that was good enough to register pulses caused by α-particles, thus proving qualitatively the feasibility of the S.T.J. particle detector. Only Sn-SnO_2-Sn junctions were successfully made due to process difficulties. The fabrication process used by WOOD was described in APPENDIX 'A' of his thesis, and the difficulties encountered in APPENDIX 'B' and 'C'. (ref. 4.9)

For the present thesis a great deal of work was done to derive a process for fabricating Sn and Pb S.T.J.s reproducibly. In the present process 36 S.T.J.s were fabricated each run (Fig. 4.1) in the form of 6 junction groups on a microscope glass slide, each group consisting of 6 S.T.J.s sharing one common electrode, [the bottom layer of the metal films forming the junctions (see Fig. 4.2 and Fig. 4.6)]. The 6 groups made per fabrication run were

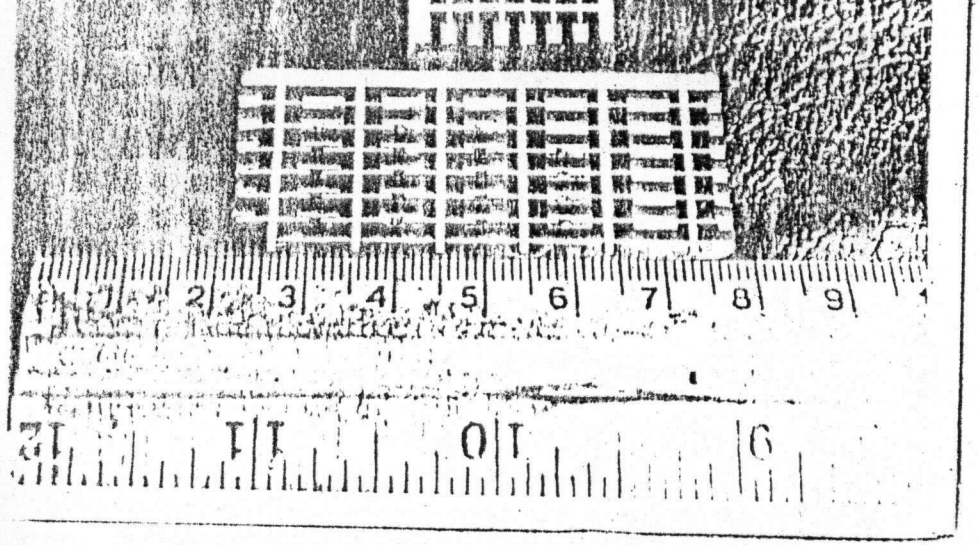

FIG. 4.1 SUPERCONDUCTIVE TUNNELLING JUNCTION SAMPLES

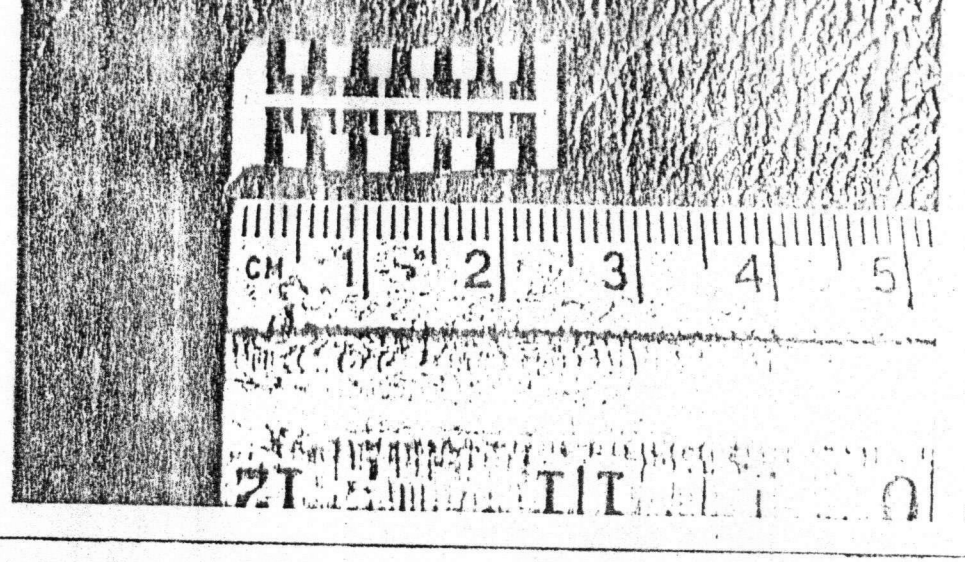

FIG. 4.2 SUPERCONDUCTIVE TUNNELLING JUNCTION SAMPLE DETAILS

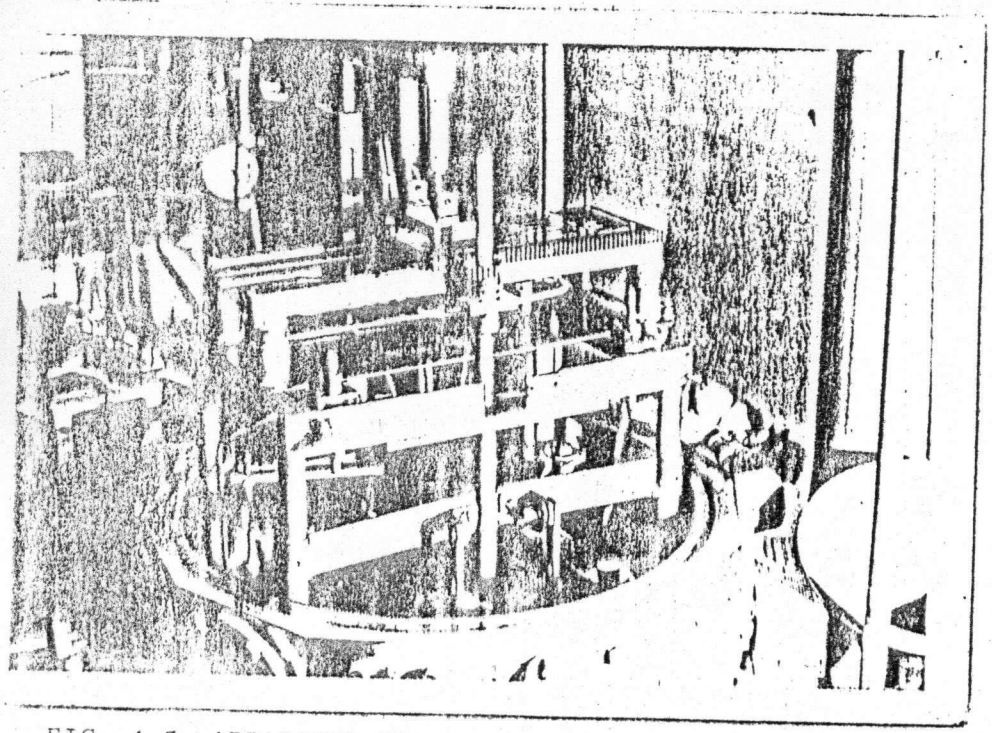

FIG. 4.3 APPARATUS FOR SAMPLE FABRICATION INSIDE VACUUM CHAMBER

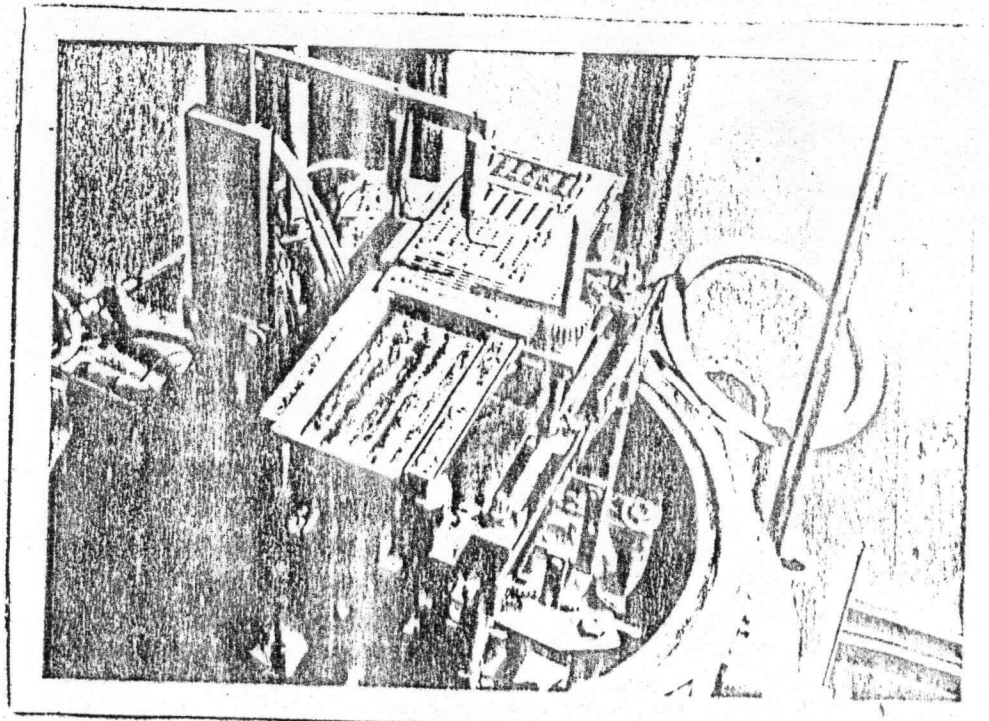

FIG. 4.4 EVAPORATION MASKS AND MASK-CHANGER DETAILS

visually inspected and the best group selected for subsequent tunnelling experiments. The test sample holder included a switching arrangement which (Fig. 5.1, 2, 3, 4 Chapter 5) permitted the selection of any S.T.J. of the group for current-voltage characteristic measurements as well as α-particle induced current pulse measurement while the group is inside the cryostat. This feature greatly improved the probability of having a good junction for measurements, which was particularly significant in the earlier stages of development of the fabrication process, when the percentage yield of good junctions was low. In Chapter 5 details will be given on how the room temperature and liquid nitrogen temperature junction resistance measurements were used to determine the quality of the S.T.J.s. If the junctions were 'bad' (leaking) the liquid helium stages of measurements were omitted, saving time and expense.

S.T.J. SAMPLE FABRICATION

The process steps of junction fabrication are standard: thin film depositions by evaporations from metal and insulator sources, and plasma cleaning and anodization (ref. 4.1, 2, 3, 4). However details of the complete process of junction fabrication are not available from any one publication. The author feels that the experience gained may be of some value to others contemplating junction-fabrication. The remainder of this chapter may be omitted if junction-fabrication is of no interest to the reader.

Substrate Cleaning This step was very critical to the successful fabrication of good S.T.J.s. The substrate, a CORNING 2947 "PROCESS CLEAN" 2.5 cm x 7.5 cm microscope glass slide was scrubbed thoroughly using a

bristle brush with a dishwasher detergent and rinsed and scrubbed under running tap water. After this preliminary scrub all the following steps were done in the dust free airflow of a clean-air hood. The substrate was cleaned ultrasonically in deionized water, then blown dry by clean bottled nitrogen and placed in the substrate holder. The substrate holder was then transferred to the vacuum-evaporator chamber (Fig. 4.3, 4.4, 4.5) in the clean-air flow, with the substrate surface facing down (to avoid dust particles if any settling on the surface). The vacuum-chamber was then closed, and pumped down with the roughing pump. A controlled leak of oxygen was then introduced to give 50 millitorr pressure, and a glow-discharge initiated, an oxygen plasma with discharge current of 50 ma, with the glow-discharge shutter closed. The glow-discharge shutter was opened five minutes later after any coating on the 'halo' electrode due to previous evaporations had been eliminated, this prevented any contaminating fragments from reaching the substrate surface. The substrate was placed on each of the four evaporation masks successively, for five minutes, in the oxygen plasma. The plasma treatment was intended to remove organic contaminants if any from the substrate and the vacuum-chamber. Then an argon glow-discharge, [pressure = 50 millitorr, discharge current = 50 ma, substrate holder (and mask carrier) biased-50 V (relative to vacuum chamber ground)] was used to ion-clean (ionic bombardment sputter clean) the substrate surface through each of the four masks used, five minutes at each location. That the plasma cleaning was effective, could be seen by subsequent examination of the water vapour condensation pattern on the substrate, the ion-cleaned area showed up as areas without condensation; this was due to the lack of condensation nuclei in the ion-cleaned areas.

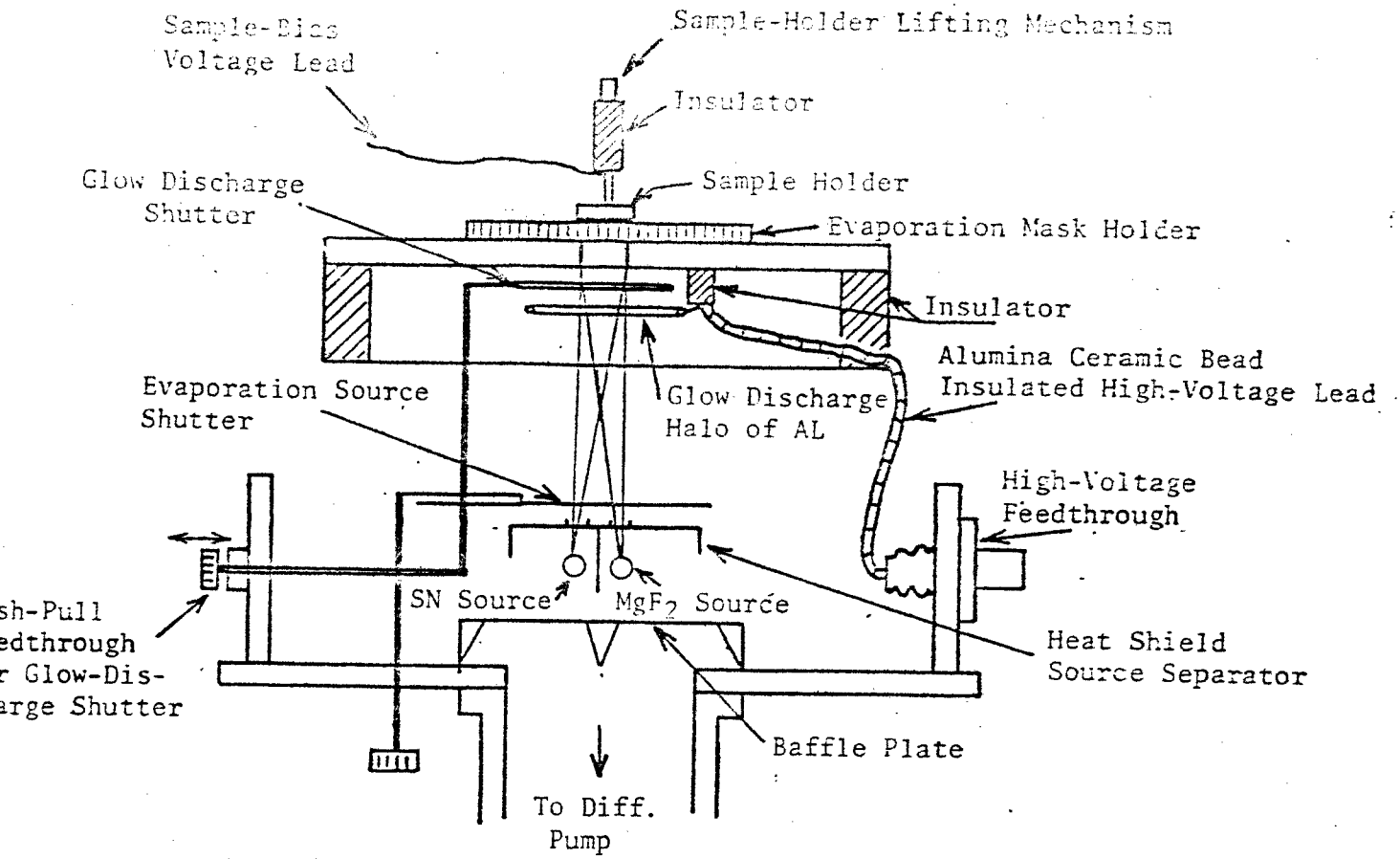

FIG. 4.5 DIAGRAM OF APPARATUS FOR SAMPLE FABRICATION INSIDE VACUUM CHAMBER.

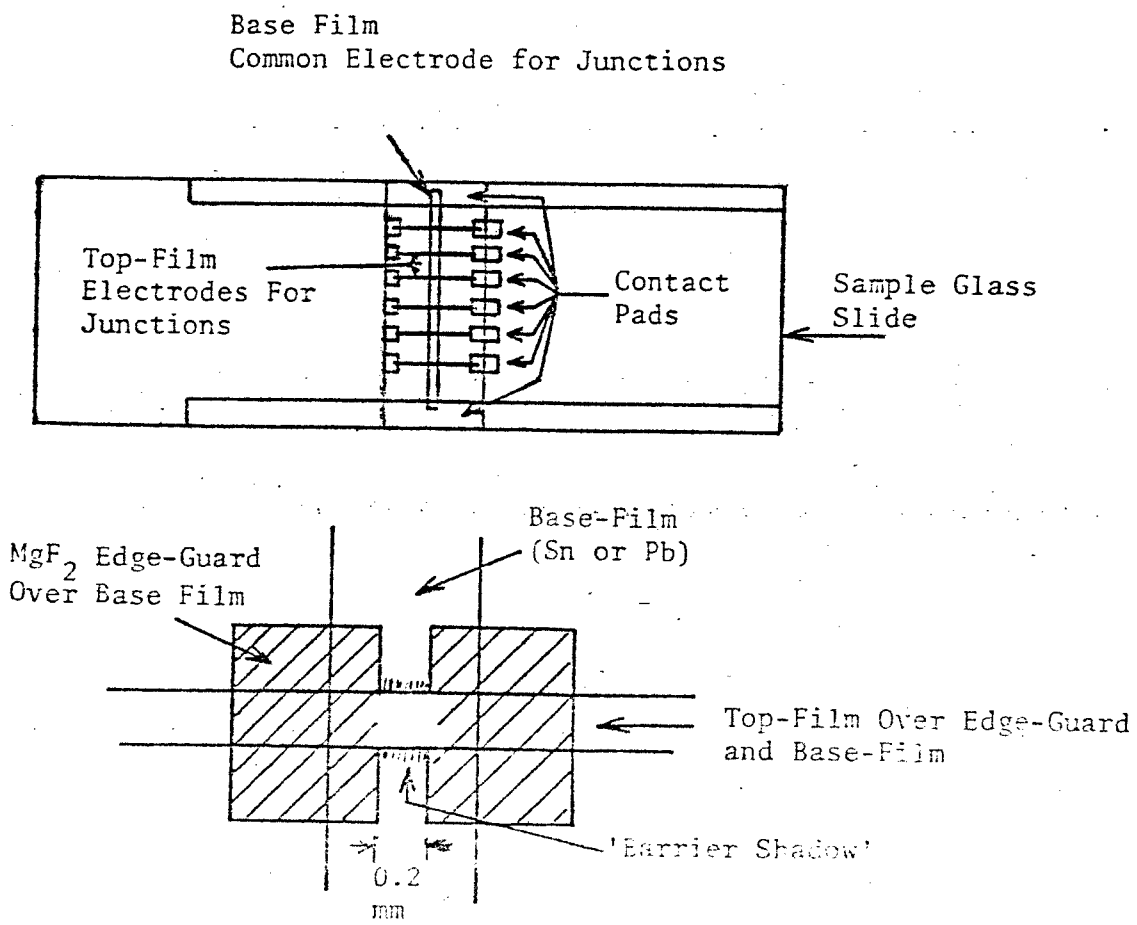

FIG. 4.6 SUPERCONDUCTIVE TUNNELLING JUNCTION STRUCTURAL DETAILS

Evaporation mask fabrication and positioning The four evaporation masks used were drawn with india ink, then photographed and reduced to size. Two actual sized negatives were aligned and taped on the edges to form a sleeve, which was slipped over a photo-resist coated 1-mil berylium bronze sheet. The photo-resist was exposed and developed, and the berylium bronze sheet etched in ammonium persulphate solution as in conventional printed circuit board etching. The finished mask was mounted on the mask-carrier slide with round-head screws (Fig. 4.4). The substrate holder had locating conical holes in positions corresponding to the four round-head screws holding each mask in position, this resulted in 'sphere and cone' alignment. The substrate holder suspended by two hooks may be raised from and lowered onto the mask holder through a rotary mechanical feed-through from outside the vacuum chamber. The mask-carrier slid in a dove-tailed slide-way, (insulated from the slide way by teflon inserts in the slide way). The mask-carrier was positioned from outside the vacuum chamber via a rotary-mechanical feed-through, coupled to a rack and pinion gearing system. The rack was mounted on the mask carrier edge and driven by the pinion. In operation the substrate holder was raised, and the mask carrier positioned, then the substrate holder was lowered gently onto the mask carrier. Due to the self-alignment feature, the alignment accuracy was better than 50 microns. Better results could have been achieved with more care, but this accuracy was good enough for the set of masks used.

Deposition of junction films by evaporation Four masks were used for the evaporations (Fig. 4.4, 4.6). Mask #1 defined the contact-pad areas, where leads were attached to finished S.T.J.s. 2000 Å of metal film was deposited in this area. Mask #2 defined the "longitudinal-strips" or the

base films of the S.T.J.s. 2000 Å of metal was deposited in this area. Mask #3 defined the "edge-guard" areas where about 1000 Å of MgF_2 was deposited. This layer served to define one dimension of the junction region and also served to eliminate an area at the edge of the longitudinal strip where there is a high probability of leakage due to stress induced cracking of the oxide-barrier at the edges of the film. Mask #4 defined the 'cross-strips' or the top films of the S.T.J.s 2000 Å of metal was deposited in this area.

Refering to Fig. 4.5, two evaporation sources were used, one for the metal (Sn or Pb) and the other for the MgF_2. The best source for evaporating the metal was the Tantalum S-18 10 mil boat pin-hole source, which gave the best results when operated carefully. Outgassing was done at slowly increasing temperatures while monitoring the vacuum ion-gauge for excess pressure rise, and an evaporation rate of < 300 Å per minute was used, to prevent explosive boiling during evaporation from causing undesirable splatter on the deposited film. Source boat corrosion with Sn as evaporant was severe and necessitated frequent source changes. A plasma-sprayed oxide coated source was tried without success due to the excessive power required for this source and consequent excessive radiative heating of the substrate. For the MgF_2 source an inhouse fabricated molydenum source was found to be most suitable. The outgassing problems with a fresh charge of MgF_2 in the source was many times worse than for the metal source, and took a few hours to complete, but due to the large capacity of the source and the small amounts of evaporant used per fabrication-run, this was not much of a problem. The two sources were separated by a heat shield/vapour separator, to prevent vapour from one source heating the other. The heat shield also defined the aperture of the

evaporant vapours, cutting down the radiation heating of the substrate by the source during evaporation, and the deposition of material in areas other than the substrate mask in the vacuum chamber. An evaporation-shutter operated through a mechanical feed through was used to control the duration of the evaporation and to allow source outgassing before deposition. A quartz-crystal oscillator deposit thickness monitor was used to monitor the evaporation process, details were given in WOOD's thesis pages 185-187, and will not be repeated here.

Plasma cleaning and anodization The oxygen plasma anodization method first proposed by MILES and SMITH[ref. 4.1] was chosen to be the process used to form the oxide-barrier for the S.T.J.s because close control possible for this process, essential for reproducibility. With plasma anodization, cleaning, mask change under vacuum, and the two evaporant sources, it was possible to start with a clean substrate and end up with completed S.T.J.s without opening the vacuum-chamber to the atmosphere, thus eliminating the possibility of contamination during the fabrication process. The actual experimental apparatus for plasma-anodization and cleaning was designed after reading MILES and SMITH[ref. 4.1], TIBOL and HULL[ref. 4.2], SCHROEN[ref. 4.3] and DELL'OCA, PULFREY and YOUNG[ref. 4.4]. The plasma for oxidation and ion cleaning was generated by the D.C. discharge between a ring shaped aluminium 'halo' cathode surrounding conductors at ground potential. A high voltage ion-pump power supply with overcurrent cutout protection provided the high voltage for the D.C. discharge, (a variac at the A.C. input to the power supply controlled the D.C. output voltage). The substrate-holder and the mask-carrier were insulated from ground and could be biased at different voltages. For ion cleaning the bias was usually

-50 volts, whereas for anodization the potential was allowed to 'float', the measured voltage while 'floating' was about - 4 volts.

TYPICAL S.T.J. FABRICATION RUN

A typical S.T.J. fabrication run went as follows:- The glass-slide substrate was cleaned and placed in the vacuum chamber, then plasma cleaned as described in the "substrate cleaning' section above. The vacuum chamber was pumped down with the oil-diffusion pump to about 2×10^{-6} Torr, then the metal source was outgased until the vacuum chamber pressure fell to 3×10^{-6} Torr. 2000 $\mathring{A}$ of metal (Sn or Pb) was deposited through mask #1 for the contact-pads at approximately 300 $\mathring{A}$ per minute. The source was then turned off and the substrate allowed to cool for 10 minutes, this cooling period was found to be necessary to produce a smooth film for the next evaporation. 2000 $\mathring{A}$ of metal was deposited next with mask #2 for the longitudinal strip. Next, $\sim$ 1000 $\mathring{A}$ of MgF_2 was deposited through mask #3 to produce the "edge-guard", the vacuum pressure for this evaporation was a relatively high 10^{-5} Torr. The diffusion pump was then turned off and valved off, and Argon gas was introduced through a controlled leak (through a liquid nitrogen cold trap to remove moisture) to raise the vacuum chamber pressure to 50 millitorr while being pumped by the roughing pump. The glow-discharge was turned on with the substrate holder (and the mask carrier) biased at -50 volts, and maintained for five minutes. This step ion-cleaned the base film of the S.T.J.s to remove any condensed film (due to vapour leakage of MgF_2 evaporation) on the portion of the base - film where the oxide-barrier was to be formed. The Argon gas was valved off and substituted by oxygen gas at 500 millitorr pressure for Sn and 50 millitorr for Pb

respectively. The substrate was allowed to stay in the oxygen for 25 minutes, then with the substrate-holder floating electrically the glow-discharge (with discharge current of 50 ma) was maintained for 40 sec. and 15 sec. respectively for Sn and Pb. This step formed the oxide-barrier for the S.T.J.s. The gas was then valved off and the vacuum chamber pumped down to a pressure < 10^{-6} Torr and 2000 Å of metal deposited on the substrate through mask #4. This formed the 'cross-strip' or the top film of the S.T.J.s. This step completed the fabrication of the S.T.J.s

VISUAL INSPECTION

It was possible to predict the quality of the junctions based on microscopic examination of the S.T.J.s. In general if the base and top films were smooth and few splatters were visible, and the edge guard was present, and the oxide-barrier was present, the S.T.J.s were good. The presence of an oxide-barrier could be determined visually. Through the oxide was only about 10 Å thick and much too thin to see, the Sn or Pb vapour that strayed to either side of the cross-strip (top film) as defined by mask #4, tended to form a brownish stain, which did not occur if the barrier layer was absent (see Fig. 4.6). This effect was probably due to the amorphous or microcrystalline form of the Sn or Pb vapour condensed on the oxide barrier as compared to the epitaxial deposition of the vapours on the bare Sn or Pb films. (I have called this effect "barrier shadow" in my laboratory notes). Generally all 36 S.T.J.s on the entire substrate were similar in quality. Sometimes, in the presence of splatter (of Sn or Pb) some junctions could be visually determined to be better because of the absence of splatter in the junction area.

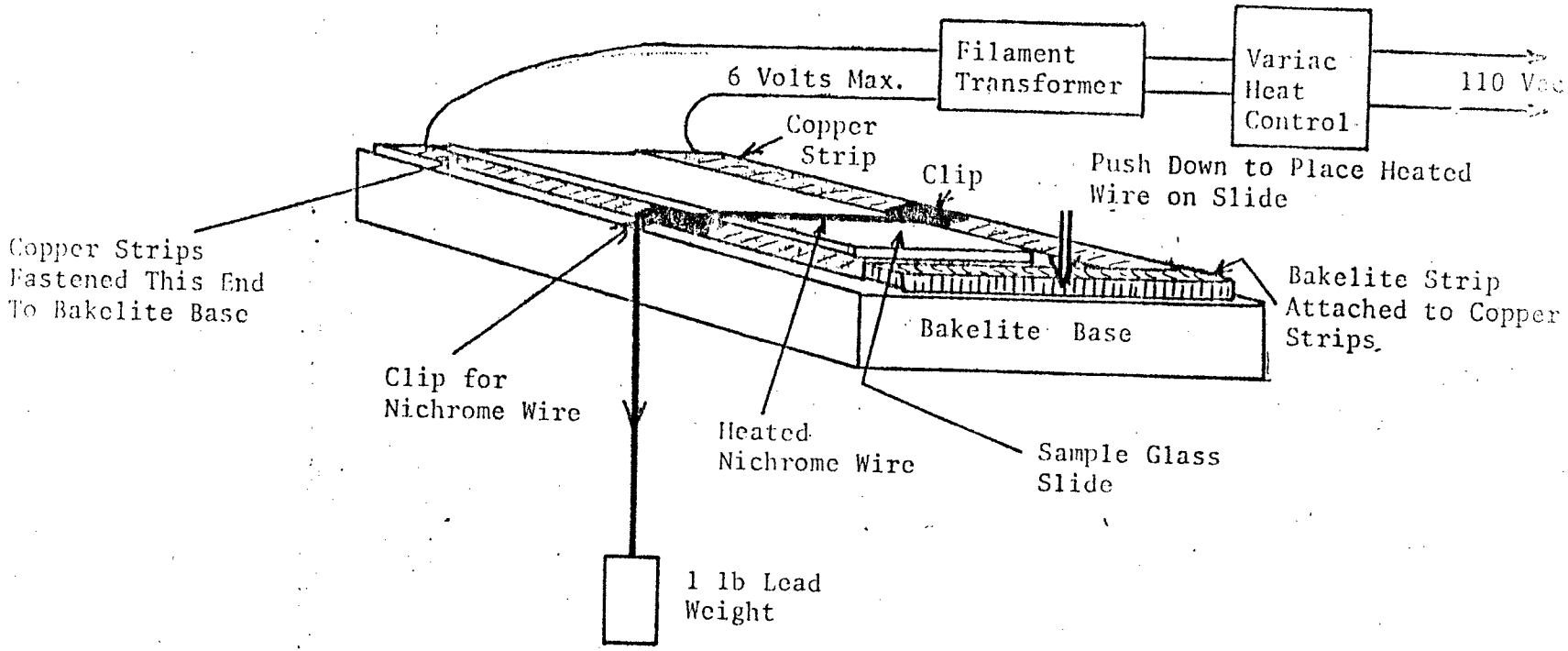

FIG. 4.7 HEATED WIRE SAMPLE SEPARATOR

Sample passivation Rosin was dissolved in ethyl alchohol and a drop of the solution was washed over each sample region on the slide leaving a $\sim$ 1000 Å residue layer of rosin. The rosin layer appeared to be effective in 'passivating' the samples, that is, to protect the sample from atmospheric originated corrosion. Without this 'passivation' Pb samples degrade rapidly in room ambient, as described by WOOD in his thesis pages 201 to 209, forming clusters of 'blisters' on the Pb film.

Group Separation The glass-slide with six groups was divided into six pieces, one group per piece, by breaking the glass substrate. First, the slide was scribed to isolate electrically the areas to be contacted by the 'hot-wire' used for breaking the glass. Then the groups were separated using an electrically heated nichrome 'hot-wire' contacting the region where the break was desired (Fig. 4.7). Even contact of the wire with the glass and correct tensioning was essential for success in this method of glass breaking. The tension in the wire was provided by a lead weight. This method of group separation prevented physical contact with the S.T.J.s, which could easily be damaged.

Lead attachment The selected group was provided with electrical leads by soldering 1 mil gold wires to the contact-pad regions with indium solder. The previously applied rosin-solution in alchohol was a good flux, so no problems were encountered from room temperature to 1.2 K with leads attached in this manner.

Sample stability The S.T.J.s, though stable if kept at or below liquid nitrogen temperatures for indefinite periods, degraded at room temperature rapidly, and were usually unusable in 24 hours. The degradation mechanism

involved was probably recrystallization, which can occur at room temperature for tin and lead. A spectacular example of this recrystallization was the growth of tin or lead whiskers from contaminated films and which were observed to grow up to 1 mm in length in a few hours. This effect is also observed elsewhere (ref. 4.5). The same process could cause leaks across the 10 Å barrier rendering the S.T.J. useless for our purposes. Thermal stresses resulting from thermal cycling could cause junction failures, but in fact, junctions had been repeatedly cycled between 77 K and 1.2 K without visible degradation.

VARIATIONS OF SAMPLE FABRICATION PROCEDURES

Vapour deposition of polyethylene (ref. 4.7) Polyethylene was evaporated in place of the MgF_2 to form a more flexible edge-guard layer. The deposited polyethylene was cross-linked by the Argon glow-discharge. The procedure was successful but the use of evaporated polyethylene resulted in vacuum chamber contamination, which caused 'whisker' growth problems in the metal films. The conclusion was that the polyethylene evaporation procedure could be useful, but must be carried out in a separate vacuum chamber.

Photoresist covered substrate The photoresist layer produced a phonon barrier between the substrate and the S.T.J. films. This layer must be thin to prevent thermal stresses occurring due to the different coefficients of thermal expansion of the polymer and the metal films. Ideally the photoresist film should be on top of a lead or tin foil stuck on the glass substrate. This would remove any thermal stresses resulting from the

difference in thermal-expansion of the glass substrate and the metal film. This work was not carried out because the problem did not appear in this area, there was no thermal-cycling problems between 77 K and 1.2 K, but must be done if room-temperature stable junctions can be produced.

AL_2O_3 barrier To guarantee a strong barrier layer, < 100 Å of Al was evaporated on top of the base-film, followed by the usual anodization, and evaporation procedures. This resulted in a S.T.J. with a $P_b.AL.AL_2O_3.P_b$ structure. The AL_2O_3 layer was much stronger than a comparable P_bO_x layer. The AL layer had little effect on the superconductive characteristics of the junction due to the 'proximity' effect (ref. 4.8). The problem in this procedure was in the change of evaporant source, that necessitated opening of the vacuum chamber to atmosphere which resulted in the formation of a thick barrier oxide (and contamination of the vacuum chamber). The resulting junctions had normal resistances too high to be of use in this study. If an evaporant-source changer was available this procedure of producing S.T.J.s should be feasible.

CHAPTER FIVE

EXPERIMENTAL METHODS AND RESULTS

CRYOGENICS

The cryogenic apparatus was the same as that used by G.H. WOOD, my predecessor in this study. Referring to Fig. 5.1A, it consisted of a liquid-helium dewar, contained in a liquid nitrogen dewar. The liquid helium dewar was sealed by a dewar-cap to allow pumping as a means of lowering the liquid helium temperature. The sample holder assembly entered the liquid helium dewar through a collar with an 'o' ring seal, to allow the adjustment of the sample holder height above the liquid helium as the liquid helium level fell. The 'push-rod' used for junction selection and α-particle source shuttering also went through an 'o' ring seal to allow movement relative to the sample holder. The helium-dewar "vacuum" jacket was connected to a rotary pump, gauges and bottled N_2 gas through a valve, so that the dewar jacket could be pumped out occasionally to eliminate the helium that diffused into the space, and back-filled with 1 to 2 torrs of nitrogen gas. The function of the nitrogen gas was to enable effective cooling of the liquid helium dewar by the surrounding liquid nitrogen. On adding liquid helium to the liquid helium dewar the N_2 gas in the jacket was "frozen-out" leaving a good vacuum insulating the liquid helium. The Helmhotz-coils provided the adjustable magnetic field used to suppress the Joselphson super-current. All the electrical leads to the sample and low-temperature preamplifier went through the octal feed-through on the sample-holder. The temperature of

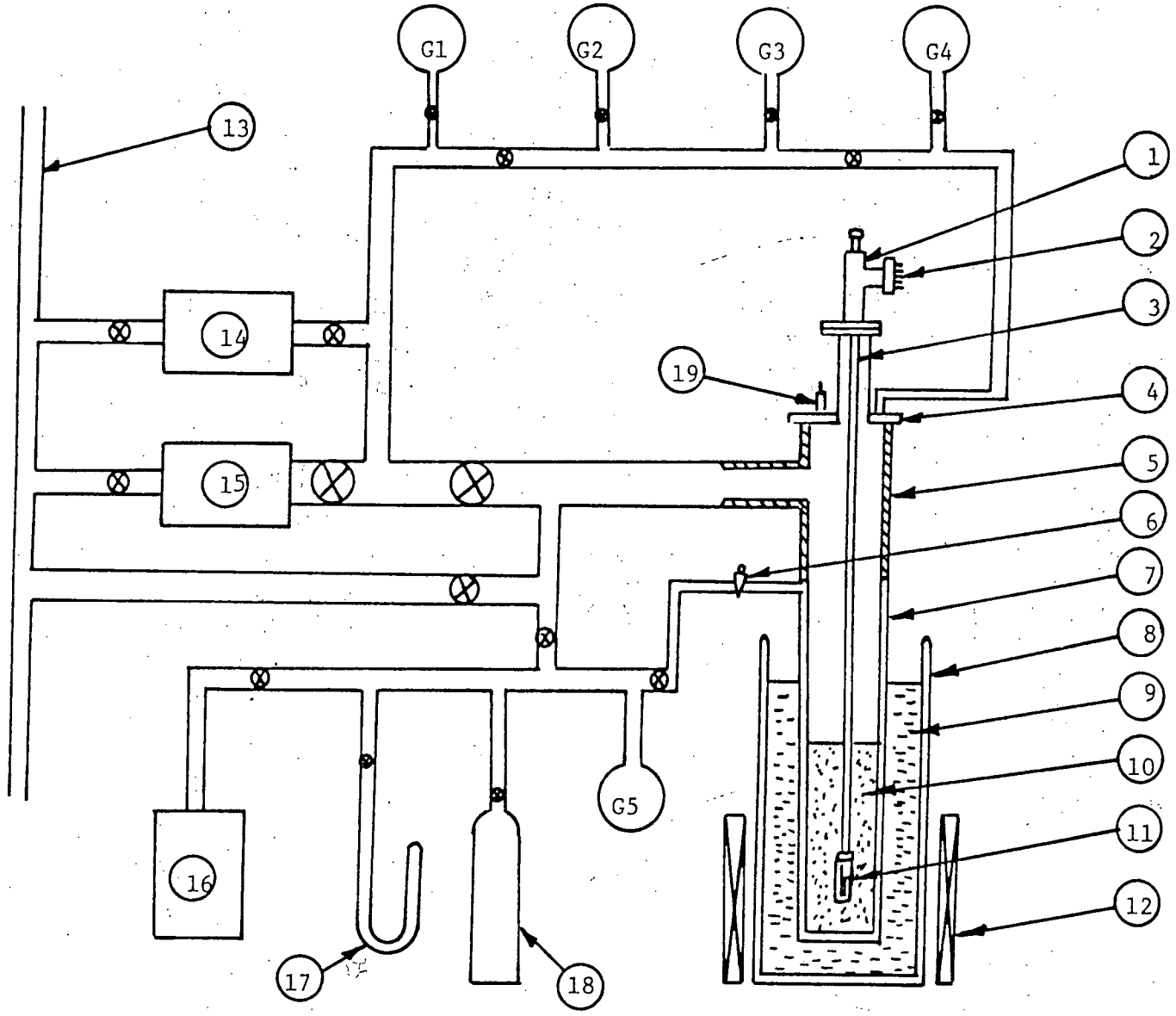

Figure 5-1A Cryogenic Apparatus (Schematic) (see page following for key).

KEY TO FIGURE 5-1A

G1 Marsh Dial Gauge, Type 100 0-760 Torr

G2 Edwards Dial Gauge, Type C.G.3 0-20 Torr

G3 Edwards Vacustat, Model 2E, 0-1 Torr, Lowest Reading Sensitivity = 0.001 Torr

G4 Marsh Dial Gauge, (no type No.) 0-760 Torr

G5 Ashcroft Dial Gauge, Type 1850 0-760 Torr (vac), 0-380 Torr (press. gauge)

1. Sample mount.
2. Electrical lead feedthroughs.
3. Sample mount support and control tubes.
4. Dewar cap.
5. Pyrex Tee (3 x 3 x 2 in.).
6. Helium Dewar Interspace pumpout port.
7. Helium Dewar, glass, 76 mm i.d., 90 mm o.d., approx. 48 in. long.
8. Nitrogen Dewar, glass, 116 mm i.d., 150 mm o.d., approx. 38 in. long.
9. Liquid Nitrogen.
10. Liquid Helium.
11. Sample.
12. Helmholtz coils.
13. He return line.
14. Welch Rotary Pump, Model 1402B, 5 cfm.
15. Stokes Pump, Model 49-10, 80 cfm.
16. Welch Rotary Pump, roughing purposes, Model 1405.
17. Mercury manostat (0-100 Torr).
18. Bottled dry N_2 gas; flushing purposes.
19. Transfer siphon port.

the liquid helium was monitored by the vapour-pressure of the liquid helium using the well known temperature-pressure relationship of helium gas in equilibrium with liquid helium (ref. 5.1).

JUNCTION SELECTION

A reproducible process for junction fabrication was described in Chapter 4 of this thesis. The selection step could be dispensed with, but to obtain the best junctions for tests as STJ particle detectors, each sample contained a group of six junctions (in a small area) and the sample was mounted on a sample-holder with a two-pole, six position slide switch. The switch allowed the selection of each of the junctions in turn to be connected for electrical measurements while at liquid helium temperatures. Thus the junctions under test had to be cooled to liquid helium temperature only once, this was important because the superconductive tunnelling junctions were found to degrade on thermal cycling from liquid helium temperature to round temperature and back. My predecessor in this investigation G.H. WOOD had difficulty in obtaining a reproducible process for fabricating S.T.J.s, and so he first tested the six junctions fabricated per run, at liquid helium temperatures and selected a junction showing the best D.C. characteristics, using a D.C. test sample holder. Following the selection, he warmed the samples to room temperature, mounted the selected junction in an A.C. 'sample mount' (at room temperature) and tested the junction at liquid helium temperatures again, for sensitivity to α-particle bombardment. The junctions were cycled to liquid helium temperatures twice and the junction characteristics were always degraded (current leaks developed) rendering the S.T.J.s unsuitable for particle detection.

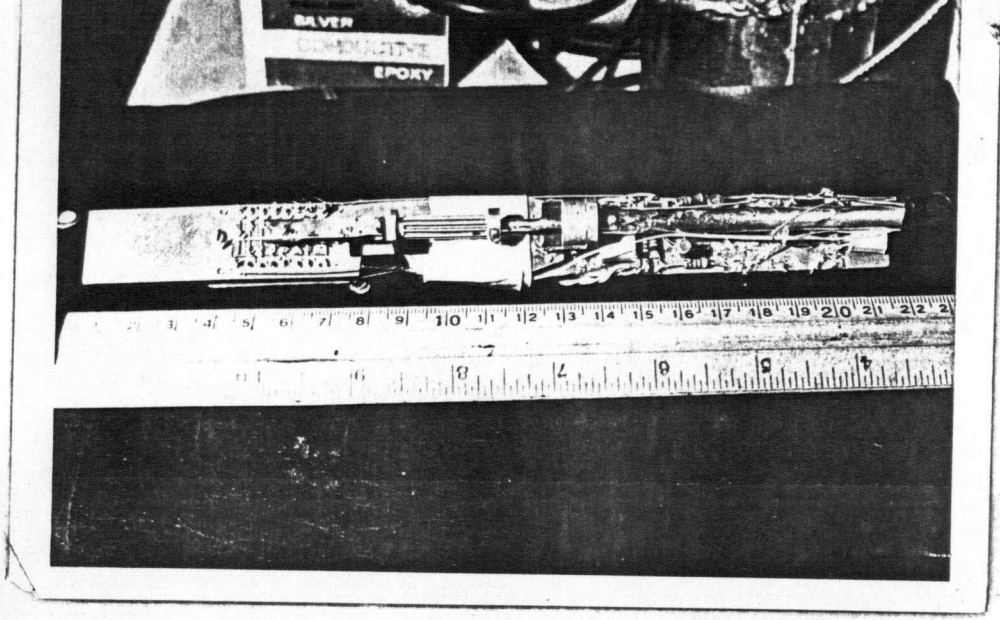

FIG. 5.1 SAMPLE HOLDER WITH SAMPLE MOUNTED, α-PARTICLE SOURCE & LOW TEMP. PREAMPLIFIER

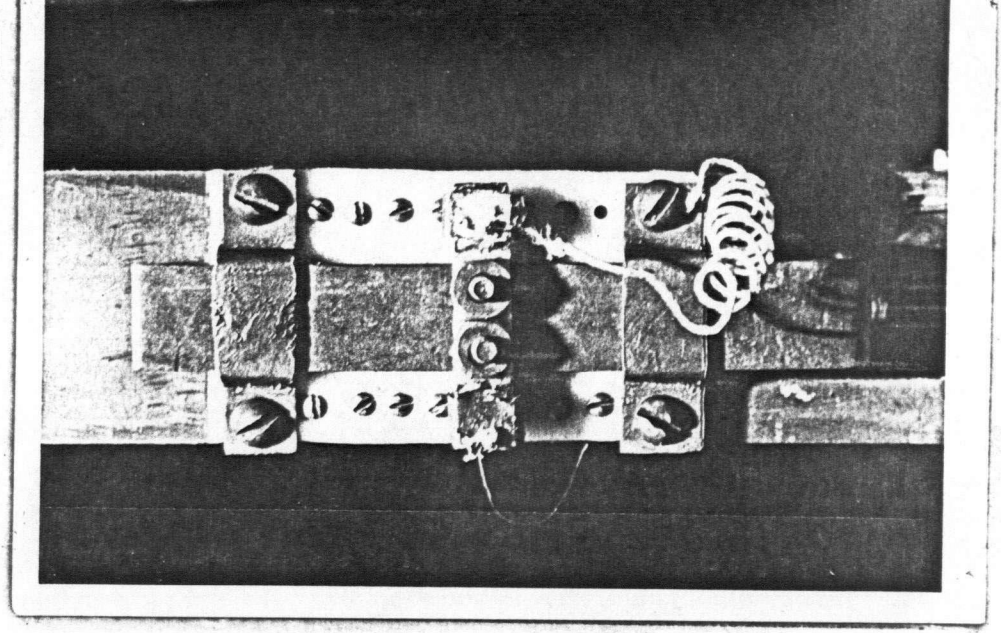

FIG. 5.2 SLIDE-SWITCH DETAILS ON SAMPLE-HOLDER

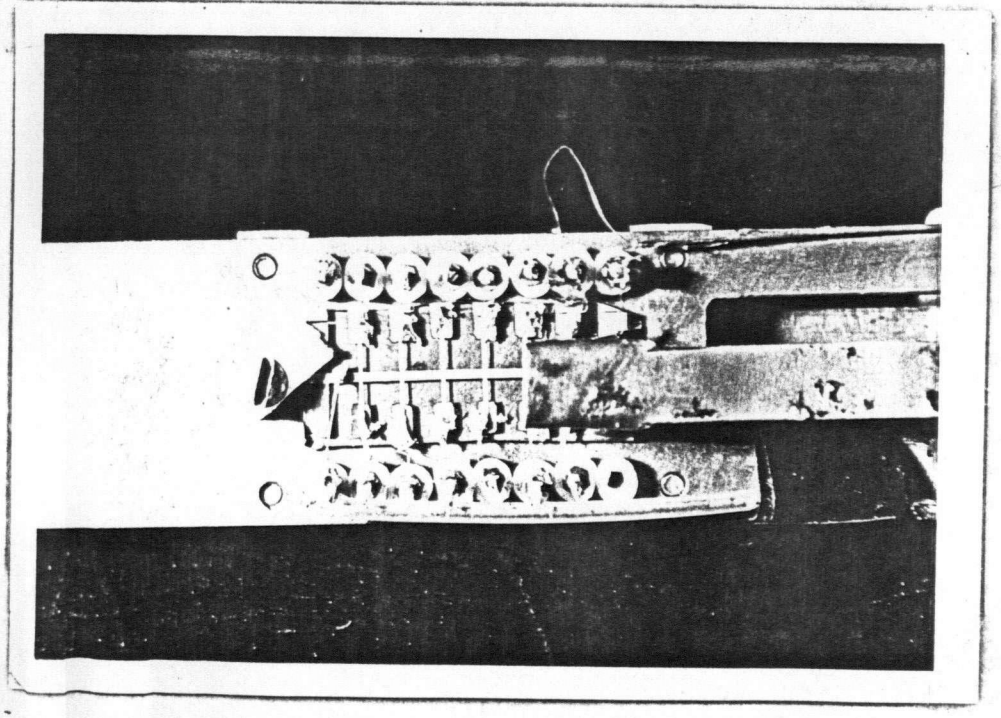

FIG. 5.3 SAMPLE MOUNTED ON SAMPLE HOLDER, WITH α-PARTICLE SOURCE FACING JUNCTIONS

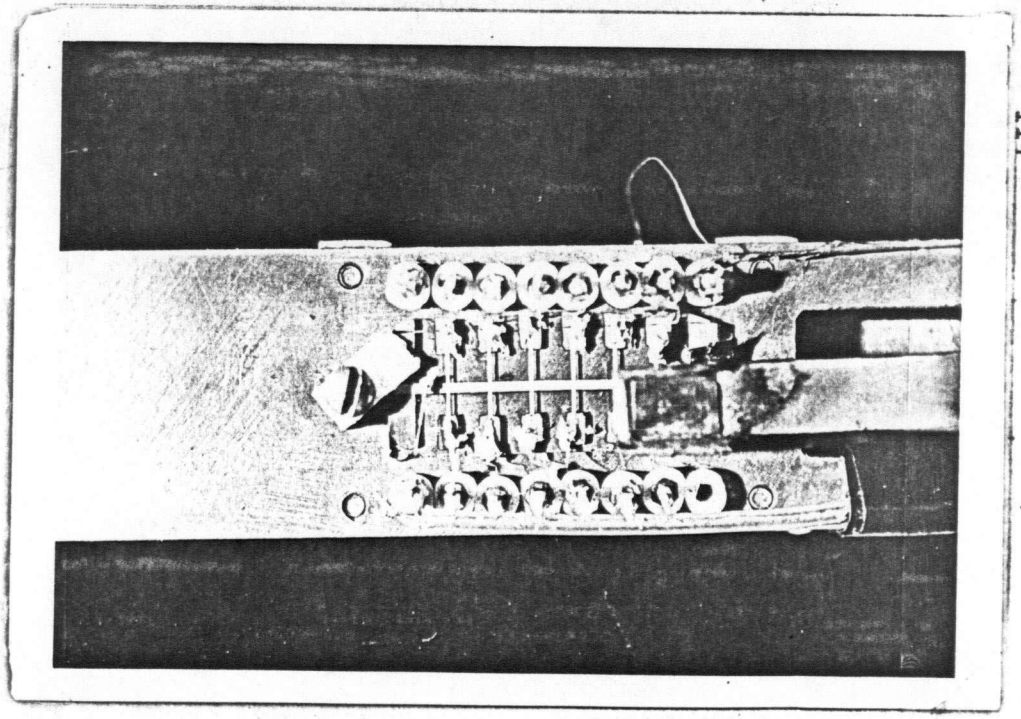

FIG. 5.4 SAMPLE MOUNTED ON SAMPLE-HOLDER, α-PARTICLE SOURCE TURNED AWAY FROM SAMPLE

Referring to Fig. 5.3, 5.4, the sample consisted of six junctions sharing one electrode, the base film (longitudinal stripe). The two ends of this film were connected to the I^- and V^- terminals respectively, i.e. the bias current negative terminal and the voltage sense negative terminal respectively. The ends of the top films of the junctions (cross-stripes) were connected to the switch pole pairs, which when selected were connected to the I^+ and V^+ terminals. Fig. 5.2 shows the details of the slide-switch. Fig. 5.1 shows the sample-holder with a sample mounted, the 'slide' of the slide-switch connected to a push-rod, and the Pu239 5.13 MeV α-particle source is thus positioned directly over the junction selected by the switch. The α-particle source was 'shuttered' by the rotation of the push-rod, causing the source or the shield to face the junction as shown in Figs. 5.3, 5.4, respectively.

JUNCTION D.C. CHARACTERISTICS MEASUREMENT

The four-terminal I, V measurement method was used as the large and unknown magnitude of the voltage-drops along the junction-films leading to the junction and connecting wires relative to the voltage drops across the junctions made two-terminal measurements meaningless. Referring to Fig. 5.5, a four-point I, V measurement was essentially as follows: current I flowed through the I^+ terminal, through R_{S_1}, R_J, and R_{S_2}, and out I^- terminal causing a voltage drop of IR_J across R_J the junction resistance; this voltage was sensed by the V.T.V.M. (vacuum Tube Voltmeter) through the V^+ and V^- terminals. Thus I and V were measured accurately. The 1KΩ resistor on the I^+ line and the 1MΩ resistors on the V^+, V^- lines served to isolate the junction from A.C. interference pickup. The

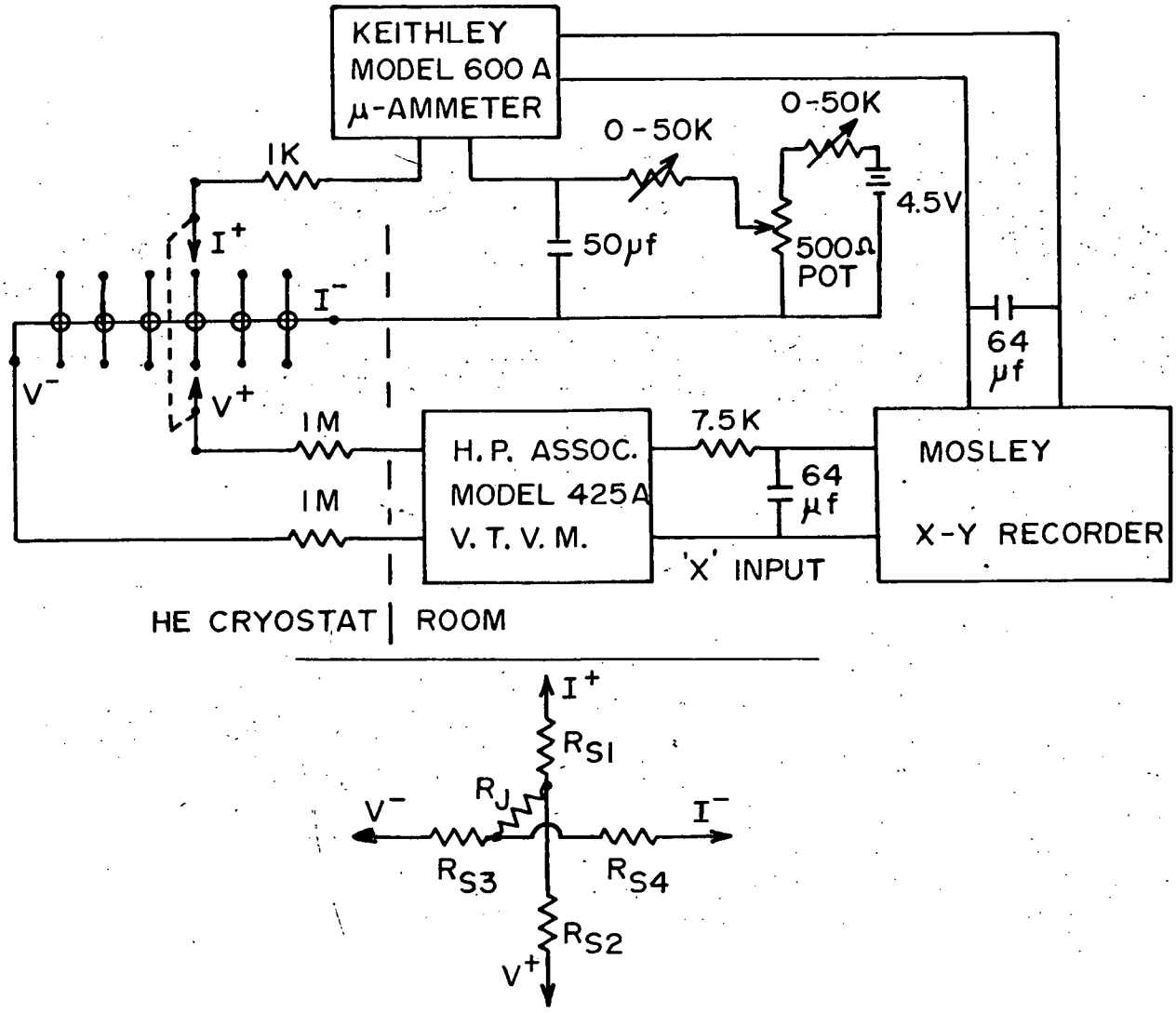

FIG. 5.5 JUNCTION D.C. CHARACTERISTICS MEASUREMENT CIRCUIT USING 4 POINT METHOD

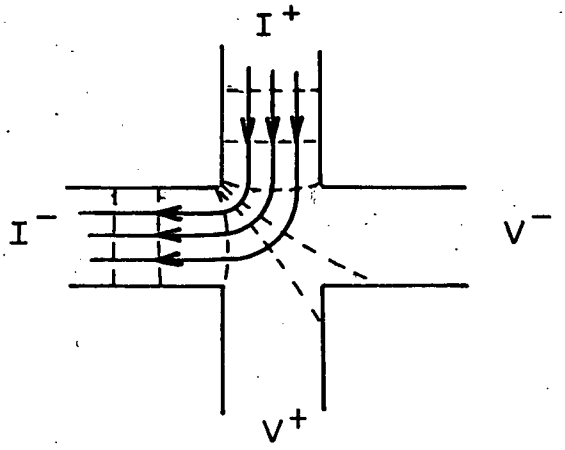

FIG. 5.6 CURRENT STREAM-LINES AND VOLTAGE EQUIPOTENTIALS FOR A JUNCTION WITHOUT OXIDE-BARRIER, GIVING RISE TO 'NEGATIVE-RESISTANCE' IN D.C. 4-POINT MEASUREMENTS

α-particle induced pulses were measured across the I^+ and I^- terminals.

The D.C. junction characteristics were plotted using an X-Y recorder, as shown in Fig. 5.5. D.C. measurements were made at room temperature and 77 K to determine the normal tunnel-conductances at these temperatures. It was observed that if the resistance at R.T. (room temperature) was negative, the junction was heavily shorted, or the barrier-oxide was exceedingly thin or absent. Fig. 5.6 shows the expected current-streamlines and voltage equipotential for overlapping metal films without a barrier, (by analogy with two-dimensional fluid-flow). It is clear that the V^- terminal in such a case is more positive than the V^+ terminal, causing an apparent negative-resistance reading. Note that the magnitude of this effect is directly proportion to the metal-film sheet resistivity. GIAVER has observed this effect, see page 27, 28 of ref. (5.9). Another interesting observation was that for good junctions the junction resistances increased with decreasing temperature, this was probably due to the decrease of carrier-density of the (barrier) semiconducting oxides (SnO_2 or PbO_2) with temperature. The ratio of the resistances at 77 K and R.T. are of the order 1.6 for junction normal resistances of greater than 1 ohm. For smaller junction-resistances, the mechanism described above causing the 'negative-resistance' readings is more dominant and because of the larger metal-film resistivity at room temperature than at 77 K acts to decrease the R.T. reading more than the 77 K reading, thus causing a larger ratio. For Sn junctions which were not superconducting at 4.2 K a further junction normal conductance reading could be made, and the junction resistances showed a further increase of the order of 1.1 → 1.2 over the 77 K value. A 'bad' or leaky junction

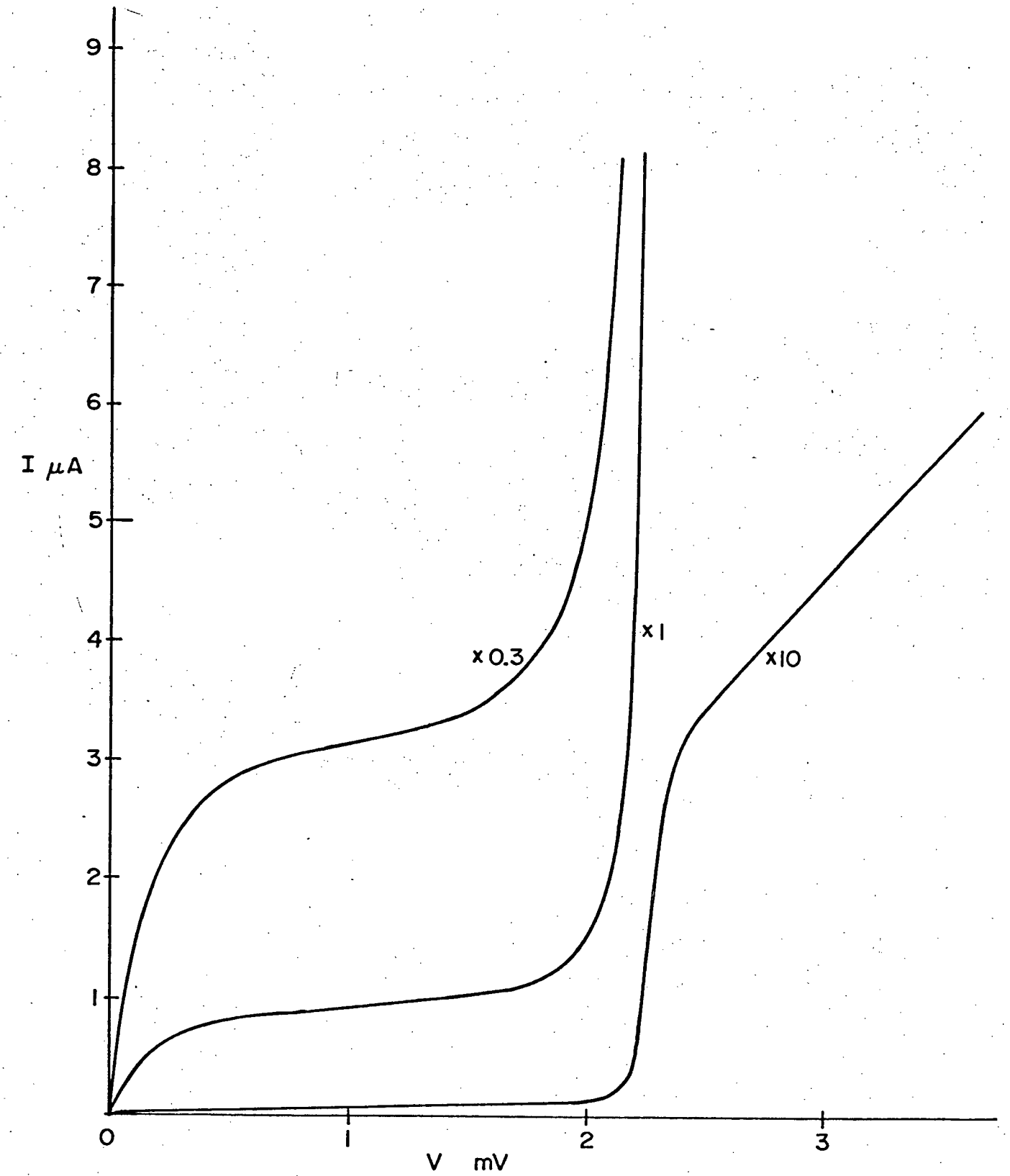

FIG. 5.7 D.C. JUNCTION CHARACTERISTICS OF R123S6J2 (Pb) AT 4.2K.

showed a decrease in junction resistances with decrease of temperature as expected, since the metallic bridges causing the shorts decrease in resistance with temperature decrease. Based on the above observations measurements on a sample were stopped at R.T. or at 77 K if the readings indicated a poor sample, thus saving a lot of experimental time and expense.

At 4.2 K (liquid helium at atmospheric pressure) lead is a superconductor, thus the Pb junctions showed superconductive-tunnelling characteristics. The voltage current characteristics were plotted for each of the six junctions on the sample, and the 'best' junctions (no leaks, high junction-conductance) noted at this stage. Further D.C. measurements at lower temperatures and α-particle induced signal pulse measurements concentrated on these junctions. Fig. 5.7 shows the D.C. I, V characteristics of the Pb junction R123S6J2 at 4.2 K with bias-magnetic field of 10 gauss. The characteristic was plotted at three different current scales to show details of the curve. As the bias-voltage was increased the current at first increased rapidly until a plateau was reached. This section of the characteristic represented the increasing tunnelling probability of the thermally generated quasiparticles, until the limit imposed by the Q.P. density and the junction tunnelling conductance was reached. As the bias-voltage neared the $2\Delta/e$ value Q.P.'s were created by the breakups of cooper pairs and the current rose rapidly but bounded by the normal tunnelling characteristic, which represent the limiting case where all the charge carriers are quasiparticles (unpaired electrons) (ref. 5.2). The junction R12356J2 had a $R_N \approx 45\Omega$, two orders of magnitude higher than the junctions used for particle detection. This junction was chosen in order to show the complete tunnelling characteristic,

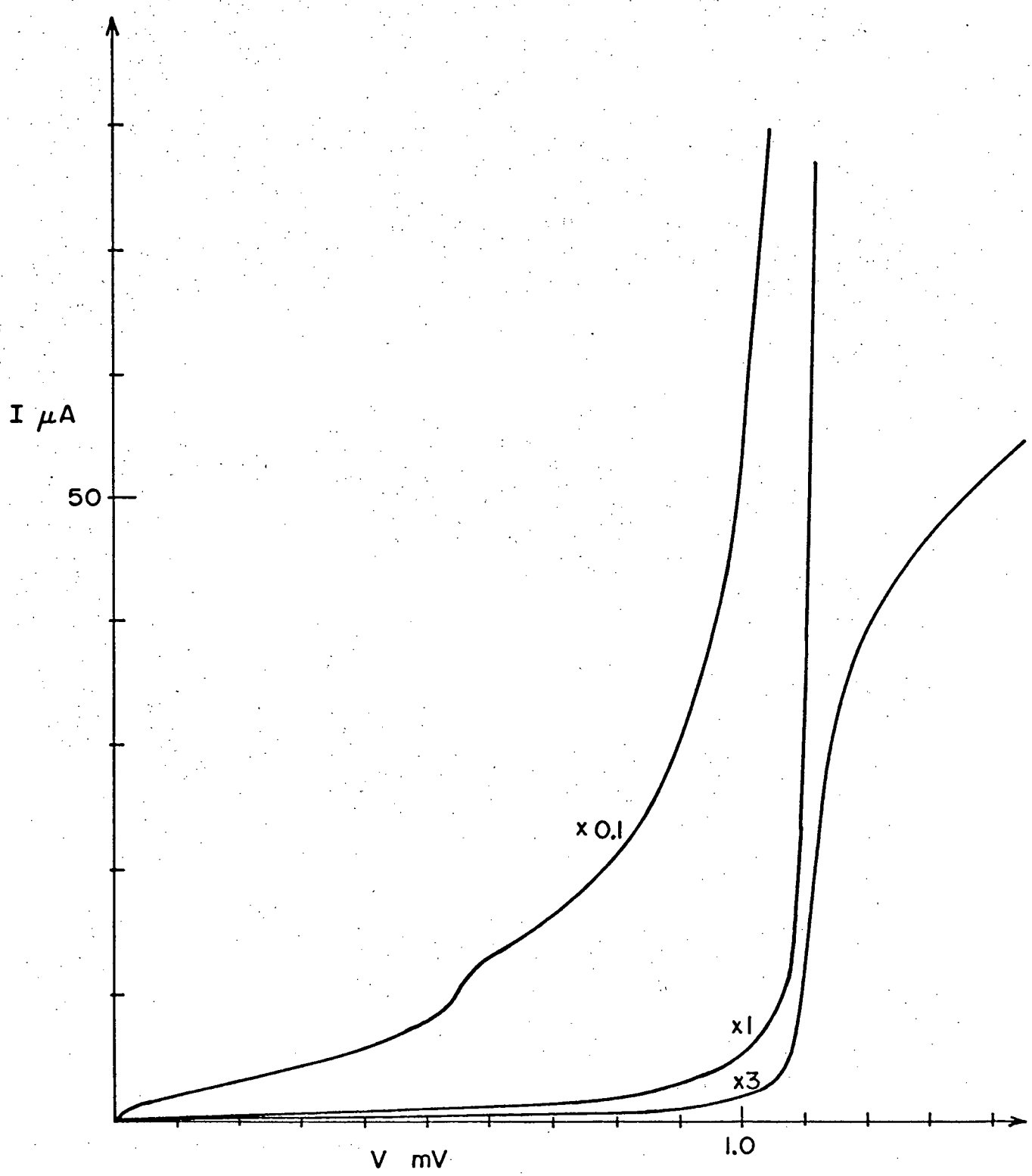

FIG. 5.8 I.V. CHARACTERISTICS OF Sn JUNCTION R77S1J3.

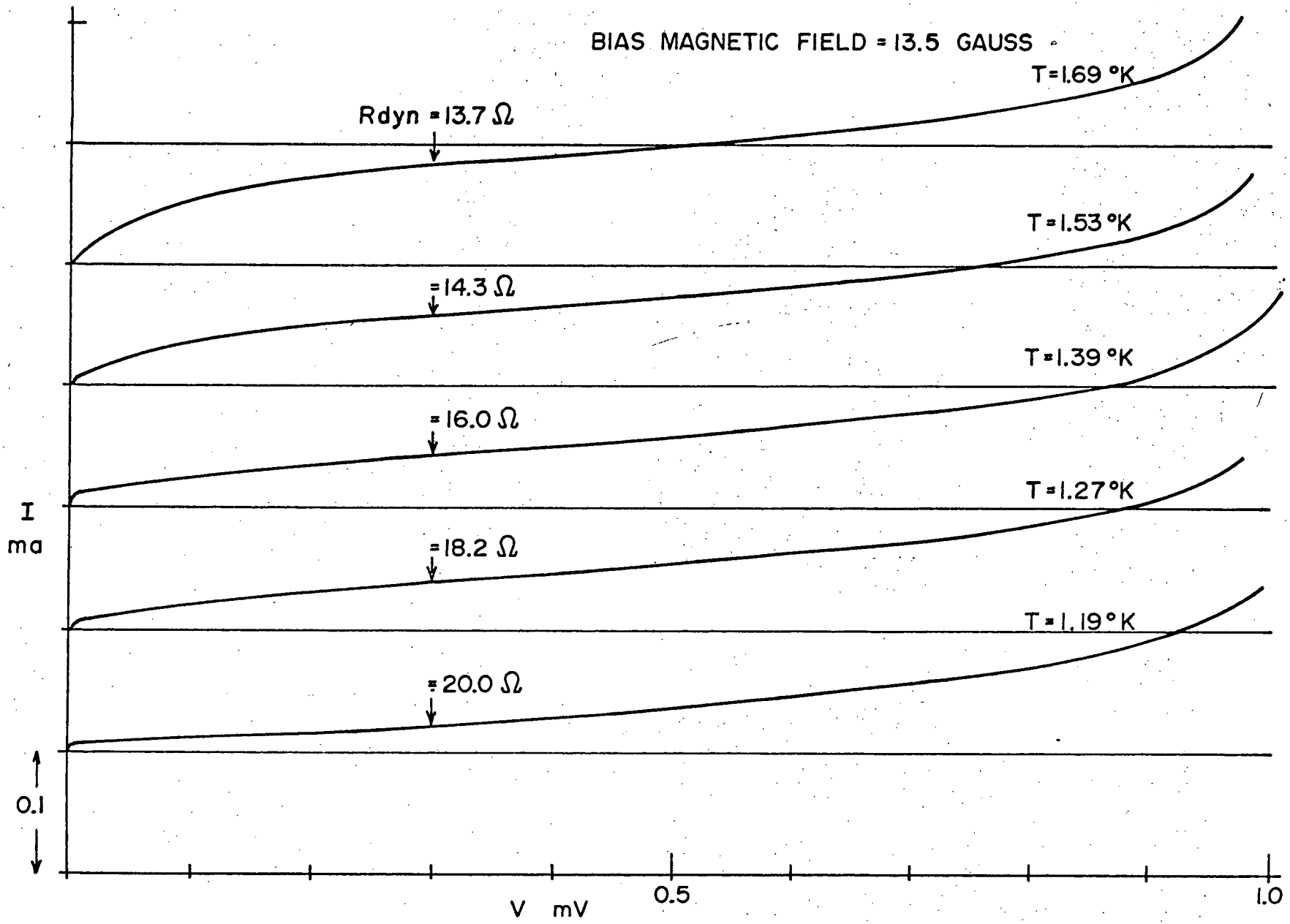

FIG. 5.9 TEMPERATURE DEPENDENCE OF I.V. CHAR. OF Sn JUNCTION R67S1J3.

since the junctions with low R_N showed a 'foldback' effect which made plotting the true I. V. characteristic impossible.

With the biasing magnetic field 'off' Josephson super-current was observed. This current was easily distinguished from shorts, by its sensitivity to magnetic fields. When the junction current exceeded the maximum super-current limit (for the operating temperature and ambient magnetic field) or when the biasing magnetic field was increased (which cause a decrease of super-current maximum value) the junction switched abruptly to the quasiparticle tunnelling mode. A general decrease of super-current maximum with increase of biasing field was observed but the theoretical $|\sin x/x|$ type of dependence could not be resolved due to the noisy electromagnetic environment.

At 4.2 K Sn is a normal conductor, (Tc of Sn is 3.75 K) thus only the normal-tunnelling characteristics was measured at this temperature. The Helium cryostat was then pumped down to 1.2 K where the superconductive tunnelling junction I. V. characteristics were measured. A representative set of I.V. characteristics for a Sn junction is shown in Fig. 5.8. Other than a slight 'bump' in the characteristic at Δ/e, which is a frequently observed feature for Sn junctions the curves are similar to that of Pb junctions traced at the same $\beta\Delta$ value, i.e. at $\sim$ 2.3 K. The 'bump' is theorized as due to two particle tunnelling by Adkins (ref. 5.2) Schrieffer and Wilkins (ref. 5.3). Fig. 5.9 shows the variation of the I. V. characteristics with temperature of the Sn junction R67S1J3. Note the increase of junction current and decrease of R_{dyn} with increasing temperature at the bias point of 0.3 mv in agreement with theory.

JUNCTION-DEGRADATION

Sn and Pb junctions fabricated in this lab (with SnO_2 and PbO_2 oxide barriers) deteriorate at room temperature. Most junctions with barriers thin enough for their use as particle-detectors develop leaks of large enough conductances in 24 hours at room temperature to ruin their usefulness as superconductive particle detectors. Thermal-cycling to room temperature and back to liquid helium temperatures caused irreversible degradation of characteristics. For example, in sample R67S1, junctions 1 to 5 showed super-shorts (superconductive short circuits) and the dynamic resistance of junction 6 decreased from 5.4Ω to 0.7Ω after thermal cycling. The degradation due to cycling may simply be due to the actual time spent at room temperature rather than the thermal cycling. Thermal cycling between 1.2 K and 77 K caused only minor changes in the junction characteristics, and junctions have been kept for weeks at 77 K without degradation.

The mechanism for degradation at room temperature appear to be diffusion and recrystallization of the Sn and Pb films. One dramatic phenomenon confirming this is the rapid growth of Sn and Pb whiskers on the junction films at room temperature, whiskers grew to millimeter lengths in a few hours, when the evaporations of the films were carried out in a contaminated vacuum chamber. This phenomenon had been observed by others (ref. 5.4).

'S' TYPE NEGATIVE-RESISTANCE (foldback)

With junctions of high tunnelling conductances suitable for SPD applications the D.C. current at the "current-step" (i.e. at the rapid-current rise near $2\Delta/e$) caused sufficient heat dissipation to increase the

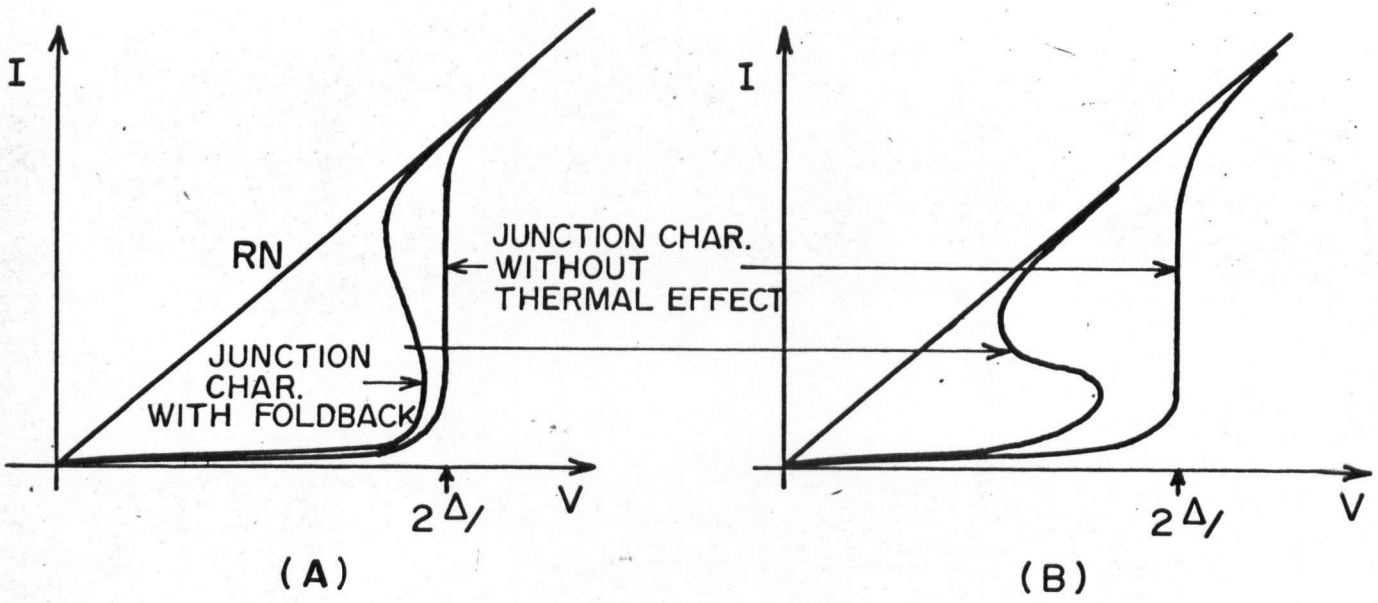

FIG. 5.10 'S' TYPE NEGATIVE RESISTANCE IN JUNCTION I.V. CHARACTERISTICS OF THERMAL ORIGIN.

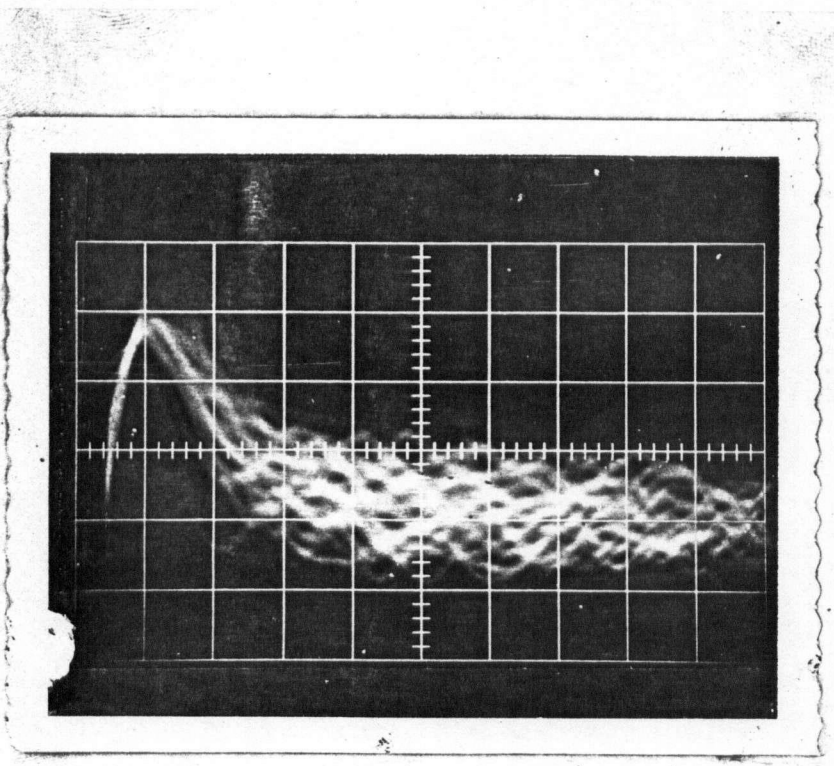

HORI. = 0.2μs/cm
VERT. = 50 mV/cm
ORTEC
INTEGRATOR OUT
DIFF. OUT
COARSE GAIN 'x 3'
FINE GAIN 'x 1'
ORTEC VOLT. GAIN = 152
R.T. PREAMP. V.G. = 35.2
JUNCTION BIAS V. = 0.3 mV
MAGNETIC BIAS = 13.5 Gauss
TEMP. = 1.2°K

FIG. 5.12 α-INDUCED PULSES IN Sn JUNCTION R67S1J3.

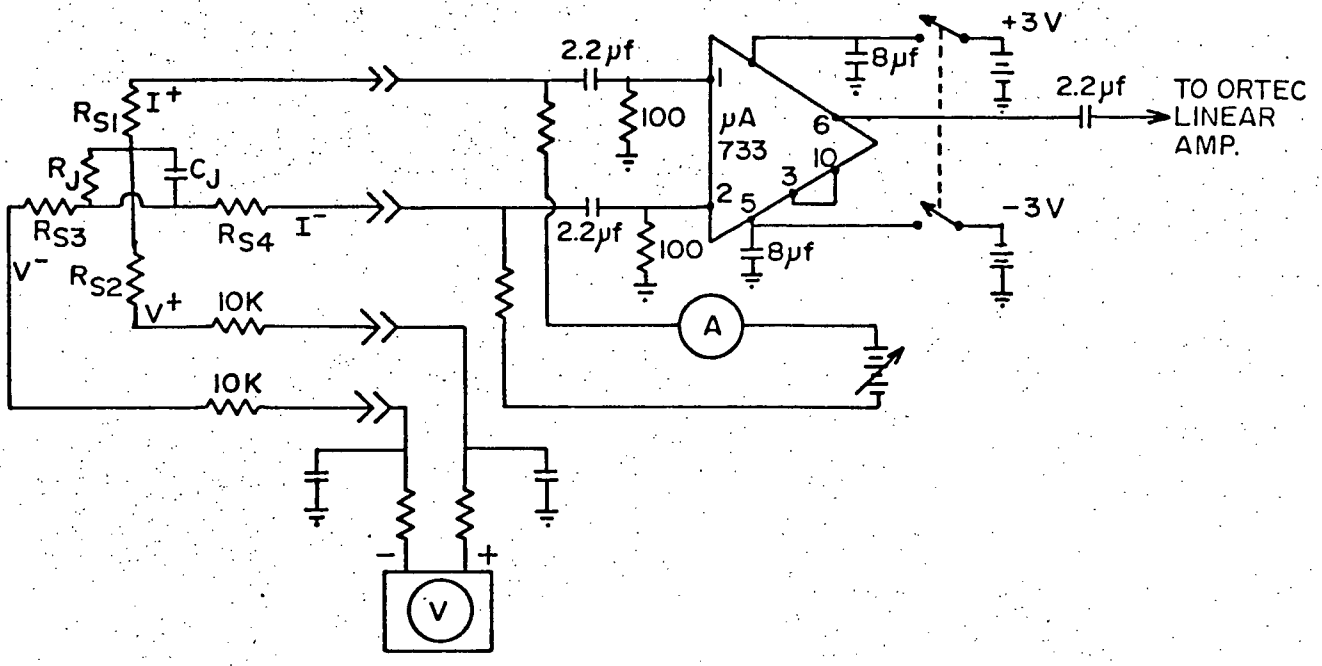

FIG. 5.11 AMPLIFIER CIRCUITRY FOR α-PARTICLE INDUCED PULSE OBSERVATIONS

TIME	SHUTTER	DISC. SETTING	COUNT	COMMENTS
7:57 → 8:02	Open	0.088	1619	Usual Transients
8:03 → 8:08	Closed	"	45	"
8:09 → 8:14	Closed	"	91	1 burst ∿60 pulses
8:15 → 8:20	Open	"	1980	1 burst
8:34.5 → 8:39.5	Open	"	1705	Quiet
8:43.5 → 8:48.5	Closed	"	25	"
8:49.5 → 8:54.5	Closed	"	11	"
8:59 → 9:04	Open	"	1652	"

TABLE 5.1 DISCRIMINATOR COUNTER READINGS ON α-INDUCED PULSES FROM R67S1J3.

junction temperature and decrease the superconductor energy gap. This effect is observed to be more pronounced for Pb junctions, probably because of the larger energy gap. Thus with a junction current of 0.5 ma and 2Δ = 2.54 ma, the dissipation is 1.27 μW which is sufficient to produce a local temperature increase and lower the energy gap because of the low heat-conductivity of the glass at the operating temperatures, Fig. 5.10A shows this effect. In junctions of larger tunnel conductance the 'foldback' was observed to occur before the 'current step'. In this case an increase of current through the junction increases dissipation, causing the junction to heat up, thus the voltage is determined by the I. V. characteristic of the increased temperature, which results in a lower voltage, i.e., a current controlled or 'S' type negative resistance, cf. Fig. 5.10B. Further the effect was more pronounced when the junction was above the liquid-helium level than when the same junction was immersed, confirming the probable thermal origin of the negative resistance effect.

PULSE MEASUREMENTS WITH ROOM TEMPERATURE PREAMPLIFIER

When D.C. measurements were completed and a 'good' junction selected, the amplifier-system shown in Fig. 5.11 was used to observe the α-particle induced pulse-signals from the junction. The amplifier system was calibrated using a "dummy-junction" consisting of a resistor and capacitor in parallel, having values 100Ω and 2000pF respectively (i.e. the expected maximum-dynamic resistance, and capacitance of a representative junction) and injecting into it square-wave pulses or simulated junction signal current waveforms. The preamplifier voltage gain was found to be 35.2 (linear). The equivalent input noise was approximately 3 microvolts R.M.S.

The Johnson noise from the dummy input accounted for 1 μV and the amplifier and pickup of interference 2 μV. This is much better than the manufacturer's specification of 9 μV, probably because of the low supply voltage of ± 3 volts used, instead of the allowed maximum of ± 8 volts. The ORTEC linear amplifier had a measured voltage gain of 152 at X3 coarse gain and X1 fine gain settings, the equivalent input noise was approximately 3 μV R.M.S., negligible compared to the preamp contribution.

Sn junctions R67S1 J1 → J6 were found to have desirable characteristics for operation as STJ particle detectors from the D.C. characteristics measurements. In particular junction #3 (J3) was the best junction, having a low R_N = 0.22Ω (normal tunnelling resistance) and the best R_{dyn}/R_N ratio, indicating little leakage, and a R_{dyn} = 20.0Ω . Pulse-amplified measurements confirmed that J3 gave the best signal-amplitude (Fig. 5.12). This junction was used for further measurements.

That the signal-pulses were in fact induced by α-particle bombardment was proved by 'shuttering' the α-particle source, or by stopping the α-particles by immersing the junction in liquid helium. A series of count-readings using the discriminator-counter is shown in table (5.1). The counting was done with the pulses monitored on the C.R.O., and any unusual interference was noted. From the readings in table 5.1, it is clear that α-particle induced pulses are definitely observed, and electrical interference is minimal, as low as 2 C.P.M. in quiet periods and at most 18 C.P.M. in noisy periods, (these may be compared to G.H. WOOD's count rates of 1.3 → 1.8 x 10^4 C.P.M. without noise burst grating). The interference was mostly common-mode, thus by using the Fairchild μA733 differential amplifier as a preamplifier, with the high common mode rejection ratio of

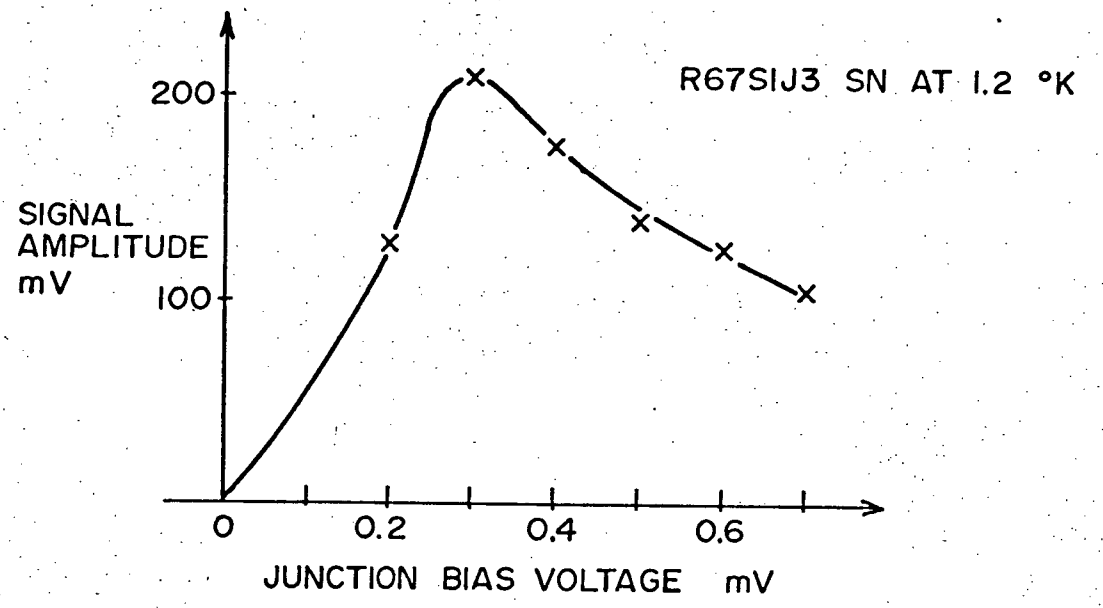

FIG. 5.13 PULSE-AMPL. Vs BIAS VOLTAGE

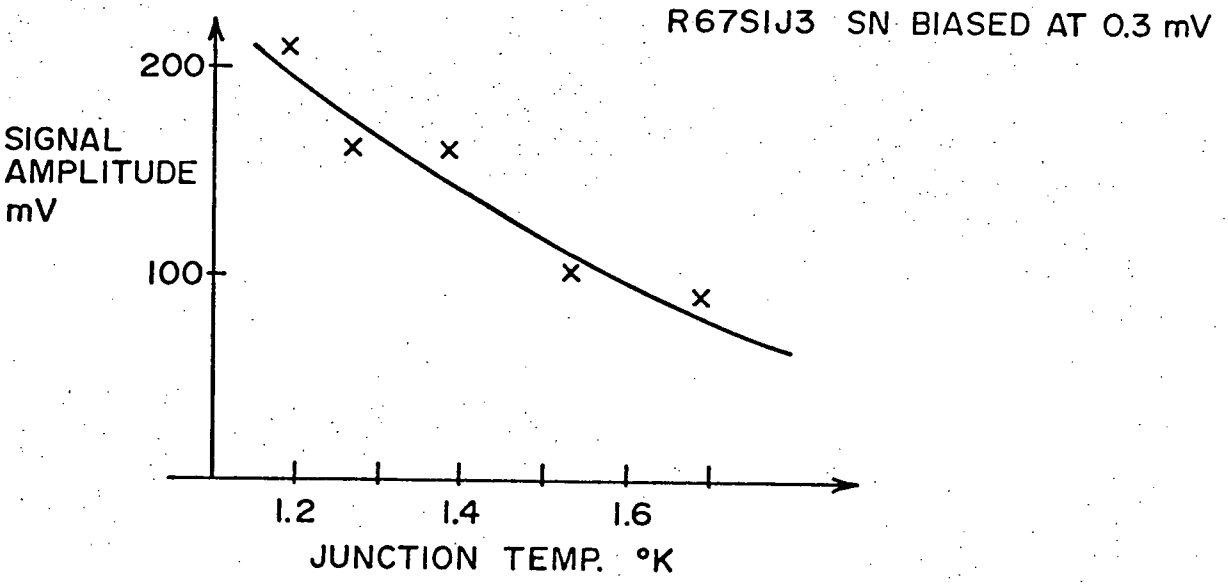

FIG. 5.14 PULSE-AMPL. Vs TEMPERATE OF JUNCTION

70db interference was drastically reduced.

PULSE-AMPLITUDE DEPENDENCE ON BIAS-VOLTAGE

The pulse-amplitude which is dependent upon $(\frac{\partial I}{\partial T})_V . R_{dyn}$ was found to vary with the voltage at the operating-point, (the point at which the bias- resistor load-line intersects the I. V. characteristic of the junction at the operating temperature). The largest maximum-amplitude pulses were observed at 0.3 volt bias, corresponding to the point of maximum R_{dyn}. Fig. (5.13) shows the pulse-amplitude maximum Vs. bias voltage for the Sn junction R67S1J3. From the calculations in Chapter 2 $(\frac{\partial I}{\partial T})_V$ is expected to be nearly independent of bias-voltage for $\beta\Delta$ of >5.4 (Sn at 1.2 K) and bias-voltage > 0.5 Δ/e ($\sim$0.3mV) (C.F. Eqn. (2.6), thus the observed decrease of $R_{dyn} = (\frac{\partial I}{\partial V})_T$ with increase of bias-voltage beyond 0.3mV results in a decrease of $(\frac{\partial I}{\partial T})_V . R_{dyn}$. With decrease of bias-voltage below 0.3mV, both $(\frac{\partial I}{\partial T})_V$ and R_{dyn} decreases, thus $(\frac{\partial I}{\partial T})_V . R_{dyn}$ also decreases.

PULSE-AMPLITUDE DEPENDENCE ON TEMPERATURE; Sn JUNCTIONS

From Fig. (2.6) Chapter 2 the voltage-response sensitivity $(\frac{\partial V}{\partial T})_I$ Vs $\beta\Delta$ curve for a frequency of 1 MHz frequency peaks at $\beta\Delta$=5.8. Assuming this is representative of the response to the α-particle induced thermal-pulse, an increase of operating temperature of the Sn junction above 1.28 K ($\beta\Delta$ = 5.8) should result in a decrease of $(\frac{\partial V}{\partial T})_I$. Further, with increased operating temperature the specific-heat of the glass-substrate increases, resulting in a smaller rise in temperature for the same heat-pulse, contributing to the decrease of output pulse amplitude with increased

temperature. This is in fact observed, the variation of pulse amplitude with temperature is shown in Fig. (5.14).

α-PARTICLE INDUCED PULSE-SIGNALS AND NOISE

The observed pulse signals as shown in Fig. (5.12) vary between 130 to 160 mV, the lower limit being a C.R.O. trigger threshold. The density of traces by visual inspection appear to be uniform to 160 mV. The pulse-amplitudes corresponded to signal-voltage amplitudes of 24.3 to 29.9 mV at the preamp input, and as the R_{dyn} for the junction was 20Ω , this corresponded to signal-current amplitudes of 1.2 to 1.5 μa, disregarding the junction capacitance (the effect of which is to increase the rise-time, decrease the peak voltage, and increase the fall time). The 'noise' voltage visible on the C.R.O. trace appeared to be approximately 60 mV peak to peak, corresponding to approximately 3.3 μV Rms at the input to the preamp. The slight increase in 'noise' could only be accounted for by the increased pickup of interference when the sample was connected to the preamp. The shot-noise, the only significant source of inherent junction noise, generated in the junction by the bias-current of 0.025 ma was only 0.056 μV Rms. Thus the noise originating in the junction was negligible compared with interference pickup and preamplifier noise, and to improve the signal to noise ratio, a low-temperature preamplifier physically close to the junction is necessary. Pb junctions were not tested with the room temperature preamplifier because Pb junction fabrication technology was not developed at the time. The Pb junctions were tested later when a low temperature preamplifier had been developed.

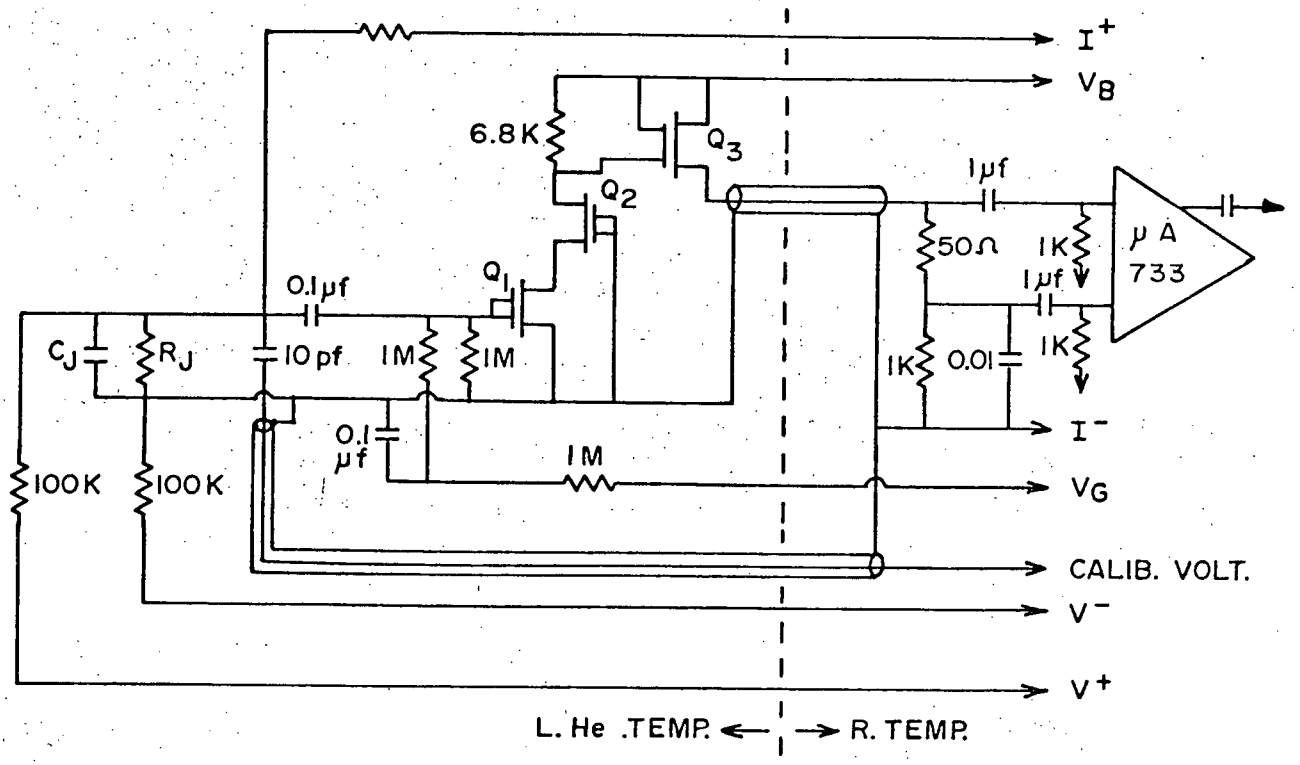

FIG. 5.15 DIRECT-COUPLED LOW. TEMP. PREAMPLIFIER, CONNECTED TO JUNCTION AND 'POST' AMPLIFIER.

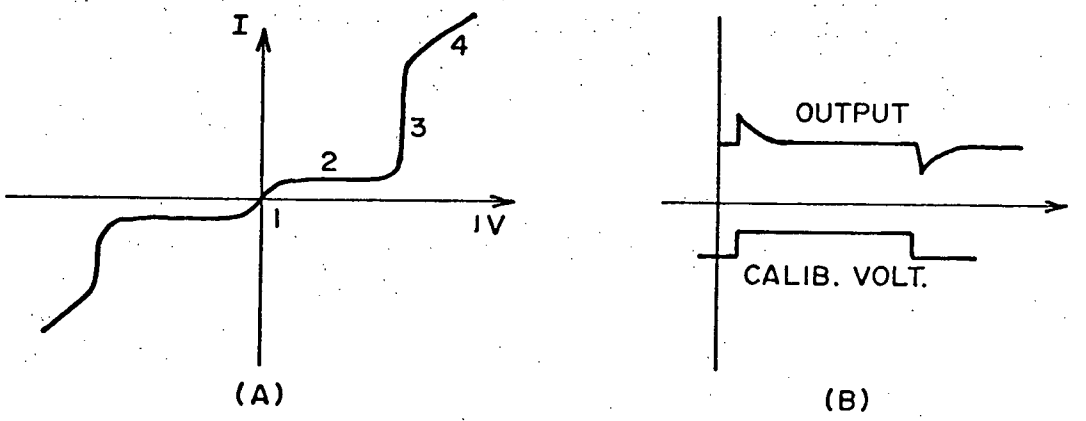

FIG. 5.16 JUNCTION CAPACITANCE MEASUREMENT AND AMPLIFIER CALIBRATION USING THE IV CHARACTERISTICS.

PULSE MEASUREMENTS WITH DIRECTLY-COUPLED LIQUID HELIUM TEMPERATURE AMPLIFIER

LIQUID HELIUM TEMPERATURE AMPLIFIER DETAILS

Available literature (ref. 5.5 → 5.11) and private communications indicated that at liquid helium temperatures only superconductive amplifiers, some M.O.S.F.E.T.'s (Metal Oxide Semiconductor Field Effect Transistors), and some GeJF.E.T.'s (Germanium Junction Field Effect Transistors) were usable as amplifiers. Superconductive amplifiers such as the Cryotron type required too much research and development to be feasible for this project, though this is probably the most suitable type for eventual applications using the S.T.J. Such GeJ.F.E.T.'s as the TIM301 (Texas Instruments) had good performance figures at 4.2 K according to O. PARRISH, (private communications). The charge carriers in Ge are frozen out at 4.2 K and the J.F.E.T. works only because of impact ionization of the impurity. The problem with using the GeJ.F.E.T. is that T.I. no longer manufacture these devices, therefore they are not easily available. M.O.S.F.E.T.'s work at 4.2 K (and below) by injection of charge carriers from the 'source' contact, and these devices are easily available and inexpensive. The N-channel depletion mode M.O.S.F.E.T. 3N140 manufactured by R.C.A. was recommended for liquid helium temperature operation by Fred Witteborn (of Stanford Research Institute in a private communication to Professor GUSH of the Physics Department, U.B.C.); this is the device used for the present low temperature preamplifier.

Referring to Fig. (5.15) the low temperature preamplifier had a 'cascode' type input, followed by a 'source-follower' to drive the 50Ω

impedance of the microcoaxial cable connecting the preamplifier to the post amplifier. In Q_1, Q_2 of the cascode stage the gates 1, and 2 of the F.E.T.'s were connected together and used as a single gate. This reduced the operating drain-current in the cascode stage to reduce power dissipation. In Q_3 gate 2 of the F.E.T. was tied to the positive supply voltage to increase the transconductance and thus lower the source impedance. This increased the current through the device but the dissipation in the device was kept low by keeping the drain-source voltage low by the circuit shown. The D.C. bias of Q_1 was adjusted externally, this was essential as the optimum operating bias varies with temperature. It was found that for the set of transistors used the room temperature optimum bias was $\sim$-2.8 volts and the liquid helium temperature optimum bias was $\sim$+0.8 volts. For better performance the bias of Q_2, Q_3 should also have been externally adjustable, but this would have required two more pins on the feed-through into the sample-holder and two more electrical leads down to the liquid helium portion of the liquid helium cryostat, increasing the heat-leak. Thus for convenience and to decrease liquid helium usage rate Q_2, Q_3 were not externally biased. The output Q_3 of the preamplifier drives the microcoaxial line terminated by a 50Ω resistor to match the coaxial line-impedance. In series with the 50Ω resistor is a capacitively by-passed 1KΩ resistor. This resistor was used to decrease the drain-source voltage of Q_3. The signal across the 50Ω resistor fed the inputs of the post-amplifier (a Fairchild μA733, previously used as a room temperature preamplifier). The post-amplifier then drove the ORTEC linear amplifier, which in turn drove the other devices as before. The preamplifier gate-bias control and battery, the

preamplifier-supply controls and batteries, the post-amplifier supply voltage regulator and batteries, the junction-bias controls and batteries, and a μa meter used for monitoring junction bias-current, were housed in a metal box called the 'control' box physically mounted on the sample-holder octal electrical feed-through during operation. This was to minimize interference pickup. Another microcoaxial cable was used to feed a calibration pulse to a 10pf capacitor connected to the input of the preamplifier. A step voltage V applied to the 10pF capacitor dumped a $V \times 10^{-11}$ coul. charge into the junction capacitance, causing an 'instantaneous' rise of voltage across the junction and approximately exponential decay, dependent on junction characteristics. This voltage was amplified by the preamplifier, and the output from the preamplifier (via the postamplifier) used to calibrate the gain of amplifier system.

The preamplifier was checked at room temperature together with the post-amplifier, as shown in Fig. (5.15). The preamplifier voltage-gain was found to be 25. The post-amplifier-gain was 35.2. Output wideband noise was approximately 0.01 volts Rms at the post-amplifier. Since the post-amplifier alone contributes only < 105 μV Rms at the output most of the noise came from the preamplifier, corresponding to 11.3 μV Rms equivalent input noise at the preamplifier. This could in future be improved by transistor selection, and/or adjusting the gate bias of Q_2, Q_3 externally. Such a procedure may result in an expected equivalent input noise of approximately 5 μ volts[Ref. 5.9, 10], but it was decided that the improvement was not worth the efforts at the time. Despite the apparently higher equivalent input noise for the low temperature amplifier, the actual noise-performance when used in conjunction with an input step-up pulse

transformer is much better than the room temperature preamplifier, as will be shown in the following sections.

LOW TEMPERATURE PREAMPLIFIER TEST AND CALIBRATION AT LIQUID HELIUM TEMPERATURE AND MEASUREMENT OF JUNCTION CAPACITANCE

Referring to Fig. (5.16A) we see that as the junction bias-voltage increases the R_{dyn} increases from a small value at (1) to a maximum value at point (2), and with further increase in bias-voltage R_{dyn} decreases and becomes very small at (3) the "current-step", and with further increase takes a value approaching R_N (normal tunnel resistance) at (4). With a small calibration voltage step V_C, smaller than $2\Delta/10.e$ say, applied to the calibration capacitance C_C, the voltage across the junction rises abruptly by an amount

$$V_{So} = V_C \cdot \frac{C_C}{C_J+C_{IN}+C_C} \qquad (5.1)$$

where C_J is the junction capacitance, and C_{IN} is the preamplifier input capacitance with all the associated stray capacitances. The voltage increment then decays as:-

$$V_S(t) = V_{So} \cdot \frac{-t}{e^{(C_C+C_J+G_N).R_{dyn}}} = V_{So}\, e^{-t/\tau} \qquad (5.2)$$

Since R_{dyn} at any bias-voltage can be measured from the junction D.C. characteristics the C_J can be found by measuring τ, knowing C_C, C_{IN} and R_{dyn}. Note that this procedure is valid only for small voltage-steps as R_{dyn} cannot be regarded as a constant over large ranges of voltages.

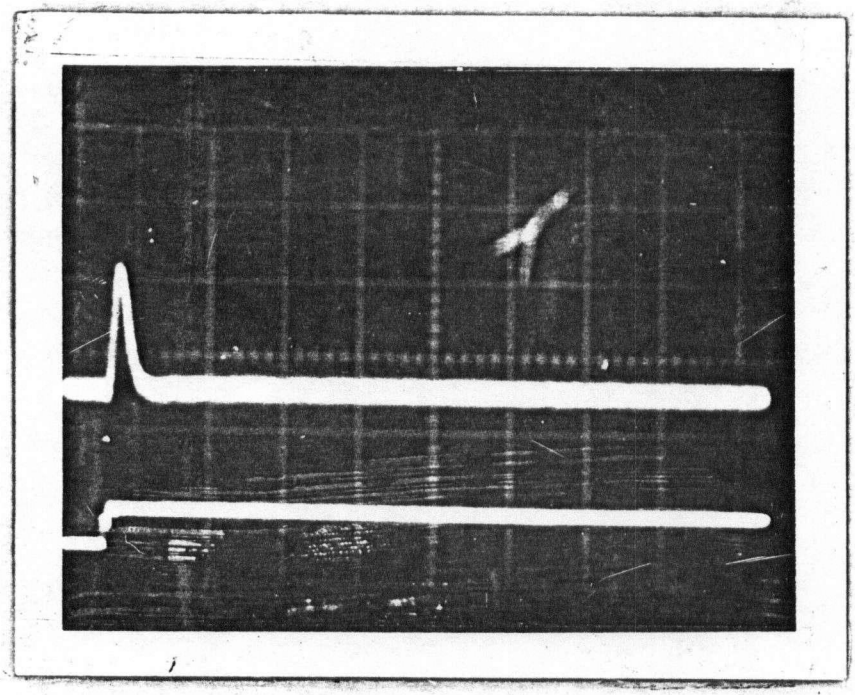

R137S1J1Pb
JUNCTION BIAS VOLT. = OV

HORI. = 0.5μs/Div
VERT. = 100mV/Div
BOTH TRACES, BOTH PICTURES

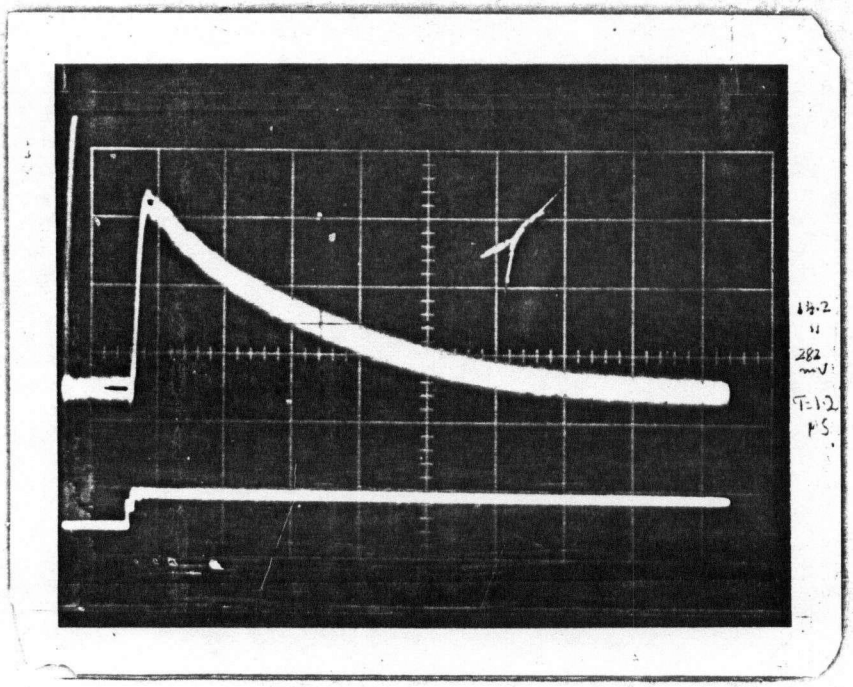

R136S1J1Pb
JUNCTION BIAS VOLT. = 0.7 m
at max. R_{DYN} POINT.

FIG. 5.17 VARIATION OF DECAY TIME-CONSTANT OF VOLTAGE-RESPONSE TO CALIBRATION CHARGE WITH JUNCTION BIAS VOLTAGE.

Having found C_J, V_{So} is known from eqn. (5.1), thus knowing the output voltage from the preamplifier, the voltage-gain can be calculated. The variation of the decay time constant with bias-voltage is clearly shown in Fig. (5.17).

For R136S1J4Pb, a lead-junction used in the above described measurement procedure, the R_{dyn} maximum bias point was located by adjusting the bias-voltage for maximum time-constant. The time-constant τ measured from the output waveform was 1.2 μs, R_{dyn} maximum was found to be 935Ω and $C_{IN} \simeq$ 10pF, thus using eqn. (5.2) C_J was found to be 1270pF. This junction had a R_N of 11Ω, corresponding to a barrier oxide thickness of $\sim$ 12Å (ref. 5.12). For a junction with $R_N \simeq 0.5\Omega$, more suitable for S.P.D. use, the corresponding barrier thickness is $\sim$10Å, and thus the junction capacitance has a value of 1520pF, (since the junction capacitance is inversely proportional to oxide barrier thickness). The C_J values for the junctions used in the α-particle induced pulse measurements were estimated in this manner. Following the above described procedure the preamplifier voltage gain was found to be 25.8 at 1.2 K as compared to 25.0 at room temperature. The equivalent Rms noise input voltage was found to be 9.9 μV as compared with 11.3 μV at room temperature. The preamplifier equivalent input noise was too-high for observation of α-induced signal-pulses with direct coupling of the junction to the preamplifier input. Since the preamplifier input impedance is high compared with the junction impedance, consisting at the frequencies of interest, <1 MHz, of approximately 5pF, and stray capacitances of another 5pF, a step-up pulse-transformer could be used to improve the voltage gain of the input amplifier and reduce the equivalent input noise voltage. For example a step-up ratio of 15:1 could

reduce the equivalent input noise voltage to 0.66 μV, (the transformer itself was not expected to contribute significant noise). The advantage of the present low-temperature preamplifier over the room temperature amplifier is intrinsically the relatively higher input impedance of the low-temperature preamplifier, and the possibility of placing it close to the superconductive particle detector and the step-up transformer. The high impedance input of the preamplifier enables the use of the step-up transformer, and the high impedance of the secondary of the step-up transformer necessitates short leads to the preamplifier. The preamplifier can then drive a 50Ω coaxial line feeding the room temperature amplifier system with an amplified signal, cutting down the effect of interference pickup. It might be suggested that the superconductive particle detector a low impedance device, would drive a transmission-line which then would feed the step-up transformer/preamplifier combination at room temperature which would give an equivalent input noise of only 0.75 μV Rms, but this configuration would have the disadvantage of the long transmission line carrying an unamplified-signal and subjected to interference pickup, and the thermal-noise contribution of the transmission line.

MEASUREMENTS WITH LIQUID HELIUM TEMPERATURE AMPLIFIER WITH INPUT VOLTAGE STEP-UP PULSE-TRANSFORMER

Voltage step-up pulse-transformer fabrication and tests

Commonly available commercial pulse-transformers were either ferrite core or tape wound core types. The ferrite core type could not be used because the ferrite material loses permeability at low temperatures. The

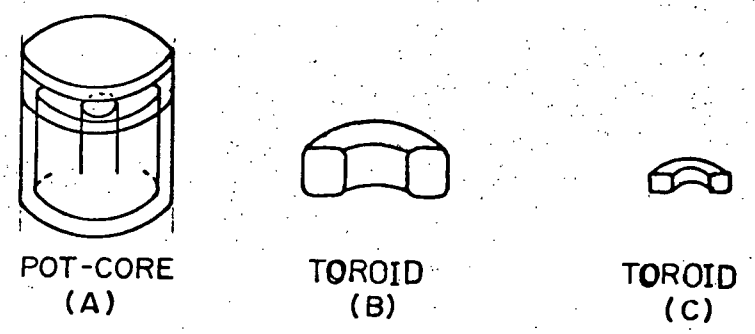

FIG. 5.18 DUST-IRON PULSE-TRANSFORMER CORE CONFIGURATIONS 1.4 TIMES ACTUAL SIZE.

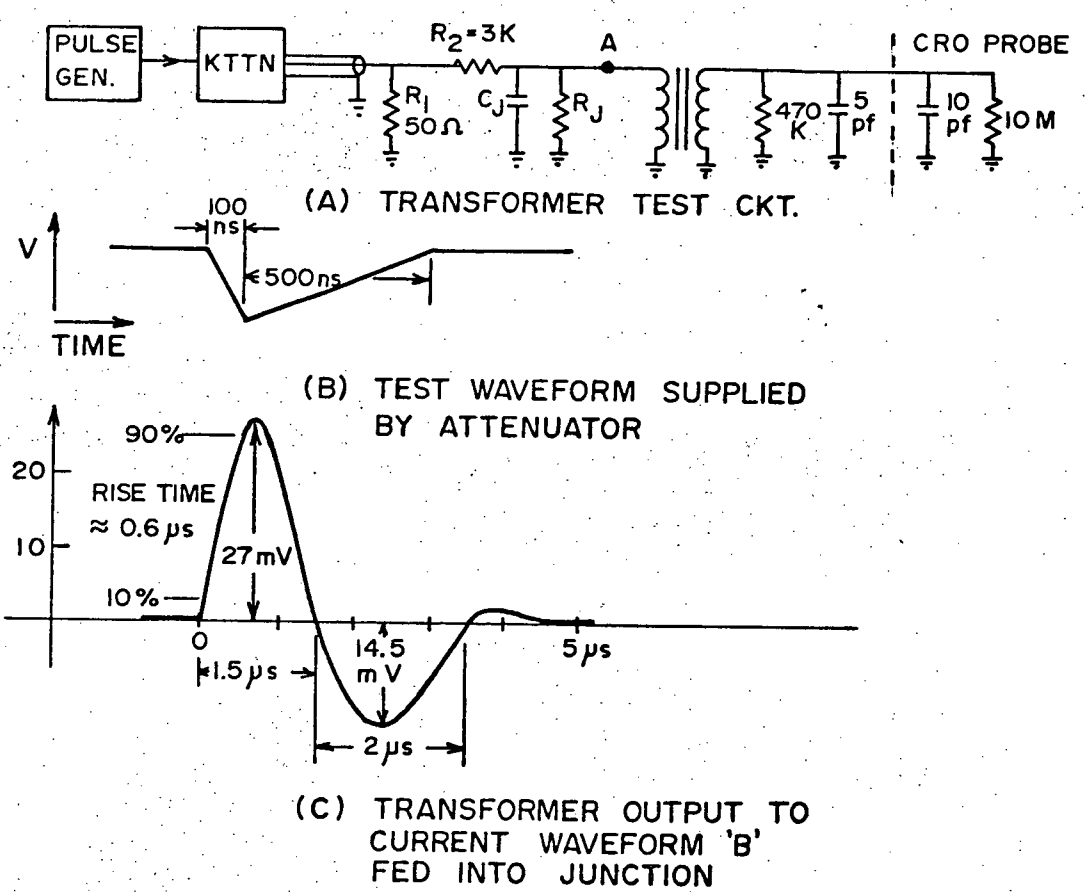

FIG. 5.19 . PULSE-TRANSFORMER TESTS CIRCUIT AND WAVEFORMS.

tape wound core type could not be used for the frequencies of interest because of eddy-current losses. 'Dust-iron' cores are satisfactory because of good permeability even at liquid helium temperatures and low losses, but dust-iron cores are now nearly obsolete, not available commercially on short notice. Three dust-iron cores were obtained non-commercially. Fig. (5.18A) shows a 'pot-core' machined from a TV I.F. tuning component. Fig. (5.18B) shows a dust-iron toroid machined from a tuning-slug. Fig. (5.18C) shows a miniature toroid obtained from Farinon-Electric of Santa Clara, California,privately. Because of the desirable small size of 'C' eight attempts were made to wind approximately 10^3 turns secondary and 10^2 turns primary for the required impedance levels without success, each time the secondary was found to be open circuited, probably because of the accumulated strain on the fine wire used for the windings. 'A' and 'B' cores were wound successfully, and on measurements 'A' performed better and was chosen despite the larger size. The pulse-transformer was wound such that for the expected waveforms of the α-particle induced pulses the primary had an input impedance of approximately 100Ω to match the desired R_{dyn} value of a junction, and the secondary was wound with as many turns as physically practical, about 1500 times.

The impedance of the primary for the waveforms of the expected signals (Fig. 5.19B), was measured using the circuit of Fig. (5.19A). Knowing the input-voltage at (A) and the voltage at the dummy-junction load at (B), with and without the transformer, the primary impedance ≃ 97Ω, (assuming the primary z is real), close to the planned 100Ω. The value was determined by measuring the amplitude of the voltage pulse at point (A) (Fig. 5.9A) with, and without the connection to the primary of the transformer.

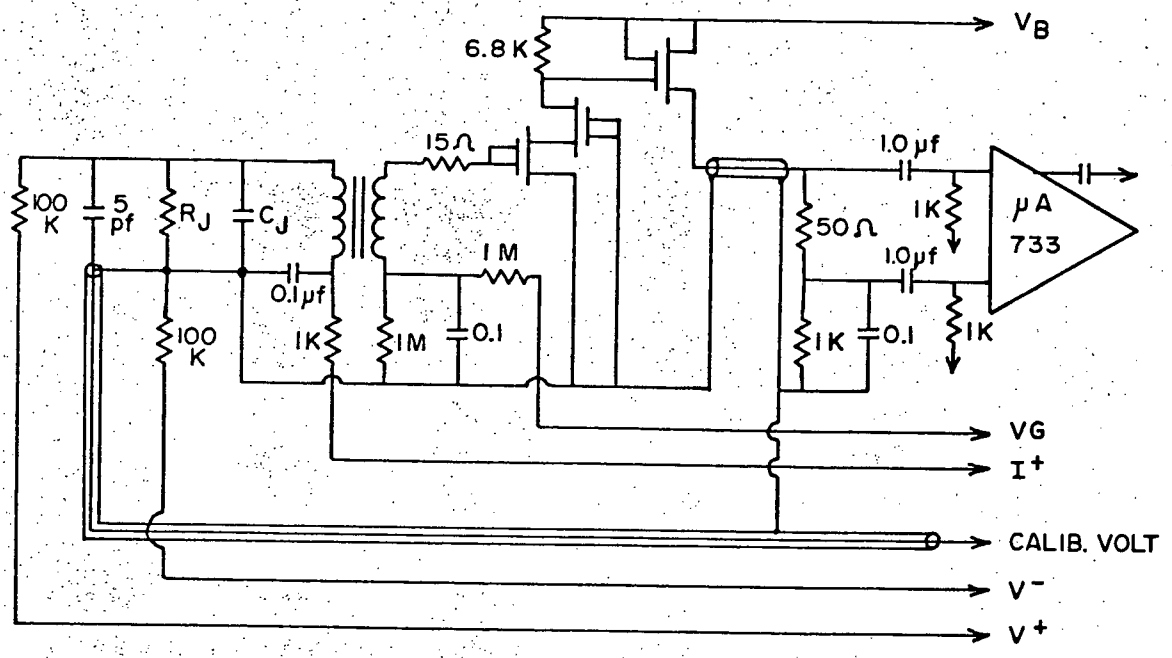

FIG. 5.20 TRANSFORMER INPUT LOW-TEMP. PREAMP. CONNECTED TO JUNCTION and 'POST'-AMPLIFIER.

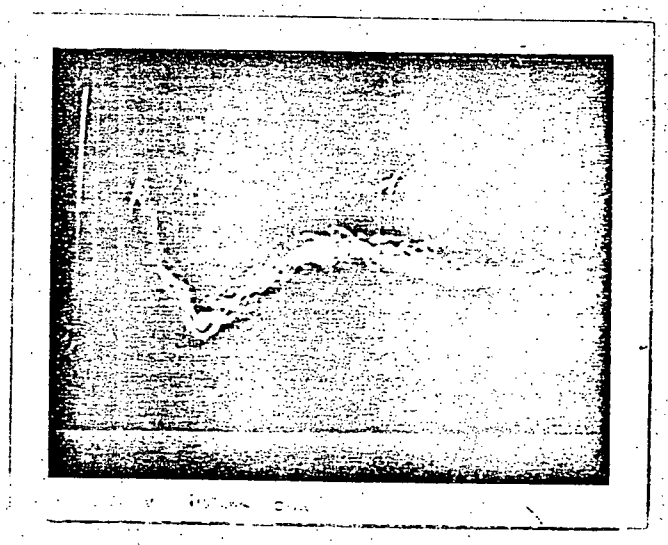

R148S2J2Pb at 1.43°K,
Mag. Bias = 28 Gauss
Horizontal = 0.5μs/div
Vertical = 0.2μs/div
Ortec Coarse Gain x 3
" Fine Gain x 1
" V.G. = x 152
Post Amp Gain = x 35.2

FIG. 5.21 α-PARTICLE INDUCED PULSES FROM Pb JUNCTION R148S2J2, USING THE TRANSFORMER INPUT LOW. TEMP. AMPLIFIER.

Knowing R_1, R_2 and R_J this allowed the calculation of the impedance at the input of the transformer. With the input current-waveform of Fig. (5.19B), the waveform Fig. (5.19C) was observed at the secondary, with a rise-time of 0.6 μsec. Note that the output-pulse is much slower than the input pulse, and the ratio of input pulse-amplitude to the output pulse-amplitude is 1:8.2, and the ratio of input peak to peak and output peak to peak voltage ratio is 1:12.6, smaller than the turns ratio of 1:15. The pulse-transformer acts as an 'integrator' for pulses shorter than 0.6μs, thus although the output-pulse amplitude is lower than indicated by the turns ratio for short input pulses, the duration of the output-pulse is longer. In response to a current-step input, the input voltage pulse-amplitude:output pulse-amplitude was 1:14.9, close to the expected value of 1:15. During the tests on the transformer it was found that the secondary lead corresponding to the outside windings must be used as the hot-lead otherwise the response rise-time is much longer and the amplitude less.. This effect resulted from the capacitive coupling between the primary and the secondary inner winding layers, the primary windings providing a low-impedance path to ground, thus effectively increasing the winding stray capacitance of the secondary. The transformer was then wrapped in lead-foil providing a superconducting transformer shield.

Pulse-transformer input low-temperature preamplifier room temperature tests

The low temperature preamplifier and STJ biasing circuit was modified to include the pulse transformer, to the configuration shown in Fig. (5.20). A dummy-junction was used in place of the STJ for room temperature tests. It was found that for Vpp output: $\sqrt{V^2}_{\text{Noise out}}$ of 1:1 the input voltage

required at the transformer input was ∿ 0.5 μV. For a voltage-step applied to the calibration lead, a 10 mV step resulted in Vpp out: $\sqrt{V^2}_{\text{Noise out}}$ of 1:1. Since the calibration capacitor was now 5pf, the corresponding calibration signal charge was 0.05 picocoulomb for a SNR of 1.

Measurements of Pb junctions with the transformer input low temperature amplifier

A large effort was made to obtain a reproducible process for Pb STJ's, because of the promise of junctions stable at room temperature and immune to thermal cycling(ref. 5.13). However the Pb junctions fabricated in this laboratory degraded at room temperature. Pb junctions were required also to check the present theory for the STJ's for high $\beta\Delta$ values. Sn (junctions) at 1.2 K corresponded to $\beta\Delta \simeq 5.4$, while Pb at 1.2 K corresponded to $\beta\Delta = 12.3$, thus Pb junction measurements provided the data for STJ's at $\beta\Delta$ between 5.4 to 12.3. The Pb junction R148S2J2 was used for the following measurements. On cooling to liquid helium temperature the amplifier system was calibrated. A 20 mV voltage step was applied to the calibration capacitor, resulting in a test charge of 0.1 picocoulombs in C_J. This charge gave an output signal peak to peak voltage of 80 mV. The observed noise voltage at the output was 25 mV Rms. Thus a signal charge of 0.03 pc would be observable, using $Vpp/V_{\text{Noise Rms}} = 1$ as the observability criterion. Here we have switched to describing the signal by "signal-charge" instead of "signal-voltage". "Charge" is a more significant parameter in view of the "ballistic" or integrating nature of the step up pulse transformer in the input circuit of the low-temperature preamplifier for signal pulse durations much smaller than the

DISC. SETTING	COUNT	DURATION	COUNT/MIN.	COUNTS PER DISC. SET. INTERV.
010	19015	1 min.	19015 →	17649
012	1366	"	1366 →	1103
014	263	"	263 →	100
016	163	"	163 →	62
018	101	"	101 →	69.5
020	63	2 min.	31.5 →	17.5
022	28	"	14.0	

TABLE 5.2 RECORD FROM DISCRIMINATOR COUNTER MEASUREMENTS OF R148S2J2 AT 1.2°K.

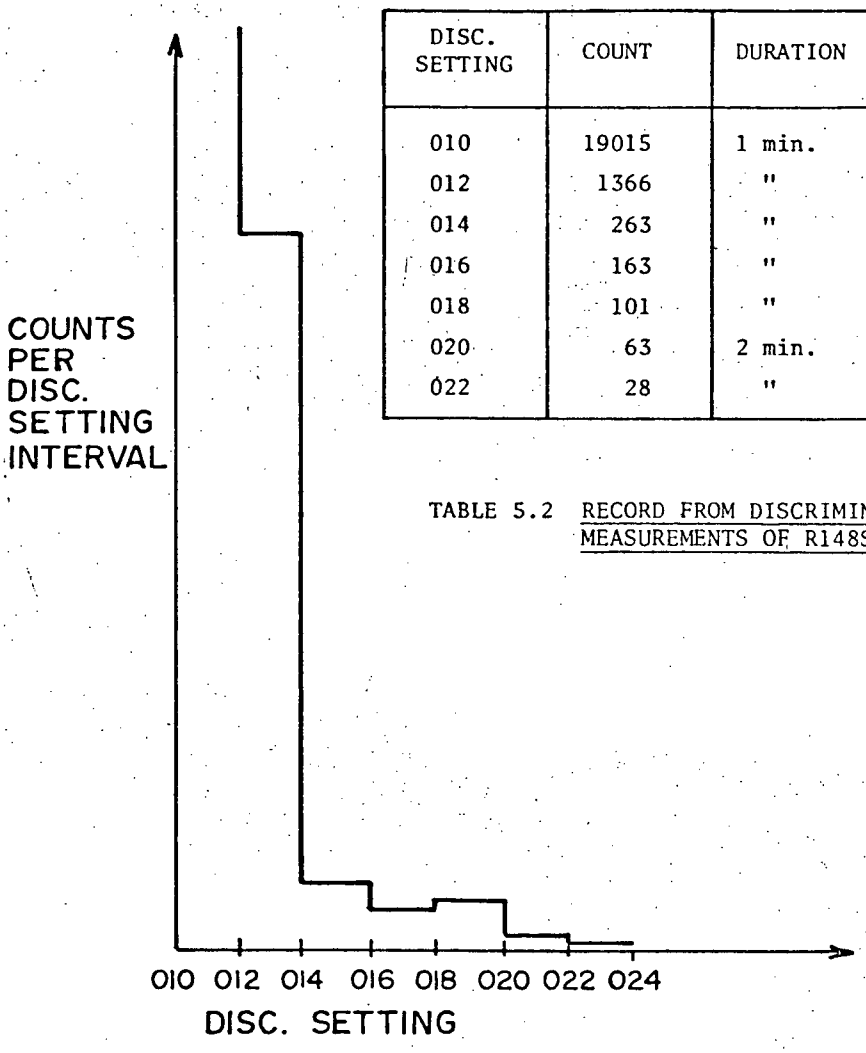

FIG. 5.22 PULSE-AMPLITUDE DISTRIBUTION USING DISCRIMINATOR-COUNT. FOR Pb JUNCTION R148S2J2.

resonant period of the transformer output circuit.

Discriminator-counter readings α-particle induced pulses were clearly observed with the Pb junction R148S2J2, of the expected waveform and with good signal to noise ratio, as shown in the C.R.O. record Fig. (5.21). No kicksorter was available at the time of the experiment but the discriminator-counter was used to obtain the data shown in table (5.2) and the histogram in Fig. (5.22). At discriminator setting 020 a sharp drop off in count-rate occurs, preceded by a slight rise at setting 018. This agrees with the theoretical prediction of a slight rise followed by a sharp cut off at the high energy end (C.F. Fig. 3.15, 3.16). If a 'line' was present it could lie between 018 and 020 and be of low amplitude, since in the histogram Fig. 5.22 at that point such a line could conceivably be obscured by the low resolution.

Effect of temperature variation on signals we wished to make measurements at temperatures in the range 1.2 K to 4.2 K. At 4.2 K the helium gas in the liquid-helium cryostat was at atmospheric pressure. Assuming the helium gas was also at 4.2 K, then the range of the 5.13 MeV α-particle was only 0.3 cm. Since the spacing between the source and the detector was 0.5 cm, the particle would be stopped before reaching the detector. To try to obtain higher junction temperatures while maintaining low helium gas pressure in the cryostat, measurements were made by raising the cold-finger of the sample holder above the liquid helium surface, and monitoring the junction temperature by the junction-current at a voltage bias-point having been previously measured at different temperatures. This scheme

Temp.	$\beta\Delta$	Pulse Ampl.	Sig. Charge Q	Therm. Cond.	Normalized Sig. Charge Q*	Q* Corrected for α-Attn.
1.19°K	12.38	540 mV	.675 pc	0.34 x $10^{-1}_{w/mk}$	0.675 pc	0.675 pc
1.34°K	11.00	660 mV	.825 pc	0.39 "	0.946 pc	0.946 pc
1.45°K	10.17	560 mV	.825 pc	0.41 "	0.994 pc	0.990 pc
1.93°K	7.64	520 mV	.650 pc	0.55 "	1.051 pc	1.077 pc
2.16°K	6.82	470 mV	.588 pc	0.60 "	1.037 pc	1.092 pc

Table 5.3. Temperature Dependence of α-Particle Induced Pulses in Pb Junction R148S2J2.

was found to be impractical because the temperature changed too rapidly. The output pulse amplitude was therefore measured at five different temperatures up to 2.16 K ($\beta\Delta$ = 6.82) where the helium vapour pressure was 36 torr, and did not significantly attenuate the α-particle energy ($\Delta E/E \sim .047$) and the results are listed in table (5.3). The pulse amplitude initially increased with increasing temperature, even though the increased temperature decreased the R_{dyn}; this was due to the increase of $(\frac{\partial I}{\partial T})_V$ with temperature. With further increase in temperature R_{dyn} decreased further and the impedance becomes smaller than the junction-capacitance impedance ($X_c \approx 106\Omega$ at 10^6Hz) and leakage resistance in parallel, if any, and because significant in the reduction of signal amplitude, overcoming the increase in $(\frac{\partial I}{\partial T})_V$ with increased temperature. Further, the increase in temperature increased the specific heat of the glass substrate, thus the same heat-pulse resulted in a smaller temperature rise with increased substrate temperature, consequently a smaller signal current amplitude. The signal-charge depended on the duration and the current-amplitude. Since the duration was inversely proportional to the diffusivity $(\frac{K}{\rho Cp})$, the signal-charge was inversely proportional to $Cp.(\frac{K}{\rho Cp}) = K/\rho$. Since the density ρ is nearly constant over the temperature range of interest, the signal-charge varies as K, the thermoconductivity. Thus by multiplying the observed signal-charge at temperature T by $(K_T/K_{1.2\ K})$, (where K_T, $K_{1.2\ K}$ are respectively the thermoconductivities of the glass substrate at temperature T, and 1.2 K) we get a 'normalized' signal-charge Q_T^*. Q_T^* is the signal-charge from a superconductive-tunnelling junction at temperature T subjected to the same small temperature excursion as that at 1.2 K due to a 5.13 MeV

α-particle impact. Thus the Q_T^*'s indicate the S.T.J. characteristics independent of substrate properties. The above discussion is valid qualitatively only because of the assumption of a small and uniform excursion of temperature in the S.T.J. whereas for an α-particle impact the temperature excursion is localized near the α-impact site and not small (i.e. thermal properties change values significantly during the temperature pulse) correcting further for α-particle energy attenuation of ~ 0.047 for the 2.16 K (36 Torr) and ~ 0.025 for the 1.93 K (19 Torr) cases, the largest signal-charge Q_T^* occurs at $\beta\Delta = 6.8$. Referring to Fig. 2.6, Chapter 2 the voltage-response sensitivity to temperature change of a S.T.J. curve $(\frac{\partial V}{\partial T}|_{\omega=10^6}$ Vs $\beta\Delta)$, has a maximum at $\beta\Delta = 5.8$, thus despite the qualitative nature of the above discussion the theoretical and experimental values of peak $\beta\Delta$ are close. The above discussion attempts to explain the physical nature of the change of signal-charge amplitude with temperature. The exact treatment requires numerical solution of a non-linear problem which is of little help in understanding the physics, and was not done.

The S.N.R. for Pb junction R148S2J2 From Fig. (5.21) we can see that the peak to peak noise voltage at the output is approximately 80 mV, V_N Rms = 32 mV (for gaussian noise). The maximum signal-amplitude peak to peak is approximately 660 mV, thus $Vpp/\sqrt{V^2_N} = 20.6$. Sn junctions are expected to give better signal to noise ratios as explained in the theory chapter.

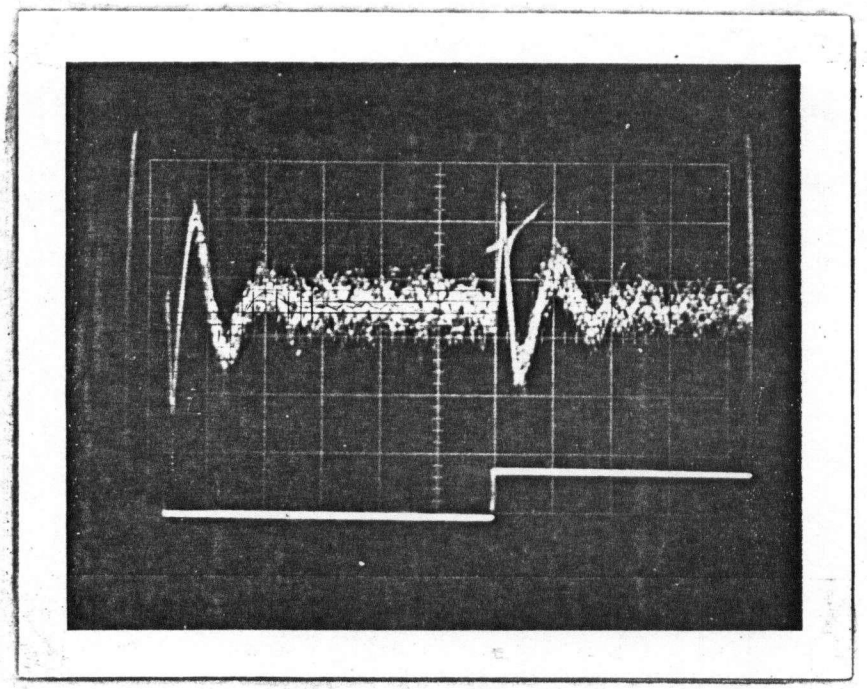

R164S1J5Sn
at 1.2°K, V_{Bias} = 0.3 mV

HORI. = 5μs/Div
VERT. = 200 mV/div top
= 50 mV/div bottom

Ortec Coarse Gain x 3
" Fine Gain x 2
(Ortec V:G. = 304)
'Post-Amp' Gain = 35.2

FIG. 5.23 AMPLIFIER SYS./JUNCTION COMBINATION CALIBRATION CURVE

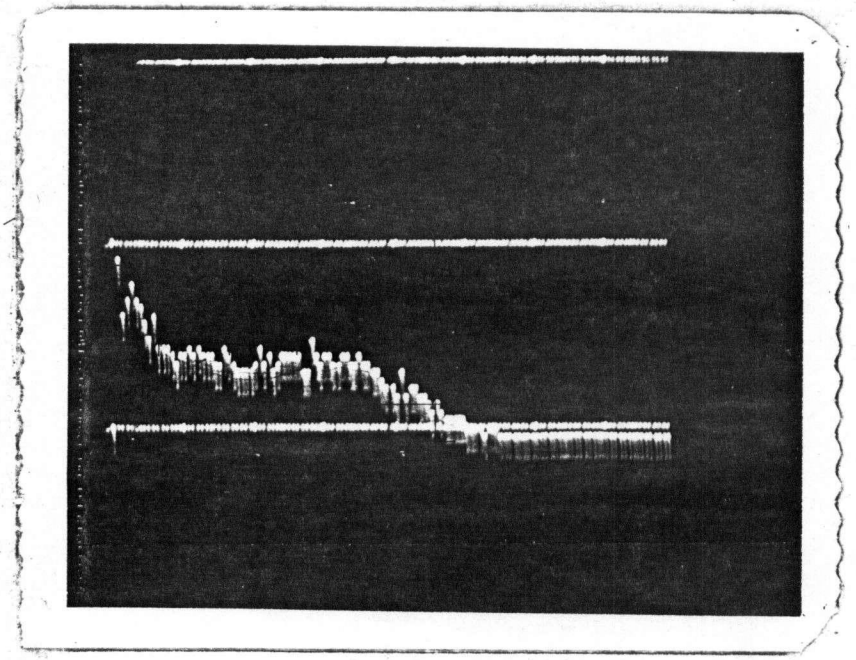

R164S1J5Sn
at 1.2 °K, V_{Bias} = 0.3 mV.

FIG. 5.25 KICKSORTER RECORD OF PULSE-AMPLITUDE DISTRIBUTION FROM Sn JUNCTION R164S1J5 (MADE WITH LOW-TEMPERATURE TRANSFORMER INPUT PREAMPLIFIER).

MEASUREMENTS ON Sn JUNCTIONS USING THE TRANSFORMER INPUT LOW-TEMPERATURE PREAMPLIFIER

Sn STJ's are expected by theory to give better signal-amplitude because the optimum STJ response to a temperature is at a lower temperature (than Pb), where the thermal conductance and specific-heat of the substrate is lower. The inherent SNR is also expected to be better for the Sn STJ, because of the $\sqrt{\Delta}$ dependence of the Rms shot noise (cf. Eqn. 2.48, Chapter 2). For the present measurements, amplifier noise dominated so the improvement of SNR results from the increased signal amplitude for Sn junctions.

Amplifier system calibration Fig. (5.23) shows the response of the amplifier system to an approximately δ-function calibration charge of 0.2pc. (This response-curve was used in Chapter 6 to calculate the expected output waveforms from α-particle induced signal-currents in the STJ.) R164S1J5 was biased at maximum R_{dyn} for this calibration curve. The charge sensitivity for the Ortec linear amplifier setting of V.G. = 304 was 3.2 volts/picocoulomb. The peak to peak noise voltage was ∿ 200 mV at the output corresponding to V Rms of ∿ 79.9 mV, (equivalent to a noise-charge of 0.0221 pc.).

α-particle induced pulses, direct oscilloscope measurements After the junction plus amplifier system was calibrated, the α-particle source was directed towards the junctions and output-waveforms resulting from the α-particle bombardment were monitored using a Tekronix 465 portable Oscilloscope. The waveforms were monitored continuously during the

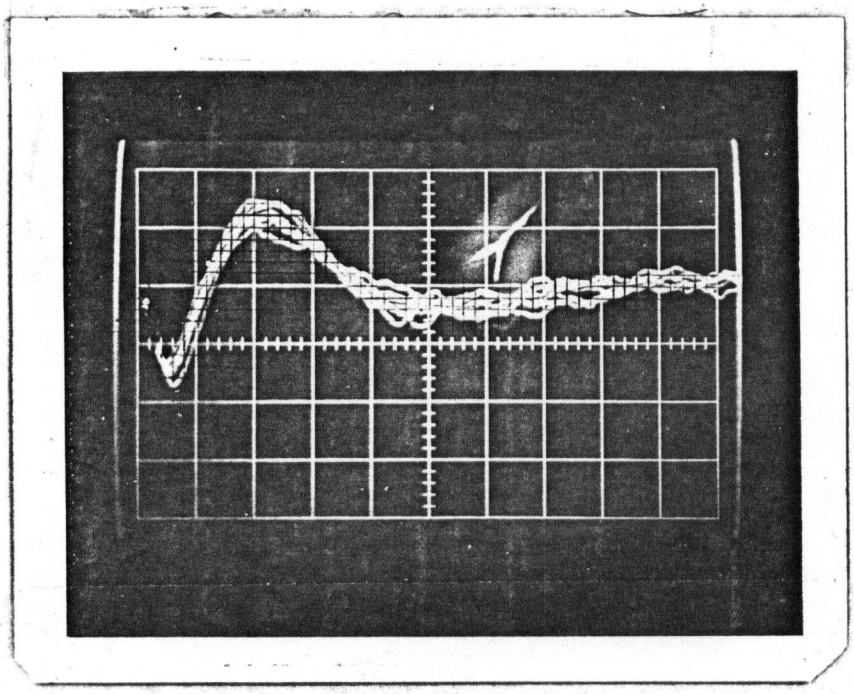

R164S1J5Sn
at 1.2°K, V_{Bias} = 0.3 mV

HORI. = 1μs/Div
VERT. = 1 V/Div

Ortec Coarse Gain x 3
" Fine Gain x 2
(Ortec V.G. = 304)
Post-Amp. V.G. = x 35.2

(A)

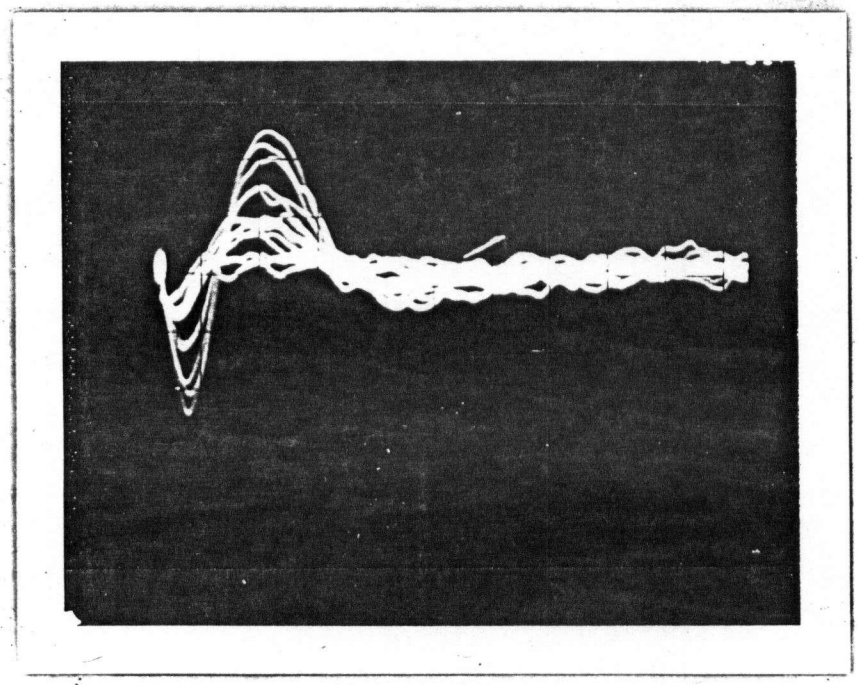

R164S1J5Sn
at 1.2 K V_{Bias} = 0.3 mV

HORI. = 1μs/Div
VERT. = 1 V/Div

Ortec Coarse Gain x 3
" Fine Gain x 3
(Ortec V.G. = x 456)
Post-Amp. V.G. = x 35.2

CRO TRIGGERING THRESHOLD SET LOW TO SHOW LOW-AMP. PULSES

(B)

FIG. 5.24 α-PARTICLE INDUCED PULSES IN Sn JUNCTION R164S1J5, USING TRANSFORME INPUT LOW-TEMP. PREAMP.

"kicksorter" (pulse amplitude distribution analyser) accumulation runs as a precautionary measure against unforseen noise sources (if any) and equipment failure. Two of the α-particle induced output oscilloscope records are shown in Fig. (5.24A, 5.24B). 'A' shows the output signal before the kicksorter run Acc. 9 and 'B' shows the output-signal from the same junction before kicksorter run Acc. 20, with the oscilloscope triggering threshold set low to show lower-amplitude pulses. The maximum signal-output peak to peak voltage for 'A' was 3.2 volts for the same amplifier setting as the calibration curve. This signal output corresponded to a signal charge of 1.0 picocoulomb. The maximum peak to peak signal-output voltage for 'B' was 4.85 volts at amplifier voltage gain = 456, this corresponded to a Vpp of 3.2 at the settings for 'A' (voltage gain = 304). Thus the maximum α-particle induced signal charge is also 1 pC for 'B'. Note the good signal to noise ratio in 'A' and 'B' C.R.O. records and the wide range of signal amplitudes visible in 'B'.

The signal to noise ratio $Vpp/\sqrt{V^2_N}$ is 40.0 for R164S1J5SN compared to 20.6 for Pb junction R148S2J2 pc. The Pb junction had R_N = 0.12Ω, R_{dyn} > 1.75K at 1.2 K, compared to the Sn normal junction tunnelling resistance R_N of 0.30Ω and R_{dyn} = 72.5Ω, clearly verifying the theoretical predictions, as the Sn junction was definitely better even with a smaller junction normal conductance ($G = {}^{1}/R_N$).

Kicksorter measurements The signal to noise ratio of this junction-amplifier combination was sufficiently high that the kicksorter output would definitely show a 'line' or peak if the pulse amplitude distribution had such a peak. 20 kicksorter records were made Acc 1 to Acc 20

(Acc = Accumulation). Acc 1 to Acc 3 showed a false peak due to 'clipping' resulting from inadvertent biasing of the junction close to a current-step in the I.V. characteristics the origin of this effect will be described in detail in Appendix 5.1. Acc 7, 8 were records of runs made with junction R164S1J1. The remaining fifteen records were of kicksorter runs with R164S1J5. The large number of runs were made to be sure that no peak was missed. A good representative record was Acc 16 shown in Fig. (5.25). No peak was visible, the record was of the form predicted by the present theory. To further ensure that noise did not smear out any 'peaks' the record Acc 6 was made, and then with identical setting and accumulation time record Acc 6 was made with the particle source shuttered. Acc 6 recorded no pulses in any of the channels displayed, i.e. all the pulses accumulated in Acc 6 were signal pulses.

Summary of Measurements Chapter

- α-particle induced pulses were definitely observed verifying GHW's results.
- temperature dependence of pulse-amplitudes in Pb and Sn junctions were measured, the results agree with theory.
- the S.T.J. capacitance was measured directly and voltage gain of the low temperature preamplifier simultaneously measured.
- a low-temperature preamplifier was developed to improve the SNR.
- junction/amplifier combined response to charge deposited in the junction was measured, (this was required for theoretical derivation of the output waveform for comparison with the experimentally measured waveform).

CHAPTER SIX

Reduction of Experimental Results and Comparison with Theory

Introduction

This chapter is organised into three parts. The first part compares the theoretical expressions for I_{SS}/G and $1/R_{dyn}/G$ as functions of $\beta\Delta$ at constant voltage bias (derived in Chapter 2) with experimental data, to establish the validity of these expressions and other expressions and conclusions derived from these. The theoretical junction voltage response for a high frequency temperature change as a function of $\beta\Delta$ is qualitatively compared with the experimental data (from Chapter 5).

The second part of this chapter uses the junction current $I_S(t)$ calculated in Chapter 3, as a basis to calculate the expected signal voltage output from the room temperature amplifier system and the low temperature amplifier system (with transformer input) for comparison with the respective experimental waveforms.

The third part of this chapter compares the theoretical peak signal current and total signal charge amplitude distribution curves (derived in Chapter 3) with the experimental signal output amplitude distribution curves from Chapter 5.

Junction quasiparticle tunnelling current dependence on temperature at constant bias voltage.

From eqn. (2.15) of Chapter 2 we get for bias voltage $V = \Delta/e$:-

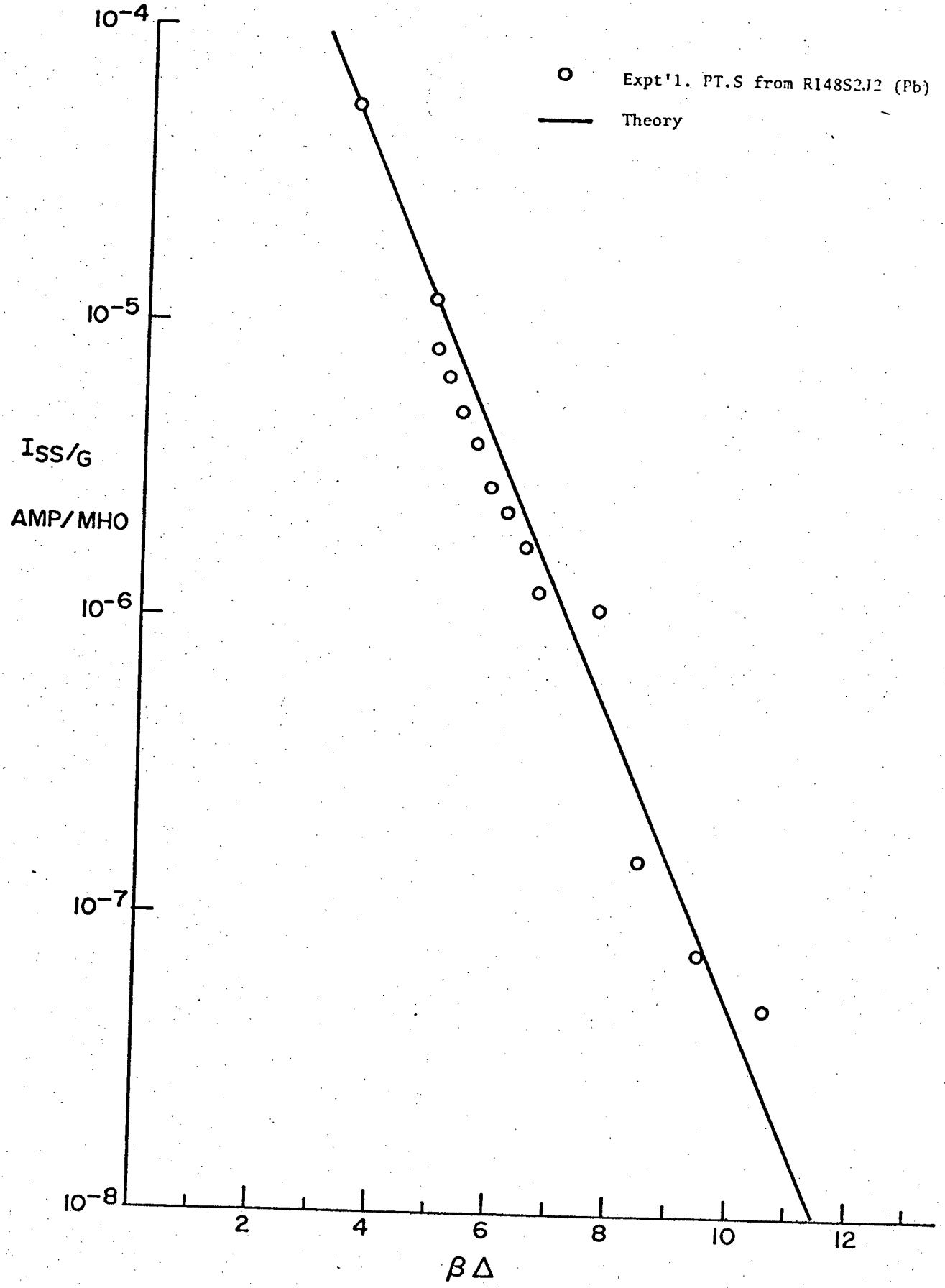

FIG. (6.1) I_{SS}/G as a function of $\beta\Delta$.

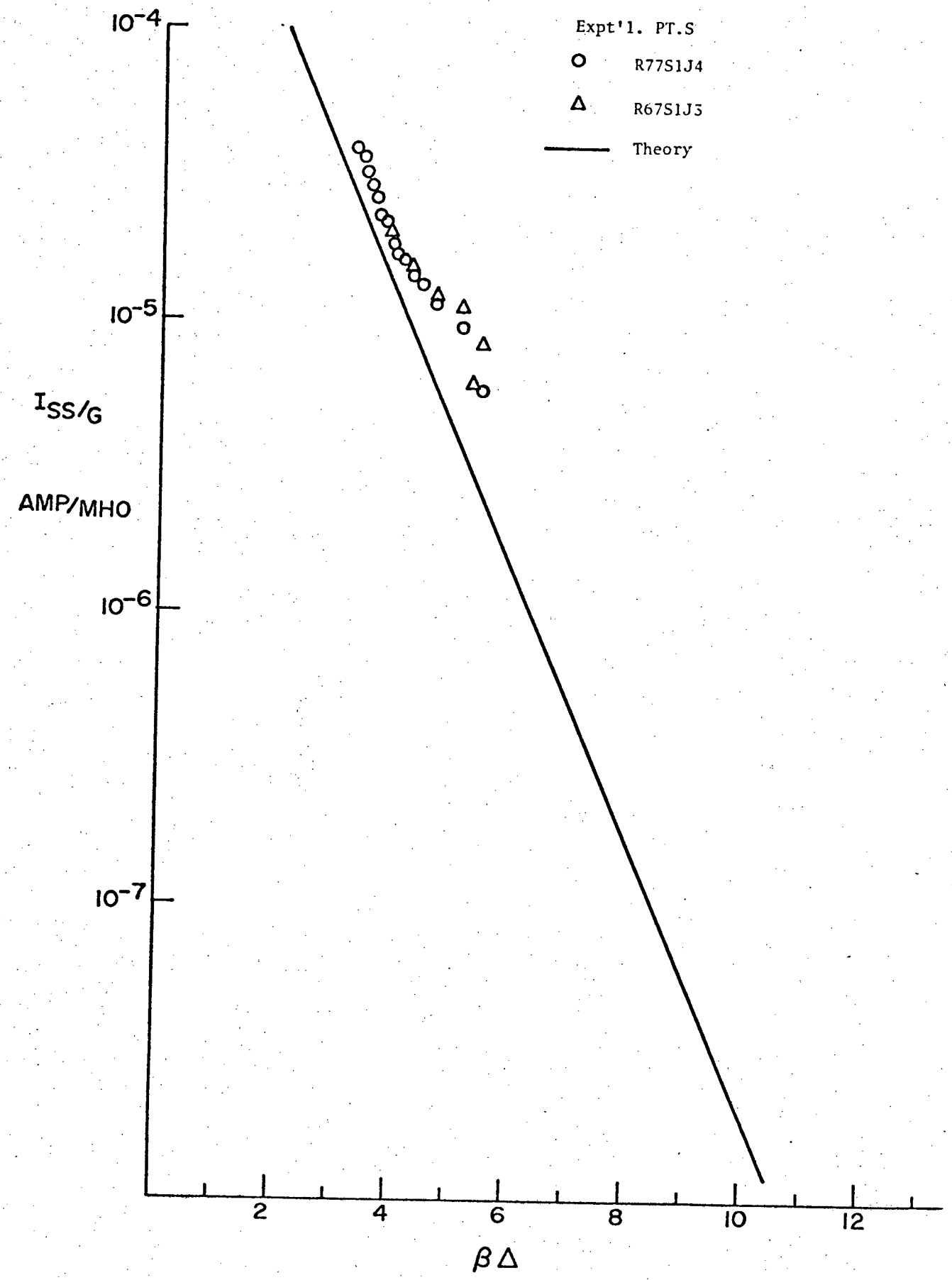

FIG. (6.2) I_{SS}/G as a function of $\beta\Delta$.

$$I_{SS}/G = \frac{2\Delta}{e} K_1(\beta\Delta) [1-e^{-\beta\Delta}] \quad (6.1)$$

where as explained in Chapter 2, we approximate Δ by $\Delta \approx \Delta(o)$ for $\beta\Delta > 3.5$. The equation is shown in graphical form in Fig. (6.1) for lead, and Fig. (6.2) for tin junctions. The experimental values of I_{SS}/G as a function of $\beta\Delta$ obtained from one lead S.T.J. and two tin S.T.J.s are plotted in Fig. (6.1) and Fig. (6.2) respectively, using constant energy gap values of 1.12 mV and 2.54 mV for tin and lead respectively to calculate the $\beta\Delta$ values of the experimental points. Referring to Fig. (6.1) the experimental points fall close to the theoretical curve. Theoretically the experimental points are expected to fall slightly above the curve, due to the approximations leading to eqn. (2.15) (C.f. Chapter 2). This deviation may be accounted for if we assume that Δ for the lead junction films is slightly larger than the value used ($\sim$ 17% larger). Referring to Fig. (6.2) we see that the experimental points for tin S.T.J.s fall close to but above the theoretical curve, as required by theory for $\beta\Delta < 4.5$. For $\beta\Delta > 4.5$ the deviation increases, probably due to the increasing significance of leakage currents with increasing $\beta\Delta$. Thus it appears that the lead S.T.J. we used for Fig. (6.1) data is a better (lower leakage) junction than the tin S.T.J.s we used for Fig. (6.2) data. From the above discussion we can conclude that (6.1) is justified experimentally to the degree of accuracy required for the theoretical discussions in Chapter 2.

The $\frac{\partial I_{SS}}{\partial T}/G$ Vs. $\beta\Delta$ curve was plotted in Fig. (2.7) Chapter 2. Since the $\frac{\partial I}{\partial T}/G$ expression was derived from eqn. (2.15) by partial differentiation, the verification of the I_{SS} expression also justifies the expression for

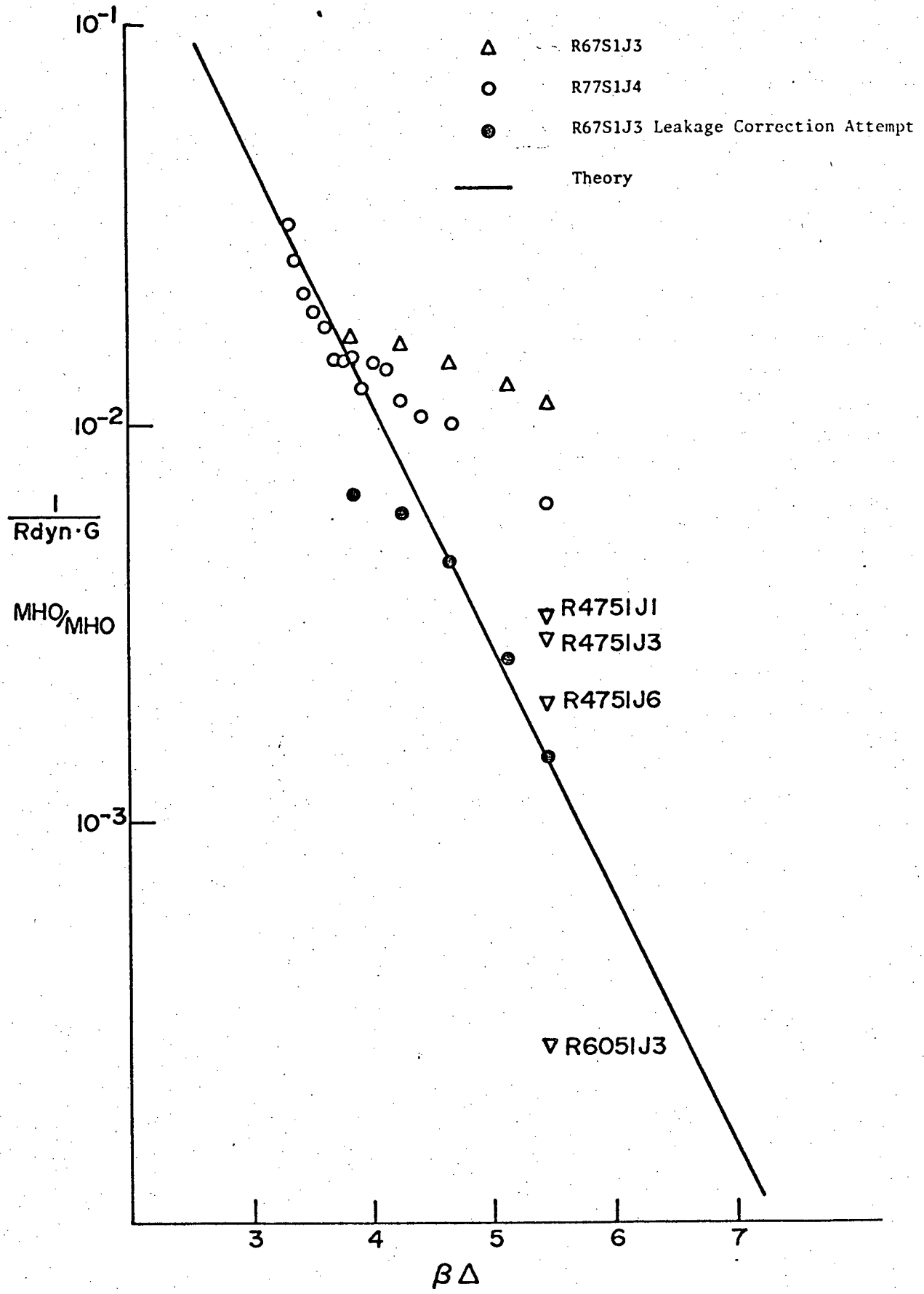

FIG. (6.3) Variation of $1/R_{dyn}.G$ with $\beta\Delta$

$(\partial I_{SS}/\partial T)/G$ at constant bias voltage.

Variation of R_{dyn} with temperature at constant bias voltage.

From the I.V. characteristic for junction R67S1J3 shown on Fig. (5.9) we see that the dynamic resistance R_{dyn} of the junction does decrease with increased temperature (decreased $\beta\Delta$) as required by the following theoretical expression derived from eqn. (2.5) of Chapter 2:

$$1/(R_{dyn}.G) = 2\beta\Delta K_1(\beta\Delta)e^{-\beta eV} \qquad (6.3)$$

The maximum R_{dyn} for experimental Sn junctions occurred at junction bias voltage of 0.3 mV, corresponding to $eV = 0.536\Delta$ instead of $eV = \Delta$ because it was found experimentally that multiparticle tunnelling effects caused a 'bump' in the I.V curve at $eV = \Delta$ thus lowering the R_{dyn} around this point. Thus the eqn. (6.3) becomes for Sn junctions at this bias value:

$$1/(R_{dyn}.G) = 2\beta\Delta K_1(\beta\Delta)e^{-0.536\Delta\beta} \qquad (6.4)$$

This equation is shown graphically in Fig. (6.3). Experimental results for tin junctions R67S1J3, R77S1J4, R47S1J1,3,6 were used to calculate $1/(R_{dyn}.G)$ and plotted Vs $\beta\Delta$ in the same figure. The point corresponding to $\beta\Delta \approx 3.85$ for R67S1J3 falls close to the theoretical curve but the rest of the data points for large $\beta\Delta$ are above the theoretical curve. For R77S1J4 the data points corresponding to $\beta\Delta \sim 3.3$ to 4.0 fall closely on the theoretical curve, and for larger $\beta\Delta$, the data points are above the curve but to a lesser extent. The data points for R47S1J1, R47S1J3, R47S1J6 at $\beta\Delta \sim 5.46$ ($T \sim 1.19$ K) were progressively closer to the theoretical curve

than the corresponding points for R67S1J3, R71S1J4. The above described deviations from theory are interpreted as the presence of leakage resistance. R67S1J3 had R_N = 0.22 Ω, while R77S1J4 had R_N = 7.33 Ω. R77S1J4 having the larger junction normal tunnelling resistance probably had relatively less leakage than R67S1J3. Thus as $\beta\Delta$ increased, R_{dyn} increased and the specimen with the smaller leakage resistance exhibited a smaller deviation from the theoretical curve. Note that for smaller $\beta\Delta$ values, R_{dyn} is sufficiently small to swamp out the effects of the leakage, and the experimental points fall close to the theoretical curve. To further verify this hypothesis, data (at 1.19 K) from R47S1J1,3,6 junctions with still higher R_N than R77S1J4 were plotted. As described above these points fall closer to the theoretical curve. ($R_{N\ R47S1J6}$ = 620 Ω). On removing the effect of the leakage resistance component from the data points for R67S1J3 at β = 5.45, such that this point falls on the theoretical curve, the next two data points (for higher temperature) fall on the theoretical curve but the points corresponding to $\beta\Delta$ = 3.84 and 4.25 now fall below the curve. This indicated temperature dependence of the leakage: the leakage conductance decreases with increased temperature.

The experimental R_{dyn} value was obtained by measuring the slope of a tangent at the point of interest on the I.V. characteristic curve, thus the accuracy of the R_{dyn} value depended on the accuracy in drawing the tangent line to the curve at the indicated point, which is unlikely to be better than 10% in most cases. Within this accuracy and the approximations in the derivations of the theoretical expression the experimental data agree with the theoretical expressions for R_{dyn}.

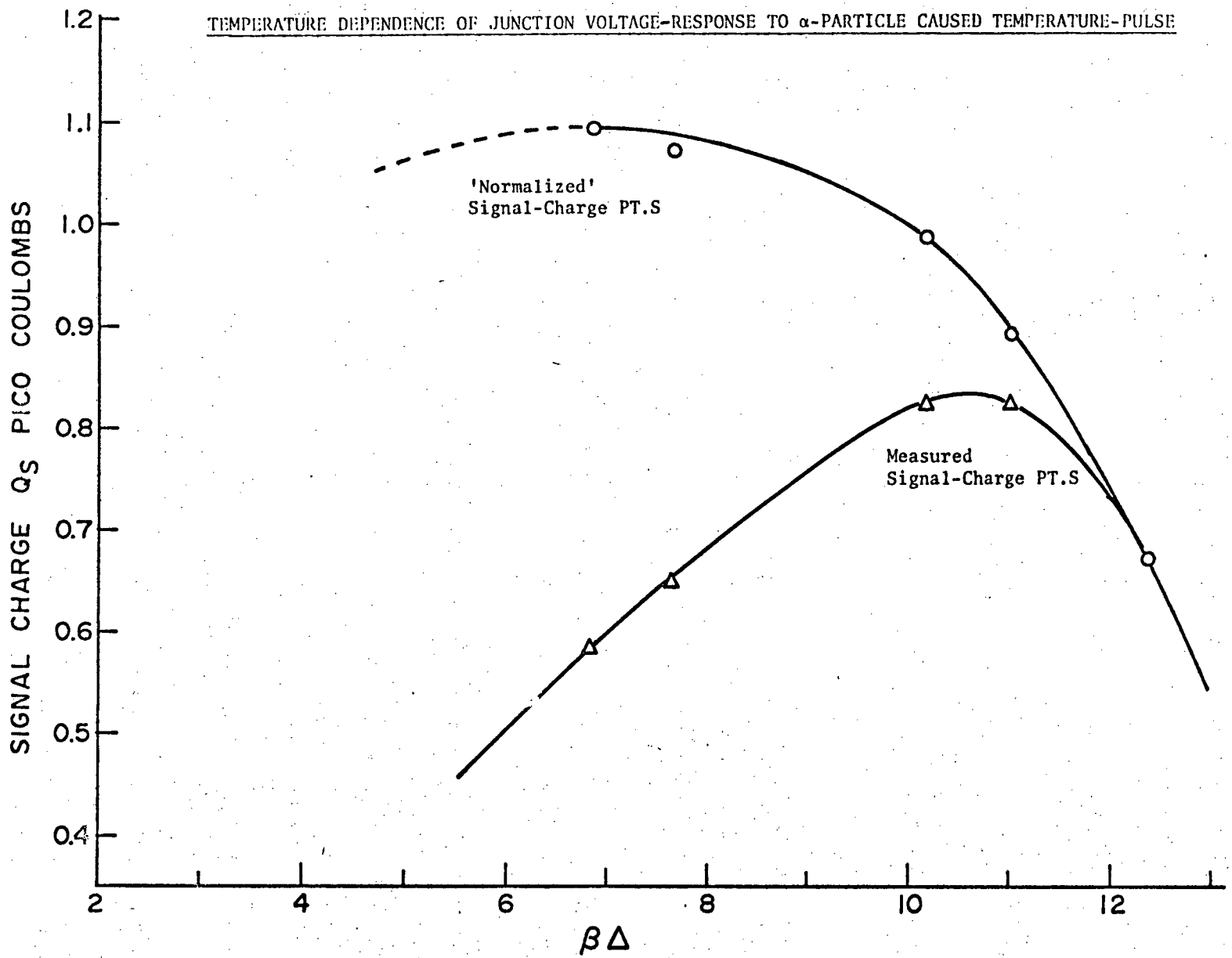
TEMPERATURE DEPENDENCE OF JUNCTION VOLTAGE-RESPONSE TO α-PARTICLE CAUSED TEMPERATURE-PULSE
SIGNAL CHARGE Q_S PICO COULOMBS
1.2
1.1
1.0
0.9
0.8
0.7
0.6
0.5
0.4
'Normalized'
Signal-Charge PT.S
Measured
Signal-Charge PT.S
2
4
6
8
10
12
$\beta\Delta$

FIG. (6.4)

Dependence upon ambient (mean junction)temperature of junction voltage response to low and high frequency temperature changes.

Since the junction voltage response for low frequency temperature changes is given by:-

$$\frac{\partial V}{\partial T} = \frac{\partial I}{\partial T} . R_{dyn} .$$

and the theoretical expressions for the two factors on the RHS were shown to be supported by experiment the theoretical expression for the low frequency voltage response:

$$\frac{\partial V}{\partial T} = \frac{K}{2e} . \beta\Delta \frac{1-3e^{-\beta\Delta}}{1+e^{-\beta\Delta}} \qquad (2.25)$$

can be considered as verified.

For the response to high frequency temperature changes we can use the experimental data on the dependence on mean junction temperature of the amplitude of α-particle induced signals for R148S2J2, shown in Table (5.3), Chapter 5. Since we are interested here in the response of the junction to a standard temperature pulse as a function of $\beta\Delta$, it is necessary to correct the measured junction signals to allow for the temperature dependence of the substrate thermal characteristics. If uncorrected, the temperature pulse produced by a given α-particle energy loss will depend on the mean temperature and thus on $\beta\Delta$. In Table (5.3) the normalized signal charge response is the calculated equivalent signal-charge value produced at a normalizing standard temperature of 1.2 K, based on a small signal (small uniform temperature change) model. This procedure therefore removes the substrate properties as a factor affecting the S.T.J. response,

leaving the S.T.J. response to a 'fixed' temperature pulse. The observed values of the normalized signal charge response does decrease with increasing $\beta\Delta$ beyond $\beta\Delta \sim 6$, confirming the expected voltage response behavior described in Chapter 2. It must be emphasized that the procedure used in Chapter 5 to get the 'normalized' signal charge was an approximation accurate only for temperature charges which are small and uniform over the junction. The actual α-particle heat spike induced temperature changes were of the order of 1 K near the impact area at the time of signal current peak ($\sim 10^2$ ns after α-particle impact) and were not uniform over the junction. Thus the above discussion is valid only qualitatively. It is possible to calculate numerically the current, voltage and charge response of a glass substrated S.T.J. to α-particle impact at different bath (and therefore average junction) temperatures as described in Chapter 3 by simply setting the bath temperature input to the computer program to different desire values and run the program, but this was not done because it was felt that the gain in understanding, if any, does not justify the large amounts of computation. Other than the above crude qualitative argument and the numerical approach, very little can be said because of the complex non-linear nature of the problem.

Effect of Junction-Capacitance on junction voltage waveform.

Fig. (2.7) shows the equivalent circuit of S.T.J. The current source $I_S(t)$ is the signal-current, that is, the thermally-generated excess junction current. R_{Load} is the twin-lead cable terminating resistance at the room temperature preamplifier input. The signal current $I_S(t)$ can be considered as a sequence of charges Q_i, deposited in the junction. A single-charge Q_i deposited in the junction causes the following voltage

across the junction:

$$V_{S_j}(t) = \frac{Q_i}{C_J} e^{-t/\tau} \qquad \text{where } \tau = C_J.(1/R_{dyn} + 1/R_{leak} + 1/R_{load})^{-1} \tag{6.5}$$

Thus by linear-superposition the junction voltage is given by:

$$V_S(t_K) = \sum_i V_{S_i}(t_K - t_i) = \sum_{N=0}^{K} \frac{Q_N}{C_J} e^{\frac{-(t_K - t_N)}{\tau}}$$

$$= \sum_{N=0}^{K} \frac{I_S(t_N)}{C_J} \delta t \, e^{\frac{-(K-N)\delta t}{\tau}} \tag{6.6}$$

where δt is the length of the discrete time interval between the arrival of successive charges. Q_N is the charge deposited at $t_N = N.\delta t.$, and $Q_N = \int_{t_{N-1}}^{t_N} I_S(t)\, dt \approx \delta t . I_S(t_N)$.

Going over to the integral gives:

$$V_S(t) = \frac{1}{C_J} \int_o^t I_S(t') \, e^{-(t-t')/\tau} dt' \tag{6.7}$$

(6.7) is derived in this manner because it gives a better physical picture and the equation (6.6) is used later in this chapter for numerical calculations of the junction signal voltage based on the signal current $I_S(t)$ calculated numerically in Chapter 3.

Scaling of theoretical signal current for a reference junction $I_{Sref}(t)$ to specified junction parameters.

In Chapter 3 we calculated the signal current by integrating the thermally caused excess current over the junction expressed methematically:

$$I_S(t) = \int_{A_J} (J_{SS}(T) - J_{SS}(T_B))dA \qquad (6.8)$$

where $J_{SS}(T)$ = current per unit area of the junction at temperature T.

T = $T(x,y,t)$ i.e., temperature is a function of location and time.

T_B = bath or ambient temperature.

A_J = junction area.

we can thus write for the reference junction:-

$$I_{Sref}(t) = \int_{A_{Jref}} (J_{SSref}(T) - J_{SSref}(T_B))dA \qquad (6.9)$$

Since $J_{SS}(T) = \frac{\delta I_{SS}(T)}{\delta A}$ and $J_{SSref}(T) = \frac{\delta I_{SSref}(T)}{\delta A}$

where δA is a small area element of the junction and $\delta I_{SS}(T)$, the current flowing in this element at temperature T; the same size of area δA is chosen both in the actual junction and in the reference junction.

Thus $\frac{J_{SS}(T)}{J_{SSref}(T)} = \frac{\delta I_{SS}(T)}{\delta I_{SSref}(T)}$

Confining our attention to this junction element for the moment and referring to the first paragraph of the scaling theory section where we showed that $\frac{I_{SS}}{I_{SSref}} = \frac{G}{G_{ref}}$, we get $\frac{\delta I_{SS}}{\delta I_{SSref}} = \frac{\delta G}{\delta G_{ref}}$, where δG, δG_{ref} are the conductances for the area elements δA.

Assuming that the junctions are uniform, such that

$$\frac{\delta G}{\delta G_{ref}} = \frac{G/A_J}{G_{ref}/A_{Jref}}$$

where G, G_{ref} are respectively the junction conductances for the junction under consideration and the reference junction respectively. We get:-

$$\frac{J_{SS}(T)}{J_{SSref}(T)} = \frac{G/A_J}{G_{ref}/A_{Jref}}$$

and (6.8) becomes:-

$$I_S(t) = \frac{G/A_J}{G_{ref}/A_{Jref}} \int_{A_J} (J_{SSref}(T) - J_{SSref}(T_B))dA$$

Thus:

$$\frac{I_S(t)}{I_{Sref}(t)} = \frac{G/A_J}{G_{ref}/A_{Jref}} \cdot \frac{\int_{A_J}(J_{SSref}(T) - J_{SSref}(T_B))dA}{\int_{A_{Jref}}(J_{SSref}(T) - J_{SSref}(T_B))dA} \qquad (6.10)$$

If $A_J = A_{Jref}$ then the ratio of the integrals clearly equals unity. For the case of an 5.13 MeV α-particle impact at the junction centre even when A_J is infinite, and $A_{Jref} = 4 \times 10^{-4}$ cm^2. the ratio is only <1.13. As calculated in Chapter 3 and shown in Fig. (3.17), an α-particle impact on an 'infinite' area junction gave a peak current of 2.09 μa and an impact in the centre of a finite junction of area $4 \times 10^{-4} cm^2$ and the same junction conductance per unit area gave a peak current of 1.84 μa, thus limiting the ratio of integrals in (6.10) to less than 1.13. The ratio is clearly close to unity if the junction area is comparable to the reference junction area, thus we can write

$$\frac{I_S(t)}{I_{Sref}(t)} \simeq \frac{G/A_J}{G_{ref}/A_{Jref}} \qquad (6.11)$$

This scaling relation is used later in this chapter.

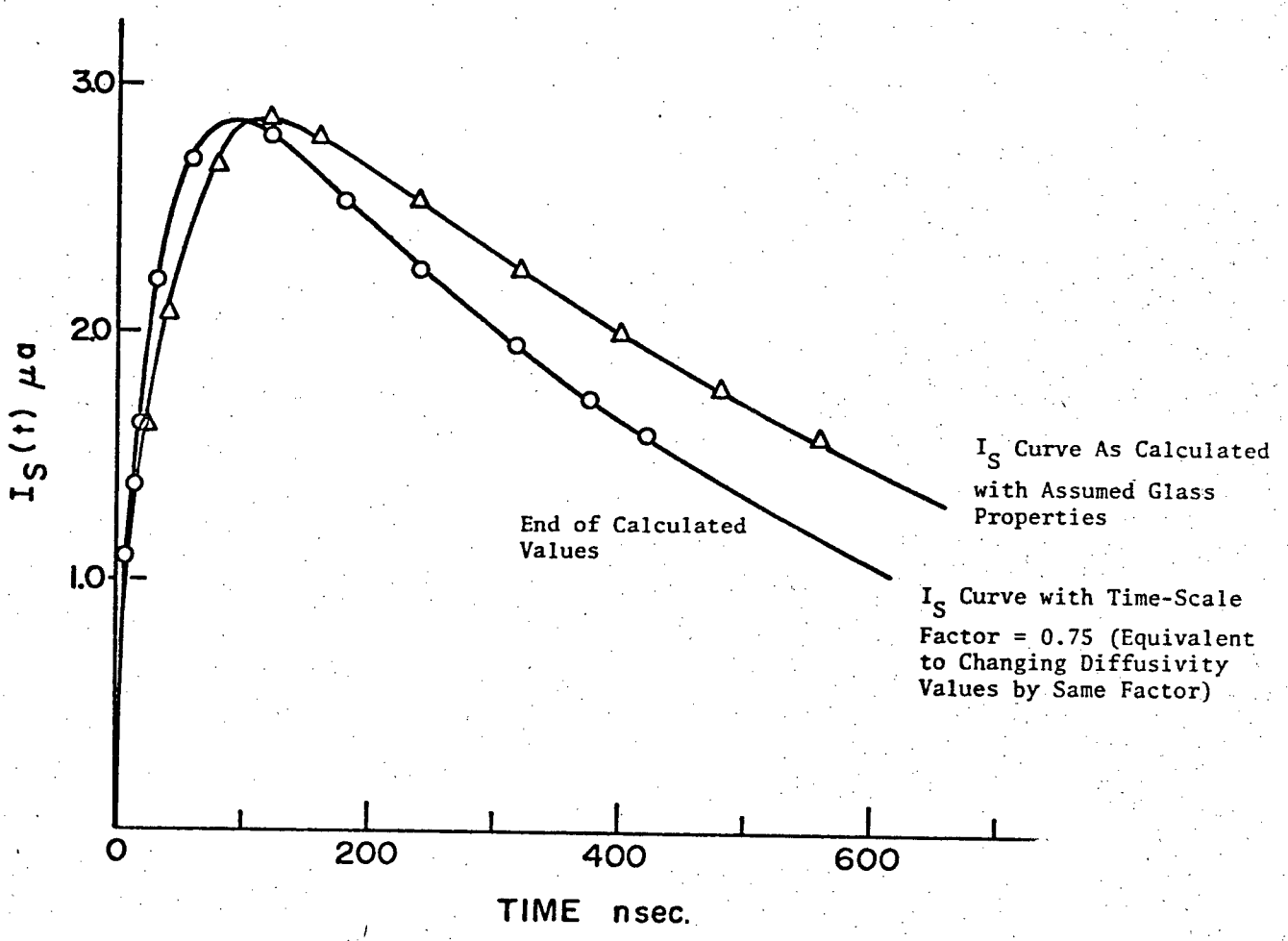

FIG. (6.5) Calculated Reference Junction Signal Current.

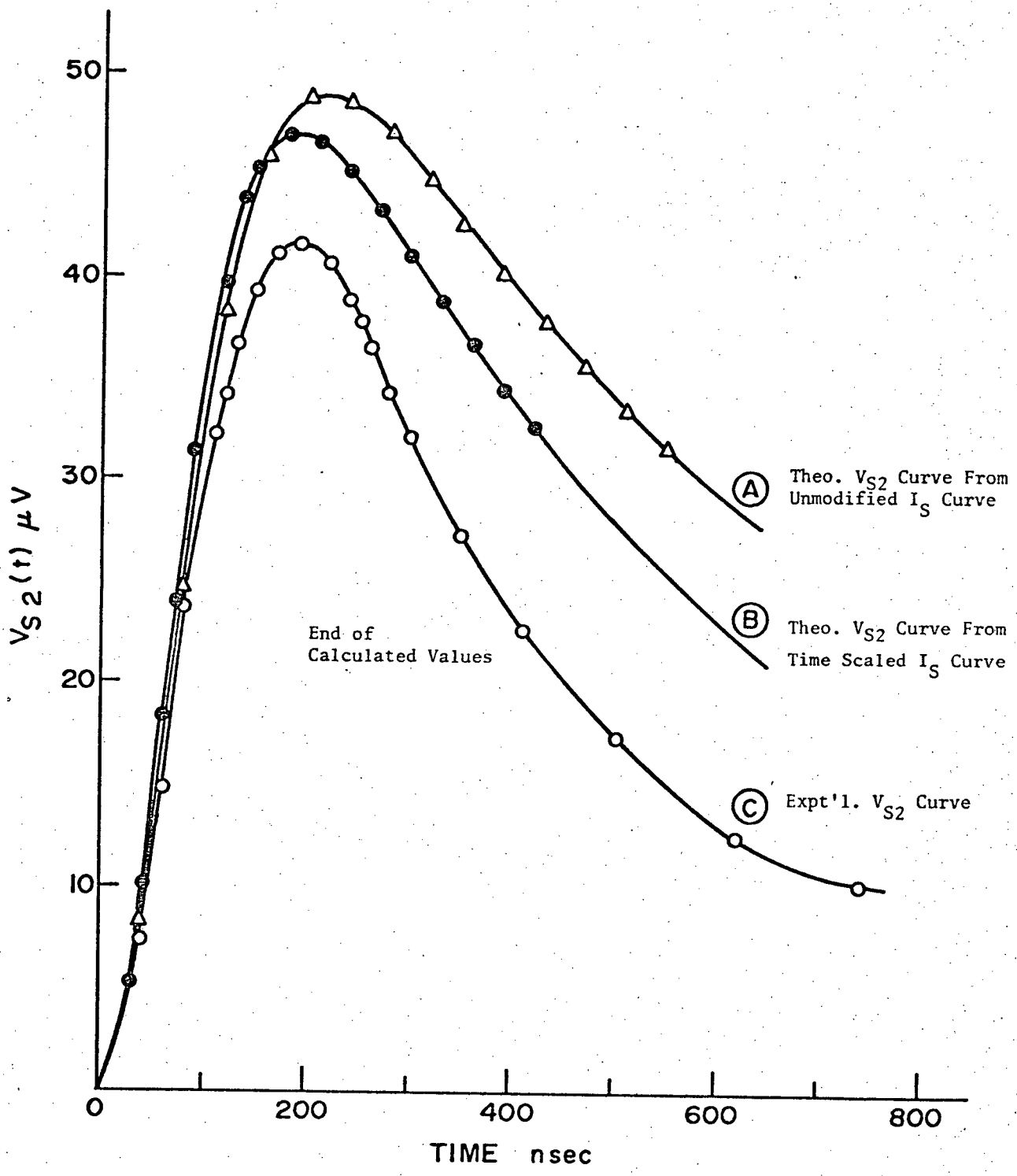

FIG. (6.6) Output Signal Voltage from Room Temperature Amplifier System.

Numerical calculations of the effect of junction capacitance and amplifier rise time on signal-voltage output waveform and comparisons with experimental observations.

Room temperature preamplifier case. We shall consider the observations made with the Sn junction R67S1J3 and the room temperature amplifier first. As the amplifiers in the system were wide-band RC coupled types the output waveform resembles the junction signal voltage waveform $V_{S_1}(t)$, which is related to the junction signal current $I_S(t)$ by equation (6.7). The pre-amplifier rise time of $\sim$5 ns can be ignored as it is much smaller than the minimum rise time 80 ns of the following Ortec linear-amplifier. Assuming the linear-amplifier had a RC type rise and fall characteristics (e.g. $(1-e^{-t/\tau})$ rise, $e^{-t/\tau}$ fall) then the 80 ns rise-time from 10% to 90% corresponds to an equivalent RC integration time constant of 38.5 ns. Thus $V_{S_2}(t)$ the signal-voltage output waveform was obtained from $V_{S_1}(t)$ by convolution with this RC time constant.

R67S1J3 had $R_N = 0.22\ \Omega$ and $A_J = 0.0586 \times 10^{-4}\ m^2$. Using equation (6.11) this gives $I_S(t) = 1.55\ I_{ref}(t)$ (Fig. 6.5). The estimated junction capacitance $C_J = 1500$ pf combined with the parallel sum of R_{dyn}, R_{leak}, and R_{load} (18 Ω) gives a junction RC time constant of 27 ns. Using the procedure outlined above and the values of $I_{ref}(t)$ for a (0,0) α-particle impact (see Fig. 3.14 for coordinates) $V_{S_2}(t)$ was calculated and plotted in Fig. (6.6). The amplitude of the theoretical $V_{S_2}(t)$ curve (A) was 1.176 times that of the experimental $V_{S_2}(t)$ curve (C) and the peaks occurred at 220 ns and 190 ns respectively. Considering the uncertainty in the low temperature thermal properties of glass, the agreement is very good. The later peak time of the theoretical curve indicated that the glass thermal

diffusivity values used were too low. A change in the glass thermal diffusivity values would result in a similar change in the time scale; thus to seek a better fit of calculated curves to experiment, various changes in the $I_{ref}(t)$ time-scale were tried, each new time-scale giving a set of trial $I_{ref}(t)$ values. For each set of $I_{ref}(t)$ values a corresponding set of $V_{S_2}(t)$ was calculated and compared with the experimental curve for match in peak time and match in the rising portion of the curve. A good match was obtained for a time-scale reduction factor of 0.75 (corresponding to a diffusivity increase of 1.33; this is shown in curve (B) Fig. (6.6). The ratio of theoretical to observed amplitude is now 1.13 and the waveform match is better.

In Chapter 3 when we calculated the $I_{ref}(t)$ curves we ignored the parallel radial thermal-conductance of the junction films, which was found to be ~ 0.178 that of the radial heat conductance of the thermally affected portion of the glass substrate. To account for the effect of heat transfer along the junction-films exactly we would have to go to a model of the heat-diffusion problem including the thermal presence of the junction films. The effort required for this is not presently justifiable. We can see that the effect of this extra heat path is to lower the temperatures in the impact area more rapidly, this being reflected in a slightly lower signal-current amplitude and a faster decay rate for the current waveform. Thus the inclusion of the junction-film heat conductance would bring the theoretical waveform closer to the experimental waveform.

Numerical calculation of α-particle induced output signal voltage from the transformer input amplifier system and comparison with experiments.

The response of the system (junction under test plus the amplifier system) to an externally applied calibration test charge was recorded. This gave the junction plus amplifier system response to a near delta-function deposition of charge in the junction. Thus as in the derivation of eqn. (6.7), the system output response to the signal current $I_S(t)$ is a convolution of $I_S(t)$ with delta-function charge response R(t):

$$Y(t) = \int_0^t I_S(t')\, R(t'-t)dt' \qquad (6.12)$$

where Y(t) is the output response and R(t) is the system response to unit charge, R(t) = 0 for negative argument. The experimental output response curve was obtained using Sn junction R164S1J5, with R_N = 0.30 Ω area = 4A2 x 10^{-4} m^2, thus using the signal-current $I_S(t)$ scaled by eqn. (6.11) we derived above for the input, we can calculate the expected output using (6.12). Unfortunately $I_S(t)$ values are available only to 0.42 μs, (the $I_{ref}(t)$ curve was calculated to 0.56 μs, which when contracted by the time-scale factor 0.75 described above gives an $I_S(t)$ curve from $0<t<0.42$ μs. Because of the complexity of the problem, with the present U.B.C. computer ∿ 1250 sec CPU time is required per μ sec of the thermal pulse computation. To compute values of $I_S(t)$ out to ∿ 8 μs, needed for the convolution (6.12), is not justifiable in terms of results. Thus extrapolated values of $I_S(t)$ were used in the calculations. The values $\frac{dI_S}{dt}/I_S$ were calculated at a series of points along the falling portion of the I_S curve. It was found that this ratio is nearly constant but decreases slowly beyond 0.30 μs indicating an exponential type of decay with time e^{-kt}. The small decrease

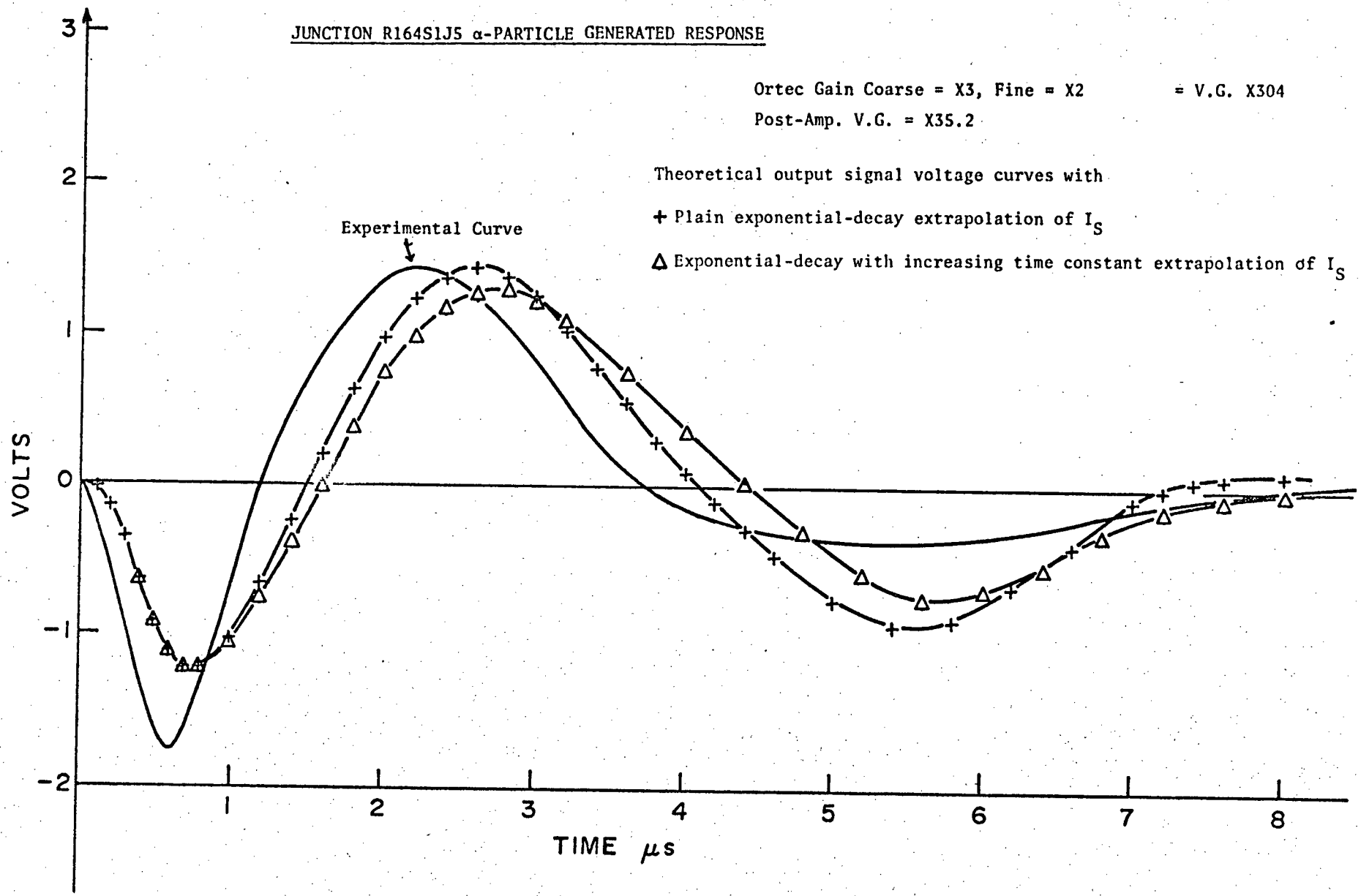
JUNCTION R164S1J5 α-PARTICLE GENERATED RESPONSE
Ortec Gain Coarse = X3, Fine = X2 = V.G. X304
Post-Amp. V.G. = X35.2
Theoretical output signal voltage curves with
+ Plain exponential-decay extrapolation of I_S
Δ Exponential-decay with increasing time constant extrapolation of I_S
Experimental Curve
VOLTS
TIME μs
3
2
1
0
-1
-2
1
2
3
4
5
6
7
8

FIG. (6.7)

in the ratio can be accounted for by a progressive decrease of k with time. Two Y(t) curves were calculated and plotted in Fig. (6.7). One Y(t) curve was calculated with exponential decay extrapolation of $I_S(t)$ with a constant time constant. The other used an exponential decay with the time constant increasing by a factor of 1.013 for each 6 ns. These two curves bracket that expected from the observed change of the time constant in the $I_S(t)$ curve, estimated at a value of t near the end of the computer calculated section of the curve. Referring to Fig. (6.7) the different extrapolations produced no change in the first peak of the signal voltage. The successive peaks are smaller for the extrapolation with increasing time constant with time (the increasing time constant can be thought of as a decrease in diffusivity with decrease in temperature). On the whole the differences between the curves are minor. The theoretical curves had a smaller first peak-amplitude than the experimental curve and the peak occurs slightly later. The time-shift of this peak may be accounted for by the uncertainty in the oscilloscope triggering delay. But even with this correction the first peak is narrower than the theoretical curve, thus suggesting a junction signal current with a narrower and more pronounced peak. The second peak more closely approximates the observed curve. The third peak is much lower in amplitude, suggesting a more gradual decay of I_S. The maximum peak to peak voltage ratio for the theoretical and experimental curves is 1.24 (using the 'plain' exponential decay extrapolation of I_S curve). The agreement of theory and experiment is reasonable.

Comparison of theoretically derived and observed output pulse amplitude distribution.

In Chapter 3 it was shown how α-impacts at different locations relative to the junction can produce different signal-current amplitudes and waveforms. C.f. (Fig. 3.13) and (Fig. 3.14). The resultant theoretical signal-current peak amplitude and total signal-charge to 0.56 μs for all points of the impact coordinate-grid were tabulated and amplitude distribution histograms plotted in Fig. 3.15, 3.16. The uneven appearance of the histogram is due to the coarseness of the impact coordinate grid used for the computations; too much computer time is needed for a finer grid. Fig. (5.25) Chapter 5 shows a representative experimental "kicksorter" record of the α-particle induced output pulses made with the transformer input low temperature preamplifier amplifier system described in Chapter 5. As the amplifier system is linear and the output voltage amplitude is signal charge dependent due to integration in the input transformer it is reasonable to assume that the expected output amplitude is directly proportional to the total signal charge accumulated up to 0.56 μs. Thus the curve in Fig. 3.16 should closely resemble the output amplitude probability density curve. Fig. 3.15 shows a histogram plot of signal current amplitude Vs. probability density. If the waveforms of all the pulses were similar, then the signal current amplitude would be proportional to the total signal charge and thus proportional to output voltage amplitude. In fact the waveforms are only roughly similar, so that Fig. 3.15 should only approximately resemble the output amplitude probability density curve. These theoretical distribution curves (Fig. 3.15 3.16) are in fact clearly similar to the experimental distribution curve in Fig. (5.25). The experimental curve contains in addition to the size effect,

the results of the "angle of impact" and of amplifier system noise which all tend to smear the distribution, thus the high amplitude cut off is not as sharp as the theoretical curves. The agreement of theory and experiment here is very important as only a 'thermometer model' of the glass substrated SPD can give rise to the observed pulse amplitude distribution using a monoenergetic α-particle source.

Summary:-

The theoretical expressions for I_{SS}/G, $^{1}/R_{dyn}G$, and $(\frac{\partial I}{\partial T})$ Vs. $\beta\Delta$ were in agreement with experiments thus the theoretical expression for $\frac{\partial V}{\partial T}$ may be correctly used to analyse low frequency signals. 'Scaling' of theoretical junction currents to obtain theoretical values for comparisons with experiment was discussed. Comparison of observed junction signal voltage pulses with theoretical junction signal voltage pulses was made, and the observed output signal with the transformer input preamplifier compared to the theoretical waveform with good agreement. The experimental pulse amplitude distribution (kicksorter record) was compared to the theoretical I_S peak and Q_S amplitude distribution, again with good agreement.

CHAPTER SEVEN

A PROPOSED SUPERCONDUCTIVE PARTICLE DETECTOR

THE HEAT-SINK CHIP TYPE

Referring to Figure (7.1) this hypothetical type of particle detector consists of a S.T.J. deposited on a chip of electrically insulating material with high heat conductivity at low temperature, such as diamond and sapphire, and the chip mounted such that heat loss from the chips occurs slowly, mainly by radiation and heat transfer to superfluid helium film; (if any). The heat from the particle impact quickly diffuses in the chip resulting in a quasi uniform increase in the temperature of the chip and of the S.T.J. deposited on the chip. In this case the thinner the junction films the better, to reduce the heat-capacity of the chip-junction combination, (since the thermal-mass is decreased).

The uniform increase of the S.T.J. temperature results in increased quasi-particle tunnelling-current providing the signal output.

This type of S.P.D. appears potentially to be the best of the three described. Because of the more uniform increase in temperature over the junction area, signal variations from junction non-uniformity, if any, are reduced. The "angle-effect" and "finite junction size effects" (described later in this chapter) factors which severely degrade resolution in the previous types do not affect this type of S.P.D. Because of confinement of the heat to the heat-sink chip, the particle energy utilization is much better resulting in an order of magnitude improvement expected in signal output. Radiation damage to the S.T.J. is avoided in the proposed version of the heat-sink chip S.P.D. in Figure (7.1) because the particle never reaches the junction film.

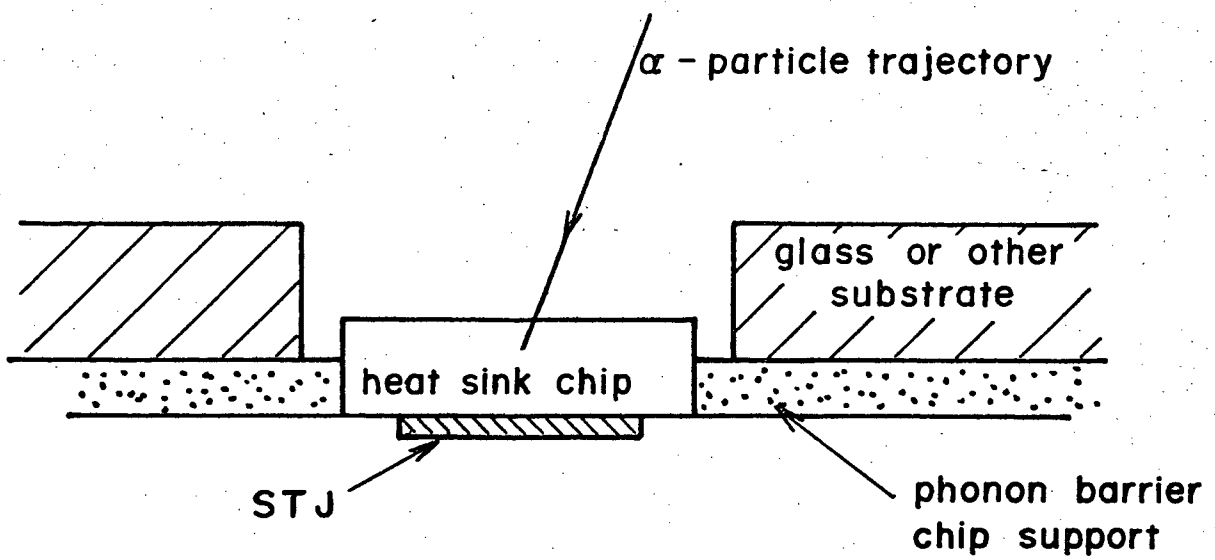

Fig. 7.1 Alpha-Particle Impinging on Heat Sink Chip Type Superconductive Quasiparticle Tunnelling Junction Particle Detector.

The heat-sink chip model is justifiable if the time for temperature averaging is much smaller than the temperature decay time. As the range of a 5.13 MeV alpha-particle in diamond is 19.6 μ a 20 μ thickness in the chip is sufficient to stop the alpha-particles assuming that the chip is the same area as the junction, the dimensions of the currently used S.T.J. are 0.2 mm x 0.2 mm., we have the chip dimensions as 0.2 mm x 0.2 mm x 20 μm. The mean free path of phonons in diamond at <2 K is much greater than the chip dimensions (Reference 7.1). The acoustical velocity in diamond is $>10^4$ m/sec. thus the single transit time <20 n sec. with consequent temperature averaging time a few times this value, much smaller than the expected thermal decay time of > 1μ sec.

Based on the heat-sink chip model we can write the following equations:-

$$M.Cp.\ \delta T = \delta Q \qquad (7.1)$$

$$\frac{\partial Q}{\partial t} = K\ (T^4 - T_B{}^4) \qquad (7.2)$$

where: M = mass of heat-sink chip,

Cp = Specific heat of the heat-sink chip.

δT = small change in temperature of the chip,

δQ = small change in the quantity of heat in the chip,

T = temperature of the chip, assumed uniform,

T_B= 'bath' or surrounding temperature,

K = constant structurally dependent, (can be selected within limits), depends on the area weighted sum of the radiation heat loss rate proportionally constant and the super fluid helium film heat loss rate proportionality constant.

Equation (7.1) expresses the definition of heat capacity, i.e. $\frac{\partial Q}{\partial T} = M.C_p$.

Equation (7.2) expresses heat-loss rate due to radiation (or like processes).

Since $\delta Q = \frac{dQ}{dt} \cdot \delta t$

We get from Equations (7.1), (7.2) $Mc_p \delta T = \frac{dQ}{dt} \delta t = -K(T^4 - T_B^4)\delta t$ - (7.3)

For diamond at low temperatures, $C_p = \alpha T^3$ where α is the Debye constant thus we get from (7.3)

$$\frac{dT}{dt} = - \frac{K \ (T^4 - T_B^4)}{M\alpha \ T^3} \qquad (7.4)$$

$$\therefore dt = -\frac{M\alpha}{K} \ dT \ \frac{T^3}{(T^4 - T_B^4)}$$

or $(T^4 - T_B^4) = A \exp\left(\frac{-4K}{M\alpha}\right) t$

where A is a constant of integration, equal to $(T_o^4 - T_B^4)$.

Thus we get finally

$$T^4 = (T_o^4 - T_B^4)\, e^{-\frac{4K}{M\alpha} t} + T_B^4$$

or $$T(t) = \left[(T_o^4 - T_B^4)\, e^{\frac{-4K}{M\alpha} t} + T_B^4 \right]^{1/4} \qquad (7.5)$$

We next calculate the initial temperature T_o when a quantity of heat δQ_o is deposited in the heat-sink chip by the alpha-particle:

From (7.3)

$$\delta Q_o = \int_{T_B}^{T_o} M\alpha\, T^3\, dT$$

$$= \frac{M\alpha}{4} [T_o^4 - T_B^4] \qquad (7.6)$$

The integration is necessary because of the temperature dependence of heat capacity of the chip.

$$\therefore\ T_o = \left[\frac{4.\delta Q_o}{M\alpha} + T_B^4\right]^{1/4} \qquad (7.7)$$

and by differentiation:-

$$\frac{\delta T}{\delta Q_o} = \frac{\left[\frac{4\delta Q_o}{M\alpha} + T_B^4\right]^{-3/4}}{M\alpha} \qquad (7.8)$$

and $$\left.\frac{\delta I_{SS}}{\delta Q_o}\right|_V = \left(\frac{\partial I_{ss}}{\partial T}\right)_V \frac{\partial T}{\partial (Q_o)}$$

$$= -\frac{2G\Delta\alpha K_B\beta^2}{eM\alpha} e^{-\beta\Delta} [e^{-\beta ev}(ev+\Delta) - \Delta] \left[\frac{4\delta Q_o}{M\alpha} + T_B^4\right]^{-3/4} \quad (7.9)$$

From equations (7.7) we get the initial temperature of the chip T_o, when a particle of energy δQ_o is stopped in the heat sink chip. Substituting T_o in equation (7.5) we get the chip (and S.T.J.) temperature as a function of time. Substituting this temperature in equation (2.8) for N.S. and equation (2.15) for S.S. junctions we get I_{NS} or I_{SS} as a function of time, thus all necessary S.P.D. parameters can be derived analytically. Equation (7.9) gives a useful sensitivity parameter, and can give the signal-current for a low-energy particle impact. It is possible to improve resolution further at low particle-energy by reducing the chip thickness and thus the heat capacity. The improvement is limited by the heat capacity of the S.T.J., and heat leakage through electrical connections to the S.T.J. This type of S.P.D. is different from the glass substrate type mainly in the effective thermal size and thermal conductivity of the substrate in contact with the junction films. The heat-sink chip is chosen such that it has the smallest possible heat

capacity consistent with stopping the impacting particle, and conducting the heat rapidly to all parts of the junction film to obtain the maximum rise in temperature at the junction film. None of these features exist for the glass substrate type.

Limits on Performance of the SPD.

The heat-sink chip type SPD offers the best theoretical prospects for high performance, hence only this type will be dealt with in this section. One of the limitations is the heat capacity of the STJ films. For the junctions used in our experiments, the film thickness was about 4000 A (top and bottom films), of Sn. The heat capacity of this STJ at 1.2 K (the operating temperature) is $\sim$ 2.43×10^{-12} J/ K. Conceivably a STJ can be made with films $^{1}/_{10}$ as thick, with cooled substrate, thus with heat capacity of 0.243×10^{-12} J/ K. A diamond heat-sink chip with the same heat capacity at 1.2 K must then be 65.7 μm thick, if it is of the same dimensions as the STJ, e.g. 0.2 mm x 0.2 mm. Assuming R_{dyn} = 100Ω and $\frac{\partial I}{\partial T} = 0.526 \times 10^{-4}$ amp/ k (these have been experimentally achievable values by the author) we get 0.575 KeV/μV of signal (or 1.739 μV/ KeV).

From equation (2.)

$$\overline{V_{NT}^2} = \Delta \cdot \frac{e^{\beta\Delta}-1}{2C_J}$$ and putting in numbers, $\beta\Delta = 5.375$

$\Delta = .8905 \times 10^{-22}$ J

$C_J = 1.5 \times 10^{-9}$ Farad

or $\sqrt{V_{NT}^2}$ = 0.917 μV , this is an overestimate as we assumed infinite bandwidth.

Thus for a 1:1 SNR criterion of resolution, it is possible to resolve 0.527 KeV, (assuming a noiseless amplifier).* This figure can be improved

---

* in fact our present low-temperature amplifier can give 1:1 SNR for 0.5 μV signal.

if STJ's with lower heat capacity can be made. With this sensitivity we come against a large-signal limit, a large current-response cause 'saturation'. This saturation can be avoided by biasing not at the max. R_{dyn} point, but at a high current low R_{dyn} point, such that for the desired signals, the device operate at the point of max. R_{dyn}., thus we have an electronically adjustable 'window', of $\sim 2\Delta$ in width for our example this means a window of 1.11×10^{-3} volts or $\sim$ 639 KeV width. This limitation is inherent, if S is the sensitivity of the detector in volts/ KeV and 2Δ is expressed in volts, then the window W is given by $W < 2\Delta/S$. Lower operating temperatures are achievable, for example using He^3 temperatures of 0.3 K are readily attainable by simple pumping. With He^3/He^4 dilution refrigerator temperatures of $\sim$ 0.015 K can be attained. The He^3 refrigerator appears to be more practical. Assuming 0.4 K is attained at junction films of Al, (corresponding to $\beta\Delta = 5.3$, as in the previous example with Sn). The heat capacity for the 0.2 mm x 0.2 mm x 400 A junction films is 0.896×10^{-14} J/ K. Assuming the same junction parameters as before (since $\beta\Delta$ is the same) we get 47.2 μV/KeV for the sensitivity of the detector. Further, since the total inherent noise is proportional to Δ (C.F. equation 2.45) the total inherent junction rms noise-voltage is <0.522 μV. Thus the inherent resolution limit for SNR (signal peak voltage/rms noise voltage) = 1 is 11.3 eV, assuming a noiseless amplifier.

We next consider the magnitude of statistical-fluctuation noise for the Al junction at 0.4K. Assuming a particle energy of 20 KeV, we should get 0.943 mV of signal voltage or 9.43 μa of signal current. Assuming a current-decay time constant of 5 μs, the signal charge is then $Q_s = 47.15$ pC. Corresponding to a number of charge carriers $N = 0.2943 \times 10^6$. Thus

if Fano factor = 1 the resolution is

$$\frac{\sigma_q}{\bar{q}} = \frac{1}{\sqrt{N}} = \underline{1.842 \times 10^{-3}} \text{ corresponding to } \underline{86.6 \text{ eV FWHM}} \text{ assuming gaussian line peak}$$

If the Fano factor is the same as that for Ge, F = 0.08, then

$$\frac{T_q}{q} = \frac{F}{N} = \underline{0.521 \times 10^{-3}} \text{ corresponding to } \underline{24.5 \text{ eV FWHM}} \text{ assuming gaussian line peak}$$

This compares with $N = 0.6803 \times 10^4$ for a 20 KeV particle detected by a Ge junction-detector, and $\sigma_q/\bar{q} = \underline{0.343 \times 10^{-2}}$, corresponding to $\underline{161.2 \text{ eV}}$ FWHM. Using the value of N we had for the SPD, above for 20 KeV particle energy, we get the energy per charge carrier $w = \underline{0.068 \text{ eV}}$ as compared to $w_{Ge} = \underline{2.94 \text{ eV}}$.

If our assumptions and calculations above, based on the hypothetical 'Heat-sink Chip' type superconductive particle detector are correct, then the SPD is a practical device, an improvement over the currently available detectors. It may be of use in the spectrometry of X-rays in the range 100 eV to 20 KeV say, where the statistical noise is smaller and the inherent noise (11.3 eV) would be dominant.

CHAPTER EIGHT

CONCLUSIONS

Principal Results from the Present Work

The signal-current pulse through a superconductive tunnelling junction, resulting from the impact of an α-particle on the junction (deposited on a glass-substrate) was found to be nearly entirely due to the subsequent rise in temperature of the junction area near the impact point, increasing the quasiparticle density and thus the tunnelling current in that area. Numerical calculations based upon this mechanism for junction signal-current production, and upon classical heat-diffusion, gave signal-voltage waveforms resembling observed signal voltage waveforms (C.f. Ch. 6 Fig. 6). This approach also predicted that for a finite area junction on a glass substrate an output pulse amplitude distribution (for a monoenergetic source of α-particles of energy 5.13 MeV) would have no lines or peaks. A pulse-amplitude distribution with a rapid decrease in pulse-density (per unit energy) with increasing energy, followed by a plateau region and a sharp high amplitude cut off was predicted (C.f. Fig. 3.15, 3.16). A very similar amplitude distribution was experimentally observed. Based on the agreement of theory and experiment we can conclude with reasonable confidence that thermal-model for the production of junction signal-current is valid.

The parameter $\beta\Delta$ was used in studying superconductive-tunnelling junction characteristics. The results were thus applicable to superconductive tunnelling junctions made with any superconductor. The

derived theoretical expressions for junction characteristics were verified for SS junctions by experimental data, thus the theoretical predictions based on these expressions should be valid. The main theoretical results are that an optimum $\beta\Delta$ value exist for a specified junction-capacitance C_J and bandwidth of the expected signal, Δf, this value being $\beta\Delta \sim 6$ for $C_J = 1500$ pf and $\Delta f = 10^6$ Hz, and that noise power associated with the junction is proportional to Δ. From these results we conclude that for the best signal to noise ratio we select the lowest Δ such that at the optimum $\beta\Delta$ value for the junction, the corresponding temperature is obtainable experimentally. The theoretical expressions for NS junctions were not verified experimentally, but these were based on well accepted theoretical derivations (for example I. GIAVER, ref. 2.1). The theoretical comparison between SS and NS junctions showed conclusively that SS junctions are better for use as superconductive particle detectors for bandwidth $< 10^9$ Hz.

Experimentally, α-particle induced signal pulses were observed with Sn and Pb junctions. For the Sn junction R67S1J3 using the room temperature preamplifier (C.f. Ch. 5), the maximum junction signal voltage amplitude was 29.9 μV, and the measured equivalent input noise was 3.3 μV RMS corresponding to a SNR of 9.06. Using the transformer-input low temperature preamplifier a signal to noise ratio of 20.6 was observed for Pb junction R148S2J2 and a SNR of 40.0 for the Sn junction R164S1J5, sufficient to give a resolution of $\sim$ 128 KeV line-width if a line-type pulse amplitude distribution were present. With the 5.13 MeV α-particles used, as mentioned above no lines or peaks were present in the pulse amplitude spectrum. Based on the agreement between

theory and observations we can be reasonably confident that the physical phenomena associated with α-particle induced signal-current in the superconductive particle-detector are understood.

Expected Performance of Superconductive Particle Detectors

The glass-substrate type S.P.D. because of the finite junction-size effect (detailed in Chapter 3) cannot give a line-type spectrum. In addition, the 'angle-effect' further smears out the expected sharp high-energy cut off for normally incident particles if the particle penetrates deeply into the substrate. Thus the glass-substrate type S.P.D. is of no practical value as a particle energy spectrometer. Based on the understanding of the origin of the junction signal-current, a theoretically superior type of S.P.D. is proposed, the Heat-sink chip type. This type has not yet fabricated, however, based on the geometry of the S.P.D. and our theoretical understanding we can calculate the signal-current waveform of this type analytically, the detailed derivations are included in Chapter 7. For an Al-Al_2O_3-Al junction operated at 0.4 K junction temperature (using a He^3 cryogenic system) the inherent noise for the S.P.D. was estimated to correspond to <11.3eV, energy resolution and the energy per charge carrier (per electronic charge) w=0.068eV (see Ch. 7). For comparison the best particle energy spectrometers available at present are lithium drifted germanium junction detectors which have an inherent noise ∿ 115 ev (ref. 1.3) and energy per charge-carrier w = 2.94 ev. Thus used with a low noise preamplifier like the superconductive amplifier of Ref. 5.7., the heat-sink chip type S.P.D. promises to be an improvement over existing particle energy spectrometers in the studies of low energy (<10 kev)

particles and x-rays.

Future work

As estimated above the heat-sink chip type of S.P.D. should be a useful device in the spectrometry of low energy particles and x-rays. Actual samples of this proposed S.P.D. must be fabricated to verify the estimates. Further improvements are theoretically possible with the use of lower temperatures and lower energy gap superconductors for the tunnelling-junctions, (the lower temperatures to be reached with a He^3 dilution refrigerator). To fully realize the potential of the S.P.D., superconductive preamplifiers mentioned above should be investigated and developed. Technically it should be possible to fabricate both devices simultaneously in the same fabrication run. A conventional semiconductor low temperature amplifier may be used with the superconductive preamplifier stage, if necessary, before feeding the signal out of the cryostat. It would be necessary to separate the He gas from the S.P.D. (using a cold finger) toprevent loss of resolution due to scattering of the particle by the gas. As the proposed S.P.D. uses an Al-Al_2O_3-Al tunnel junction, the room temperature degradation and thermal-cycling degradation problems may not exist, as these junctions are known to be durable, however, should there be such problems then this is another area of possible improvements.

APPENDIX 5.1

For low bias magnetic fields current steps can occur in S.T.J. I.V. characteristics due to Josephson effect. (Fig.1) If the junction is biased near this current step then the current rise produced by a particle impact would cause the voltage across the junction to change less than otherwise, that is, the voltage change is 'clipped' by the current step. This clipping causes an increase in the number of pulses with amplitude equal to the difference between the bias point voltage and the voltage at the current step, thus producing a 'false' peak in the kick-sorter record (Fig. 2). This must obviously be prevented if the STJ is to be used as a particle energy spectrometer.

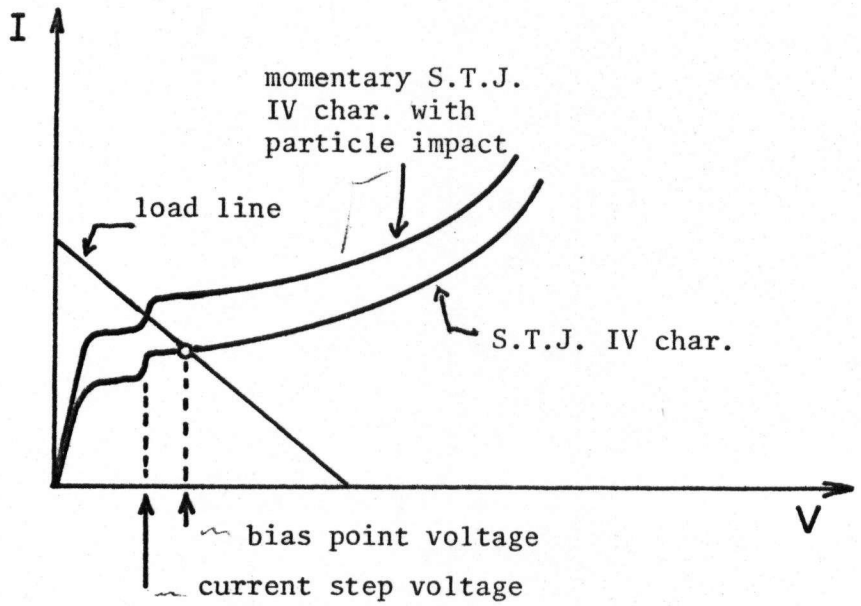

FIG. 1. CURRENT-STEP SIGNAL-VOLTAGE CLIPPING EFFECT.

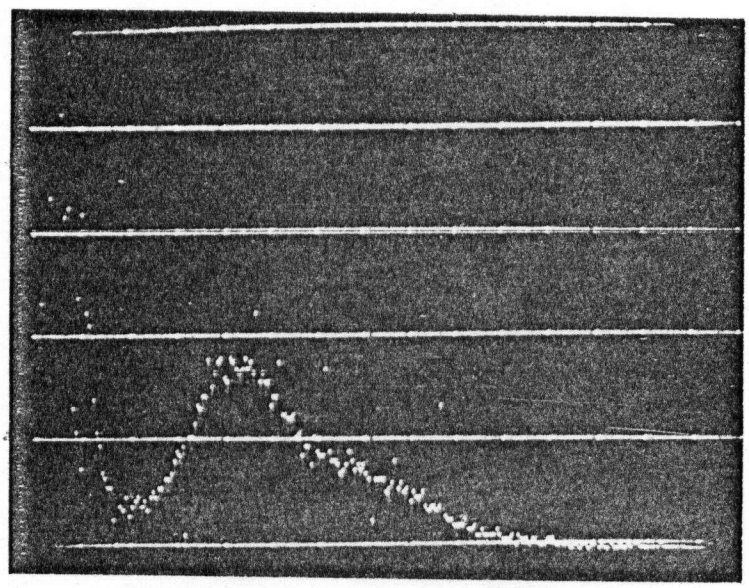

FIG. 2. OBSERVED FALSE-PEAK EFFECT DUE TO CLIPPING FOR JUNCTION R164S1J5.

BIBLIOGRAPHY

References Chapter 1

(1.1) Dearnaley, and Northrop, "Semiconductor Counters for Nuclear Radiations" 2nd Ed., E. and F.N. Spon Ltd., London, (1966).

(1.2) as above, page (89→91).

(1.3) Goulding, Walton and Pehl "Recent Results on Optoelectronic Feedback Preamplifiers", IEEE Trans. on Nuclear Science (U.S.A.) Vol. NS-15 #3, p.218, (1967).

(1.4) Goulding, Walton and Malone "An Opto-Electronic Feedback Preamplifier for High Resolution Nuclear Spectroscopy", Lawrence Radiation Lab., UCRL-18698 (1969).

(1.5) Giaver. I., Phys. Rev. Lett., 5, 147, (1960); 5, 464, (1960).

(1.6) Josephson, B.L. "Coupled Superconductors", Rev. Mod. Phy., 36, p. 216-220, (Jan. 1964).

(1.7) Solymar, L. "Superconductive Tunnelling and Applications" Ch. 3,4. Chapman and Hall Ltd. (1972).

(1.8) Wood, G.H., Ph.D. thesis U.B.C. "The detection of α-particles with superconducting tunnel junctions", Department of Physics, University of British Columbia, (August 1969).

(1.9) Wood, G.H. and White, B.L., Appl. Phy. Lett., 15, 237, (1969).

(1.10) Wood, G.H. and White, B.L. "The detection of α-particles with superconducting tunnel junctions", Can. J. Phys., 51, #19, p.2032-2046, (1973).

References Chapter 2

(2.1) I. Giaver and K. Megerle, Phys. Rev. 122 1101 (1961).

(2.2) P.G. De Gennes, "Superconductivity of Metals and Alloys" W.A. Benjamin (1966).

(2.3) A. Erdelyi, "Table of Integral Transforms" McGraw-Hill, New York (1954), p. 136.

(2.4) B. Muhlshlegel, Z. Phys., 155 313 (1959).

(2.5) J. Nichol, S. Shapiro and P.H. Smith, Phys. Rev. Lett. 5, p. 461 (1960).

(2.6) S. Shapiro, P.H. Smith and J. Nichol et al., IBM J. Res. Dev. 6 p. 34 (1962).

(2.7) Dearnaley and Northrop, Semiconductor Counters for Nuclear Radiations E. & F. N. Spon Ltd. (London), (1966).

(2.8) B.I. Miller and A.H. Dayem, Phys. Rev. Lett. 18 1000 (1967).

References Chapter 3

(3.1) "The Transport of Heat Between Dissimilar Solids at Low Temperatures", W.A. Little, Can.J. of Phys. Vol.37 (1959) page 334-349.

(3.2) Wilks, J. "The Properties of Liquid and Solid Helium" page 422-430, Oxford, Clarendon Press, (1967).

(3.3) E.C. Crittenden Jr., & Donald E. Spiel, "Superconducting Thin-Film Detector of Nuclear Particles", J. App. Phy. Vol. 42, #8, pages 3182-3188, (Jul. 1971).

(3.4) Jaeger & Carslaw, "Conduction of Heat in Solids" Oxford Clarendon Press (1959).

(3.5) Thermophysical Properties Research Center, Databook Vol. 1, Fig. 1059, Purdue University (1966).

(3.6) Kunzler & Kenton, Phy. Rev. 108 139T (1957).

(3.7) Andrew, E.R., Proc. Phy. Soc. (London) 62 88 (1949).

(3.8) Chopra (P.349) "Thin Film Phenomena", McGraw-Hill (1969).

(3.9) L.I. Maissel & M.H. Francombe, "An Introduction to Thin Films", page 161, Gordon & Breach Publishers, New York (1973).

(3.10) "Specific Heat of Pyrex" Curve 4.401, WADD Technical Report 60-56, Part 2, "A Compendium of the Properties of Materials at Low Temperatures" Phase II, Victor T. Johnson General Ed., N.B.S. Cryogenic Eng. Lab. October 1960.

(3.11) "Thermal Conductivity of Glasses and Plastics" Curve 3.501 Same publication as (3.10).

(3.12) "Low Temperature Techniques", A.C. Rose-Innes, English Universities Press Ltd., (London) England (1964).

(3.13) "Specific Heat of Sn" 1K- 10K, 10K- 300K Curves 4.142-3
"Thermal Conductivity of Tin and Lead" 4K- 300K Curve 3.142-3
WADD Technical Report (Cf. Ref. 3.10).
"Thermal Conductivity of Tin" 1K- 30K Curve 105, Fig. 1027, Thermophysical Properties Research Centre Data Book, Vol. 1, Purdue University (1966).

(3.14) "Specific Heat of Lead" 1K- 10K, 10K- 300K, Curves 4.142-3.
"Thermal Conductivity of Lead" 4K- 300K, Curve 3.142-3,
WADD Tech. Report (Cf. Reference 310).
"Thermal Conductivity of Lead", 1K- 4K, Curve 28, Fig. 101,
Thermophysical Properties Research Centre Data Book, Vol. 1,
Purdue University (1966).

(3.15) K. Mendelsohn, "Cryophysics", p.120, Interscience, (1960).

References Chapter 4

(4.1) "The formation of metal oxide films using gaseous and solid electrolytes", J.L. Miles and P.H. Smith, J. of the Electrochem. Soc., Vol. 110 p. 1240 Dec. (1963).

(4.2) "Plasma anodized aluminium films", G.J. Tibol and R.W. Hull, J. of the Electrochem. Soc., Vol. 111 p. 1368 Dec. (1964).

(4.3) "Physics of Preparation of Josephson- Barrier", W. Schroen, J. Appl. Phy., Vol. 39 #6 p. 2671 May (1968).

(4.4) "Anodic Oxide Films", C.J. Dell'Oca, D.L. Pulfrey and L. Young, U.B.C. Department of Electrical Engineering, Private Communications.

(4.5) "Tin Whiskers"
Kehrer and Katdereit, Appl. Phy. Lett. 16 #11 p. 411 June (1970).

(4.6) Holland, L., Vacuum Deposition of Thin Films, London, Chapman & Hall (19

(4.7) P.P. Luff and M. White, Vacuum, 18 #8 p. 437-450, Pergamon Press (May 19

(4.8) Degennes, Superconductivity of Metals and Alloys, W.A. Benjamin, New York, p. 227-238 (1966).

(4.9) G.H. Wood, "The Detection of α-particles with superconductive tunnelling junctions", Ph.D. thesis, Department of Physics, U.B.C. (1969).

References Chapter 5

(5.1) G.K. Mendelsohn, Cryophysics, Interscience, New York (1960).

(5.2) C.J. Adkins, Phil. Mag. 8, 105 (1963).
Rev. Mod. Phys. 36, 211 (1964).

(5.3) J.R. Schrieffer, and J.W. Wilkins, Phys. Rev. Letts. 20, 581 (1966).
J.W. Wilkins, "Tunnelling Phenomina in Solids" Plenum Press, (E. Burstein and S. Lundquist, Eds.) (1967).

(5.4) H.P. Kehrer and H.G. Kadereit "Tracer Experiments on the Growth of Sn Whiskers", Appl. Phys. Letts. 16, No. 11, p. 411 (1 June 1970).

(5.5) R.J. Harris and W.B. Shuler, "500 Volt Resolution with a Si(Li) Detector using a cooled F.E.T. Preamplifier". Nuclear Insts. and Methods. 51 341 (1967).

(5.6) E. Elad and M. Nakamura, "Hypercryogenic Detector-F.E.T. Unit, Core of High Resolution Spectrometer". IEEE Trans. Nuclear Sci. (U.S.A.), Vol. NS-15 No. 3 p. 477-85, June 1968.

(5.7) K.T. Burnette and V.L. Newhouse, "Observation of Single Fluxon Drift through a Superconductor". J.A.P. 42, No. 1 p. 38-146 (January 1971).

(5.8) V. Radhakrisnan and V.L. Newhouse "Noise analysis for amplifiers with superconducting inputs", J.A.P. 42, No. 1 p. 129-139 (Jan 197

(5.9) R.R. Green "Mosfet Operation at 4.2^{o}K" Rev. Sci. Inst. 39, No. 10 1495-1497, (October 1968).

(5.10)O. Parrish, Report on low temperature amplifiers, private communication.

(5.11)F. Witteborn, (Stanford Research Inst.) private communication to Professor Gush, Physics Department, U.B.C.

(5.12)G.H. Wood, Table 3.3, page 76, Ph.D. Thesis, Department of Physics, U.B.C (1969).

(5.13)W. Schroen, "Physics of Preparation of Josephson-Barriers", J.A.P. 39, No. 6, p. 2671 (1968).

(5.14)E. Burstein, S. Lundquist, "Tunnelling Phenomena in Solids", Plenum Press (1967).

References Chapter 7

(7.1) Berman Simon & Wilks, Nature 168 227 (1951)

PUBLICATIONS & PATENTS (PARTIAL LIST)

"Seismic work with light-weight equipment on arctic glaciers". Axel Heiberg Island Research Reports, McGill University, Prelim. report 61-62

"The Design of a Monolithic Integrated RST-JK Flip-Flop".+ Can. Electronic Eng. Sept. 1966

"Large-Scale Integration by Redundancy Adjustment of Probabilities"+ Can. Electronic Eng. Nov. 1967

"An Improved Avalanche Injection Transistor" Proc. I.E.E.E., Letters. Jan. 1968. Vol. 56 No. 1 p. 105

"The Schottky-Barrier-Collector Transistor"+Solid-State Electronics, Pergamon Press, Vol. 11, pp. 613-619. 1968

+Patented, patents assigned to Northern Electric Ltd.

"Potentiometer"	U.S. Pat. 3,284,697 Nov. 1966	Issued
"Voltage-Scanned Device"	U.S. Pat. 3,388,255 Jan. 1970	Issued
"Voltage-Scanned Device"	Can. Pat. 793,399 Aug. 1968	Issued
"Spot Scanner"	U.S. Pat. 3,558,897 Jan. 1971	Issued
"Spot Scanner"	Can. Pat. 901,687 May 1972	Issued
"Electronic Digital Telephone Exchange"	pat. Pending	